Recycling of Titanium Alloys from Machining Chips using Equal Channel Angular Pressing

---

by

Qi Shi

Doctoral Thesis

Submitted in Partial Fulfilment of the Requirements for the Award of Doctor of Philosophy

2015

School of Aeronautical, Automotive, Chemical and Materials Engineering, Department of Materials

ACKNOWLEDGEMENTS

I would like to take this opportunity to express my deepest appreciation to the following people without whom I would never have finished this project:

First and foremost, I owe my greatest debt of gratitude to my supervisors, Dr Yau Yau Tse and Dr Rebecca Higginson. I want to thank Yau Yau because not only she has given her help, guidance and friendship throughout this project, but also she has kept encouraging me when I met with difficulties. She has given me many opportunities to present my work at various conferences, which increased my confidence and overcame my fear. I must also express my gratitude to Dr Rebecca Higginson, a respectable, responsible and resourceful scholar. She has provided me with invaluable advice, constant encouragement and precise modification during the mould design, experiment and thesis writing. She is always patient and generous to give me constructive and insight comments when I felt confused and hopeless.

Second, my sincere thanks also go to the workshop of Materials Department, David Insley, Mac Callender and Mike Kemp, who have helped to fabricate the mould and build up the hydraulic pressing system. Thanks for being the first person to help me every single time when I was stuck in front of the worktable. Additional thanks must also go to the workshop of Aeronautical and Automotive Engineering, Pradip Karia and Martin Cramp, for their support in fabricating the heating controllers.

All members of Loughborough Materials Characterization Centre (LMCC), especially Scott Doak, Zhaoxia Zhou, Keith Yendall and Geoff West, should also receive thanks for their guidance and assistance with microscopy working.

Financial support from Materials Department, Loughborough University is gratefully acknowledged. I would also like to thank Dr Roy Anish and Dr Riaz Muhammad for material providing.

Finally, I wish to express my highest appreciation to my mum and dad. Your spiritual support makes me brave enough to chase my dream in the foreign land. Thank you so much.

ABSTRACT

During the traditional manufacturing route, there are large amount of titanium alloys wasted in the form of machining chips. The conventional recycling methods require high energy consumption and capital cost. Equal channel angular pressing (ECAP), one of the severe plastic deformation techniques, has been developed to recycle the metallic machining chips. The purpose of the PhD work is to realize the ECAP recycling of titanium alloys, in particular Ti-6Al-4V and Ti-15V-3Cr-3Al-3Sn, and investigate the effects of processing parameters on the resultant relative density, microstructure evolution, texture development and microhardness homogeneity.

The microstructures of Ti-6Al-4V and Ti-15V-3Cr-3Al-3Sn machining chips obtained from conventional turning (CT) and ultrasonically assisted turning (UAT) were initially investigated. It was found that ultrafine grains were formed in the primary and secondary shear zones. For Ti-6Al-4V chips, the β phase in the shear zones was refined into nano-sized equiaxed grains and aligned up to form banded structures. For Ti-15V-3Cr-3Al-3Sn chips, the nano-crystalline grains were enveloped in the shear zones and have clear boundaries to the surrounding matrix. It was observed that in terms of microstructure, there is no significant difference between CT and UAT chips.

Recycling of Ti-6Al-4V machining chips was carried out at moderate temperatures with various back-pressures. For single-pass samples, the relative density was increased with the applied back-pressure and operating temperature. It was found that after multiple passes, near fully dense recycled Ti-6Al-4V can be fabricated. The microstructure observations showed that the nano-sized equiaxed and elongated grains co-existed with relatively coarser lamellar structures which were initially refined after the first pass. In the subsequent passes, the fraction of equiaxed nano-grains increased with the number of passes. The original β phase banded structures were fragmented into individual nano-sized grains randomly distributed within α matrix. The chip boundaries were eliminated and nano-crystalline microstructure region was observed at the chip/chip interface after multiple passes. In the sample processed at 550 °C, <$\vec{a}+\vec{c}$> type dislocations were observed and oxide layer at chip/chip interface was detected. The texture evolution was investigated using electron backscatter diffraction. It was found that the recycled samples performed a strong basal texture along the normal to ECAP inclination direction after the first pass. After multiple passes, in addition to the normal to inclination direction, the recycled Ti-6Al-4V exhibits a basal texture towards the transverse direction. Microhardness mapping showed that the average hardness and degree of homogeneity were increased with number of passes, while the imposed back-pressure had little effect on the average value and homogeneity.

Recycling of Ti-15V-3Cr-3Al-3Sn machining chips was implemented using similar ECAP conditions. The effects of processing parameters, such as back-pressure, operating temperature and number of passes, on the relative density were similar to those for Ti-6Al-4V. Microstructural characterization showed that equiaxed instead of needle shaped α precipitates formed in the β matrix due to the high dislocation density and sub-grain boundaries introduced during ECAP. In terms of microhardness, the maximum hardness was obtained at the specimen pressed at 450 °C. It was found that the applied back-pressure and number of passes enabled to improve the homogeneity, but had little effect on the average hardness.

TABLE OF CONTENTS

1. INTRODUCTION

Titanium and Ti alloys have been used in a wide range of high performance applications in recent decades, including aviation, aerospace, automotive and biomedicine [1]. However, the processing and production costs of Ti and its alloys are still relatively high, which has become the major barrier to broadening their applications [2]. In addition to the extraction and processing costs [3] [4], the high cost of Ti also derives from significant material loss during machining.

Traditional recycling methods for Ti scraps usually involve the process of re-melting and re-casting, which requires high energy consumption and protective environments. Substantial efforts have been made to overcome these problems, for example using thermal plasma furnace [5] [6]. To widen the application range of Ti alloys, it is necessary to reduce the recycling cost and retain the mechanical properties of the recycled products.

Recently, solid state recycling routes, in which the alloy scraps are undergoing severe plastic deformation (SPD) at temperatures below solidus, have been developed for some easy-to-work materials, such as Al [7] [8] and Mg alloys [9]. Of the various SPD procedures, equal channel angular pressing (ECAP) is the most promising one, as it allows a high strain to be repeatedly imposed in the specimen without the introduction of significant change in the cross-section dimensions, and hence the high density products. In addition to achieving low-temperature and low-energy-consumption recycling, the utilization of ECAP also gives the possibility to enhance mechanical properties of recycled materials. However, limited systematic studies have been carried out on researching the feasibility of ECAP recycling for difficult-to-work metals and alloys, such as Ti alloys. It is clear that such an investigation has great research value and practically enhances the possibility of industrialising ECAP recycling.

Two types of Ti alloys were chosen for this study: Ti-6Al-4V, an α+β titanium alloy, and Ti-15V-3Cr-3Al-3Sn, a β titanium alloy. Ti-6Al-4V, as the most widely used Ti alloy, has attracted attentions from aerospace and biomedical industries due to the combination of excellent specific strength, corrosion resistance and outstanding biocompatibility [10] [11] [12] [13]. During the fabrication of Ti-6Al-4V components, up to 80% of raw material is removed in the form of machining chips by using conventional manufacturing methods, such as turning, drilling and milling [14]. Due to its high cold formability and age-hardenability, Ti-15V-3Cr-3Al-3Sn is used as the replacement for hot-formed Ti-6Al-4V, for example, welded pipes and ducts in airframes are made by welding thin Ti-15V-3Cr-3Al-3Sn sheets [15].

The primary aim of this project is to realize the ECAP recycling for the two different Ti alloy machining chips. Through measuring the relative density and microhardness homogeneity, the influences of processing parameters on the quality of recycled products were assessed. The optimized recycling conditions were to be proposed. The study of microstructural evolution of ECAPed titanium alloy chips helps the understanding of the reasons behind the consolidation and mechanical property improvement of the recycled products.

The thesis consists of 8 chapters: Chapter 1 gives the introduction, Chapter 2 reviews the current literatures including physical metallurgy of titanium, microstructures and mechanical properties for the two Ti alloys, machining process for Ti alloys, the principle of ECAP, the texture evolution of ECAPed HCP materials and the state of the art of ECAP on solid state consolidation applications. In Chapter 3 the experimental procedures used in current research are described, including the ECAP die design and characterization techniques. The results of preliminary studies on the microstructures of machining chips are given in Chapter 4. Chapter 5 presents and discusses the results of recycling of Ti-6Al-4V machining chips using ECAP. The results include consolidation in macro-scale, relative density measurement, microstructure evolution, crystallographic texture, microhardness homogeneity and post heat-treatment effects. The recycling of Ti-15V-3Cr-3Al-3Sn using the same consolidation method and characterization techniques is given in Chapter 6, followed by the conclusions in Chapter 7 and suggestions for further work in Chapter 8.

2. LITERATURE REVIEW

2.1 Overview

This chapter consists of the literature review divided into: the basic properties of titanium alloys (Section 2.2 to Section 2.5), machining of titanium alloys (Section 2.6) and the principle of ECAP (Section 2.7), texture development of HCP materials during ECAP (Section 2.8) and the applications of ECAP on metallurgy consolidation (Section 2.9).

2.2 Metallurgy of Titanium

2.2.1 Crystal structures and phases of titanium

Titanium has two allotropic forms in nature: hexagonal close-packed (HCP) and body-centered cubic (BCC). For pure titanium, the allotropic phase transus temperature is 882 °C. Below this temperature, a stable α phase of HCP crystal structure can be obtained, a unit cell of which is shown in Fig. 2.1(a). As indicated in the figure, at room temperature the lattice parameter ***a*** is 2.95 Å, and ***c*** is 4.68 Å, thus the **c**/**a** ratio is 1.587, which is smaller than the ideal value (1.633) for normal HCP structure. As a close packed structure (atomic packing factor = 74%), HCP crystal structure has three types of densely packed planes: basal planes (0002); prismatic planes $\{10\bar{1}0\}$ and pyramidal planes $\{10\bar{1}1\}$. At higher temperature, pure titanium changes to a BCC crystal structure (β phase), as shown in Fig. 2.1(b). The densely packed planes for BCC structure are $\{110\}$ planes.

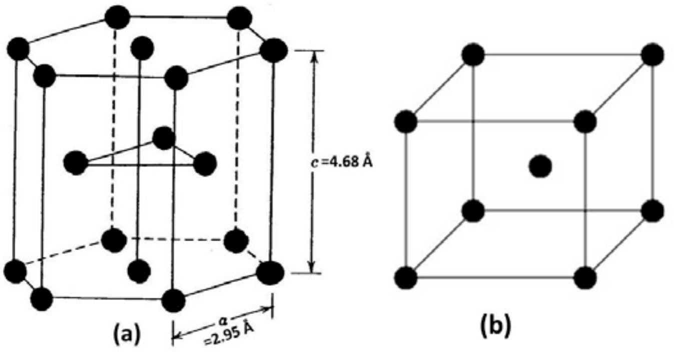

Fig. 2. 1 Unit cells of titanium (a) α phase and (b) β phase, following **[16]**.

The phase transus temperature of titanium is significantly influenced by the substitutional and interstitial elements. Additional elements in titanium alloys can be conventionally classified into three groups: α stabilizers, β stabilizers and neutral elements. The transus temperature increases with the concentration of α stabilizers, as shown in Fig. 2.2(a). Aluminium is the most commonly used α stabilizing substitution element because it has large solubility in both α and β phases. Oxygen, nitrogen and carbon are all effective α phase stabilizing interstitial elements. The maximum solubility of oxygen, nitrogen and carbon in α-Ti are 30 at. %,19 at. % and 2 at. %, respectively [17]. Here, take oxygen as an example. The atomic radius of oxygen is ~0.60 Å. The octahedral and tetrahedral vacancy sizes in α-Ti and the tetrahedral vacancy size in β-Ti are 0.61 Å, 0.33 Å and 0.44 Å, respectively. Thus, the interstitial oxygen atoms are expected to reside in the octahedral sites of α-Ti and to be α-phase stabilizer [17]. The Ti-O phase diagram is shown in Fig. 2.3. In contrast, beta stabilizers lower the α/β transformation temperature. Depending on the effects on the binary phase diagram, β stabilizing elements are sub-divided into two categories: isomorphous elements and eutectoid elements, the corresponding phase diagrams are given in Fig. 2.2 (b) and (c), respectively. The β isomorphous elements, such as molybdenum (Mo) and vanadium (V), are miscible in the β phase, and the transus temperature decreases with increasing solute content. The β eutectoid elements, such as chromium (Cr) and manganese (Mn), result in an eutectic phase diagram which is similar with Fe/C system. Additionally, some elements behaving neutrally are also alloyed in titanium, such as zirconium and tin. The corresponding phase diagram is shown in Fig.2.2 (d).

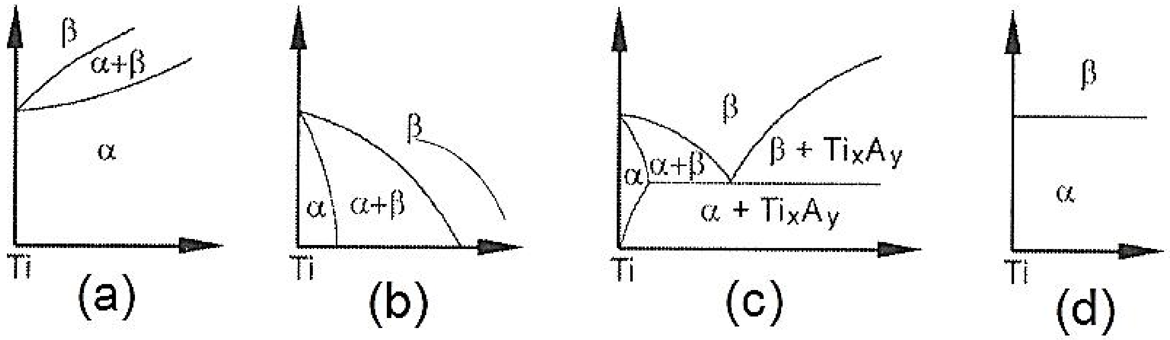

Fig. 2. 2 Effects of alloying elements on titanium α/β phase diagrams; (a) α stabiliser, (b) isomorphous β stabiliser, (c) eutectoid β stabiliser and (d) neutral element **[16]**.

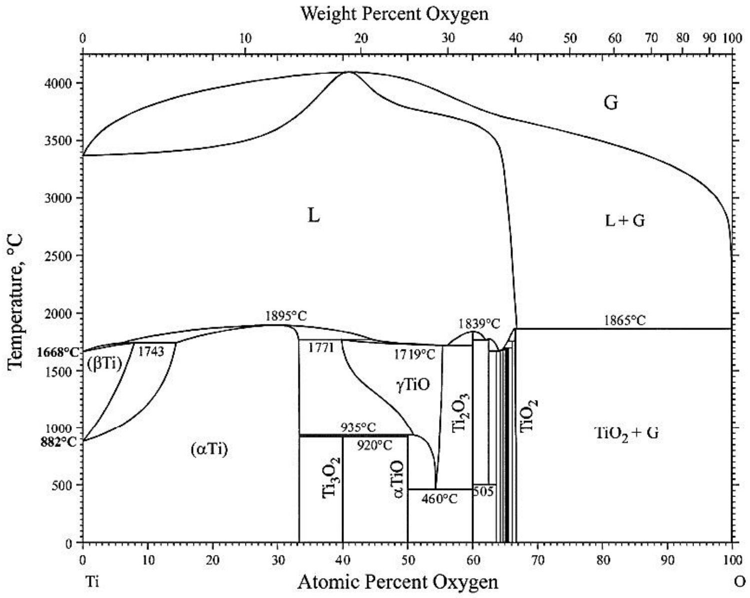

Fig. 2. 3 Ti-O phase diagram **[18]**.

According to the retained phases, titanium alloys can be usually classified into three different categories: α, α+β and β alloys.

2.2.2 Deformation mechanism of titanium alloys

Dislocation slip and deformation twinning are two major types of deformation modes to accommodate plastic strain for titanium alloys.

2.2.2.1 Deformation modes of α titanium

In α titanium (HCP structure), dislocation slip has been observed on all three densely packed planes, i.e. basal planes, prismatic planes and prismatic planes [19]. The main slip directions on these three sets of planes are of the family $<11\bar{2}0>$. Therefore, the possible slip system including slip planes and slip directions are illustrated in Fig. 2.4 and summarised in Table 2.1. It can be seen that although there are 12 different slip systems in the directions of $<11\bar{2}0>$, only 4 independent systems exist because the slip system of type 3 can be produced by a combination of type 1 and 2. In order to satisfy the von Mises criterion of requiring at least 5 independent slip systems for plastic deformation, additional dislocation slip systems with non-basal Burgers vector need to be activated. The $<11\bar{2}3>$ dislocations were first observed to slip on planes of $\{10\bar{1}1\}$ [20] [21], whereas the $\{11\bar{2}2\}$ planes possess higher Schmid factor than the $\{10\bar{1}1\}$ planes [16], and hence preference of the slip system of $\{11\bar{2}2\}<11\bar{2}3>$ during HCP structure deformation.

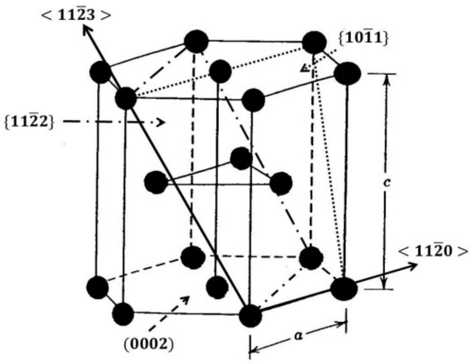

Fig. 2. 4 Slip systems in α titanium of HCP structure, following **[16]**.

Table 2. 1 Summary of slip system for α titanium, reproduced from [1]

Slip system type	**Burgers vector type**	**Slip direction**	**Slip plane**	**No. of slip systems**	
				Total	Independent
1	$\vec{a}$	$< 11\bar{2}0 >$	(0002)	3	2
2	$\vec{a}$	$< 11\bar{2}0 >$	$\{10\bar{1}0\}$	3	2
3	$\vec{a}$	$< 11\bar{2}0 >$	$\{10\bar{1}1\}$	6	4
4	$\vec{a} + \vec{c}$	$< 11\bar{2}3 >$	$\{11\bar{2}2\}$	6	5

Deformation twinning plays an important role for α titanium when the stress axis is parallel to the c-axis, i.e. none of the slip systems with $< 11\bar{2}0 >$ slip directions can be activated. The most common twinning modes are $\{10\bar{1}2\}, \{11\bar{2}1\}$ during c-axis extension and $\{11\bar{2}2\}$ when c-axis is compressed [22].

It should be noted that the activations of dislocation slip and deformation twinning strongly depend on the deformation temperature, the direction of stress applied and the contents of alloying elements.

In an early research, Akhtar [23] studied the tensile deformation in single crystal α titanium at various temperatures when the angle of inclination between the stress axis and the basal plane was fixed at 47°, 60° and 78°. It was found that basal slip was activated when the temperature was above 227 °C, and at lower temperature $\{10\bar{1}2\}$ or $\{11\bar{2}1\}$ deformation twinning occurred. Further investigation showed that $\{10\bar{1}2\}$ twins were observed at larger declination angle, whereas $\{11\bar{2}1\}$ twins occurred at declination angles of 47° and 60°.

Williams *et al*. [24] carried out studies on the influence of Al concentration on the single crystal Ti-Al alloy. They found that increasing Al content significantly encouraged basal slip and suppressed the twin occurring. Similar observations have been demonstrated by Li *et al*. [25] in a recent study. Li *et al*. [25] studied the influences of alloy content on the deformation modes for two α titanium alloys (commercially pure Ti and Ti-5Al-2.5Sn wt. %). Fig. 2.5 shows the histograms of observed dislocation slip and deformation twinning as function of global Schmid factor distribution. It is apparent that although prismatic slip systems were dominant in both Ti alloys, the amount of basal slip significantly increased in Ti-5Al-2.5Sn alloy. Meanwhile, the occurring of deformation twinning was inhibited in Ti-5Al-2.5Sn alloy with the increasing concentration of Al.

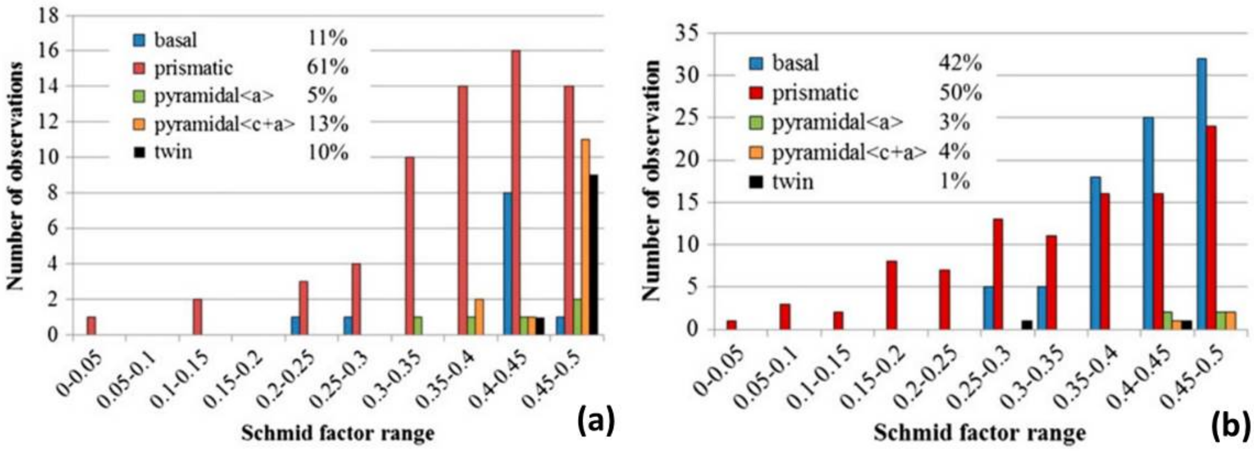

Fig. 2. 5 Histograms of slip systems and deformation twinning as function of Schmid factor for (a) pure titanium and (b) Ti-5Al-2.5Sn alloy tested under tensile stress at room temperature **[25]**.

2.2.2.2 Deformation modes of β titanium

Unlike HCP structure, the BCC structure is not truly close packed. The shortest Burgers vector in BCC crystal is in $< 111 >$ direction. Thus, in β titanium, there are 12 slip systems on the closed packed planes, i.e. $\{110\} < 111 >$. In addition, $\{112\}$ and $\{123\}$ planes were also observed to glide in the direction of $< 111 >$ [26], as depicted in Fig. 2.6.

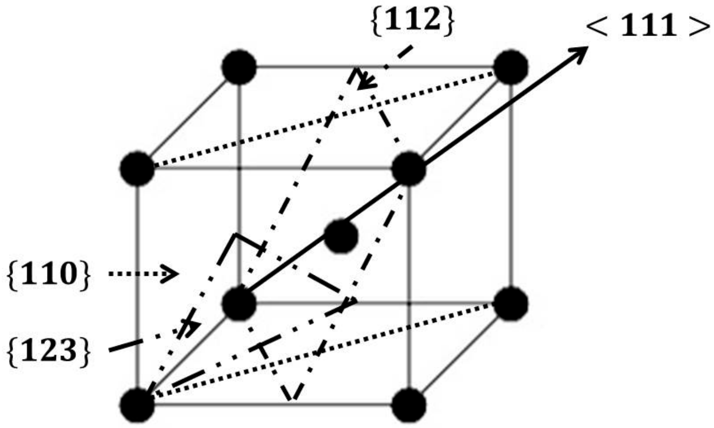

Fig. 2. 6 Slip systems in β titanium of BCC structure, following **[16]**

Apart from dislocation glide, it was demonstrated that $\{112\} < 11\bar{1} >$ deformation twins appeared in binary Ti-V alloys with vanadium concentration ranged from 20 to 40 wt. % [27]. A more systematic investigation carried out by Hanada and Izumi [28] showed that $\{332\} < 113 >$ twinning occurred in various metastable β titanium alloys, including Ti-V, Ti-Mo, Ti-Nb and Ti-Fe. The phase diagrams for each binary alloy where $\{332\} < 113 >$ deformation twinning took place were shown in Fig. 2.7.

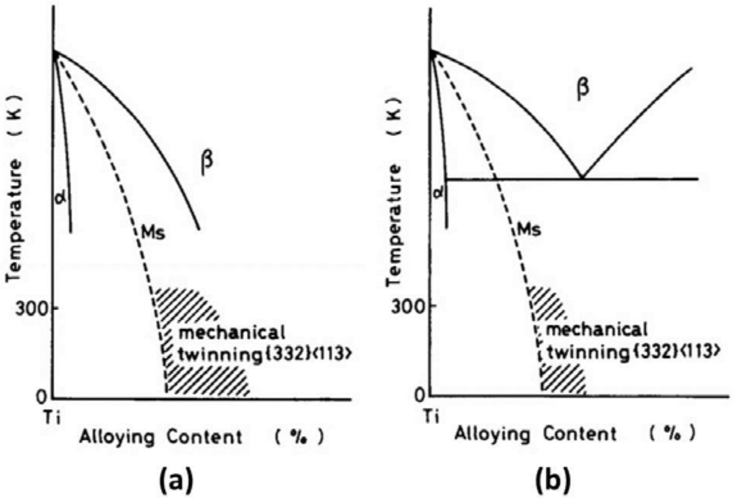

Fig. 2. 7 Phase diagrams for titanium binary alloys indicating $\{332\} < 113 >$ *twinning occurring for (a) β isomorphous elements, such as V, Mo and Nb and (b) β eutectoid elements, for example Fe* **[28]**

Alloying composition determines β titanium deformation behaviour. In most cases, the plastic strain is accommodated by dislocation slip accompanied with twins, as demonstrated by Rack *et al*. [29]. However, as claimed by Banerjee and Williams [22], β titanium alloys with high solute concentration deformed only by slip, for example Ti-15V-3Cr-3Al-3Sn. A recent study [30] was carried out on Ti-10Mo-xFe alloys in order to examine the effect of Fe content on the β titanium deformation performance. The results indicated that the deformation modes changed from $\{332\} < 113 >$ to a slip as Fe concentration increased.

2.2.2.3 Deformation modes of α+β titanium

In terms of α+β titanium, the dislocation glide occurs both in α and β phases theoretically according to Burgers Orientation Relationship, as illustrated in Fig. 2.8. It is apparent that the slip planes and directions in α phase are parallel to the slip planes and directions in β phase, respectively, i.e. $\{0002\}_\alpha \parallel \{110\}_\beta$ and $< 11\bar{2}0 >_\alpha \parallel < 111 >_\beta$.

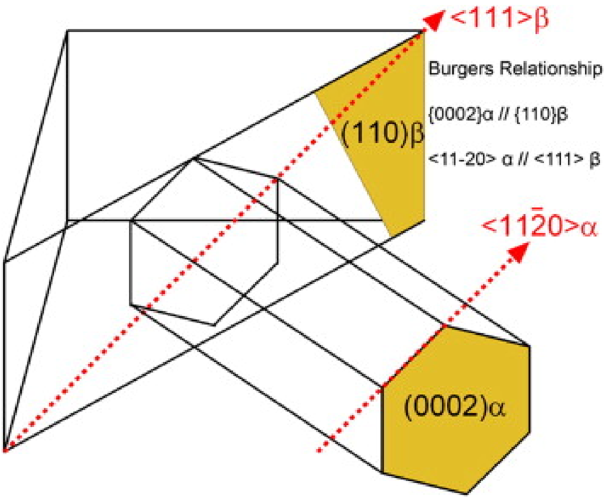

Fig. 2. 8 Burgers Orientation Relationship between α phase (HCP) and β phase (BCC) **[31]**.

However, it should be noted that according to further studies [32] [33] [34], there are misorientations between the slip directions of α phase and β phase: 0.7° misorientation between $\overrightarrow{a_1}\sim[\bar{2}110]_\alpha$ and $\overrightarrow{b_1}\sim[11\bar{1}]_\beta$, 11.1° misorientation between $\overrightarrow{a_2}\sim[\bar{1}2\bar{1}0]_\alpha$ and $\overrightarrow{b_2}\sim[\bar{1}11]_\beta$, and $\overrightarrow{a_3}\sim[\bar{1}\bar{1}20]_\alpha$ is not even closely aligned with any β slip direction. A recent investigation carried out by Salem and Semiatin [35] confirmed these misalignments. In their study, Ti-6Al-4V (α+β Ti alloy) single-colony samples tested under uniaxial compression presented a slight misalignment of 0.8° between $\overrightarrow{a_1}$ and $\overrightarrow{b_1}$, and 11.2° misalignment between $\overrightarrow{a_2}$ and $\overrightarrow{b_2}$. The transmission electron micrograph showing α/β interface and corresponding selected area diffraction pattern are shown in Fig. 2.9.

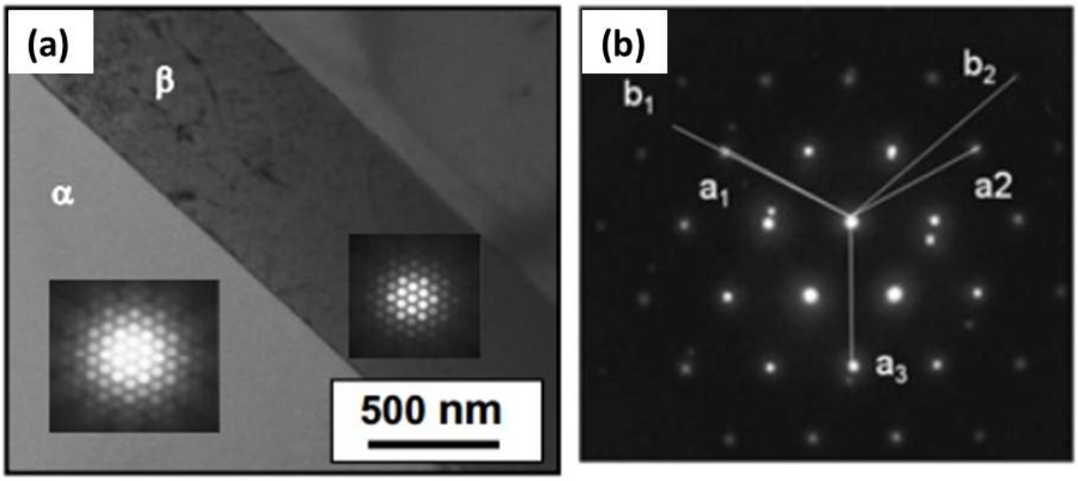

Fig. 2. 9 (a) TEM image showing α/β interface using $[\mathbf{0001}]_{\alpha}$ *and* $[\mathbf{101}]_{\beta}$ *zone axis; (b) selected area diffraction pattern taken in α/β interface showing misorientation between* $\overrightarrow{\boldsymbol{a_1}}$ *and* $\overrightarrow{\boldsymbol{b_1}}$, $\overrightarrow{\boldsymbol{a_2}}$ *and* $\overrightarrow{\boldsymbol{b_2}}$ **[35]**.

2.3 Texture Representation

Texture or preferred orientation is common in polycrystalline metals and alloys, especially after thermomechanical processes, such as extrusion, rolling and torsion. Texture can be usually subdivided into two categories: macro-texture and micro-texture. The term of macro-texture is adopted to be the average distribution of crystallographic orientation within the sample. The main approach to study macrostructure is X-ray diffraction (XRD). However, the probe size of X-rays limits its application in the exploration of micro-texture. Micro-texture offers a population of individual orientation which is linked to the location within the specimen [36]. Electron backscatter diffraction (EBSD) and transmission electron microscopy (TEM) have been popular approaches to investigate micro-texture at state of the art.

Pole figure is one of the most common representation methods for texture. Fig. 2.10 shows the schematic of $\{100\}$ pole figure for a cubic crystal in the stereographic projection.

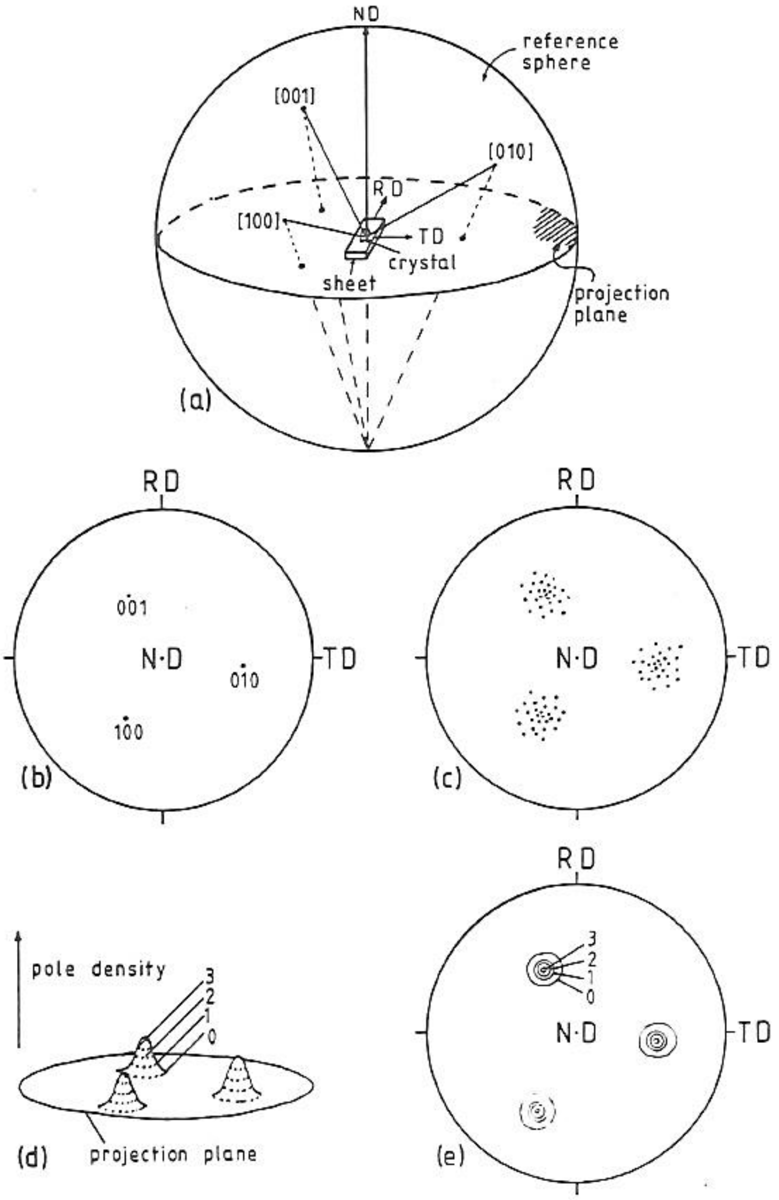

Fig. 2. 10 Schematic of $\{\mathbf{100}\}$ *poles of a cubic crystal in the stereographic projection; (a) Crystal in the reference sphere and projections onto the equator plane, (b) projection of* $\{\mathbf{100}\}$ *poles of a single grain, (c) projection of* $\{\mathbf{100}\}$ *poles of textured grains, (d) 3 dimensional pole density distribution and (e) a contour map showing the pole density* **[37]**

It is clear to see from Fig. 2.10 that in term of the pole figure, the orientation of the crystal coordinate system is represented in the specimen coordinate system. Nevertheless another means of expression for texture, named the inverse pole figure, presents texture in the opposite way: the reference coordinate system is the crystal coordinate system, to which the orientation of the specimen coordinate system is projected [36].

2.4 Ti-6Al-4V: Microstructure, Mechanical Properties and Applications

Ti-6Al-4V was developed in 1950s, and presently it is the most widely used titanium alloy occupying more than half of all titanium output in the world. As the most common α+β titanium alloy, Ti-6Al-4V has a number of formulations. Normally, the Al content ranges from 5.5 - 6.75 wt. %, and the V content ranges from 3.5 – 4.5 wt. % [38]. Al has relatively low atomic weight, thus, the addition of Al can reduce the density of Ti alloys. However, the increasing Al content will lead the formation of Ti_3Al phase. Ti-Al phase diagram is shown in Fig. 2.11. It is found that Ti_3Al phase starts to form when the Al content exceeds ~5 wt. % at the temperature of 500 °C. Therefore, in order to avoid any excess Ti_3Al precipitates, most Ti alloys limit the Al content to ~6 wt. % [16]. By adding V, the β transus temperature of Ti alloys can be decreased, and α+β phase can be retained at room temperature, which makes Ti alloys are heat treatable. However, the V content is limited because the maximum solid solubility of V in α-Ti is ~3 wt. % at 680 °C [16]. In addition, the density of Ti alloys increases with the increasing V content.

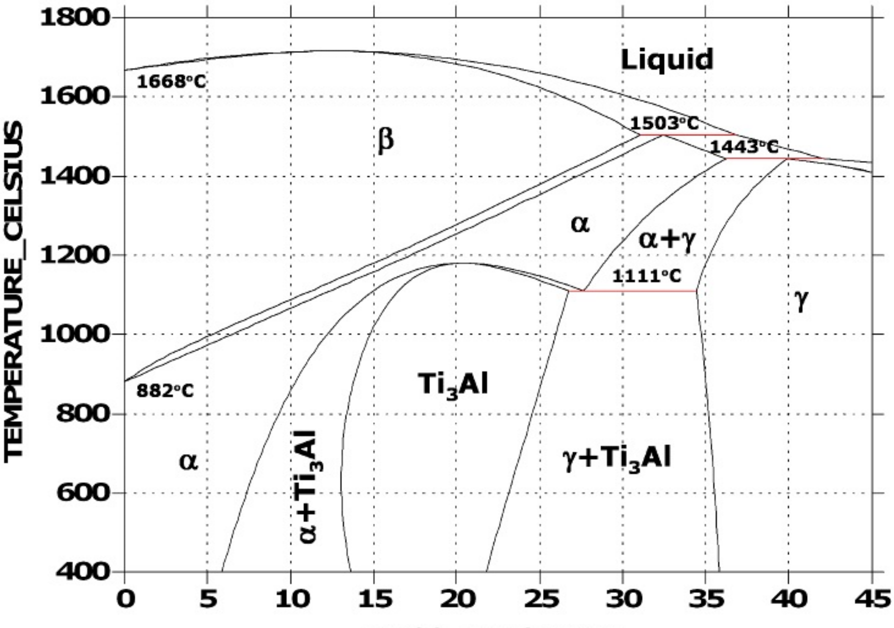

Fig. 2. 11 Ti-Al phase diagram **[39]**.

In Ti-6Al-4V alloy, three different microstructures can be achieved via various heat treatments and processing histories: fully lamellar, fully equiaxed and bi-model microstructures.

- Fully lamellar microstructures

A fully lamellar microstructure, as shown in Fig. 2.12(a), can be obtained by recrystallizing the alloy in the β phase field after high temperature deformation (either in the β phase field or in the α+β phase field). The cooling rate in the recrystallization stage is the critical processing parameter to the final lamellar microstructure: a faster cooling rate usually results in a finer microstructure: narrow α lamellae, narrow α layers at the β grain boundaries and smaller α colony size.

- Fully equiaxed microstructures

Fig. 2.12(b) represents a fully equiaxed microstructure. This microstructure can be achieved via either slow recrystallization cooling rate or low recrystallization temperature. Different mechanisms are involved in these two routes. Slow recrystallization cooling rate leads primary α to have sufficient time to grow and no α lamellae can form within β grains, while the low recrystallization temperature allows the deformed lamellar structures develop to fully equiaxed microstructures.

- Bi-model microstructures

Bi-model microstructures consist of isolated primary α separated by β grains, as shown in Fig. 2.12(c). A bi-model microstructure can be attained by homogenization in the β phase field, followed by deformation in the α+β phase filed. Then it is recrystallized in the α+β phase filed before the final aging. The most important factor is the cooling rate in the homogenization stage: the faster cooling rate results in finer equiaxed primary α size.

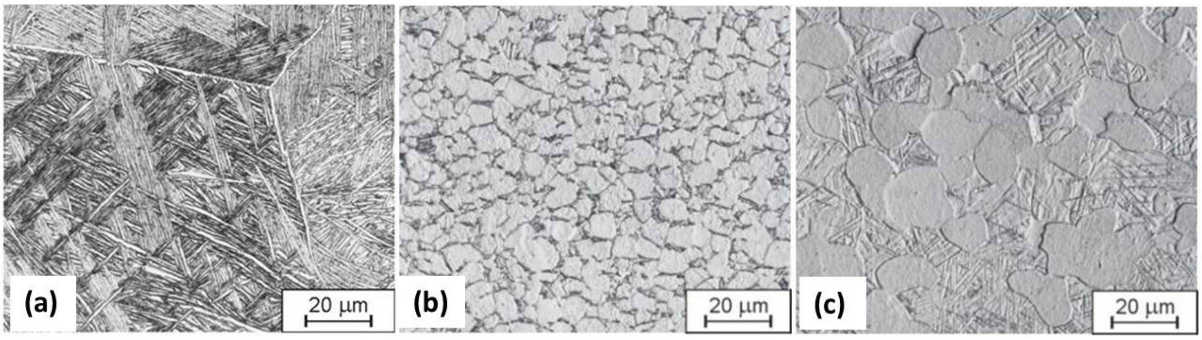

Fig. 2. 12 Typical microstructures of Ti-6Al-4V: (a) fully lamellar, (b) fully equiaxed and (c) bi-model microstructures **[40]**.

Table 2.2 presents the typical tensile strength of Ti-6Al-4V at room temperature compared with other metals. It is evident that Ti-6Al-4V locates at the mid-range for titanium alloys, and at room temperature the tensile strength of Ti-6Al-4V is comparable to steels and copper alloys.

Table 2. 2 Tensile strength of Ti-6Al-4V in comparison with other alloys, following **[38]**

Material	Tensile strength (MPa)
Ti-6Al-4V	895-1250
Titanium alloys	240-1500
Alloy steel	100-2300
Aluminium	70-700
Copper	170-1500

Fig. 2.13 shows that the tensile strength of Ti-6Al-4V reduces with temperature. Thus Ti-6Al-4V alloy is usually employed in the applications with temperature not exceeding 350 °C.

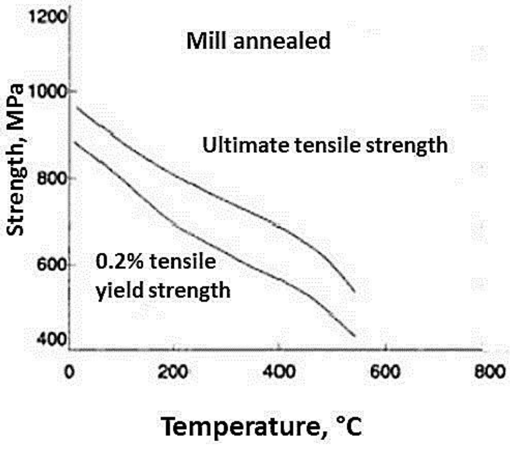

Fig. 2. 13 Ti-6Al-4V: Tensile strength vs. temperature, following **[38]**.

The mechanical properties of Ti-6Al-4V are significantly influenced by microstructure. In general, finer microstructure usually leads to superior mechanical properties. For fully lamellar microstructure, the most influential factor is the size of α colonies which is determined by the cooling rate at the recrystallization stage; in terms of fully equiaxed microstructure, the α grain size determined by the cooling rate in the homogenization stage, is the key microstructure parameter to control the mechanical properties; in bi-model microstructure, the small β grain size, which is determined by the cooling rate in the homogenization stage and the recrystallization temperature, pronouncedly affects the mechanical properties. Fig. 2.14 shows the yield strength of fully lamellar microstructural Ti-6Al-4V as function of the cooling rate in the recrystallization stage.

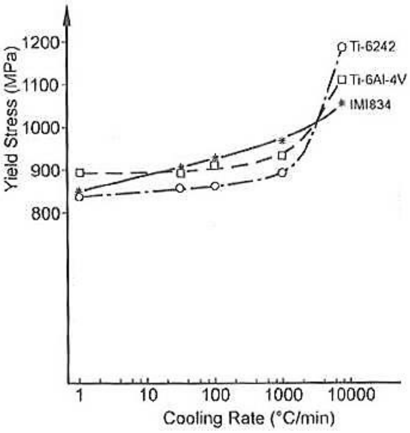

Fig. 2. 14 Yield strength vs. the cooling rate at recrystallization stage for fully lamellar microstructural Ti-6Al-4V, following **[16]**

In addition to microstructure, the mechanical properties of Ti-6Al-4V are also affected by crystallographic texture. For Ti-6Al-4V, two typical textures of α phase can be achieved via unidirectional rolling at various temperatures: transverse (T) texture (Fig. 2.15(a)) and basal/transverse (B/T) texture (Fig. 2.15(b)).

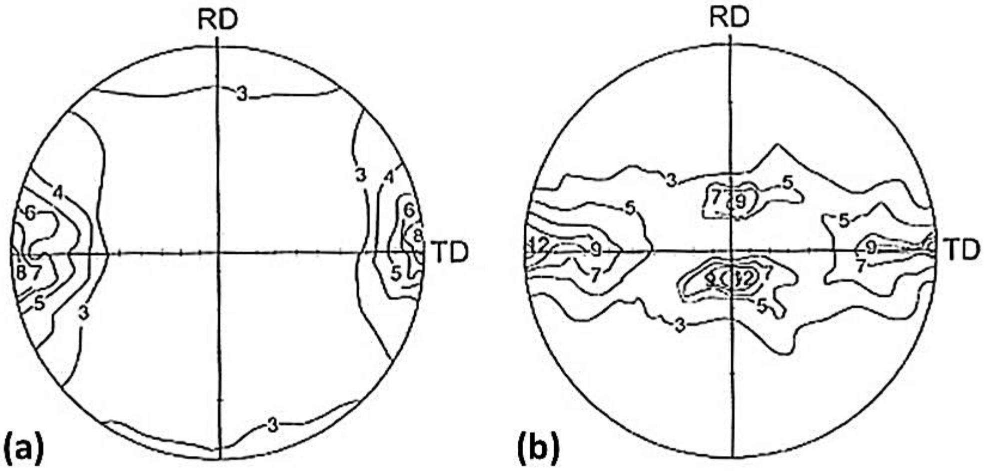

Fig. 2. 15 Two typical textures of α phase in Ti-6Al-4V (0002 pole figure): (a) Transverse texture and (b) basal/transverse **[16]**.

In theory, for Ti-6Al-4V with rolling texture (either T texture or B/T texture), the Young's modulus at the transverse direction (TD) is the highest and decreases with the angle between the stress axis and the basal pole, which had been confirmed in an early investigation carried out by Bowen [41]. A further study undertaken by Evans *et al*. [42] suggested a similar tendency occurring for the ultimate tensile strength (UTS): the specimen with the transverse direction performed the highest UTS value.

Because of the high specific strength at low to moderate temperatures and good corrosion resistance, Ti-6Al-4V is extensively used in aerospace applications. For example, Ti-6Al-4V castings are employed in variety of airframe components, including flow diverters, cargo-handling equipment and external fuel tanks in space shuttles [38]. In addition, Ti-6Al-4V is also a candidate for surgical implants because of its excellent combination of mechanical property and biocompatibility, such as artificial limbs, hip, knee and shoulder replacement joints [11]. Furthermore, wrought Ti-6Al-4V is also used in automotive production, for example connecting rods, intake valves and wheel hubs [43].

2.5 Ti-15V-3Cr-3Al-3Sn: Microstructure, Mechanical Properties and Applications

Ti-15V-3Cr-3Al-3Sn was firstly developed in 1970s as an alternate for Ti-6Al-4V especially in form of sheet components in aerospace industry because of its good cold formability and strip-producibility. Furthermore, the outstanding fracture toughness, corrosion resistance and deep hardenability let it receive attention from other application fields.

Because of the existence of heavy β stabilizers (V and Cr), the α/β transus temperature of Ti-15V-3Cr-3Al-3Sn alloy is ~760°C and an all β structure can be retained through rapid cooling. Fine α phase can precipitate during the subsequent aging treatment. In terms of the microstructure of Ti-15V-3Cr-3Al-3Sn, the β grain size is determined by the recrystallization temperature, and the fine α phase precipitation is controlled by the aging temperature and the corresponding heating rate. The processing route for beta annealed microstructure of Ti-15V-3Cr-3Al-3Sn is illustrated in Fig. 2.16.

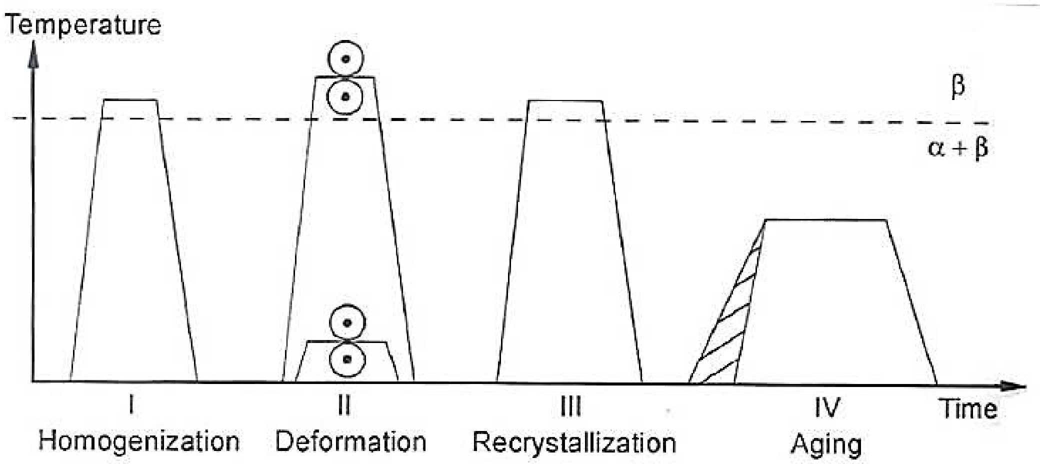

Fig. 2. 16 Processing route for beta annealed microstructure of Ti-15V-3Cr-3Al-3Sn alloy **[16]**.

A systematic study on the relationship between microstructure and mechanical properties of Ti-15V-3Cr-3Al-Sn carried out by Breslauer and Rosen [44] showed that small grain size of ~35 µm and large grain size of ~120 µm were obtained via recrystallization at 790 °C for 10 min and 830 °C for 24 h, respectively. In the subsequent aging treatment at 540 °C, both for small grained samples and large grained samples, α precipitates firstly occurred at the β grain boundaries, and with aging time they progressed into the interior, as shown in Fig. 2.17. In the same investigation, the mechanical properties of the large and small grained samples were compared. The results showed that after aging, the yield strength and the UTS of the large grained samples were higher than those of small grained ones, while the small grained samples performed the higher tensile elongation.

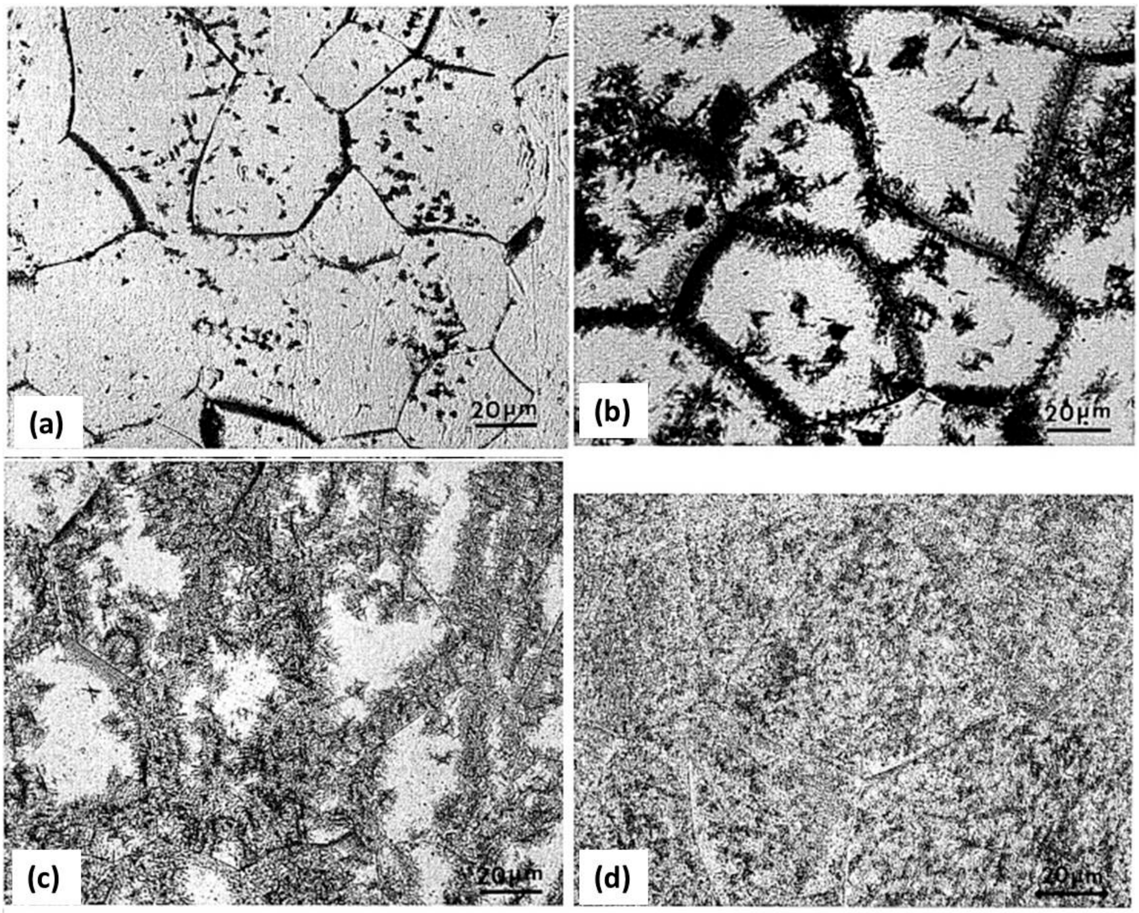

Fig. 2. 17 Optical micrographs showing the variation of α phase precipitation after aging at 540 °C for (a) 1 h, (b) 2 h, (c) 4 h and (d) 8 h **[44]**.

In order to obtain homogeneous α phase precipitation, duplex aging is an important technique to employ, i.e. a pre-aging treatment at lower temperature prior to normal aging. The schematic of the two-stage aging is illustrated in Fig. 2.18. The principle of the duplex aging is that the pre-aging acts as the pre-precipitation step when finely dispersed precursors form for the following α phase precipitation. Recently, a detailed study on the duplex aging of Ti-15V-3Cr-3Al-3Sn was conducted by Santhosh *et al*. [45]. According to their experiments, it was suggested that in comparison to the normal aging, pre-aging at 250 °C for 24 h or 300 °C for 10 h followed by 500 °C for 8 h offered a slight higher UTS and four to five fold higher high cycle fatigue (HCF) life while a loss of ductility.

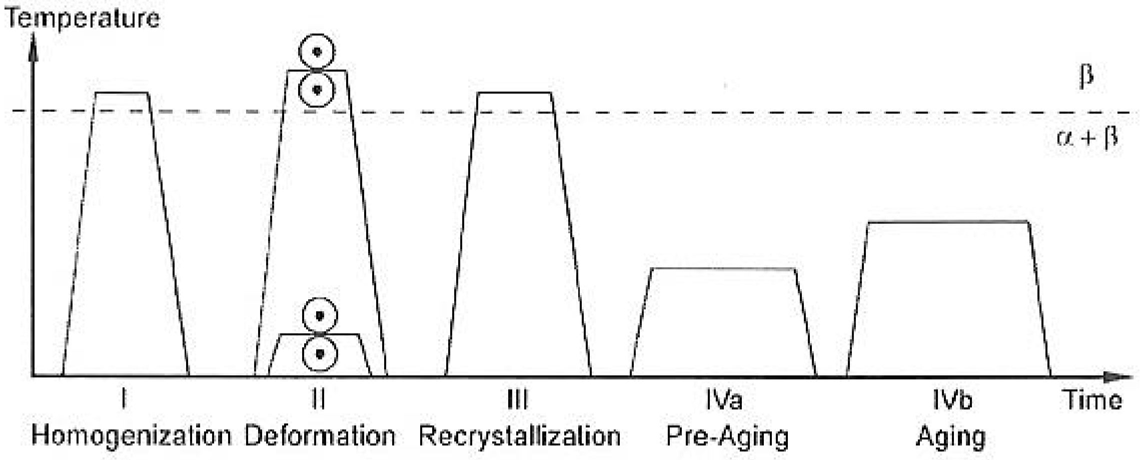

Fig. 2. 18 Duplex aging processing route for beta annealed microstructure of Ti-15V-3Cr-3Al-3Sn **[16]**.

Therefore, the strengthening of Ti-15V-3Cr-3Al-3Sn is mainly attributed to precipitation of HCP α phase in the BCC matrix during the aging stage. The yield strength of Ti-15V-3Cr-3Al-3Sn alloy in the annealed condition is typically ~770 MPa, and after a single step aging the yield strength can be increased up to 1250 MPa [46]. Fig. 2.19 shows the yield strength of Ti-15V-3Cr-3Al-3Sn sheet with 1.78 mm thick varies with the aging time.

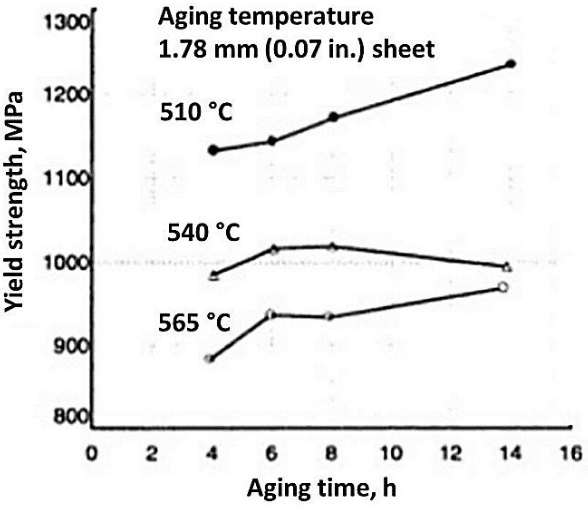

Fig. 2. 19 Ti-15V-3Cr-3Al-3Sn sheet: yield strength vs. aging time **[38]**.

Ti-15V-3Cr-3Al-3Sn is majorly applied in airframe structural components, especially as sheets, for example the Boeing 777 used formed Ti-15V-3Cr-3Al-3Sn sheets as environmental control system ducting, clips and brackets, and floor support structure [47]. In addition, Ti-15V-3Cr-3Al-3Sn castings at tensile strength of 1045 MPa are also used to replace Ti-6Al-4V at tensile strength of 830 MPa in the brake torque tubes. Higher strength allows higher carbon volume, and hence longer brake life [12].

2.6 Machining of Titanium Alloys

2.6.1 Machining chip formation

Machining is one important manufacturing method in which the cutting tool penetrates into the work-piece and cuts away material to leave the desired component shape. According to the relative motion between the tool and the work-piece, traditional machining operations can be classified into turning, drilling, milling, etc., the sketches of which are shown in Fig. 2.20.

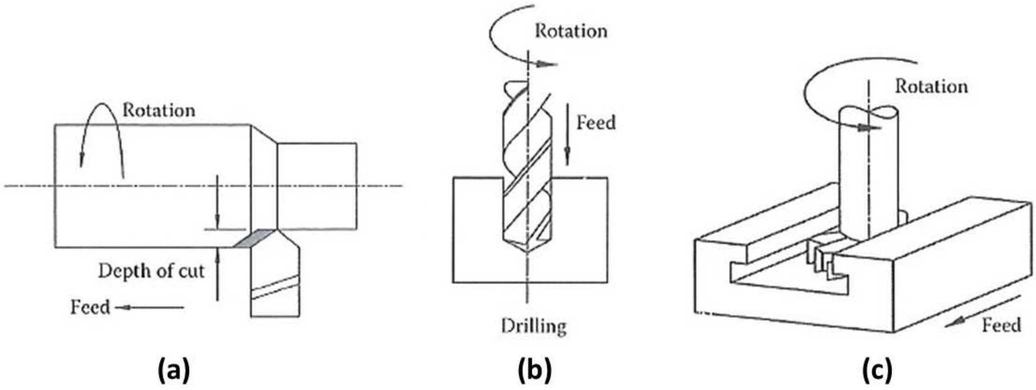

Fig. 2. 20 Sketches of three types of machining processes: (a) turning, (b) drilling and (c) milling **[48]**.

One common feature of various machining processes is that the predominant cutting action involves the formation of machining chips, followed by a new surface generation. The schematic of an idealized model of the chip formation is illustrated in Fig. 2.21. As indicated in this sketch, the cutting tool is forced into the work-part surface; as the cutting tool moves forward, a chip is formed by shear deformation occurring along the shear plane, which is orientated at an angle (ϕ) with the new surface. The angle between the rake face of the tool and the plane perpendicular to the work surface is named the rake angle (α).

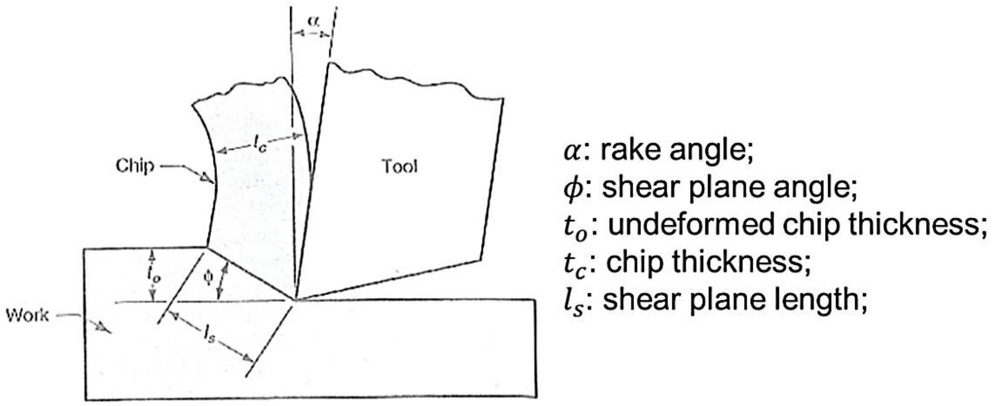

Fig. 2. 21 Schematic showing the chip formation in idealized orthogonal cutting model, following **[49]**.

According to the geometrical relationship given in Fig. 2.21, it is obvious that the length of the shear plane (l_s) can be derived as $l_s = \frac{t_0}{\sin\phi}$; it can be also represented as $l_s = \frac{t_c}{\cos(\phi-\alpha)}$. Therefore, the chip thickness ratio, *r*, is given by: $\frac{t_o}{t_c} = \frac{\sin\phi}{\cos(\phi-\alpha)}$. This equation can be rearranged to calculate the shear plane angle:

$$\boldsymbol{tan\,\phi} = \frac{\boldsymbol{r\cdot cos\,\phi}}{\boldsymbol{1-r\cdot sin\,\phi}} \text{ … \textit{Equation 2. 1}}$$

The calculation process for the imposed shear strain is depicted in Fig. 2.22. As shear strain is defined as the ratio of the element deflection to the orthogonal distance over the deflection occurring, the shear strain can be expressed as:

$$\boldsymbol{\gamma} = \frac{\boldsymbol{\Delta s}}{\boldsymbol{\Delta y}} = \frac{\boldsymbol{AD+BD}}{\boldsymbol{CD}} = \boldsymbol{cot\,\phi} + \boldsymbol{tan}(\boldsymbol{\phi}-\boldsymbol{\alpha}) \text{ … \textit{Equation 2. 2}}$$

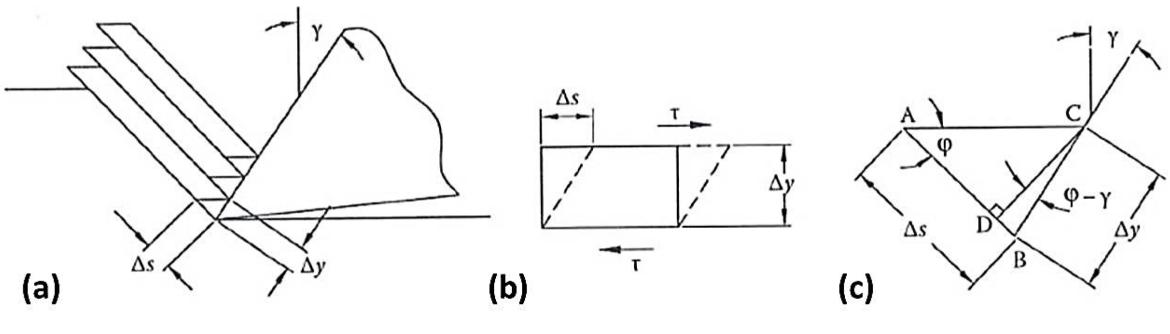

Fig. 2. 22 Calculation process of shear strain in chip formation; (a) a series of parallel shearing plates during the formation of machining chips, (b) two shear stresses in opposite directions in one thin sliding element and (c) shear strain triangle used to derive Equation 2.2, following **[48]** *and* **[49]**.

It should be noted that the derivation above is based on an assumption of idealized orthogonal model. In real machining process, the shear deformation occurs within a zone instead of a shear plane, which is called the primary shear zone. As the primary shear zone is usually very thin, the calculation processes above are still valid. In addition to the primary shear zone, further shear strain resulted from the friction between the chip and the cutting tool occurs next to the rake face, i.e. secondary shear zone. The realistic orthogonal cutting model including the primary and secondary shear zones is illustrated in Fig. 2.23.

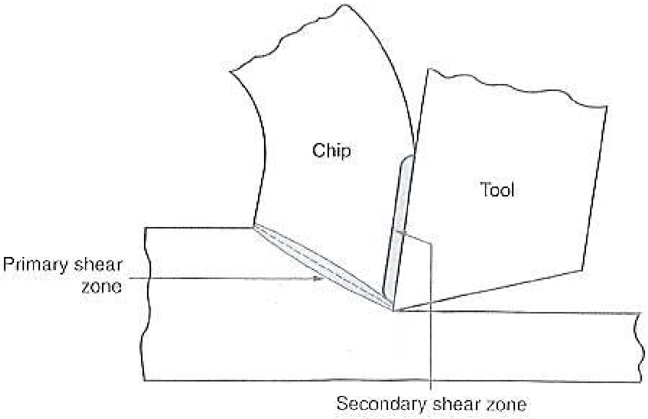

Fig. 2. 23 Primary and secondary shear zones in realistic chip formation, following **[49]**.

According to the morphology of the formed chips, three basic types of chip formation were firstly classified by Ernst in 1938 [50]: the discontinuous chip, the continuous chip and the continuous chip with built-up edge, as shown in Fig. 2.24(a) – (c) [51], respectively. The formation of different types of chips is depended on the material being machined and the cutting conditions used.

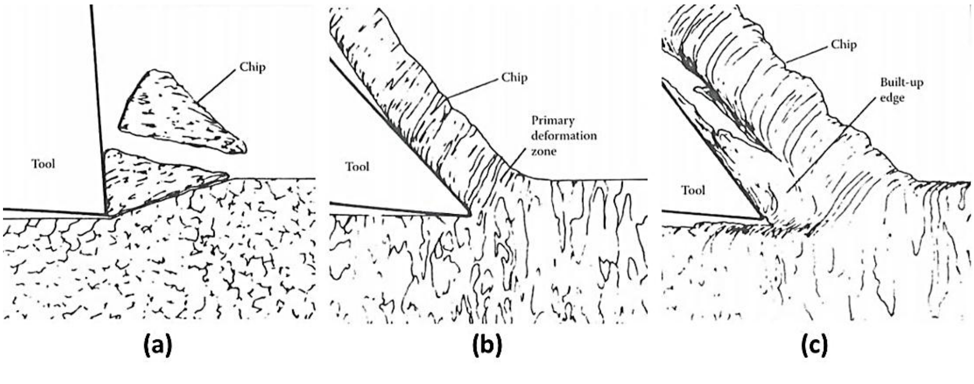

Fig. 2. 24 Sketch of three types of chips: (a) the discontinuous chip, (b) the continuous chip and the continuous chip with built-up edge **[51]**.

In addition to these three basic types of machining chips, another chip type was identified as the serrated chip or the saw-tooth chip in 1954 [52], as shown in Fig. 2.25. The serrated chip is closely associated with a relatively high speed machining of titanium alloys which are regarded as difficult-to-machine materials. In terms of the mechanism of the saw-tooth chip formation, there are two types of explanations: the formation of adiabatic shear band and the periodic growth of cracks from the outer surface. The former theory was first proposed by Shaw *et al*. [53] in 1954. They claimed that the thermal softening effect resulted from the localized shear strain within the primary shear zone outcompeted the strain hardening mechanism and caused the saw-tooth chip. This theory was supported by Komanduri and Turkovich [54] and Davies *et al*. [55]. A recent study carried out by Barry el al. [56] also confirmed the cause of the saw-tooth chip was the occurrence of thermo-plastic instability. Nevertheless, in 1974 Nakayama [57] first suggested the later theory, i.e. cyclic crack approach, which was supported Vyas and Shaw [52] and Obikawa and Usui [58]. One strong evidence that the saw-tooth chip formed at extremely low speed cutting, where the cracks initiated at the free surface and proceed downward to the tool tip, indicates that the root cause of the saw-tooth chip formation is periodic fracture rather than adiabatic shear [59].

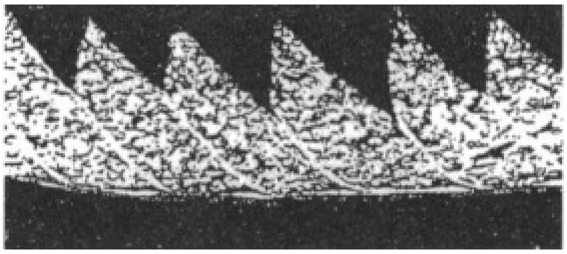

Fig. 2. 25 Photograph of the saw-tooth chip **[52]**.

2.6.2 Machinability of titanium alloys

2.6.2.1 Problems in titanium alloys machining

Historically, titanium and titanium alloys are perceived as difficult-to-machine materials due to several inherent materials properties, including low thermal conductivity, relatively low elastic modulus, high work-hardening tendency and chemical reactivity [60] [61].

Titanium alloys have low thermal conductivity and volume-specific heat, which may cause heat concentration at the tool/work-piece interface and hence high cutting temperature during machining. The thermal conductivity of Ti-6Al-4V alloy at room temperature is ~7 $W/m \cdot K$, which is lower than that of high-alloy steel (12-30 $W/m \cdot K$) [38]. This value increases significantly with temperature, as shown in Fig.

2.26(a). This growing tendency is common for most titanium alloys and beneficial for machining. The variation of thermal conductivity with temperature for Ti-15V-3Cr-3Al-3Sn is illustrated in Fig. 2.26(b). Nevertheless, for pure titanium, the thermal conductivity at 0 °C is ~22 $W/m \cdot K$ and it remains around 21 $W/m \cdot K$ at higher temperature [62], which has detrimental effect for heat dissipation during machining process. As a consequence of low thermal conductivity of the machining chips, a large proportion of the heat generated during machining is absorbed by the machining tool, which accelerates the rate of tool wear.

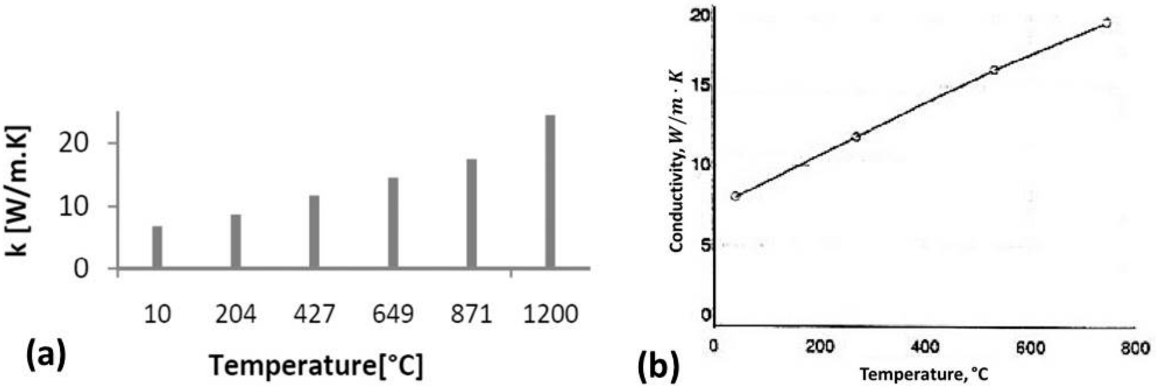

Fig. 2. 26 The thermal conductivity of (a) Ti-6Al-4V **[63]** *and (b) Ti-15V-3Cr-3Al-3Sn* **[38]** *varies as function of temperature.*

It should be noted that although titanium alloys perform extraordinarily in many mechanical properties, the Young's modulus of titanium alloys is relatively low compared with other high-strength materials, such as nickel alloys and stainless steels. Thus, there is a risk for a slender work-piece to deflect, and the adequate support is imperative [64].

The peculiar work-hardening tendency of titanium alloys induces a thin chip, and hence small chip-tool contact area on the rake face. As a consequence, much higher stress occurs in the vicinity of the cutting edge although the responsible cutting force is comparable to that used in steel and nickel-based alloy machining. As stated by Ezugwu and Wang [65], the Ti-6Al-4V cutting stress at the chip/tool interface was as large as three to four times of that in steel Ck53N machining, which affects the tool life adversely.

In addition, the high chemical reactivity of titanium alloys may cause the machining chips to weld on the tool to result in galling and smearing tool failure.

2.6.2.2 Improvements of titanium alloy machining

In order to overcome these machining problems, substantial improvements include the use of advanced cutting tools, alloy composition modification, and the combination with other techniques, such as laser irradiation and ultrasonic vibration.

In practice, various machining tools have been proposed for the titanium alloy machining, such as high speed steels (HSS), cemented carbide and synthetic diamonds. High speed steel cutting tools accompanied with heavily compounded oil or emulsion are widely used at low cutting speeds (<30 m/min), while at higher speeds (30-60 m/min), cemented carbides, for example cobalt-bound tungsten carbide (WC/Co), are usually accepted as the best tool materials for titanium alloy machining [48]. Nowadays, different coating systems are employed to extend the tool life. Dandekar *et al*. [66] compared the tool life of uncoated WC/Co cutting tool with TiC/TiN and TiAlN coated carbide cutters. Their results indicated that the TiAlN coated tool outperformed the other two materials and the corresponding tool life was about 2-3 times longer.

The modification of titanium alloy composition can improve the machinability via adding one or more elements, such as sulphur (S), selenium (Se) and rare earth metals, for example lanthanum (La) [67]. Second phase particles formed by these elements distribute on the grain boundaries, and these precipitates will soften or melt once the temperature in the shear zone of chips exceeds the softening or melting point. As a consequence, short breaking chips can be produced. The major benefits from the short chips include the reduction of the temperature at the rake face, the rate of tool wear and the roughness of the machined surface. In the study carried out by Siemers *et al*. [68], short Ti-6Al-4V machining chips were obtained by adding 0.9% pure metallic lanthanum. It should be noted that in case of Sn containing titanium alloys, lanthanum cannot improve the machinability as the formed intermetallic phase (La_5Sn_3) possesses high softening temperature. Thereby, in the investigation of improving Ti-6Al-2Sn-4Zr-6Mo machinability [69], the 2% of Sn was replaced by 3% of Zr, and the resultant Ti-6Al-7Zr-6Mo was further modified by adding 0.9% and 0.5%

of lanthanum. Short and strongly segmented chips were produced for both compositions, as shown in Fig. 2.27.

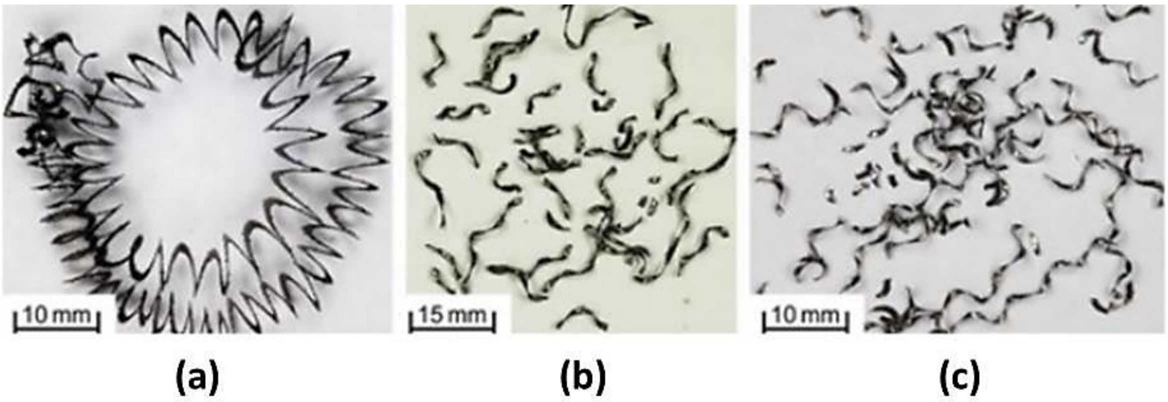

Fig. 2. 27 Chip appearances of (a) Ti-6Al-2Sn-4Zr-6Mo, (b) Ti-6Al-7Zr-6Mo-0.5La and (c) Ti-6Al-7Zr-6Mo-0.9La **[69]**.

Laser assisted machining (LAM) is an important thermally enhanced machining technique, wherein a laser beam is applied on the work-piece surface locally in front of the cutting tool. The main advantages of LAM are the reduction of the cutting force and the increase the metal removal rate and tool life. The investigation carried out by Rahman Rashid *et al*. [70] confirmed that a maximum 15% reduction of the cutting force could be obtained using LAM compared with conventional method during Ti-6Cr-5Mo-5V-4Al beta titanium alloy machining. In a recent research, a more significant reduction (~55%) of the cutting force via optimising the cutting parameters and the laser source was demonstrated in an experimental and numerical study of Ti-6Al-4V LAM [71].

Ultrasonic assisted machining (UAM) is another advanced technique for improving the titanium alloy machining process, the details of which will be described in Section 2.6.3.

2.6.3 Ultrasonically assisted turning of titanium alloys

Ultrasonically assisted turning (UAT) was first introduced in 1960s, in which high frequency vibration is superimposed on the conventional movement of the cutting tool [72]. It should be noted that in terms of UAT, the ultrasonic vibration is applied directly to the cutting tip, which is distinguished from other vibration-assisted machining processes that propel the abrasive slurry between the oscillating tool and the workpiece causing erosion [73]. In principle, ultrasonic vibration can be imposed on three directions during turning process: feed direction, radial direction and tangential direction (cutting direction), as illustrated in Fig. 2.28, while most current investigations apply vibration on the tangential direction.

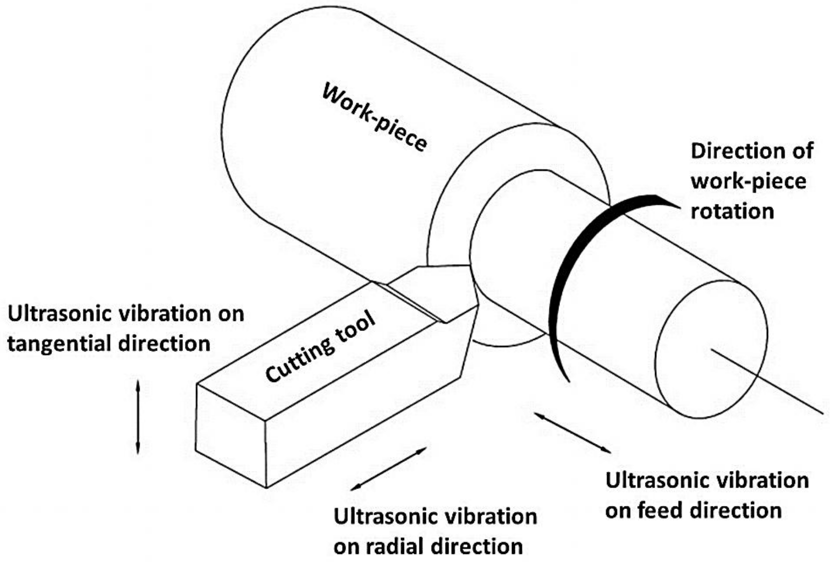

Fig. 2. 28 Schematic of three directions applied in UAT process, following **[74]**

As mentioned previously, titanium alloys are intractable for conventional machining. Thus, the employment of UAT in titanium alloy machining has attracted substantial attentions. The primary advantages of UAT include the reduction of cutting force, the improvement of machined surface roughness and the potential generation of short chips.

Maurotto *et al*. [75] compared the cutting forces imposed on the tool for conventional turning (CT) and UAT of Ti-15V-3Cr-3Al-3Sn alloy. They found significant reductions of measured cutting forces at various depths of cut when the material was processed by UAT: the maximum reduction exceeded 70%. The reduced cutting force occurred not only on the tangential direction but on the radial direction. The comprehensive results of their study were summarized in Fig. 2.29.

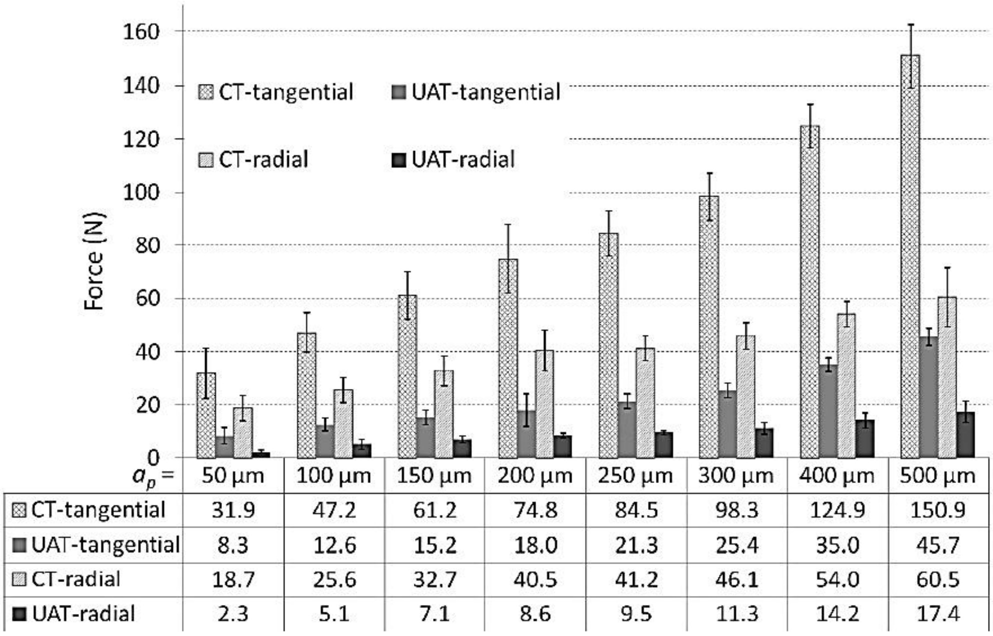

a_p =	50 µm	100 µm	150 µm	200 µm	250 µm	300 µm	400 µm	500 µm
▨ CT-tangential	31.9	47.2	61.2	74.8	84.5	98.3	124.9	150.9
■ UAT-tangential	8.3	12.6	15.2	18.0	21.3	25.4	35.0	45.7
▨ CT-radial	18.7	25.6	32.7	40.5	41.2	46.1	54.0	60.5
■ UAT-radial	2.3	5.1	7.1	8.6	9.5	11.3	14.2	17.4

Fig. 2. 29 Cutting force comparison between CT and UAT at various depths of cut **[75]**.

For the influence of UAT on the surface roughness, Silberschmidt *et al*. [76] conducted a systematic investigation showing a noticeable improvement of surface roughness produced by UAT for a broad range of materials, including copper, aluminium, stainless steel, nickel based alloys and titanium alloys. The surface topographies of Ti-15V-3Cr-3Al-3Sn machined by using CT and UAT were compared in Fig. 2.30.

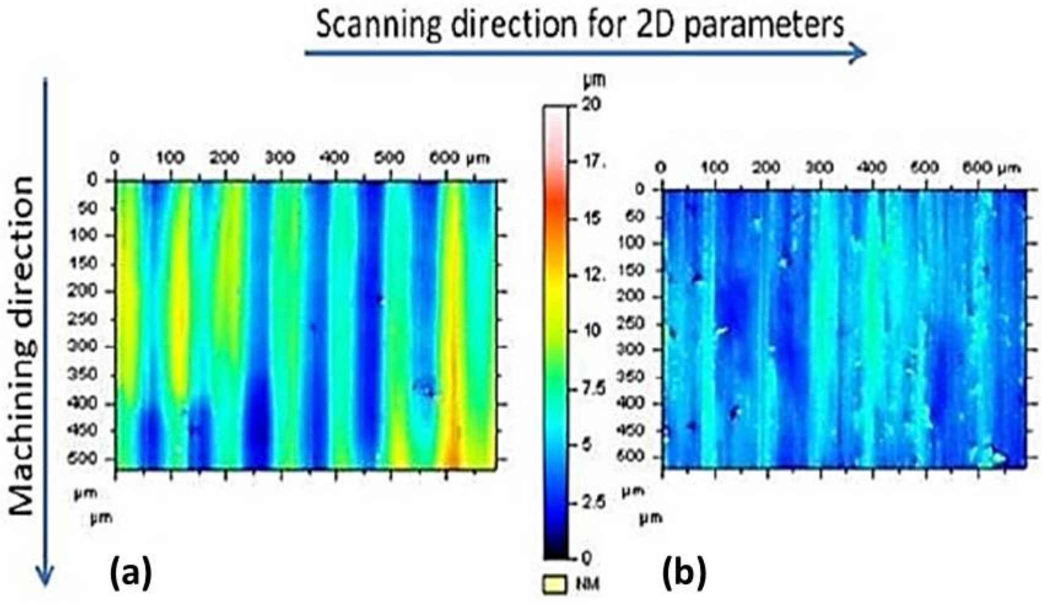

Fig. 2. 30 Surface topographies for Ti-15V-3Cr-3Al-3Sn processed by (a) CT and (b) UAT **[76]**.

2.7 Principle of ECAP

2.7.1 Ultrafine grain (UFG) materials and severe plastic deformation (SPD) processing

In general, the yield stress of metals and alloys are dominantly depended on the average grain size, which can be explained by the Hall-Petch Equation:

$$\boldsymbol{\sigma_y = \sigma_0 + k_y \cdot d^{-\frac{1}{2}}} \; \ldots \textit{ Equation 2. 3}$$

where σ_y is the yield stress, *d* is the grain size, σ_0 and k_y are constants. From this equation, it is obvious that grain refinement results in superior yield stress for metallic materials. Therefore, great interest has been attracted towards the extremely small grain size materials, or concisely, ultrafined grained (UFG) materials. Normally, UFG materials refer to materials that consist of grains with the size less than 1 µm [77].

For UFG materials fabrication, two basic approaches have been proposed: bottom-up and top-down. The bottom-up approach fabricates UFG materials from individual atoms or molecules. These nanostructured particles are assembled via specific technologies, such as electrosynthesis and inert gas condensation [77] [78]. The major disadvantage of the bottom-up approaches is that it cannot be employed in the large-scale manufacturing; furthermore, precision control is required to avoid residual porosity and contamination which leads to long fabrication time and high cost. In contrast, the top-down method, i.e. producing UFG materials from bulk materials with coarse grains, usually benefits the processing time and cost. Amongst various top-down UFG material fabrications, severe plastic deformation (SPD) is most promising, which breaks down coarse grains into finer ones via introducing high strain and high density of dislocations, and hence the formation of new grain boundaries.

Many different SPD processing techniques have been developed, including equal channel angular pressing (ECAP) [79] [80], accumulative roll-bonding (ARB) [81] [82], high pressure torsion (HPT) [83] [84], cyclic-extrusion-compression (CEC) [85], twist extrusion [86] [87], etc. Amongst these SPD methods, ECAP, ARB and HPT are well-established [77]. The schematic diagrams of ARB and HPT are shown in Fig. 2. 31, and that of ECAP will be illustrated in the following section. It is obvious that ARB is not feasible for consolidation of discrete materials because the process is carried out under unconstrained conditions. HPT can be operated under constrained conditions [83], and has been employed for metallic powder or chip consolidation [88] [89] [90]. However, the major problem of HPT process is the different cumulative strain in the centre and on sample periphery [91]. Fig. 2.32 shows the accumulative strain as a function of the distance from the sample centre after various numbers of revolutions. Another important problem is the enlargement of HPT specimen size: typical samples processed by HPT are disk-like shape with a diameter from 10 – 20 mm and a thickness of 0.2 – 0.5 mm [91]. Compared with other SPD methods, ECAP is considered as the most prospective processing technique because: First, ECAP is capable of imposing high shear strain on the work-piece without changing its cross-sectional dimensions. Second, the die construction for ECAP is relatively simple and it is possible to fabricate large size of billets. Third, reasonably homogenous strain can be attained via repetitive ECAP process [77]. The following sections will focus on the principles of the ECAP process, including a brief history, fundamental parameters and recent developments for the technique.

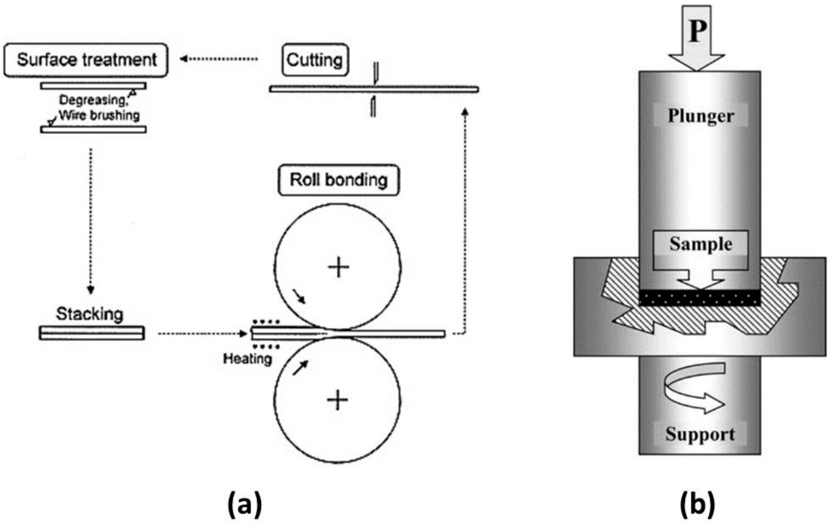

Fig. 2. 31 Schematic illustrations of (a) ARB **[81]** *and (b) HPT processing* **[84]**.

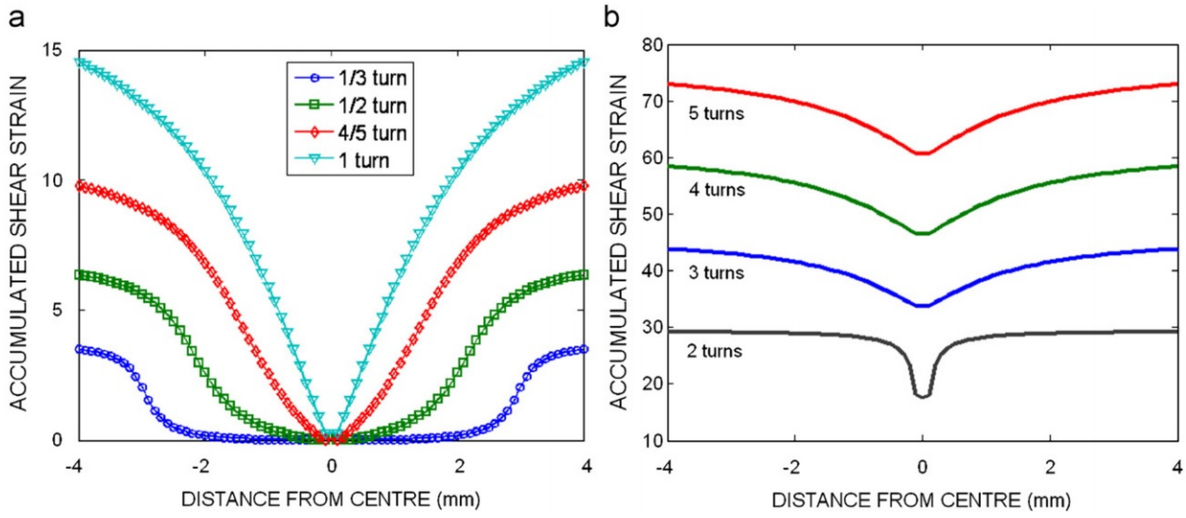

Fig. 2. 32 Accumulated equivalent strain vs. distance from the specimen centre (from modelling) **[92]**.

2.7.2 Brief history of ECAP

The process of ECAP was invented by V. M. Segal and his colleagues in 1972 in Minsk in the former Soviet Union. The original objective is to introduce high strains into metal billets by simple shear because simple shear is a near ideal deformation method for desirable microstructure and texture formation [80]. However, before fabricating UFG materials via ECAP process was realised in the early 1990s, ECAP had only been considered as a laboratory curiosity. After that, substantial attention has been attracted to employ ECAP process to enhance mechanical properties of metals and alloys. At the beginning, the major research was focused on soft metals, such as aluminium [93] [94] and copper [95] [96]. Recently, amount of research has been carried out on hard metals, for example titanium [97] [98] and its alloys [99] [100]. Meanwhile, successful attempts have been conducted on the consolidation of metallic powder or machining chips using ECAP [101] [102] [103] [104] [105] [106] [107] [108]. It should be pointed out that although ECAP has become a well-established approach to produce materials with superior properties and it starts to emerge from laboratory to practical applications [109] [110], this technique has not been widely used in industrial scale [111]. A report [112] on ECAP commercialization demonstrates that ECAP processing has been scaled up to 4000 tonnes press capacity in Honeywell, the die of which is shown in Fig.2.33. The largest ECAP product was 32.7 kg for aluminum billet and 110 kg for copper alloys.

Fig. 2.33 Production ECAP die with 4000 tonnes press capacity **[112]**.

2.7.3 Geometry parameters of ECAP die

A basic ECAP die consists of two intersecting channels with equal cross-sectional area, the schematic of which is illustrated in Fig.2.34. In the figure, two important geometry parameters are defined: the channel intersection angle Φ and the die curvature angle Ψ. The effects of these two angles on the resultant microstructure and mechanical properties are mainly incarnated by the total imposed strain. The accumulated strain ε_N after N cycles using an ECAP die with intersection angle Φ and relief angle Ψ is given by [113]:

$$\boldsymbol{\varepsilon_N = N \cdot \left[\frac{2\cot\left(\frac{\phi}{2}+\frac{\psi}{2}\right)+\psi\csc\left(\frac{\phi}{2}+\frac{\psi}{2}\right)}{\sqrt{3}}\right]} \text{ … Equation 2. 4}$$

In addition, the inclination angle (θ) and the inclination direction (ID) is indicated in Fig. 2.34. The inclination angle (θ) can be calculated by [80]:

$$\boldsymbol{\tan\theta = \frac{1}{\varepsilon+1}} \text{ … Equation 2. 5}$$

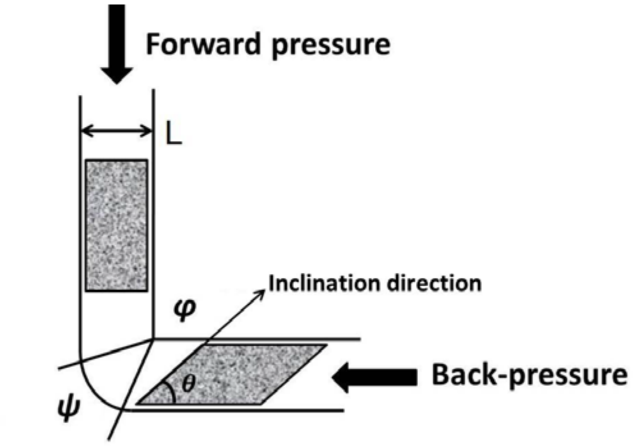

Fig. 2.34 Schematic of back-pressure associated equal channel angular pressing process.

2.7.3.1 The effect of the intersection angle, *Φ*

The channel intersection angle affects the imposed strain in each ECAP pass. According to Equation 2.4, when the channel curvature angle Ψ is zero; then the accumulative imposed strain is given by:

$$\boldsymbol{\varepsilon_N = \frac{2N}{\sqrt{3}} \cdot cot\frac{\phi}{2}} \ldots \textit{Equation 2. 6}$$

From this equation, it is apparent that the imposed strain in each pass reduces as the channel intersection angle increases. Nevertheless, it should be noted that the intersection angle published in previous reports is usually in the range between 90° to 120°. The reason for this is elaborated by the following cases.

Through decreasing the intersection angle, Φ, the imposed strain in single pass can be increased, and hence the efficiency of ECAP. However, ECAP with acute intersection angle is only feasible for those soft metals, for example, Al and its alloys. ECAP with 60° channel intersection angle were successfully conducted on pure Al and Al-1%Mg-0.2%Sc alloy at room temperature [114]. In comparison with the results obtained by using 90° ECAP die, it was shown that smaller grain sizes were achieved: for pure Al, it decreased from ~1.2 µm (90°) to ~1.1 µm (60°); for Al-Mg-Sc alloy, it reduced from ~0.36 µm to ~0.30 µm. In addition, smaller grain size of Al-Mg-Sc alloy also led to significantly improved superplastic behaviour compared with that pressed in 90° die, as shown in Fig. 2.35.

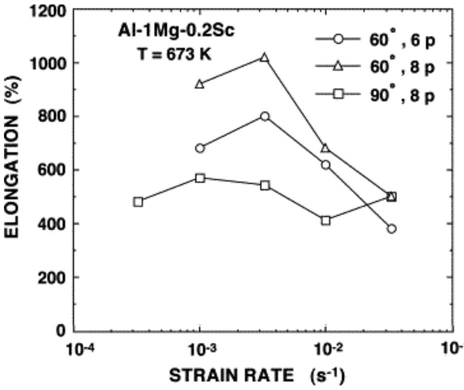

Fig. 2.35 The elongation to failure of Al-Mg-Sc alloy samples processed by 60° ECAP compared with 90° ECA pressed samples. Tensile test temperature was 673 K **[114]**.

There is one important side-effect of the intersection angle reduction: higher forward pressure is required during ECAP process, which may lead to a risk of equipment damaging and sample cracking. This is a vital consideration especially for hard-working materials or materials with low ductility. Early research [115] had proved that commercial purity (CP) titanium pressed at room temperature underwent segmented failure when 90° ECAP die was used. While one recent study [116] shown that it was feasible to process CP Ti at room temperature through a 120° ECAP die, the resultant product of which was free of cracking. The appearances of CP Ti samples pressed through 90° and 120° dies are compared in Fig. 2.36. They also found that the mechanical properties improved via single pass of 120° ECAP slightly exceeded those obtained by multiple pass of 90° ECAP at elevated temperatures [116].

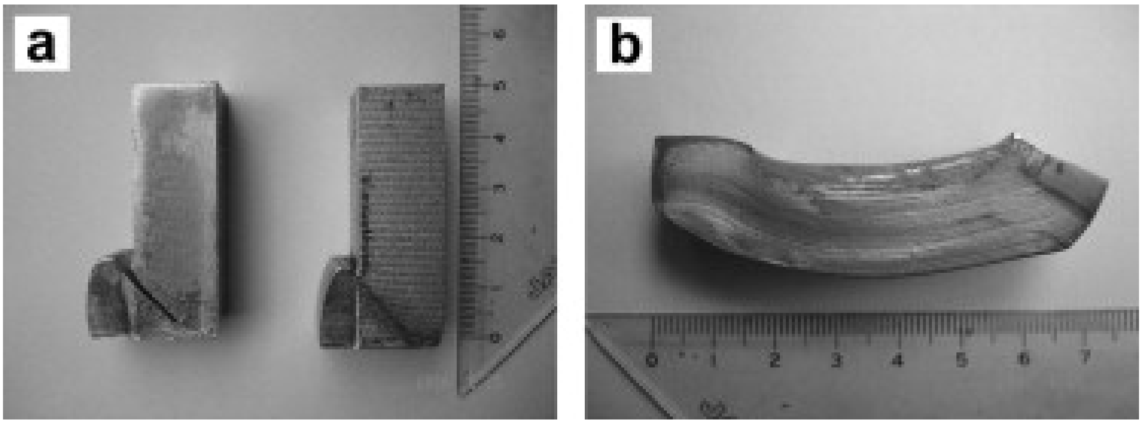

Fig. 2.36 Appearance of CP Ti samples after ECAP at room temperature using (a) 90° die and (b) 120° die **[116]**.

Despite the ease of pressing hard-working metals through ECAP dies with larger intersection angles, increasing the channel angle reduces the efficiency of ECAP process but also influence the resultant microstructure. Nakashima *et al*. [117] had carried out ECAP on pure aluminum at room temperature with the intersection angle ranged from 90^o to 157.5^o. The corresponding schematics of the dies are illustrated in Fig. 2.37. Using Equation 2.4, the equivalent strain was imposed using various ECAP dies by adjusting the number of passes. Therefore, the total accumulative strain of ~4 was introduced by processing samples for 4, 6, 9 and 19 passes for the die with channel angles of 90°, 112.5°, 135° and 157.5°, respectively. The corresponding TEM micrographs and selected area diffraction (SAD) pattern are shown in Fig. 2.38. It is apparent that although the cumulative strain was similar for different processes, equiaxed grains with ultrafine sizes were achieved via 90° ECAP, while banded microstructure occurred with the increasing channel angle. In term of SAD patterns, it is most readily to obtain diffused or ring patterns using smaller intersection angle. These results implied that in order to attain equiaxed ultrafine grains and hence potential superior mechanical properties, it is essential to impose an intensive strain in single ECAP pass rather than increasing the number of passes.

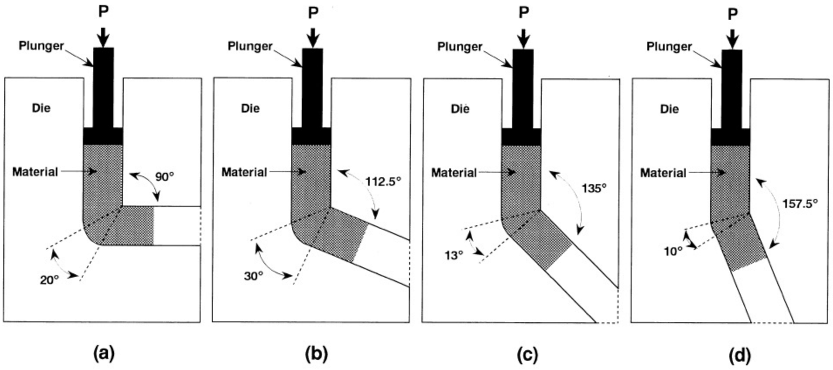

Fig. 2.37 Schematics of the die used to investigate the influence of the intersection angle **[117]**.

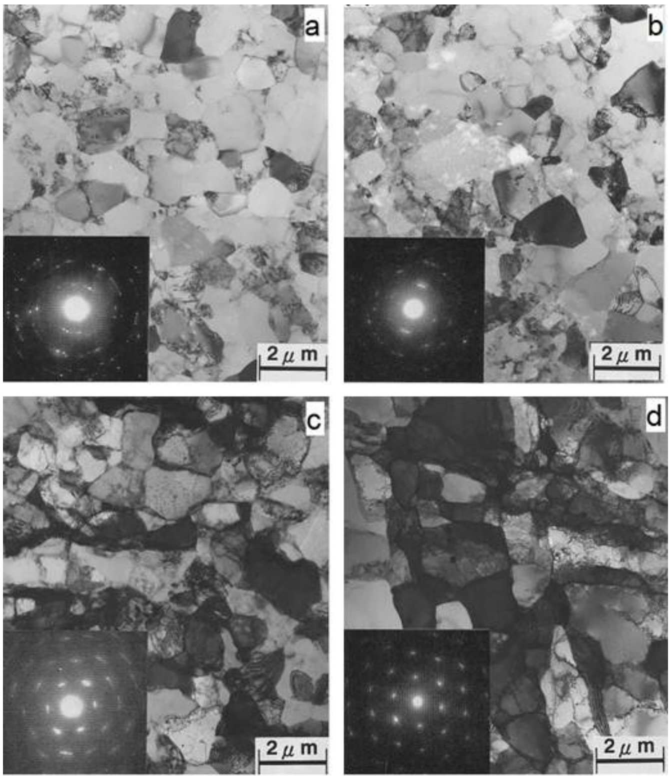

Fig. 2.38 TEM micrographs and corresponding SAD patterns obtained using ECAP dies with intersection angles of (a) 90°, (b) 112.5°, (c) 135° and (d) 157.5° **[117]**.

In summary, the larger intersection angle usually leads to an easier procedure but a reduction of imposed strain in single pass. On the contrary, decreasing the channel intersection angle is capable to introduce a high shear strain in each separated pass, but at the expense of segmentation risk. In practice, the ideal ECAP die usually has a channel angle of close to 90°.

2.7.3.2 The effect of the curvature angle, Ψ

From Equation 2.4, it is noted that the curvature angle, Ψ has influences on the imposed strain, although it is not as significant as the intersection angle does. The plot [118] in Fig. 2.39 shows the relationship between the curvature angle and the equivalent strain when the sample is subjected to a single pass and the channel angle is 90°.

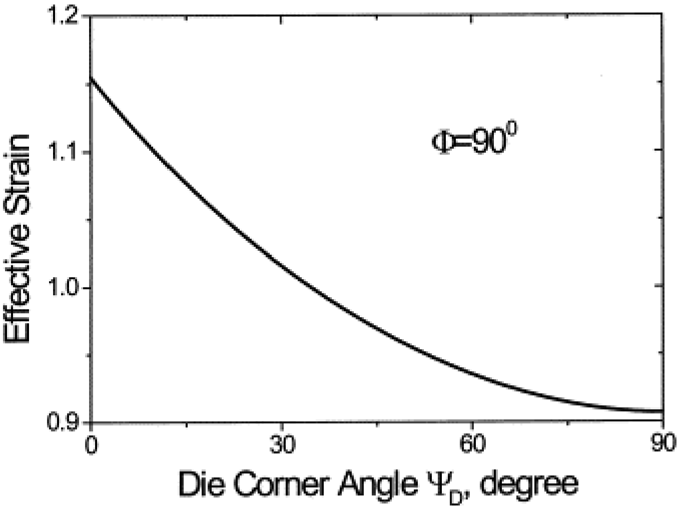

Fig. 2.39 Equivalent strain as function of the curvature angle **[118]**.

In addition to the effect on the imposed strain, the importance of the curvature angle lies in the impact on the strain inhomogeneity during ECAP process. The inhomogeneity arising from the curvature angle was widely investigated using finite element modelling (FEM) [118] [119] [120] [121] [122].

In the study carried out by Suh *et al*. [120], FEM method was employed to simulate four ECAP processes using dies with the curvature angles of 0^o, 30^o, 60^o and 90^o at fixed intersection angle of 90^o. The steady deformation patterns of each simulation are shown in Fig. 2.40. In the case of Ψ= 0°, all the grids across the whole billet were uniformly distorted; that is, all the rectangular elements became parallelogram. As the curvature angle increased, the grids at the top became parallelogram, whereas the lattices at the bottom remained rectangular. This situation became most apparent in the case of Ψ=90°, which implied less strain imposed in the lower region. It is manifest that larger curvature angle can lead to more severe strain inhomogeneity.

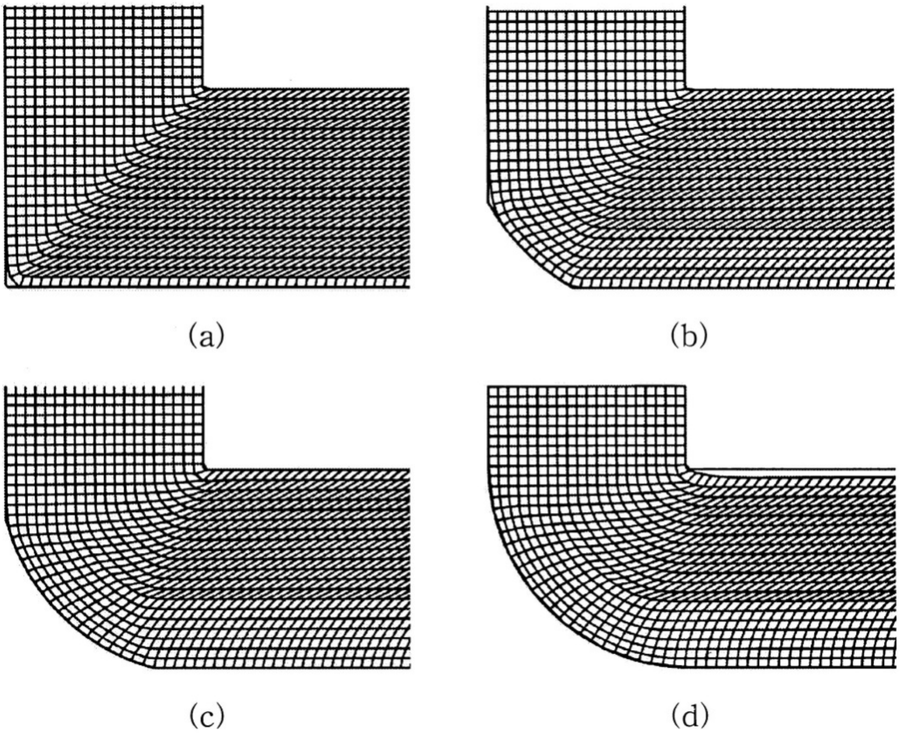

Fig. 2.40 Deformation patterns of the ECAP simulations with different curvature angle (a) Ψ=0°, (b) Ψ=30°,(c) Ψ=60° and (d) Ψ=90° **[120]**.

Although the correlation between the curvature angle and the strain inhomogeneity has been clarified, the results obtained by Xu *et al*. [123] are partially contradictory to the FEM simulations. As indicated in the report, there is no measureable microhardness inhomogeneity difference between the sample subjected to the die with *ψ*=20° and *ψ*=0°. The corresponding colour-coded contour maps of microhardness distribution are given in Fig. 2.41. In these two maps, it is obvious that both samples behaved lower microhardness values at the bottom part, which is consistent with the FEM simulation. However, there is not sufficient inhomogeneity increasement as the curvature angle changed from 0° to 20°. The most possible explanation to this phenomenon is that the 'dead zone' negates the effect of curvature angle [77]. The dead zone is a cavity area formed at the outer corner, where the sample no longer receives constraint force from the die wall. It should be noted that the corner angle subtended by the dead zone depends on the materials strain hardening behaviour. In general, there are three types of material constitutive behaviours during ECAP processing: strain hardening, ideal plastic and flow softening. The material constitutive performance is not only determined by the material itself but also influenced by the deformation temperature and stress rate

[124]. Most engineering materials exhibit strain hardening at room temperature. The typical example of perfectly plastic deformed material is Ti-6Al-4V with equiaxed microstructure deformed at 955°C with a strain rate of 1 mm/s [124]. As for flow softening behaviour, most materials perform this behaviour above the recrystallization temperature. Ti-6Al-4V with lamellar microstructure deformed at 900°C with a strain rate of 1 mm/s is a representative example [124]. It is important to point out that the flow softening materials are not suitable to conduct ECAP without curvature angle, because if strain concentration occurs, there is a high risk of deformation localization since the localized stress reduces as the strain increases. The flow stress as function of strain rate for these three behaviours is shown schematically in Fig. 2.42.

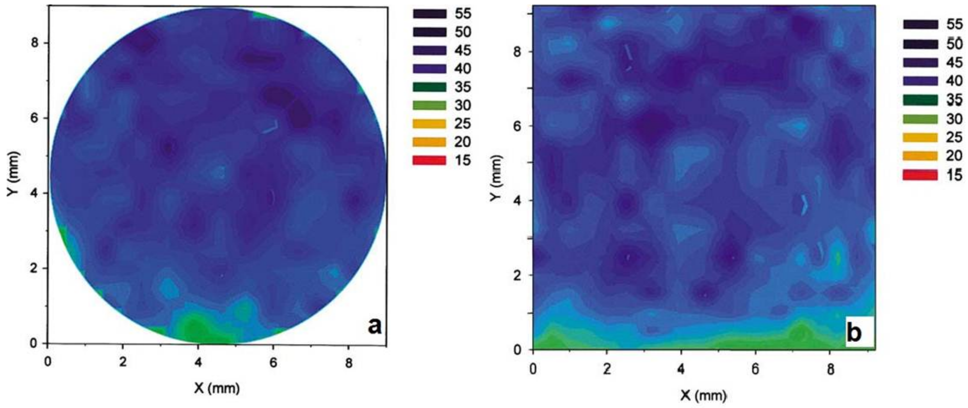

Fig. 2. 41 Colour-coded contour maps of the microhardness in the cross-section of a pure aluminium sample subjected to ECAP with (a) ψ=20° (b) ψ=0° **[123]**.

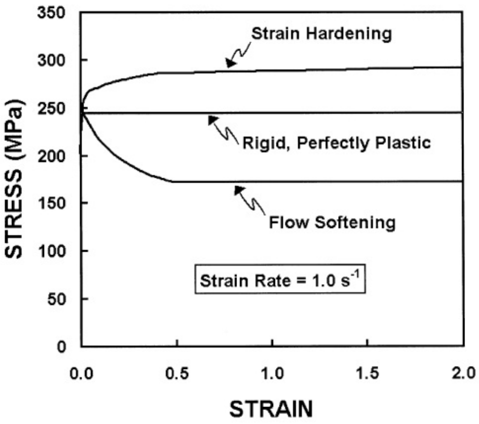

Fig. 2. 42 Schematic of three constitutive behaviours **[121]**.

As a conclusion, a reasonable reduction of curvature angle can assist in reaching an effective strain and alleviate strain inhomogeneity, but the optimal curvature angle is determined by specific materials and operation conditions.

2.7.4 Processing parameters of ECAP

In addition to the geometric parameters, several procedure variables need to be considered during ECAP process, including pressing velocity, operating temperature, back-pressure and processing routes. The following paragraphs address the effects of these processing parameters.

2.7.4.1 The effect of pressing velocity

According to previous research [125] [126] [127], it is suggested that the pressing velocity has no significant effect on the resultant grain size. A series of room temperature ECAP processes were conducted on pure aluminum at four ram speeds: 8.5 X 10^{-3}, 8.5 X 10^{-2}, 8.5 X 10^{-1} and 7.6 mm/s [125]. TEM micrographs of the samples using the slowest and fastest pressing velocity are shown in Fig. 2.43. It can be seen that the average grain sizes for both conditions are about 1.2 µm. At higher magnification, it is observed that there are many extrinsic dislocations presented with the grains after high speed pressing (Fig. 2.44(b)), whereas the dislocation density in the slow pressed sample was relatively low (Fig. 2.44(a)). It implies that recovery occurred during the slow ECAP procedure. As a consequence, the measured microhardness and yield stress were slightly higher at the faster pressing speeds.

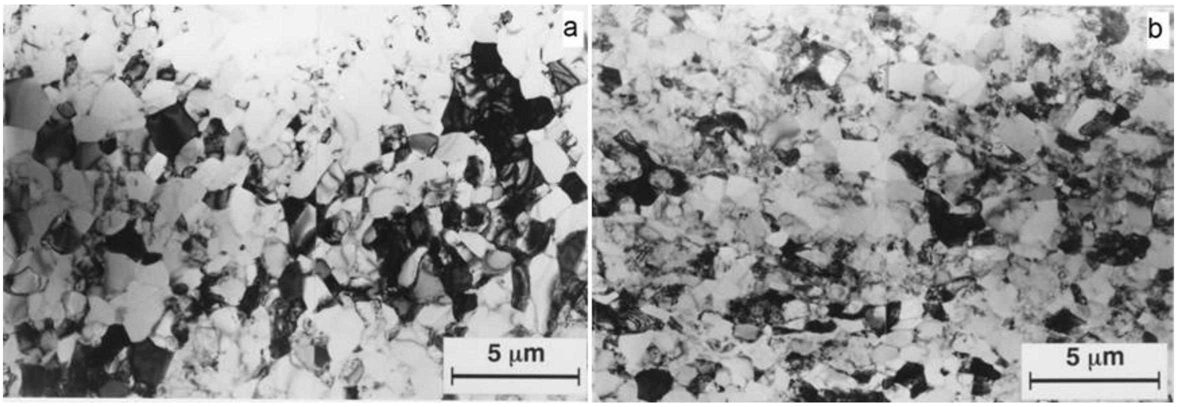

Fig. 2. 43 TEM micrographs of pure Al after four ECAP passes at pressing speeds of (a) 8.5 X 10^{-3}mm/s and (b) 7.6 mm/s **[125]**.

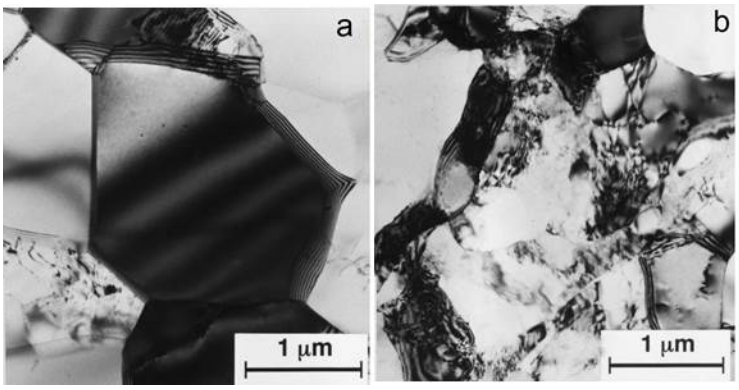

Fig. 2. 44 High magnifications of pure Al after four ECAP passes at pressing speeds of (a) 8.5 X 10^{-3}mm/s and (b) 7.6 mm/s **[125]**.

Another investigation on pure titanium [126] indicates that the ECAP pressing velocity possibly affects the accommodation mechanism of a large strain for HCP materials: changing from deformation twinning to dislocation slip. Kim *et al*. [126] conducted ECAP tests at 350 °C with pressing speeds of 2.8 and 0.2 mm/s. The TEM micrographs and corresponding SAD patterns, as shown in Fig. 2.45, revealed that deformation twins were present in the pure titanium exposed to fast ECAP; while in the case of slow pressing only slip bands existed in the sample. However, deformation twinning was rarely observed in Ti subjected to a large strain at 350 °C [126]. Therefore, further investigation is needed to determine the influence of ECAP pressing speed on deformation mechanism of HCP materials.

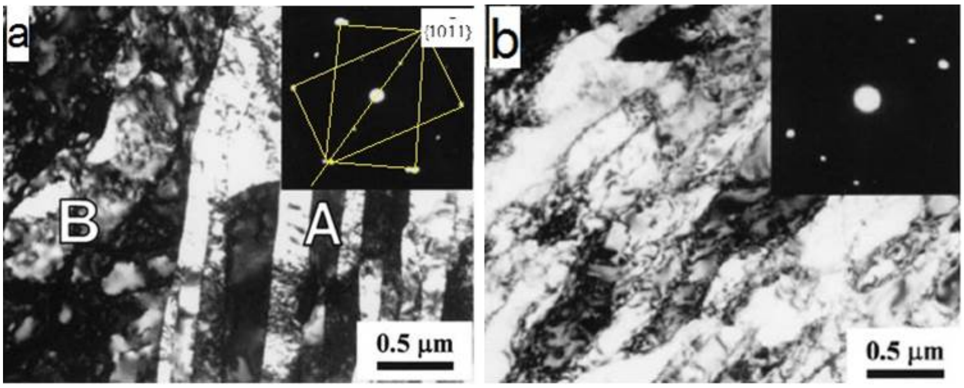

Fig. 2. 45 TEM micrographs and corresponding SAD patterns in pure Ti after single ECAP at pressing speeds of (a) 2.8 mm/s (b) 0.2 mm/s **[126]**.

In addition, the reduction of pressing speed facilitates the uniformity of material flow. In a study by Semiatin *et al*. [115], CP Ti was pressed with various velocities of 0.25, 0.81, 2.50 and 25.0 mm/s. Uniform flow was achieved at the pressing velocity between 0.25 and 2.50 mm/s, while segmented flow was obtained during ECAP at the fastest speed of 25.0 mm/s, the corresponding macrographs of which are shown in Fig. 2.46.

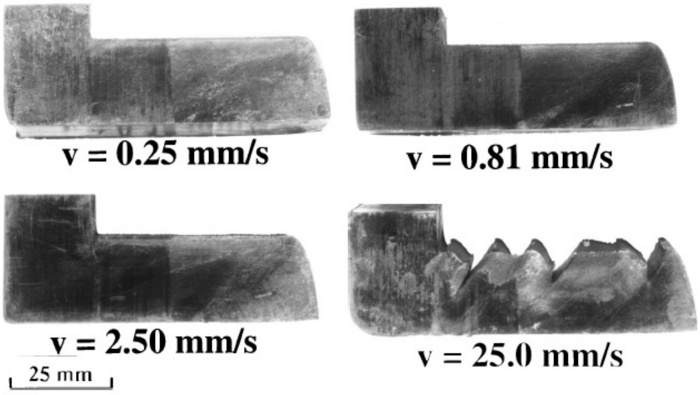

Fig. 2. 46 Macrographs of CP Ti after ECAP at 325 °C with pressing velocities of 0.25, 0.81, 2.50 and 25.0 mm/s **[115]**.

2.7.4.2 The effect of operating temperature

At the state of the art, the ECAP die is usually heated up by cartridge heaters, the schematic of which is illustrated in Fig. 2.47 [128]. In some cases, the die is constructed in a furnace, as shown in Fig. 2.48 [129]. In this configuration, the pressing temperature is normally monitored continuously and controlled by a thermocouple located in the vicinity of the shear plane.

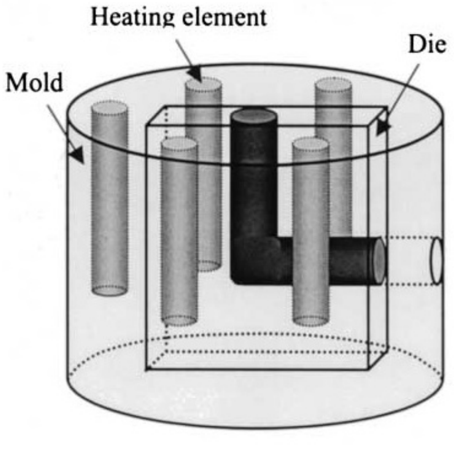

Fig. 2. 47 Schematic of an ECAP die combined with cartridge heaters **[128]**.

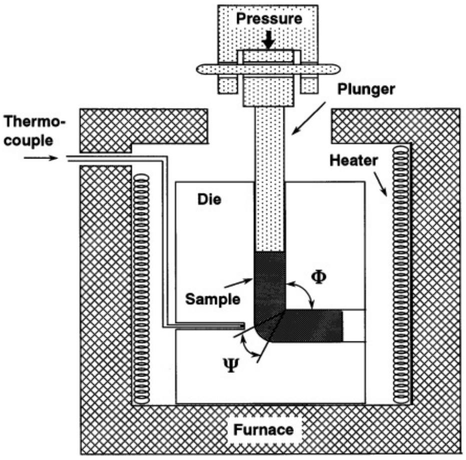

Fig. 2. 48 Schematic of an ECAP die constructed in a furnace **[129]**.

The main purpose of increasing the ECAP temperature is to enhance the material flowability, especially for hard-working metals, for example Ti and Ti alloys. Semiatin *et al*. [115] carried out an extensive study into the effect of temperature on workability of CP Ti. It was found that the minimum feasible processing temperature for CP Ti was ~275 °C, below which the sample broke into several segments. The flowing behaviour of the material was characterized by corresponding ECAP load-stroke curves, as shown in Fig. 2.49. It can be found that for uniform flow the load stayed at a steady state after a slight drop following the initial peak.

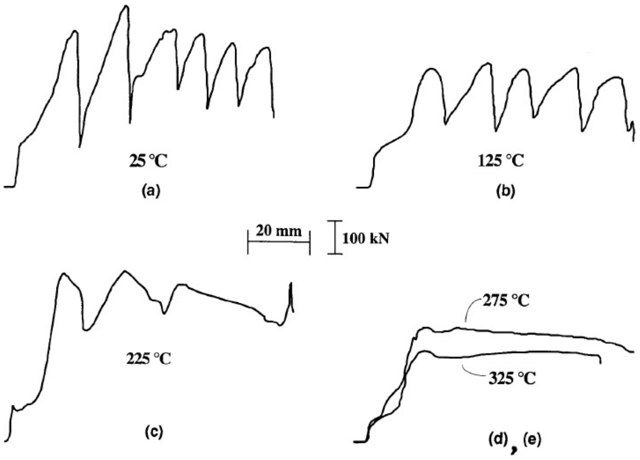

Fig. 2. 49 Load-stroke curves for CP Ti ECAP at various processing temperature: (a) 25 °C, (b) 125 °C, (c) 225 °C, (d) 275 °C and (e) 325 °C **[115]**.

In further studies of the workability of Ti alloys affected by the processing temperature, it has been suggested that the isothermal conditions can facilitate the uniform flow for hard-working materials. There are two separate reports describing the flowing performance of Ti-6Al-4V in 90° ECAP die. In the early research carried out by DeLo and Semiatin [130], it claimed that the lowest temperature for Ti-6Al-4V samples uniformly passing was 900 °C. They preheated the samples at the furnace up to 900 °C, and then the billets were inserted into a relatively ‘cool’ die at 300 °C. There was heat transfer from the specimen to the ‘chilly’ die, which was the main cause to surface segmentation. Ko *et al*. [131] performed ECAP under isothermal conditions, i.e., pressing the high temperature samples in a die at the same temperature. In their report, the minimum feasible processing temperature to obtain uniform deformation for Ti-6Al-4V reduced to ~600 °C.

Large amount of studies have been carried out to investigate the effects of operating temperature on the resultant microstructures and mechanical properties [128] [129] [131] [132] [133] [134]. In spite of various metals and alloys, similar conclusions can be drawn from these investigations: the grains enlarge and the fraction of high-angle grain boundaries reduces as the operating temperature increases. Yamashita *et al*. [129] conducted 6-pass ECAP on pure Al at temperatures ranged between room temperature to 300 °C. The comparison of TEM micrographs (Fig. 2.50) shows that the grain size is larger via high-temperature ECAP. Ring-shape and diffused SAD patterns were obtained in pure Al processed at room temperature and 100^{o}C, respectively. At higher temperature regular diffraction spots formed, which implied reduction of high-angle grain boundaries. This is because at high temperature, dislocations are more likely to annihilate during recovery and/or recrystallization, and hence less dislocation impinging. The increasing dislocation annihilation rate suppresses the formation of high-angle grain boundaries.

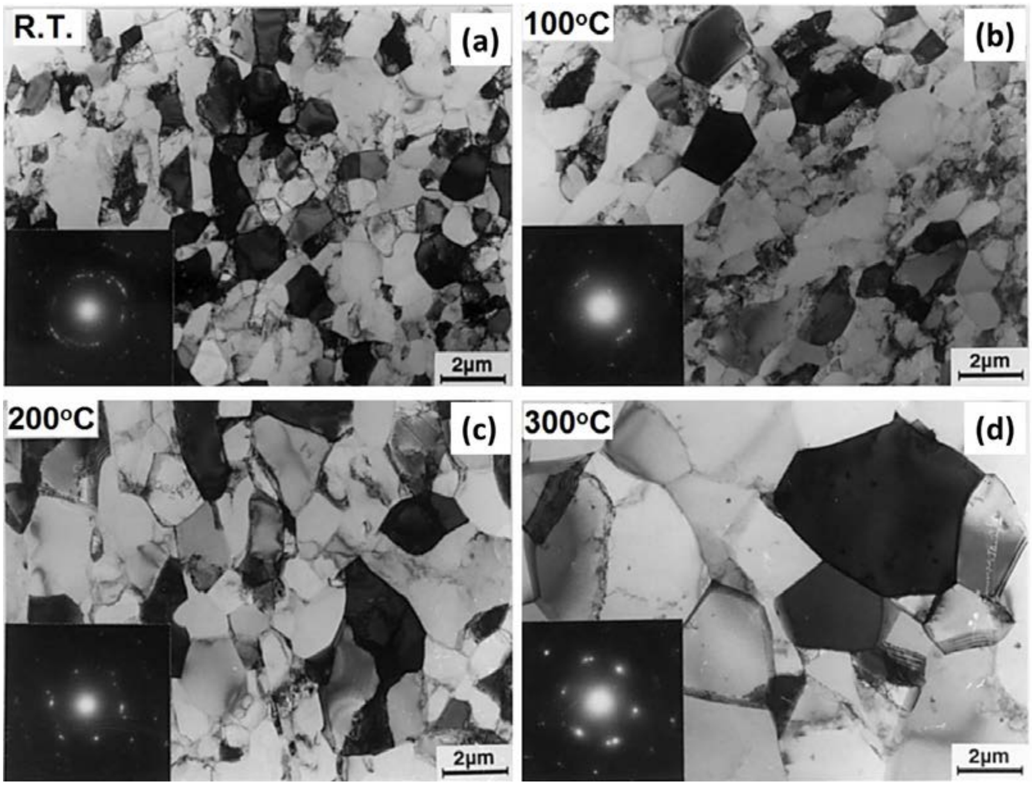

Fig. 2. 50 TEM micrographs and associated SAD patterns in pure Al after ECAP at (a) room temperature, (b) 100 °C, (c) 200 °C and (d) 300 °C **[129]**.

Kim *et al*. [132] demonstrated that the influences of ECAP processing temperature on HCP metals, for example pure Ti, lie in not only resultant microstructure but also deformation mechanisms. It was reported that the dominant deformation mode for CP Ti at 200^{o}C was <$\vec{a}$> type dislocation, and <$\vec{a}+\vec{c}$> type dislocation was also observed to accommodate imposed shear strain. Nonetheless, $\{10\bar{1}1\}$ deformation twinning bands were observed when CP Ti sample was pressed at 250 °C, accompanying with slip. The variations of dislocation and twin densities as function of ECAP processing temperature for CP Ti are illustrated in Fig. 2.51.

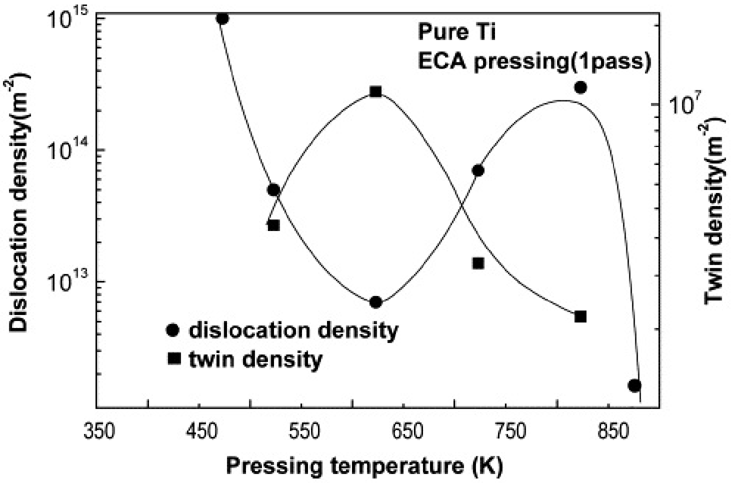

Fig. 2. 51 Variations of dislocation and twin density as function of pressing temperature for Ti **[132]**.

2.7.4.3 The effect of imposed back-pressure

As seen in Fig. 2.34, apart from forward pressure, a back-pressure can also be applied in the exit channel. Generally speaking, frictional force between the specimen and the output channel can be considered as the most immediate approach to impose back-pressure. Oruganti *et al*. [135] studied the effect of the friction coefficient on material flow behaviour during ECAP using FEM analysis. Their results suggested that although friction provided positive effects on die fill at room temperature, it is detrimental to shear strain homogeneity at high temperature. Thereby, the application of a second plunger is the popular choice for current back-pressure associated ECAP devices.

One benefits of back-pressure lies in the improvement of material workability [136] [137]. Stolyarov *et al.* [137] performed room temperature ECAP on a brittle cast Al-5 wt. % Fe alloy with/without back-pressure. In the absence of back-pressure, the specimen cracked after two passes, while accompanied with a back-pressure of 275 MPa, the sample survived free of visible surface cracking after 16 passes with consequent strain of 18.4.

Another important advantage of the application of back-pressure is to decrease the dead zone [77] [138]. The finite element simulations in Fig. 2.52 show the elimination of dead zone with the level of back-pressures. Nonetheless, the influences of back-pressure on the strain distribution and flow uniformity depend on specific materials. Kang *et al*. [139] investigated the effects of back-pressure during ECAP on perfect plastic and strain hardening materials. Their results revealed that the imposed back-pressure could prevent the ideal plastic deformation zone (PDZ) from changing to a fan-shape zone and improve the strain distribution homogeneity only in case of strain hardening materials, while the opposite effects were observed in perfect plastic materials.

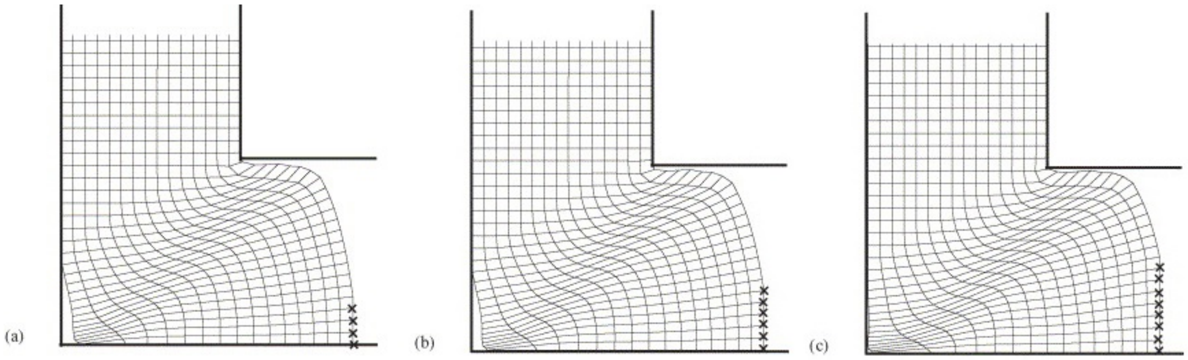

Fig. 2. 52 Elimination of the dead zone with increasing back-pressure of (a) 100 MPa, (b) 200 MPa and (c) 300 MPa **[138]**.

2.7.4.4 The effect of processing routes

ECAP allows repetitive pressings to attain expected strain as the cross section of the as-pressed samples remains unchanged. There are four fundamental processing routes have been identified and delineated in Fig. 2.53: (1) Route A: the sample is pressed repetitively without rotation; (2) Route B_A: the sample is rotated by 90^o in alternate directions between consecutive passes; (3) Route B_C: the sample is rotated in the same sense, either clockwise or counter clockwise, between each pass and (4) Route C: the sample is rotated by 180^o between passes. The processing route impacts ECAP samples comprehensively, including microstructure, mechanical properties, deformation mode and strain distribution.

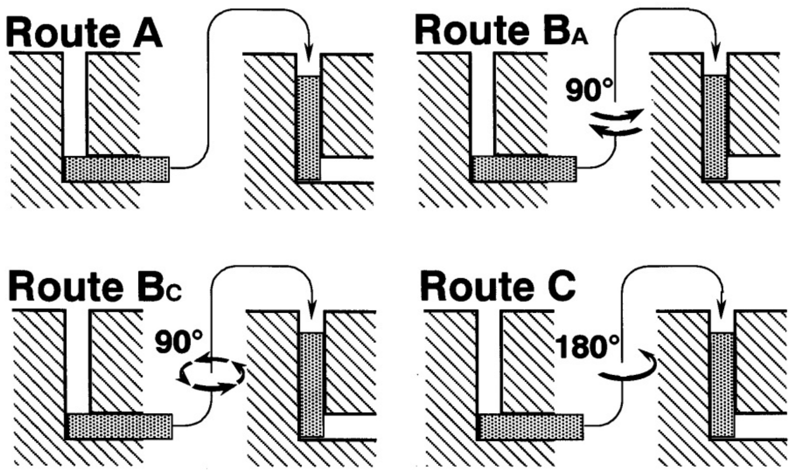

Fig. 2. 53 Four fundamental processing routes for multi-pass ECAP [47]

The first detailed experimentation of the influence of the processing route on the microstructure involved the pressing of pure Al in the research carried out by Iwahashi *et al*. [140]. They pressed pure Al at room temperature with a velocity of ~19 mm/s by using three different routes: route A, route B$_C$ (it was referred as route B in that paper) and route C. It was concluded that route B$_C$ is the most effective to generate high angle grain boundaries; the evolution process is less rapid when the sample was rotated in route C and route A is the most ineffective in ultrafine grained microstructure evolution.

In the case of Mg-containing Al alloy pressed at 200 °C repetitively by using route A, B$_C$ (it was referred as route B in that paper) and C, despite the significant grain refinement via multi-pass ECAP, various processing routes resulted in different grain morphologies and orientations [141]: the grains via route A pressing appeared to be elongated and the orientation tended to be aligned with the shear direction, and route B$_C$ and C produced the samples containing equiaxed grains with more random orientation. The tensile stress-strain curves of as-pressed samples are shown in Fig. 2.54. It is obvious that the yield and ultimate tensile strength (UTS) of route B$_C$ sample were highest, subsequently followed by route C and A samples.

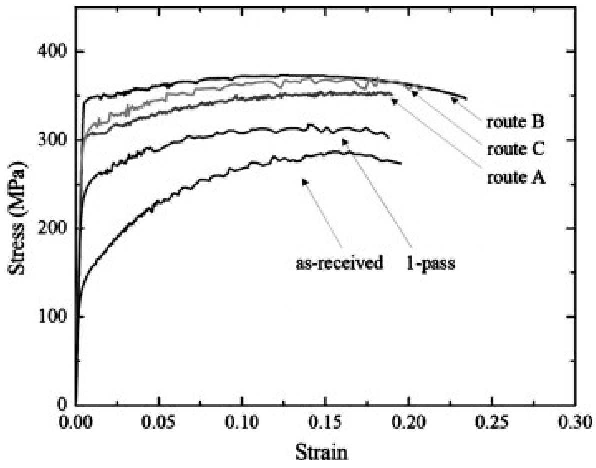

Fig. 2. 54 Stress-strain curves for various routes pressed samples **[141]**

The influence of processing routes on deformation modes for HCP materials was investigated by Shin *et al*. [142] and Suwas [143]. Shin *et al*. [142] carried out studies on CP Ti pressed at 350 °C for two passes via different routes. Their results showed that during the first ECAP pass, the shear strain was accommodated by $\{10\bar{1}1\}$ deformation twinning, while in the second pass it was dominated by dislocation glide. For the sample via route A, basal <$\vec{a}$> slip accompanied with micro-twins; for the sample via route B_C, prismatic <$\vec{a}$> slip was the main deformation mechanism; for the sample via route C, prismatic <$\vec{a}$> and <$\vec{a}$ + $\vec{c}$> dislocation slips cooperated with deformation twins were activated. However, in the later research, Suwas *et al*. [143] claimed a contradictory conclusion: a predominant basal slip accommodated the shear strain and twinning played a minor role during all three routes. The main reason behind this could be the different processing temperature: in the experiments conducted by Suwas *et al*., ECAP was performed at 400 °C.

A detailed numerical FEM study conducted by Xu *et al*. [144] compared the effective strain distribution by routes A, B_C and C. The major simulation results are concluded as follow: route A cannot provide good deformation uniformity; route C can get a uniform effective strain distribution after even passes, while the strain gradient along the cross section is relatively high after odd passes; for route B_C, the uniformity of effective strain distribution can be improved with the increasing number of passes. The effective strain distribution profiles for various processing routes during four passes and the comparison after the 4th pass were illustrated in Fig. 2.55.

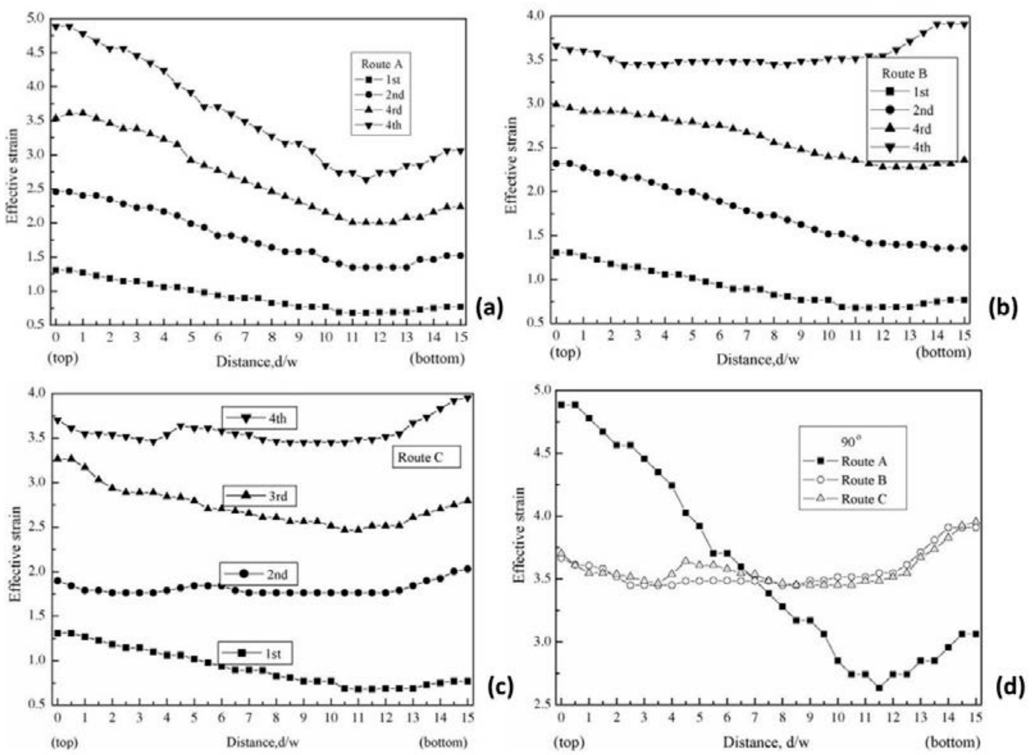

Fig. 2. 55 Effective strain accumulations in pure Al pressed for 4 passes via (a) route A, (b) route B_C and (c) route C; (d) strain distribution via different processing routes after 4th pass **[144]**.

It is noted that most research concentrated on the influences of route A, B_C and C, whereas detailed comparison between route B_A and B_C was indicated in two related reports. Oh-Ishi *et al*. [145] studied the microstructure evolution of pure Al pressed via route B_A using the same experimental conditions as [140]. The corresponding microstructures and associated SAD patterns of route B_A and B_C samples are shown in Fig. 2.56. It is clear that a more homogeneous microstructure of equiaxed grains with high angle grain boundaries can be provided by route B_C rather than route B_A.

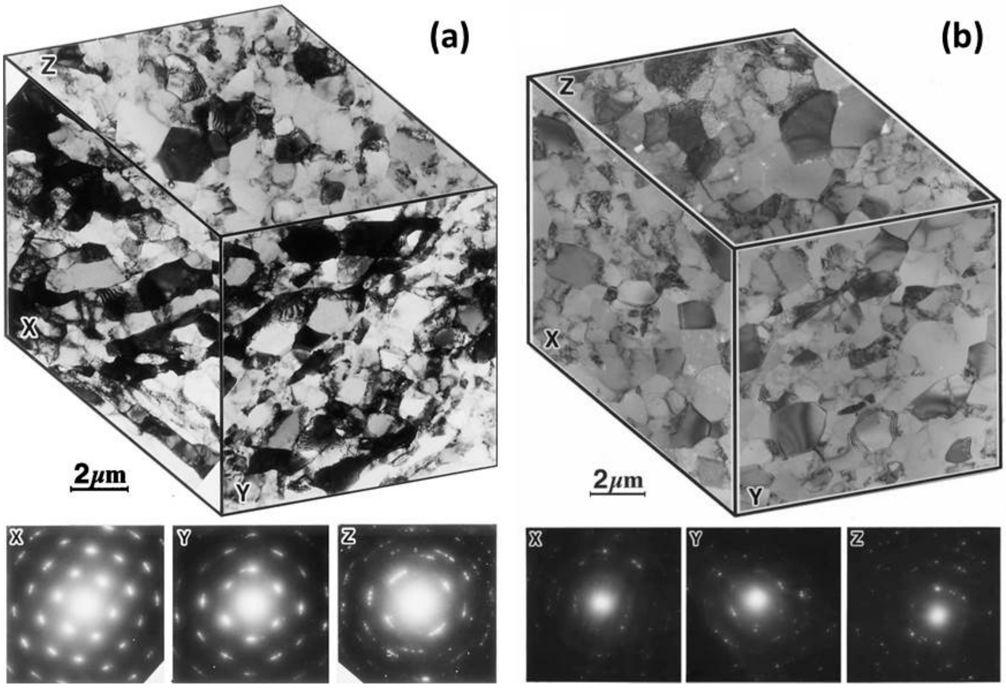

Fig. 2. 56 Microstructure in pure Al and associated SAD patterns after 4 passes via (a) route B_A **[145]** *and (b) route* B_C **[140]**

The shear characteristics associated with ECAP was examined by Furukawa *et al*. [146], a pictorial representation of which is given in Fig. 2.57. It can be found that routes B_C and C are preferable in practice because all planes can be restored after *4n* passes, while routes A and B_A exhibit continuous changes in two and three planes, respectively. Moreover, there is no deformation occurring in the Z plane for route A and C.

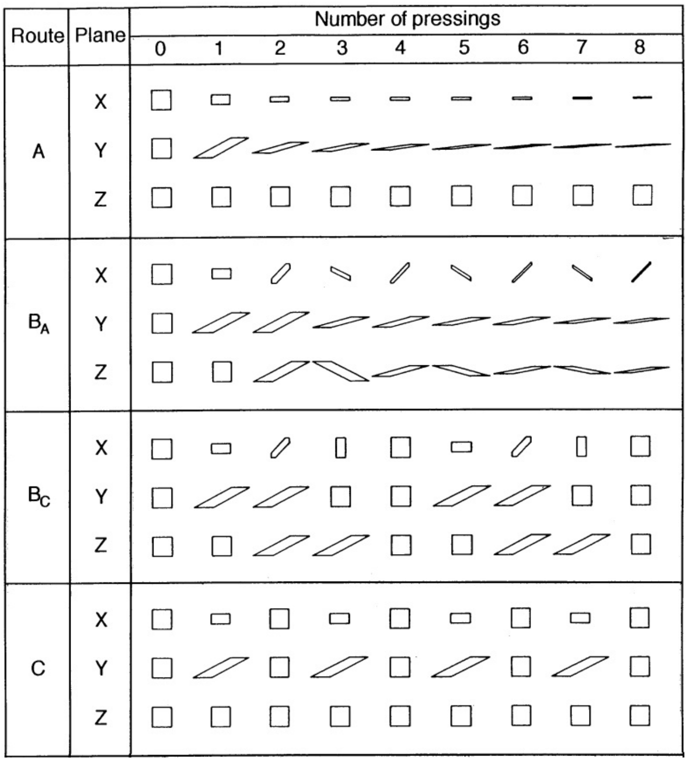

Fig. 2. 57 Shear characteristics for four fundamental processing routes **[146]**. *The plane X, Y and Z denote the transverse plane, the flow plane and the longitudinal plane, respectively.*

Therefore, it can be concluded that for purpose of attaining equiaxed ultrafine grains, better mechanical properties and homogeneous strain distribution, route B_C is superior to route A, B_A and C.

2.8 Texture Evolution of HCP Materials during ECAP

Due to the low symmetry of crystal structure, HCP materials are highly sensitive to the crystallographic texture, thus mechanical properties vary significantly with the change of loading direction. Processing by ECAP is an effective procedure for inducing strong level of texture. The ideal orientation of HCP crystals in simple shear during ECAP was proposed by Beausir *et al*. [147]. The reference system and the location of ideal fibres in ECAP texture are illustrated in Fig. 2.58. The Euler angles of these fibres are summarized in Table 2.3. The fibres are defined by: the B fibre means basal plane ∥ shear plane, the P fibre means $\langle\vec{a}\rangle$ ∥ shear plane, the Y fibre means that the c-axis is rotated towards the shear plane by 30°, and C_1 and C_2 mean that the c-axis is first rotated 90° in the shear direction then ±30° in the shear plane direction [147].

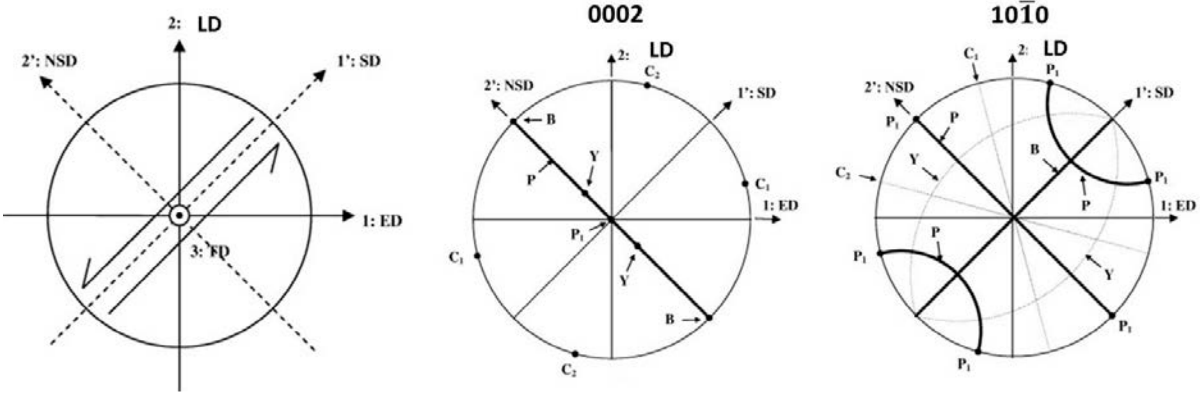

Fig. 2. 58 (a) Reference system used in the pole figure, (b) and (c) the ideal fibres in the texture of ECAPed Mg under simple shear, where LD is longitudinal direction, ED is extrusion direction, SD is shear direction and NSD is normal to shear direction **[148]**.

Table 2. 3 Ideal orientations of the fibres in ECAPed HCP materials **[148]**

Fibre	$\emptyset_1$ **(°)**	$\emptyset_2$ **(°)**	$\emptyset_3$ **(°)**
B	45	90	0-60
P	45	0-90	30
Y	45	30	0-60
C_1	105	90	0-60
C_2	165	90	0-60

Since titanium alloys with HCP crystal structure exhibit low ductility due to their limited deformation systems, ECAP processing presents a challenge, thus a large amount of the previous work examining ECAP texture of titanium alloys focused on pure Ti [143] [149] [150] [151]. Fig. 2.59 illustrates the simulated and experimental texture evolution of pure Ti subjected to ECAP using route B_C up to 3 passes. It is obvious that fibres B and P are dominant in the ECAPed pure Ti [143].

Very limited literature has been found in texture development of Ti-6Al-4V using ECAP. One example has been shown in high temperature ECAP of bulk Ti-6Al-4V which was investigated by Yapici *et al*. [152] [153]. It was reported that the basal planes were almost aligned with the ECAP maximum shear plane (~27° from the ED), as shown in Fig. 2.60. However, it is noteworthy that only 2 passes was carried out and the experiment was performed using route A [152].

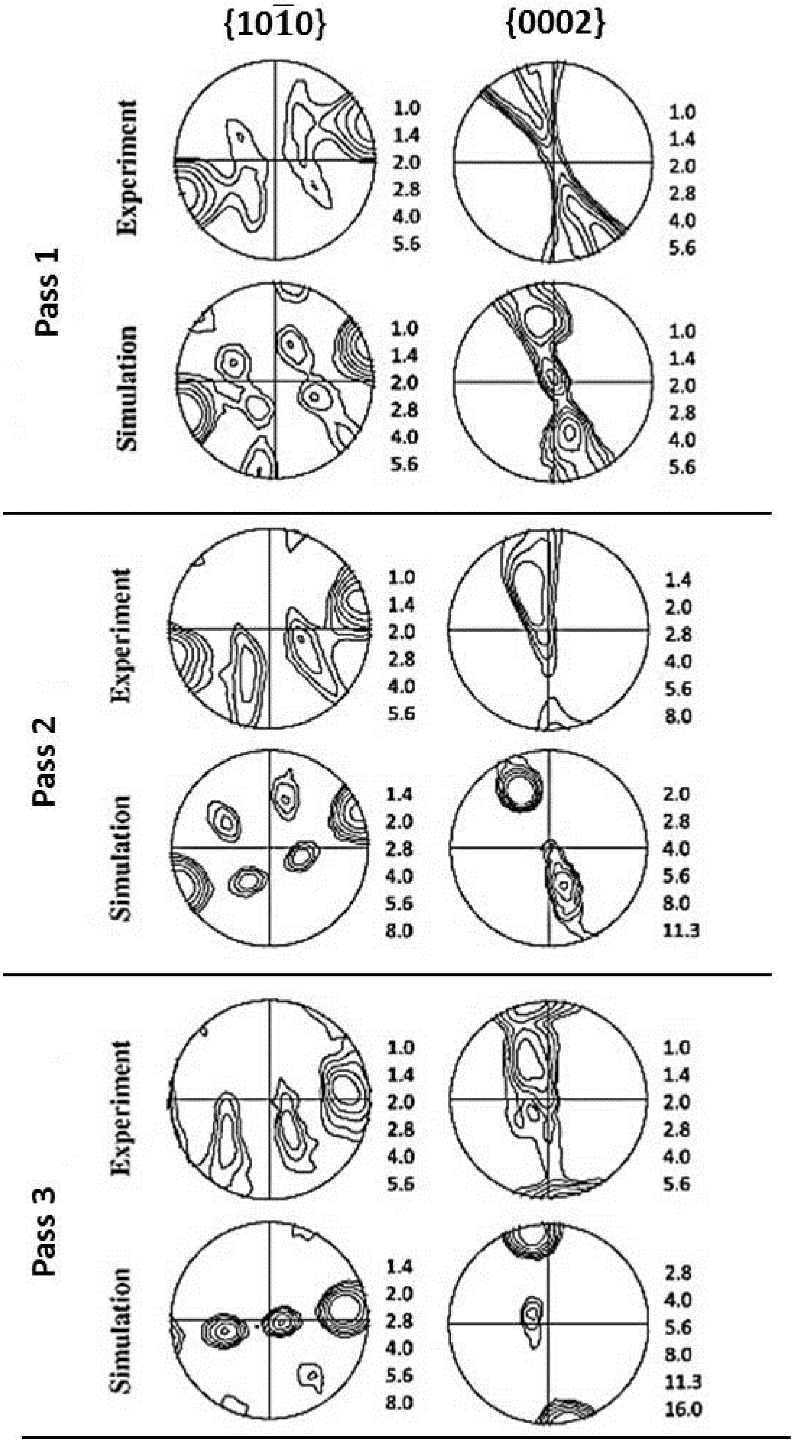

Fig. 2. 59 Texture evolution in route B_C of pure Ti after multiple-pass ECAP **[143]**.

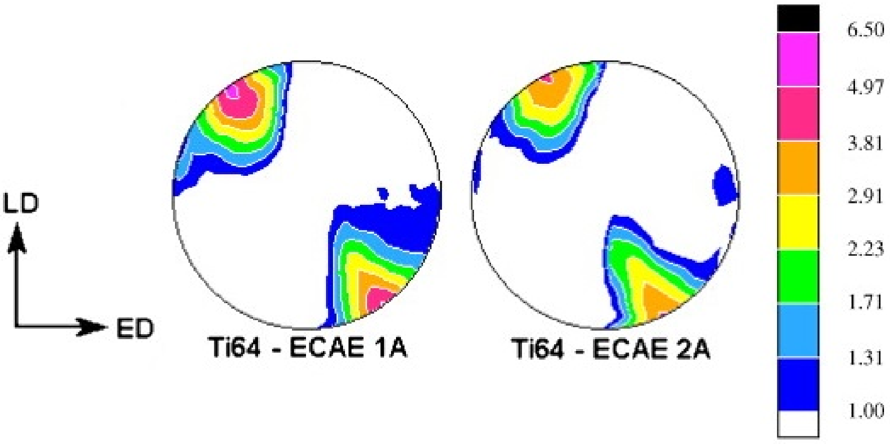

Fig. 2. 60 Basal pole figures of bulk Ti-6Al-4V subjected to ECAP at 800 °C after 1 and 2 passes using route A **[153]**.

2.9 Application of ECAP on Metallurgy Consolidation

The employment of ECAP processing in metallic powder metallurgy (PM) was initiated on Al particles in the later 1990s. In an early study, Xiang *et al*. [154] consolidated 2024Al-3Fe-5Ni powders through a two-channel ECAP device with intersection angle of 120° at 300 °C. The ECAP device profile was illustrated in Fig. 2.61. It is noted that the powders were cold isostatic pressed prior to ECAP. After three passes, the consequent density reached up to 2.933 g/cm^3, which was comparable to that via hot extrusion with a ratio of 10. However, as suggested in the later research report [155], the CIP specimens could crack even after the first pass. Thereby, Matsuki *et al*. [155] modified ECAP processing by encapsulating the CIP samples into 2024Al caps and obtained products free of surface cracks.

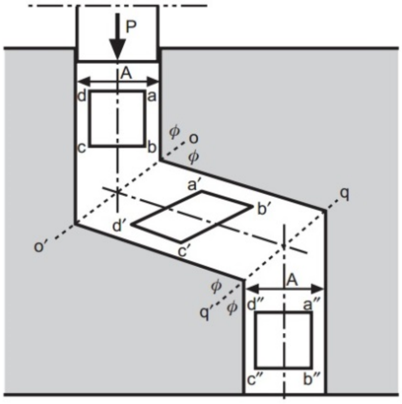

Fig. 2. 61 Schematic diagram of ECAP die used to consolidate Al alloy powder **[154]**.

In 2005, Xia and Wu [156] studied pure Al particle ECAP consolidation using back-pressure. In their experiments, Al powders wrapped in Al foil were inserted into an ECAP die preheated at 100 °C, and during pressing a constant back-pressure of 50 MPa was applied. After single pass, fully dense materials with density of 2.7 g/cm^3 were obtained. It should be pointed out that the yield strength and UTS of ECAP consolidated samples were superior to as-cast materials, although there was a big loss in the ductility.

In recent years, ECAP has been combined with other conventional techniques. Paydar *et al*. [101] densified pure Al particles using forward extrusion-equal channel angular pressing (FE-ECAP), the die of which is illustrated in Fig. 2.62. Compared with conventional FE processed samples, finer grains with superior mechanical properties (Vickers hardness, yield strength, UTS and fracture toughness) were achieved through FE-ECAP.

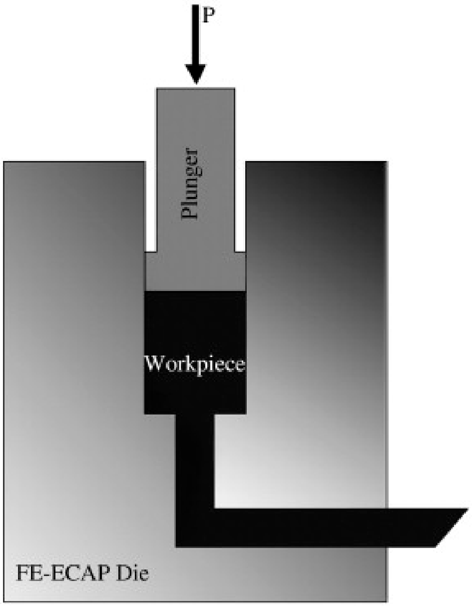

Fig. 2. 62 Schematic of FE-ECAP die **[101]**.

Another example of the combination of ECAP with traditional manufacturing methods is torsional-ECAP (T-ECAP) in the latest study conducted by Mani *et al*. [105]. In their experiments, the special ECAP die was designed and fabricated, as shown in Fig. 2.63. The pure Al powders were pressed through a conventional ECAP die, followed by rotating around the exit channel axis. In order to cramp the as-pressed sample, a reduction in cross-section with an extrusion ratio of 1.16:1 was fixed at the rotary portion. This technique allows an additional pore elimination mechanism which is arisen by torsional deformation. As a consequence, the relative density of T-ECAP specimens was higher than those processed by conventional ECAP, as shown in Fig. 2.64 and hence the Vickers hardness and compressive strength.

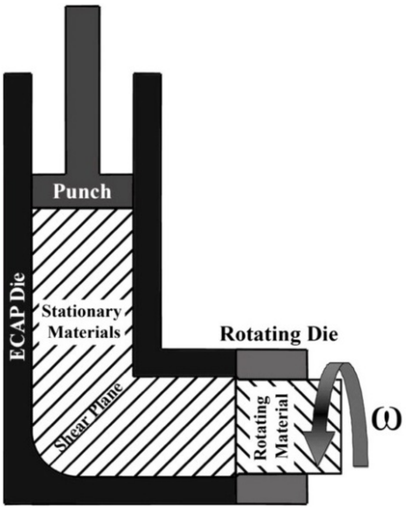

Fig. 2. 63 Schematic of T-ECAP die **[105]**.

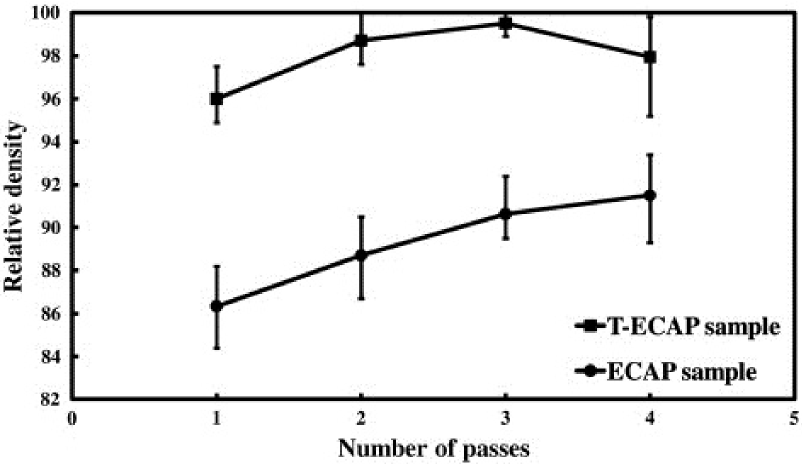

Fig. 2. 64 Relative density of T-ECAP samples compared with ECAP ones **[105]**.

Recently, substantial efforts have been paid in metallic chips consolidation via ECAP processing, especially for expensive metals and alloys, for example Ti. Luo *et al*. [106] [107] [108] investigated the microstructure and mechanical properties of pure Ti machining chips consolidated by ECAP at elevated temperatures (450-590 °C). Their results showed that fully dense materials with ultrafine grain size of ~0.8 µm were obtained and high angle grain boundaries significantly contributed to the strengthening. The latest study carried out by McDonald *et al*. [157] showed ECAP processing was feasible to recycle the machining chips of Ti-6Al-4V alloy. However, it is noted that the chip boundaries still existed in the recycled products, and further heat treatment at 700-1000 °C in an inert atmosphere was necessary to obtain a full density. Therefore, in order to realise the low energy recycling of Ti alloy chips (not only Ti-6Al-4V) using ECAP processing and understand microstructure evolution, more detailed research is essential.

3. EXPERIMENTATION

This chapter includes the descriptions of starting materials (machining chips), machining process, the ECAP recycling process, post heat treatments and various characterization techniques for studying the microstructure evolution and properties of the recycled products.

3.1 Materials and Machining Process

In the present research, two types of titanium alloys: Ti-6Al-4V and Ti-15V-3Cr-3Al-3Sn machining chips have been recycled. The bulk materials were supplied by GfE-Metalle and Materialien GmbH in Nuremberg Germany in form of a round bars with diameter of 80 mm.

The titanium alloy chips were obtained by two machining methods: conventional turning (CT) and ultrasonically assisted turning (UAT). Both machining were operated without coolant or lubricant to avoid contamination. The CT was carried out with a cutting speed of 10 m/min, a feed rate of 0.1 mm/rev and a depth of cut of 50 µm. For UAT, the cutting condition was the same as CT, and the vibration of the machining tool was monitored by a non-contacted Polytec laser vibrometer (Model: OFV-3001). The real time cutting force was measured by a Kistler piezo-electric dynamometer (KIAG-SWISS Tpye-9257A). The imposed vibration was in tangential direction and the frequency was ~ 20 kHz. Cemented carbide machine tools coated by titanium-aluminium-nitride layer (CP500) with a nose radius of 0.8 mm were used in both cutting processes, the geometry of which is shown in Fig. 3.1 [75]. The cutting tool was normal to the work-piece axis and the effective rake angle was about 14º.The experimental setup of UAT was given schematically in Fig. 3.2 [158]. The reasons for the cutting tool choice and machine setup had been explained in the previous reports by Muhammad *et al*. [75] [158] [159].

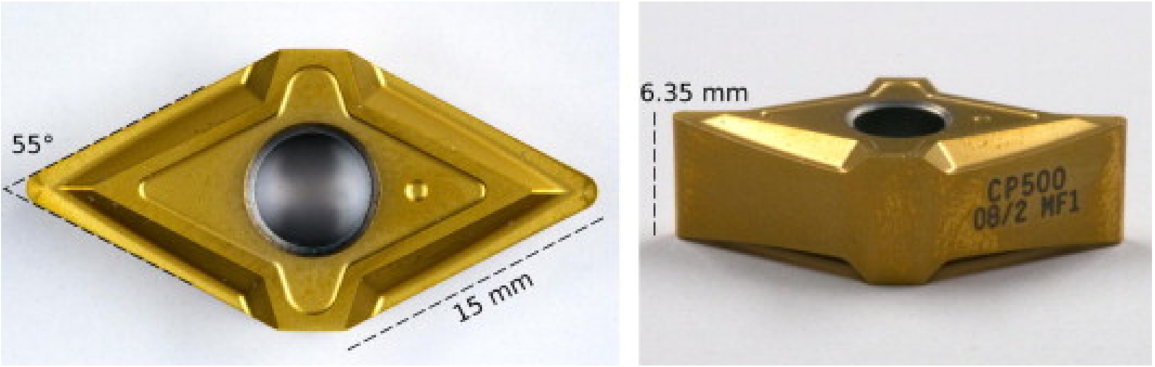

Fig. 3. 1 Cutting tool geometry **[75]**.

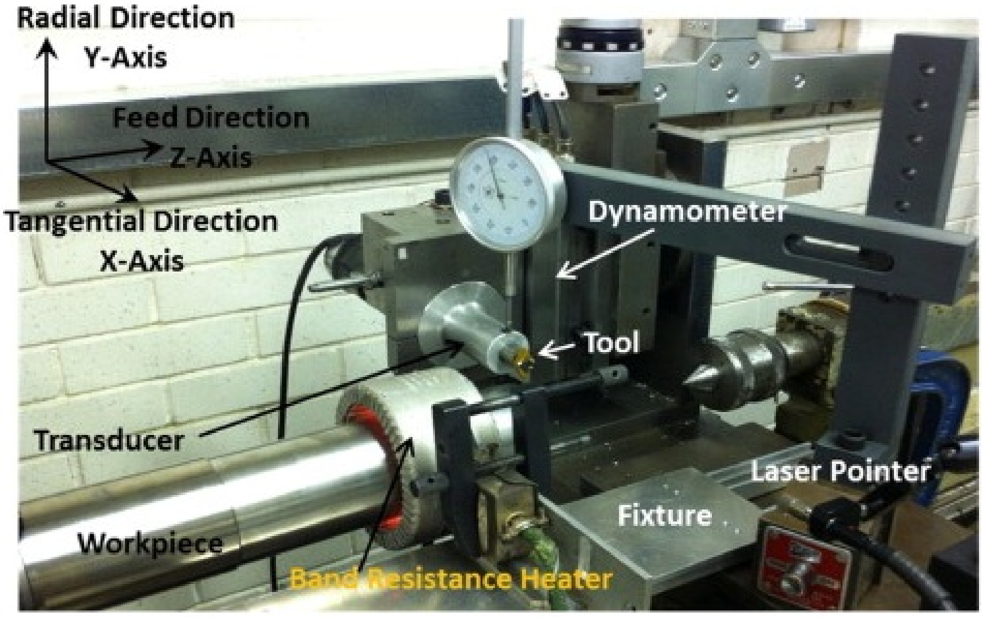

Fig. 3. 2 Experimental setup of UAT **[158]**.

3.2 ECAP System Construction

A new ECAP system has been built in house and specially designed for the current research. This system contains a hydraulic pressing machine, an ECAP die and related accessories. The construction details and technical parameters will be described in the following sections.

3.2.1 Hydraulic machine

The three sectional views of the configuration of the hydraulic machine, which is provided by ‘A1 Hydraulic Company’, are shown in Appendix A (Fig. A.1). The layout drawing of the whole system is given in Appendix A (Fig. A.2), attached with the part list. The hydraulic pressing machine requires three-phase power supply and is driven by a 2.2 kW motor. The forward hydraulic cylinder has the maximum capability of 60 tonnes, and the backward cylinder, as labelled as ‘Item 19’ is able to provide 40 tonne force. These two cylinders have the same overall dimensions, as illustrated in Appendix A (Fig. A.3), and the only difference lies in the BALLUFF transducer attached on the tail of the forward cylinder.

In practice, in order to avoid the damage of the mould and plungers, the limitation of the forward and backward pressing forces were set at 15 tonnes and 5 tonnes, respectively. The real time pressing force can be measured with accuracy to one decimal place. The forward pressing velocity is controllable and ranges from 4 – 10 mm/min. The operation instruction of the hydraulic machine is attached in Appendix B.

3.2.2 Die construction

Since the two hydraulic cylinders are mounted on a working table, accordingly, the ECAP channels in the current research are positioned horizontally. The major benefits of the horizontally designed channel are space-saving, convenience of specimen replacement and equipment cleaning.

The ECAP die consists of an inner mould and housing. The inner mould can be split into two parts, the dimensions of which are illustrated in Appendix C (Fig. C.1). The upper and bottom halves are designed to be fixed together to form two mutually perpendicular channels, whose cross-section is 10 mm × 10 mm. The inner mould is made of H13 tool steel, the required hardness of which after heat treatment is over 50HRC. Three types of holes are labelled in Fig. 3.6: B1-B8 denotes eight M20 bolts, and H1-H6 represents six cartridge heaters and the operating temperature is measured by a K-type thermocouple with diameter of 6.5 mm. As indicated, the channel intersection angle (ϕ) is 90° and the curvature angle (ψ) is ~36°, therefore the effective strain ε_N after N passes can be calculated as [113]:

$$\boldsymbol{\varepsilon_N = N \cdot \left[\frac{2\cot\left(\frac{\phi}{2}+\frac{\psi}{2}\right)+\psi\csc\left(\frac{\phi}{2}+\frac{\psi}{2}\right)}{\sqrt{3}}\right] \approx N} \ldots \textit{Equation 3. 1}$$

The inner mould is fixed in a mild steel housing whose layout is shown in Appendix C (Fig. C.1). Four M30 bolts (strength grade = 10.9) are used to mount the housing on the working table. Six vertical holes have been drilled into the housing to accommodate the cartridge heaters.

3.2.3 Accessories

In addition to the inner mould and housing, several experimental accessories were required, including two plungers, two adaptors, an insulation plate and an insulation jacket.

Fig. C.2 shows the dimensions of the plungers which is made of H13 tool steel. The corresponding hardness after heat treatment requires over 50 HRC. A hollow adaptor made of mild steel, as shown in Fig. C.3, is screwed onto the cylinder rod in order to lower the risk of heat damage to hydraulic cylinder due to heat transfer during ECAP process.

In order to prevent heat transfer to the working table, a ceramic insulation plate of 6 mm in thickness is lined beneath the outside housing. The corresponding technical data is given in Table 3.1. In addition, to reduce heat loss during ECAP process, a portable insulation jacket which is made of high density wool and coated by silica hot face, is fastened around the housing (Fig.3.3).

Table 3.1 Technical data of the insulation plate

Density	2.2	g/cm^3
Flexural strength (10 mm) at 23 °C	200	MPa
Compressive strength, vertical	400	MPa
Compressive strength at 200 °C	250	MPa
Thermal conductivity	0.29	W/mK
Coefficient of expansion	10×10^{-6}	1/K
Application temperature, long-term	600	°C
Application temperature, short-term	800	°C
Dielectric strength	25	KV/mm

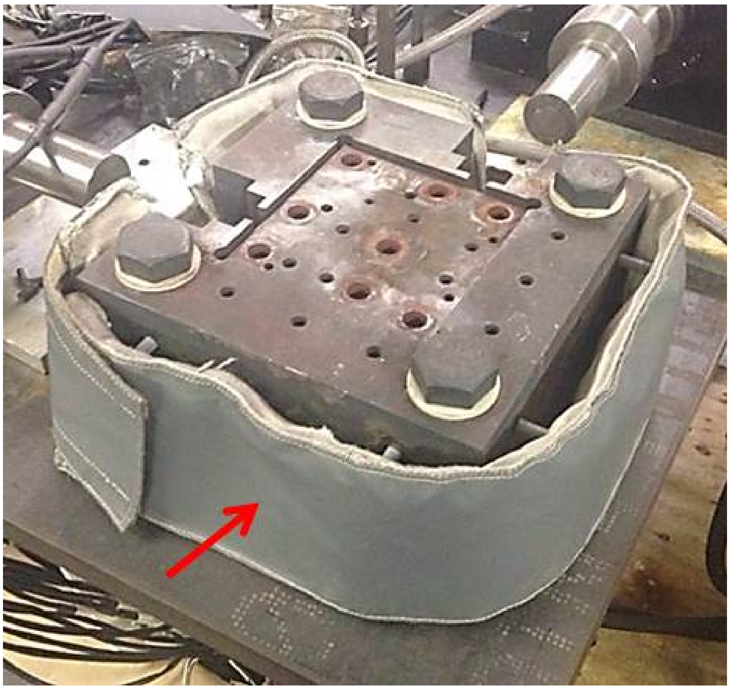

Fig. 3. 3 Insulation jacket around the ECAP housing.

3.3 ECAP Process and Post ECAP Heat Treatment

Prior to ECAP process, chips were pre-compacted under 5 tonnes using a mould as shown in Fig. 3.4, into a bar with a diameter of 10 mm and a length of ~70 mm, and then wrapped with Al foil to reduce friction during ECAP. The cross section of the pre-compacted specimen is shown in Fig. 3.5. It is obvious that the specimen after pre-compaction is still fairly loose. Samples were inserted into the entry channel that was lubricated by molybdenum disulphide (MoS_2). After closing, the mould was heated using 12 cartridge heaters and held at the target temperature for 10 minutes for stabilization. ECAP processes were conducted under isothermal conditions with the temperature ranging between 300 °C and 550 °C. The imposed back-pressure could be pre-set at a constant value using a reduction valve. In current study, the back-pressures were in the range of 50 MPa to 250 MPa. The forward pressure force is displayed on the screen of hydraulic unit. In the present experiments, the maximum force recorded was in the range of 9.0 - 13.8 tonnes. The schematic diagram of the ECAP process is shown in Fig. 3.6. The X, Y and Z planes of the as-pressed sample represent the transverse, flow and longitudinal planes, respectively. For multiple pass ECAP, the sample was rotated by 90° about X axis in the same direction between each pass, i.e. route B_C. For all ECAP tests, the constant ram speed of 4 mm/min was applied. Table 3.2 summarizes the individual experiments in the present study. In order to study the effect of heat treatment on residual stress and chip-boundary elimination, some recycled products were selected for post heat treatment, as asterisked in Table 3.2. Heat treatments were conducted in an inert argon atmosphere furnace. The detailed of the annealing heat treatments are summarised in Table 3.3.

(a) (b) (c)

Fig. 3. 4 (a) Plunger, (b) split mould and (c) assembled mould.

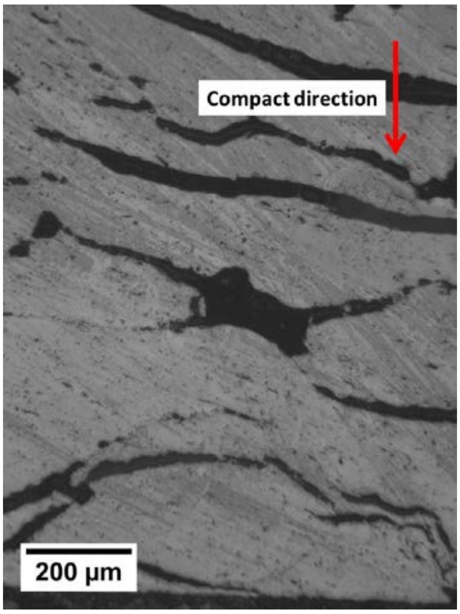

Fig. 3. 5 Optical micrograph of a pre-compacted specimen cross section.

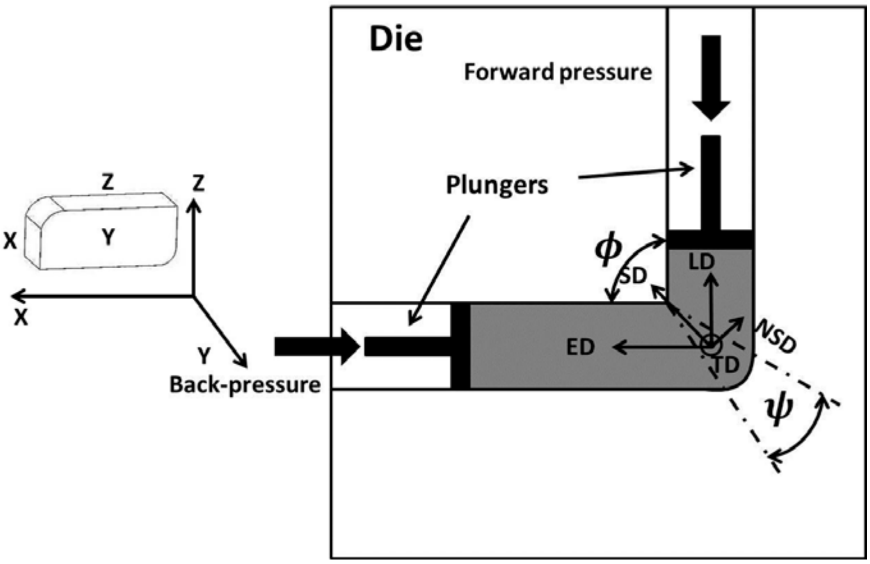

Fig. 3. 6 Schematic of the ECAP profile and as-pressed sample planes.

3.4 Characterization Techniques

3.4.1 Density measurement

The specimens for the density measurement were sectioned from the central region of the as-pressed samples, since the materials at two ends of the sample were experienced insufficient plastic flow and hence insufficient consolidation [160]. The density was measured by Archimedes' method using deionized water. The setup of the density measurement is shown in Fig. 3.7. The standard procedure is described as: (1) Place beaker filled with deionized water on metal platform, and attach thermometer to the beaker; (2) Tare balance, place the sample on upper pan on frame and weigh the sample in air; (3) Tare balance with the sample in upper pan, place the sample in the holder and record the buoyancy; (4) Read the temperature of the water and refer to density chart to determine the density of the water; (5) Calculate the specific gravity. The calculation formula is displayed:

$$\boldsymbol{Density} = \frac{\boldsymbol{W(a)}\cdot[\boldsymbol{\rho(fl)}-\mathbf{0.0012}]}{\mathbf{0.99983}\cdot\boldsymbol{G}} + \mathbf{0.0012} \ldots \textit{Equation 3.2}$$

where *W(a)* denotes the weight of sample in air, *ρ(fl)* is the density of water at experimental temperature and *G* represents the buoyancy. The measured density was then compared to the theoretical densities of Ti-6Al-4V (4.43 g/cm^3) and Ti-15V-3Cr-3Al-3Sn (4.76 g/cm^3).

Table 3.2 Summary of the conditions for ECAP recycling experiments

Materials	No.	Back-pressure (MPa)	Temperature (°C)	Pass
Ti-6Al-4V	1	50	300	1
	2	50	350	1
	3	50	400	1
	4	70	400	1
	5	100	400	1
	6	200	400	1
	7	50	450	1
	8	100	450	1
	9	150	450	1
	10	200	450	1
	11	50	500	1
	12*	100	500	1
	13	150	500	1
	14	200	500	1
	15*	250	500	1
	16	50	500	2
	17	50	500	4
	18	100	500	4
	19	100	500	8
	20	150	500	3
	21	150	500	4
	22	250	550	1
Ti-15V-3Cr-3Al-3Sn	23	50	300	1
	24	50	350	1
	25	50	400	1
	26	70	400	1
	27	100	400	1
	28	50	450	1
	29	100	450	1
	30	150	450	1
	31	50	500	1
	32	100	500	1
	33*	150	500	1
	34	50	500	4
	35	100	500	4
	36	150	500	4
	37	100	500	8

Table 3. 3 Summary of heat treatments on selected samples

No.	Materials	ECAP conditions			Heat treatment	
		Temperature (°C)	Back-pressure (MPa)	Number of passes	Annealing temperature (°C)	Treatment time (h)
12*	Ti64	500	100	1	700	2
15*	Ti64	500	250	1	500	24
33*	Ti15333	500	150	1	600	2

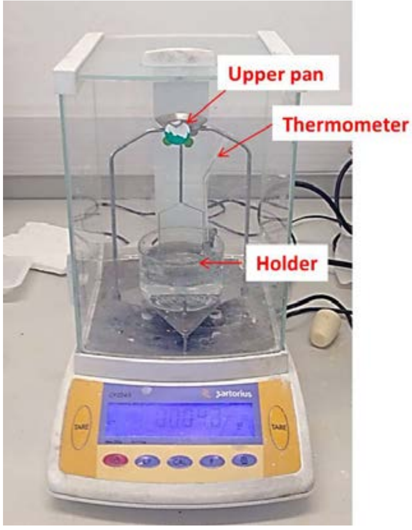

Fig. 3. 7 Setup for density measurement by the Archimedean principle.

3.4.2 Microscopy

- Sample preparation for surface characterization

For optical microscopy (OM) and scanning electron microscopy (SEM) examination, a chip was mounted edge-on in conductive Bakelite while the recycled products were mounted and sliced parallel to the flow plane (Y plane). The samples were ground progressively on finer silicon carbide papers, followed by polishing using 6 and 1 µm diamond suspensions, and final finishing using a mixture of colloidal silica and hydrogen peroxide (~20%). At the end, the specimens were washed in water, rinsed with methanol and dried with hot air. In order to reveal the microstructural features, the samples were etched by Kroll's reagent for ~15 seconds. Kroll's etchant consists of 5 ml of HNO_3, 10 ml of HF (48% concentration) and 85 ml of H_2O.

- Optical microscopy

Optical microscopy was carried out using a Reichert MEF-3 optical microscope attached with a 10 mega pixel digital camera. The images were acquired by the imaging capture software called Qcapture.

- Scanning electron microscopy (SEM)

A Carl Zeiss (LEO) 1530VP field emission gun (FEG) SEM equipped with HKL Nordlys F high speed electron backscatter diffraction (EBSD) camera was used for imaging and EBSD scanning. The EBSD scanning was operated at an acceleration voltage of 20 kV, a pre-tilted angle of 70° and with a 0.2 μm step size. Oxford Instruments Aztec EBSD microanalysis software was used to collect and analyse the data obtained. The post-processing software of CHANNEL5 suite programs was employed to measure grain misorientation, generate orientation maps and pole figures. The recrystallization fraction is estimated based on the following criteria: The software takes each grain in the scanning area and measures the internal average misorientation angle within single grain. If the misorientation angle exceeds the pre-defined value (2° in the present study) to define a subgrain, the grain is determined as being “deformed grain”. If the grain contains subgrains with the internal misorientation less than 2° but the misorientation between contiguous subgrains is above 2°, the grain is defined as “substructured”. All the remaining grains are classified as recrystallized.

- Transmission electron microscopy (TEM)

The internal microstructures of the samples were examined using transmission electron microscopy (TEM). Two types of TEM sample preparation methods were employed in the present study. Site-specific TEM specimens were lifted out using a FEI Nova 600 Nanolab Dual Beam Focused Ion Beam (FIB) SEM. The typical steps are described as follows: (1) The sample is tilted to 52° to make the surface perpendicular to the ion beam; (2) A layer of platinum with dimensions: length ~20 μm, breadth ~1.5 μm and thickness ~1.5 μm, is deposited over the region of interest; (3) Under a large current (20 nA), two terraces are formed adjacent to the platinum coated area using cleaning cross-section mode; (4) Using a lower beam current (7 nA), the two trenches are milled so as to just touch the platinum on either side; (5) Three cuts forming a ‘U’ shape are made to the wall of material, leaving the membrane attached to the bulk at one top corner; (6) Lift out the lamella using an Omniprobe and transfer it onto the TEM grid; (7) Thin the specimen with a low current (0.5 nA) by tilting the stage at 3° with respect the ion beam until the final thickness is reduced to ~150 nm. Fig. 3.8 shows the sample prepared by FIB lift-out technique.

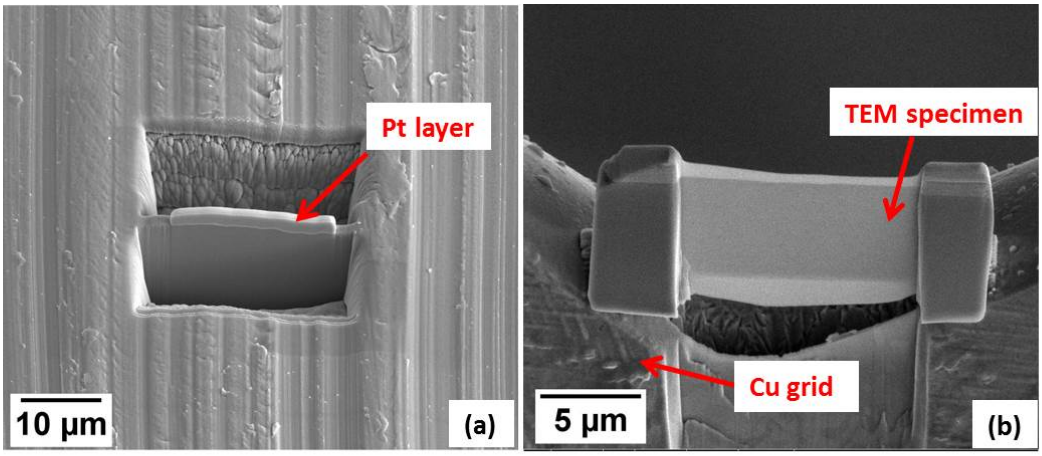

Fig. 3. 8 (a) A lamella of material at the region of interest before lift-out, (b) TEM specimen attached on Cu grid after final thinning

For conventional TEM specimen preparation, discs with a diameter of ~3 mm were cut from near the central of as-pressed samples using spark erosion. These discs were ground mechanically on silicon carbide paper finishing on 4000 grit to a thickness of ~100 µm, and then subsequently dimpled using 6 and 1 µm diamond lubricant by a dimple grinder. Finally, the specimens were thinned to perforation using an argon ion miller (Gun current: 2.6 mA, High voltage: 7 kV and Angle: ±10°).

FEI TECNAI F20 electron microscope was used for chemical analysis. Conventional TEM imaging and diffraction were undertaken by JEOL 2000FX. All of the TEM operations were carried out at 200 kV.

3.4.3 Vickers hardness mapping

The Vickers hardness mapping was conducted over a rectangular pattern of ~7 mm × 7 mm on the flow plane (Y plane) in Fig. 3.4 using DuraScan-70 hardness tester. A testing load of 1 kgf was applied and the spacing between each indentation was 0.3 mm. In order to evaluate the homogeneity of the specimens, the recorded hardness values were plotted in the form of colour-coded maps.

4. MICROSTRUCTURE CHARACTERIZATION OF MACHINING CHIPS

4.1 Introduction

In order to evaluate recycled products, it is essential to fully understand the initial microstructure of machining chips. Within this chapter, CT/UAT Ti-15V-3Cr-3Al-3Sn chips and CT Ti64 chips were examined. The corresponding microstructures, especially the ultrafine grained microstructure in the primary and secondary shear zones were compared systematically. In addition, a heavily deformed layer on Ti-15V-3Cr-3Al-3Sn work-piece sub-surface was examined.

4.2 Ti-15V-3Cr-3Al-3Sn Machining Chips

4.2.1 Ultrafine grained microstructure in CT machining chips

The optical micrograph of CT Ti-15V-3Cr-3Al-3Sn chip cross-section is shown in Fig. 4.1. It is clear that the primary and secondary shear zones appear darker compared with surrounding matrix, as indicated by rectangles A and B, respectively.

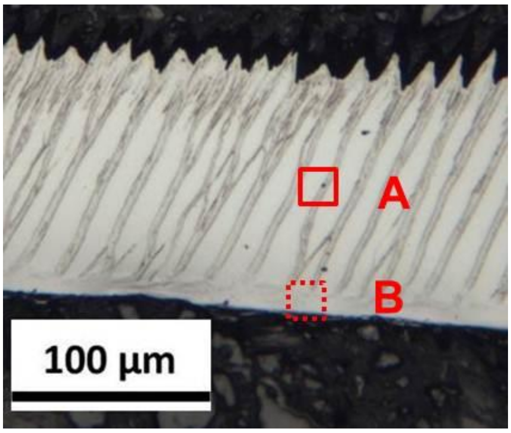

Fig. 4. 1 Optical micrograph of etched CT Ti-15V-3Cr-3Al-3Sn chip showing the primary shear zone (marked as A) and secondary shear zones (marked as B).

Fig. 4.2 shows an SEM electron micrograph of the cross-section of a CT Ti-15V-3Cr-3Al-3Sn chip. Finer microstructures in the primary and secondary shear zones are observed, as marked by arrows A and B, respectively, with clear boundaries between the shear zones and segment areas, similar to those reported elsewhere

[161] [162]. However, no detailed microstructural characterization has been carried out in the literature to illustrate the microstructural features in these shear zones.

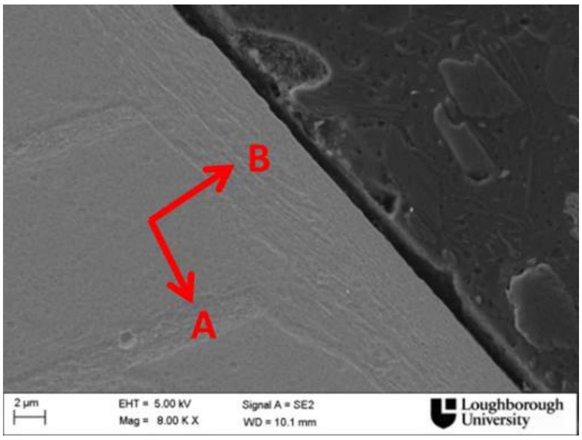

Fig. 4. 2 SEM electron micrograph of CT Ti-15V-3Cr-3Al-3Sn chip cross-section showing the primary shear zone (marked as A) and secondary shear zones (marked as B).

To understand the evolution of the shear zones further, both SEM-EBSD and TEM were performed. SEM-EBSD was carried out in a region containing shear bands from primary shear zones, as shown in Fig. 4.3. As indicated in the inverse pole figure (IPF) orientation map (Fig. 4.3(b)), the adjacent segments next to the shear bands have the same orientation (same colour) which implies that the segments are likely to belong to one grain before the chip was machined out from the bulk. An EBSD IPF orientation map (Fig. 4.4(a)) scanned in another primary shear region shows the shear bands formed continuously across two grains with misorientation of about 30° (Fig. 4.4(b)). This suggests that during the primary shear zone formation, the catastrophic shear failure occurs at a very narrow shear zone but leaves the adjacent matrix undeformed or slightly deformed as good EBSD pattern quality has been observed in the undeformed regions. The shear strain introduced in the primary shear zone can be calculated by [163] [164]:

$$\boldsymbol{\gamma = \frac{\cos\alpha}{\sin\phi\cos(\phi-\alpha)}} \text{ ... } \textit{Equation 4. 1}$$

Where γ represents the shear strain, α is the tool rake angle (14^{o} for this study) [75] [158] and ϕ is the shear plane angle, which is given by:

$$\boldsymbol{\tan\phi = \frac{\frac{t_o}{t_c}\cos\alpha}{1-\frac{t_o}{t_c}\sin\alpha}} \text{ ... } \textit{Equation 4. 2}$$

where t_o and t_c, the chip thicknesses before and after machining, are equal to ~50 µm and ~120 µm in this case, respectively. Thus the shear angle (Ø) is about 24° and the imposed shear strain is ~2.42 which is equivalent to the accumulative strain induced by 4 passes ECAP process with intersection angle of 120° [116]. Based on the microstructure observations of ECAPed pure Ti, significant refinement has been reported to occur with the imposed strain about 0.6 (after a single pass) [116]. Due to the severe plastic deformation was introduced to the primary shear zones and the quality of the EBSD patterns was impeded, no information of the grain morphology or orientation could be revealed by EBSD. Therefore the site-specific TEM foil, containing one primary shear band and the matrix, as indicated by the solid rectangle A in Fig. 4.1, was lifted out to reveal the microstructure of the shear bands.

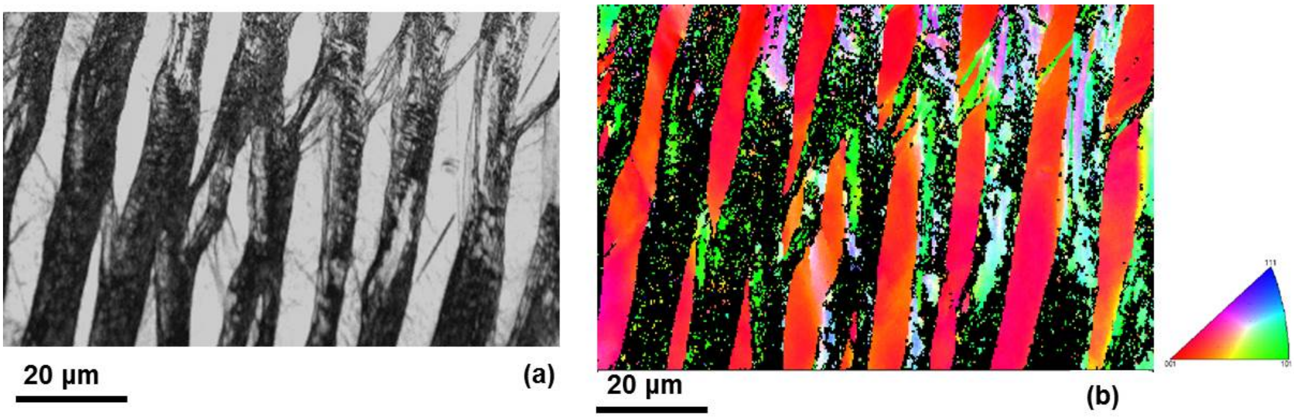

Fig. 4. 3 (a) Band contrast image and (b) IPF orientation map of a CT Ti-15V-3Cr-3Al-3Sn machining chip, the inset is the colour scheme of the corresponding orientation map.

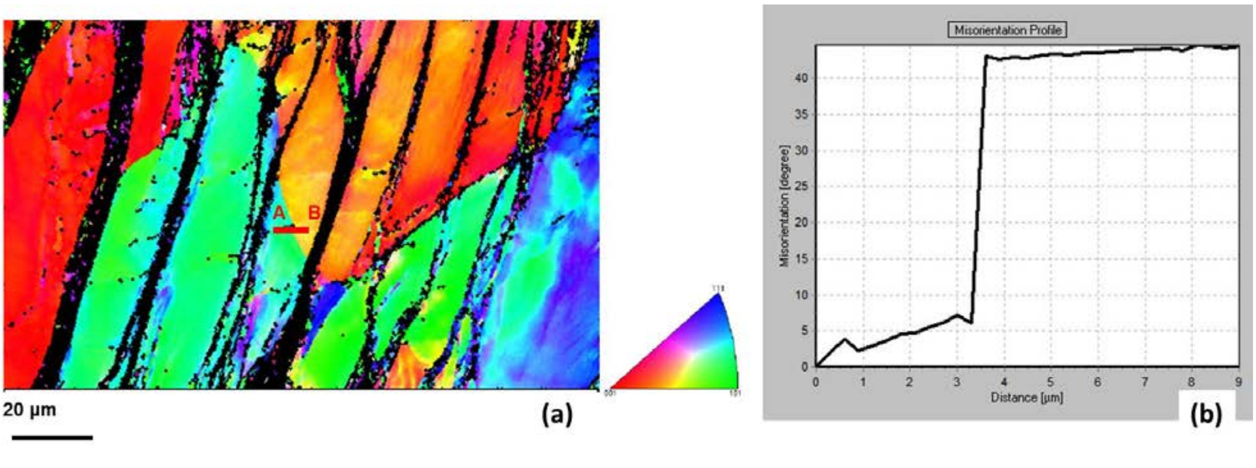

Fig. 4. 4 (a) SEM-EBSD IPF orientation map of a CT Ti-15V-3Cr-3Al-3Sn machining chip, the inset is the colour scheme of the corresponding orientation map, and (b) the misorientation profile from point A to B in (a)

Fig. 4.5(a) shows the TEM micrograph of the primary shear zone in CT Ti-15V-3Cr-3Al-3Sn chips. The ring-shape corresponding selected area diffraction (SAD) pattern confirms that the β phase in the central band is nano-crystalline. The average grain size of the nano-crystalline region is ~80 nm. The mechanism of the nano-crystalline grains in the primary shear zone involves the formation of dislocation cell structures. The dislocation cells form in the early stages of plastic deformation. With the accumulation of misorientation between neighbouring dislocation cells, the cells transform into the final fine grain structures [165]. Estrin *et al*. [166] developed a constitutive model, which applies to the dislocation cells address sufficiently large strains. The model assumes that the average dislocation cell size, *d*, is inversely proportional to the square root of dislocation density, ρ:

$$\boldsymbol{d} = \frac{\boldsymbol{K}}{\sqrt{\boldsymbol{\rho}}} \ldots \textit{Equation 4. 3}$$

where K is a constant. It is known that during the machining process, large amount of dislocations were generated because of the imposed high shear strain in the primary shear zone, and hence the formation of nano-crystalline grains.

There is a sharp boundary between the nano-crystalline region and the adjacent matrix which is consistent with the observations in the SEM. Fig. 4.5(b) shows the interface between the nano-crystalline zone and matrix at higher magnification. A SAD pattern taken from the adjacent matrix comprises regular spot pattern indicating the large grain size. No grain refinement or dislocations were found in the adjacent matrix. It proves that the high level of shear strains are only localised at the narrow primary shear zone and have negligible effects to the surrounding matrix. The sharpness of the shear deformation region is also observed in face-centred cubic (FCC) material, e.g. copper, using quick-stop optical micrographs during machining [164].

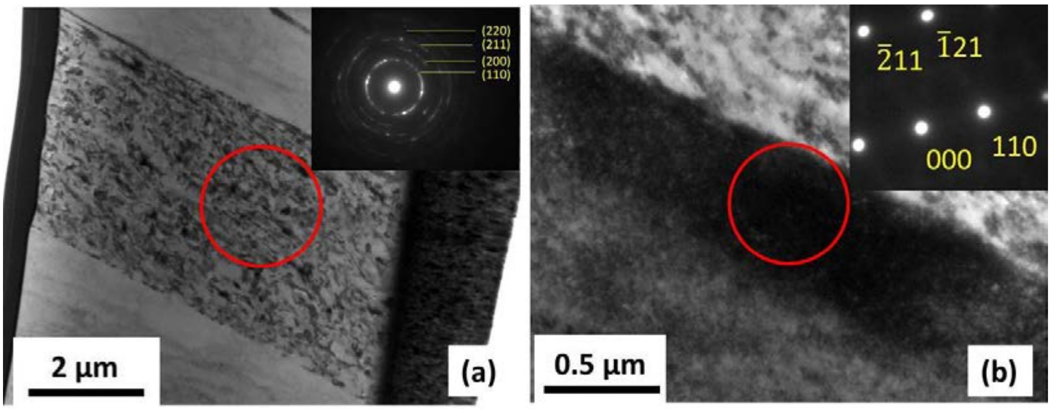

Fig. 4. 5 TEM micrographs of (a) CT Ti-15V-3Cr-3Al-3Sn chip at the primary shear zone cross-section with the inset showing the SAD pattern taking from the nano-crystalline region; (b) interface between the nano-crystalline zone and adjacent matrix. The inset is the diffraction pattern of the matrix; beam direction is $[\mathbf{1\bar{1}3}]$*.*

Fig. 4.6(a) shows the microstructure of a TEM sample lifted out from the secondary shear zone, as indicated by the dashed-line rectangle B in Fig. 4.1. Different from the primary shear zone, the secondary shear zone consists of two distinct layers: layer A which was observed near the tool tip-chip interface and layer B which was further away from the tool tip. At higher magnification, the nano-crystalline microstructure of layer A is shown in Fig. 4.6(b), and the corresponding SAD pattern taken in the nano-crystalline region shows a ring pattern. The average grain size in this region is ~80 nm. Below the nano-crystalline area (layer A), layer B contained elongated grains as marked by a circle in Fig. 4.6(c). Compared to Fig. 4.6(b), the grains in Fig. 4.6(c) appear larger with the average grain sizes of ~150 nm.

Compared to the primary shear zone (Fig. 4.5), it can be seen that the ultrafine grained region in the secondary shear zone (Fig. 4.6) is relatively wider and the grain size distribution is heterogeneous. This phenomenon was explained by the finite element modelling of the carbon steel chip formation [167]. They suggested that the effective strain gradually attenuated with the distance from the tool tip-chip interface, and the material near the tool tip-chip interface may be subjected to friction-induced deformation followed by undergoing shearing at the primary shear zone [167]. Therefore, the grain refinement effect is more significant near the chip surface and hence smaller grain size forming the equiaxed nano-crystalline region.

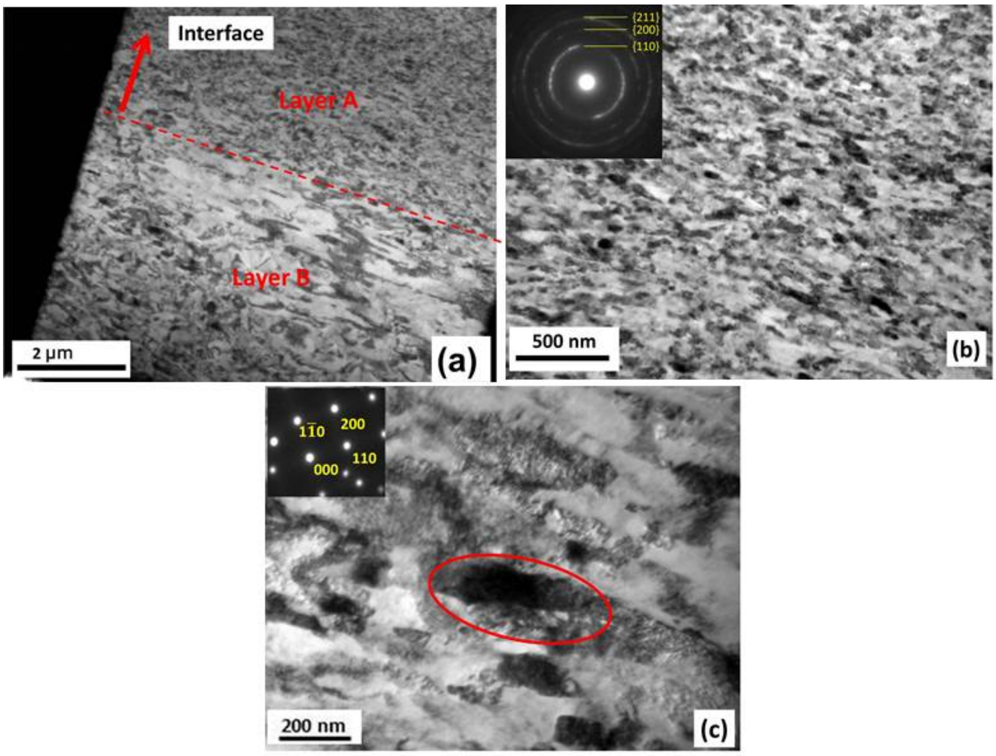

Fig. 4. 6 TEM micrographs of CT Ti-15V-3Cr-3Al-3Sn chip at the secondary shear zone cross-section. (a) low magnification; (b) nano-sized grains near the interface (layer A); (c) elongated grains away from the tool-chip interface (layer B).

4.2.2 Microstructure of UAT machining chips

Fig. 4.7 is the optical micrograph of an UAT Ti-15V-3Cr-3Al-3Sn chip. It is shown that the cross section profile of the UAT chip is similar to the CT chip: clear boundaries were observed between the shear zone and the surrounding matrix. It is noted that the thickness of the UAT chip is about 90 µm which is less than that of CT chip (~120 µm). Using Equation 4.2, the calculated shear plane angle is about 32°. It is known that a larger shear plane angle results in a smaller shear plane area and hence smaller chip formation shear force, which implies less grain refinement and facilitates the machining process [163]. This phenomenon is consistent with the cutting force reduction in UAT comparing to CT process as reported in [158] [75] [168].

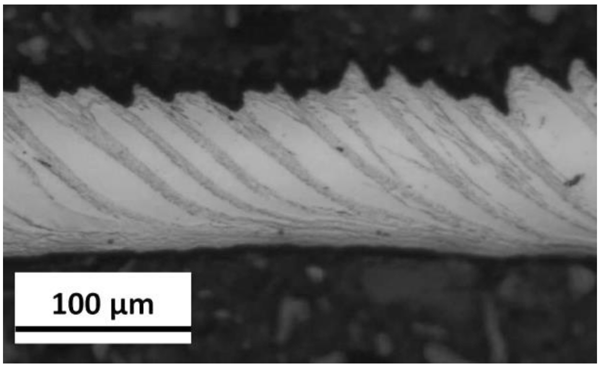

Fig. 4. 7 Optical micrograph of etched UAT Ti-15V-3Cr-3Al-3Sn chip cross section.

Similar SEM-EBSD result was also observed in the primary shear zone of the UAT chip, as shown in Fig. 4.8. According to Equation 4.1, the shear strain in the primary shear zone is about 1.93 which is still high enough to refine grains in a narrow region. TEM micrographs, Fig. 4.9(a), show the ultrafine grains in UAT Ti-15V-3Cr-3Al-3Sn chip. Measurements show that the average grain size is ~110 nm, which is larger than the nano region in CT chips. However, the ultrafine grained region was inhomogeneous: some grains of size ~ 180 μm were found, as shown in Fig. 4.9(b).

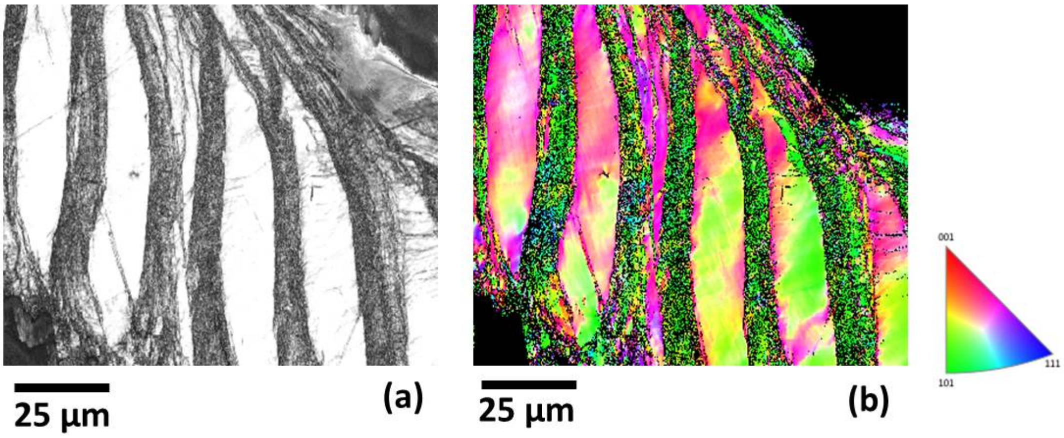

Fig. 4. 8 (a) Band contrast image and (b) IPF orientation map of a UAT Ti-15V-3Cr-3Al-3Sn machining chip, the inset is the colour scheme of the corresponding orientation map.

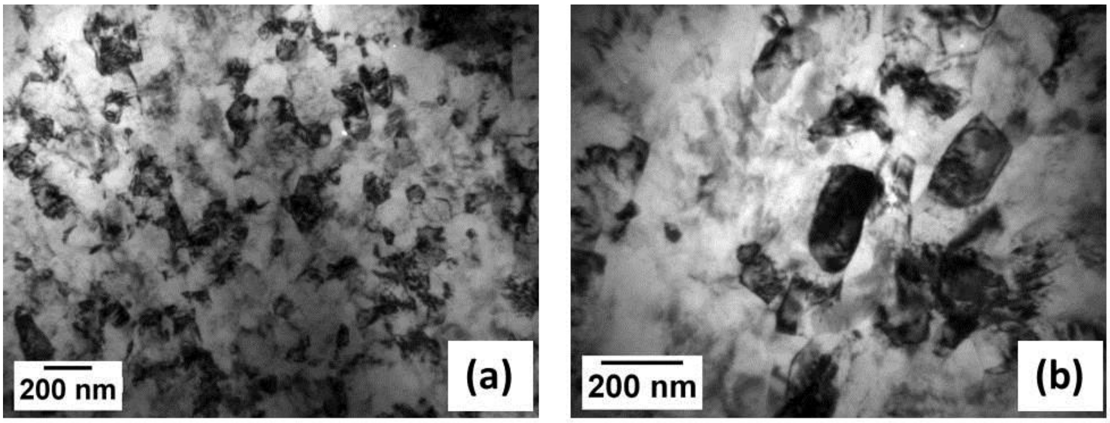

Fig. 4. 9 TEM micrographs showing (a) ultrafine grained region, and (b) individual large grains in an UAT Ti-15V-3Cr-3Al-3Sn chip.

4.2.3 Microstructure of the CT work-piece subsurface

It is known that the secondary shear zone is the sheared surface where the chips are stripped from the work-piece. Therefore, the subsurface microstructure of the work-piece is supposed to be the replica of the secondary shear zone.

Fig. 4.10(a) shows an SEM electron micrograph of the CT work-piece surface. A deformation layer of ~5 µm was observed on the subsurface, where two layers with different grain sizes were identified and marked by layer A and B. This result is consistent with the previous TEM micrograph (Fig. 4.6(a)). Fig. 4.10(b) confirms that the deformation layer possessed nano-crystalline microstructure and a clear border separated the heavily deformed region from the original substrate microstructure. At higher magnification, the nano-crystalline region (Fig. 4.10(c)) shows that the ultrafine grains are elongated along the turning tangential direction. The ring-shape SAD pattern comprising six strong spots implies that the grains in this nano-crystalline zone have preferred orientation in <110> direction parallel to the turning tangential direction.

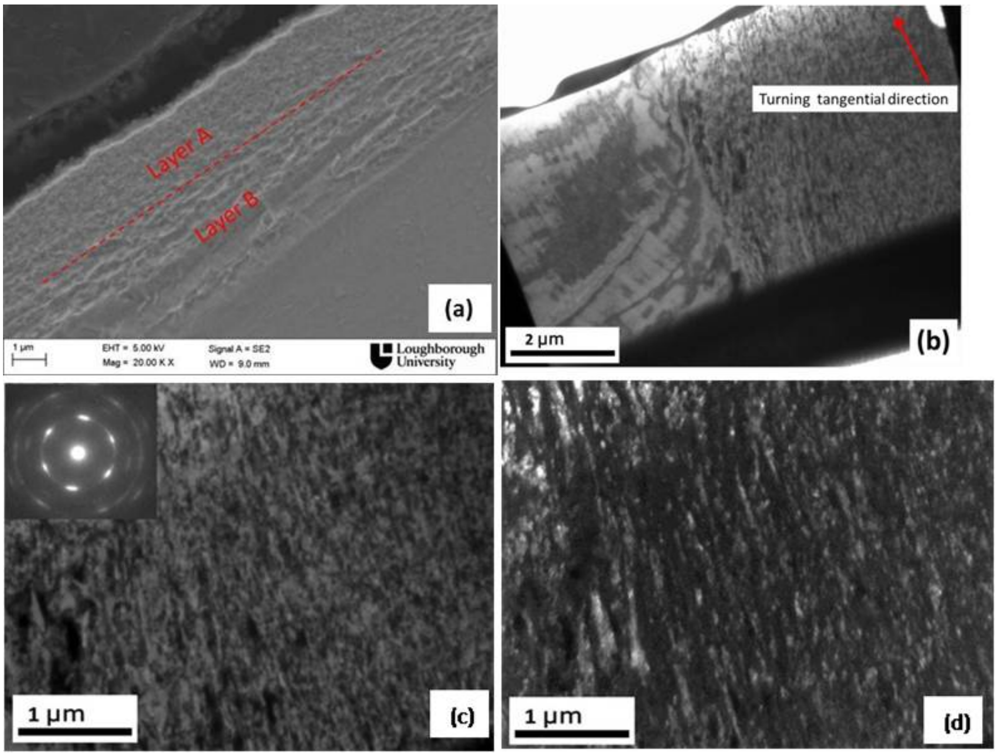

Fig. 4. 10 Deformed layer of CT Ti-15V-3Cr-3Al-3Sn workpiece surface; (a) SEM and (b) TEM cross-section micrograph; (c) bright field image of nano-crystalline grains and (d) the corresponding dark field image showing one set of <110> parallel to turning tangential direction.

4.3 Ti-6Al-4V Machining Chips

The optical micrograph in Fig. 4.11 shows the microstructure and morphology of the Ti-6Al-4V machining chip cross-section is different from the continuous chip formed in Ti-15V-3Cr-3Al-3Sn. This is because the α+β alloy Ti-6Al-4V exhibits relatively poor ductility at the same cutting conditions compared with β alloy Ti-15V-3Cr-3Al-3Sn. It reveals that although no distinctive shear bands similar to those in Ti-15V-3Cr-3Al-3Sn chips are seen, narrow shear bands, as indicated by the arrows, were observed at the saw-tooth region, where the severe plastic deformation occurs during the machining process.

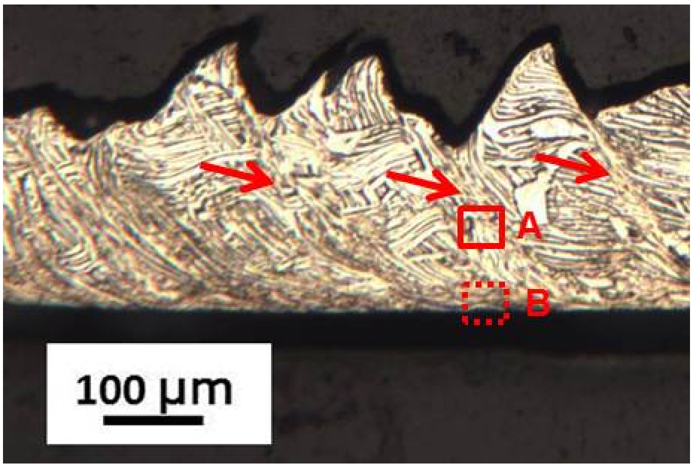

Fig. 4. 11 Optical micrograph of Ti64 machining chip cross section; Zone A: primary shear zone and Zone B: secondary shear zone.

EBSD was performed at the primary shear zone marked by the rectangle as shown in Fig. 4.11(a). From the IPF orientation map (Fig. 4.12(b)), it can be seen that the α grains at the vicinity of the shear band have experienced the shear force and elongated parallel to the shear bands. The gradual change of microstructures at the border of the primary shear zone is clearly different from that observed in Ti-15V-3Cr-3Al-3Sn chips. It was pointed out that in the centre of the shear bands non-diffusional phase transformation leading to the loss of β phase occurs due to the high temperature and compressive stresses during the machining process [169]. On the contrary, some other authors [170] confirmed that no phase transformation takes place in the shear bands. However, due to the tremendous plastic strain accumulation, most of the EBSD patterns formed by diffraction of the grains near the shear band were not indexed, and because of the limitation of the spatial resolution of the EDX probe in the SEM, no β phase can be found in the area of interest. In order to confirm the existence of β phase and reveal the corresponding microstructure, a FIB lift-out TEM sample was analysis, as shown in Fig. 4.13. It can be seen that two band structures with width of ~ 200 nm are present in the TEM sample. The STEM-EDX results, as shown in Fig. 4.13(b) and (c) confirm that the band structures are aluminium depleted and vanadium rich phase. Close inspection at the band structure (Fig. 4.14(a) and (b)) reveals that the bands comprise nano-grains of size ~50 nm. The corresponding SAD ring pattern was indexed and suggested the BCC structure of β phase. This result is partially in agreement with that reported by Puerta Velásquez *et al*. [170]. They suggested that the β grains dragged inside the shear band became very thin (less than 20 nm). In the current study, the β grains in the raw material were observed to be forced into the primary shear zone and refined down to nano-equiaxed microstructure. The ultrafine β grains constituted band structures with width of ~200 nm. The observed difference of the β band width is possible due to the different cutting speed: 6 m/s for the reference [170] and 10 m/min for this experiment.

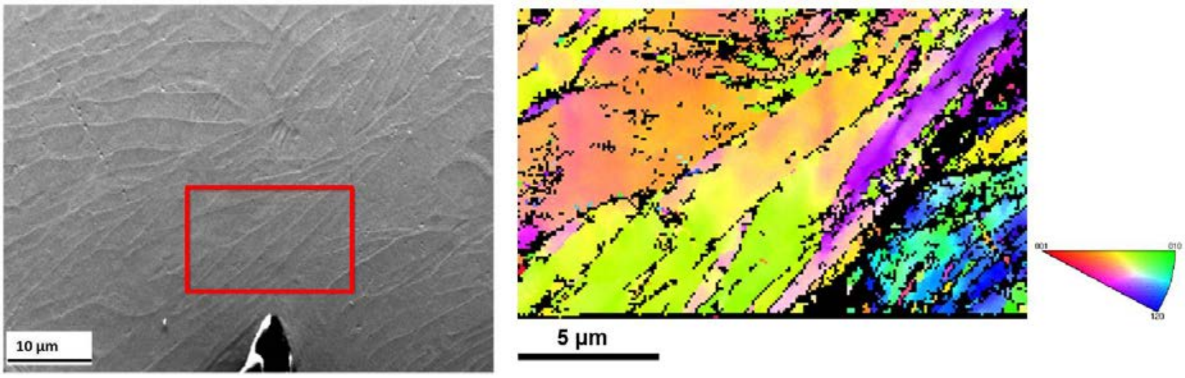

Fig. 4. 12 (a) Secondary electron image and (b) orientation map of a Ti64 machining chip with inset of the IPF colour scheme.

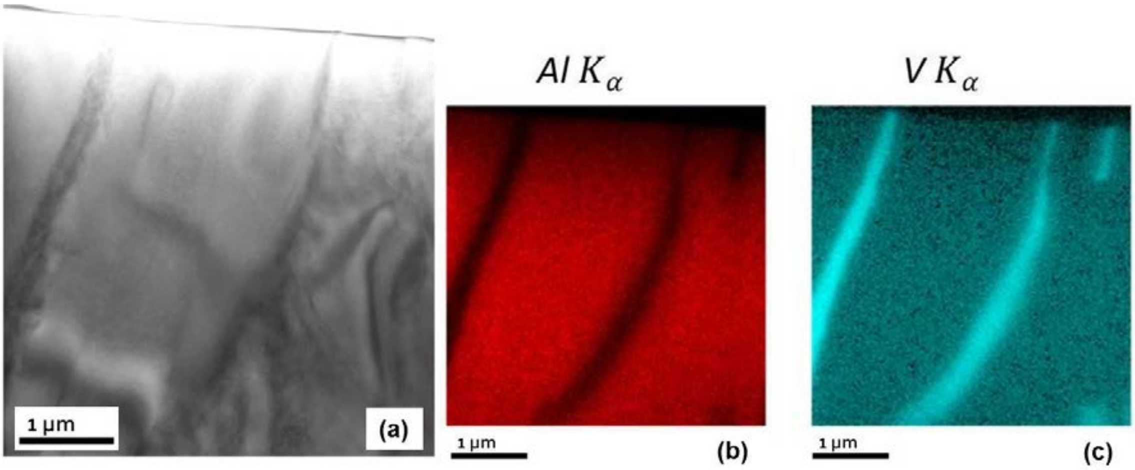

Fig. 4. 13 (a) STEM electron micrograph and simultaneously collected EDX maps of (b) aluminium and (c) vanadium of the primary shear zone for Ti64 chip.

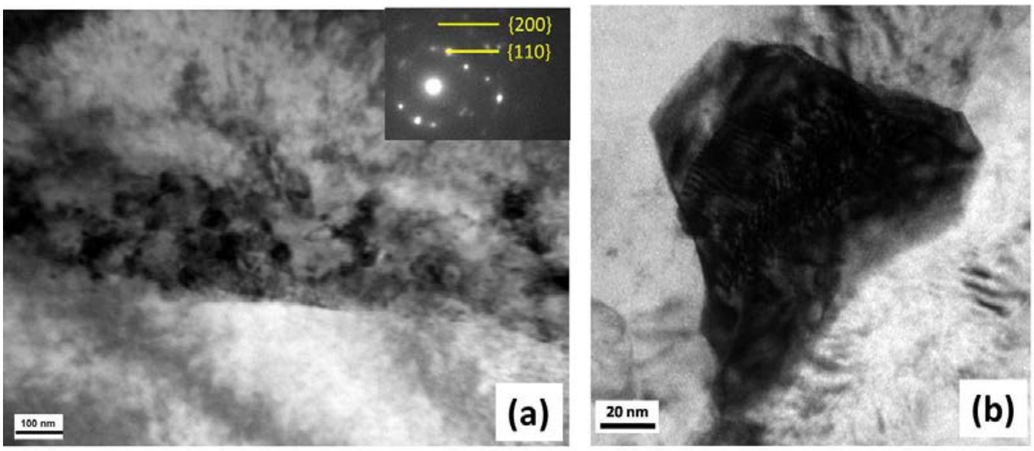

Fig. 4. 14 (a) TEM electron micrograph of the band structure in Ti64 chip primary shear zone with the inset of the SAD pattern of the nano-crystalline region, and (b) higher magnification micrograph of an individual β grain.

The secondary shear zone was also lifted out for TEM analysis (Fig. 4.15) in the region indicated by the dash rectangular box B in Fig. 4.11. A band structure with a width of ~200 nm, which is similar to that in the primary shear zone, was observed near the tool-chip interface, as marked by Zone A. Additionally, two lamellar structures with a width of ~100 nm were clearly found, as marked by Zone C. The region between Zone A and C with width of ~500 nm is indicated as Zone B. A high magnification micrograph of Zone A and the corresponding SAD pattern as shown in Fig. 4.16(a) gives evidence that Zone A is composed of equiaxed nano-sized β grains. A comparison between the virgin material before machining and Zone B is given in Fig. 4.16(b) and (c). The TEM results demonstrate a significant increase of dislocation density when the material experienced high level of shear strain. The EDX analysis conducted in Zone C suggests that the two lamella are also vanadium rich (~8.37±0.83 wt%). The corresponding SAD pattern (Fig. 4.16(d)) confirms they are β phase in $(11\bar{3})$ direction. Replicated to the secondary shear zone, a β phase lamella was also observed in the micrograph of the machined surface cross-section, as shown in Fig. 4.17.

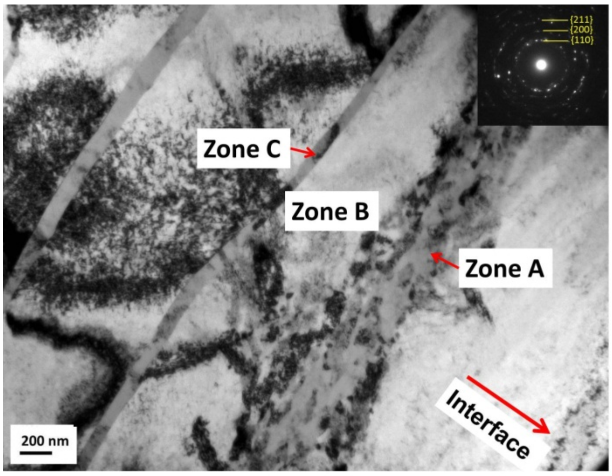

Fig. 4. 15 TEM micrograph of Ti-6Al-4V chip at the secondary shear zone.

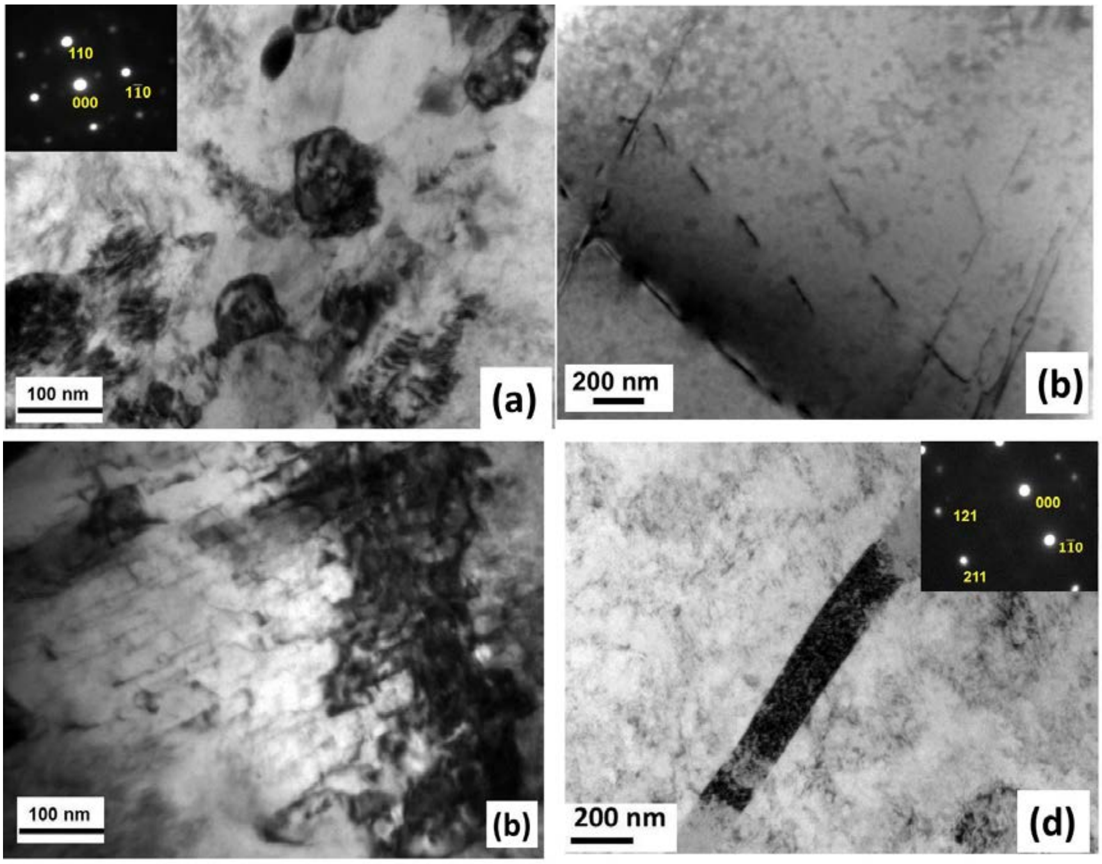

Fig. 4. 16 High magnification micrograph showing (a) nano-sized β grains of Zone A, dislocation density comparison between (b) raw material and (c) Zone B and (d) the lamellar structure of Zone C.

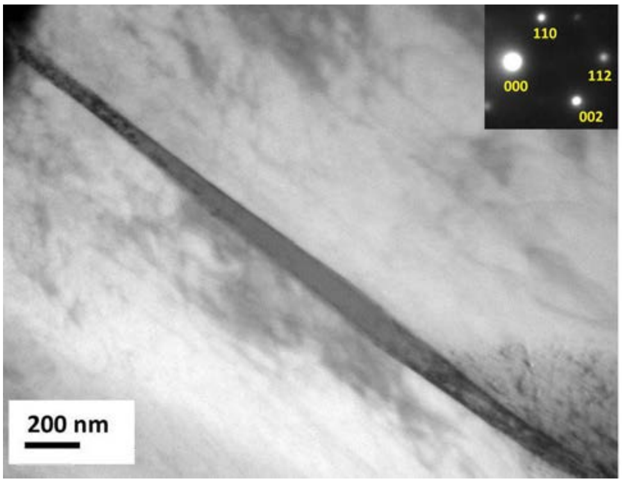

Fig. 4. 17 TEM cross-section micrograph of Ti-6Al-4V machined work-piece surface. The inset is the diffraction pattern of the lamellar structure.

5. RECYCLING OF Ti-6Al-4V MACHINING CHIPS USING EQUAL CHANNEL ANGULAR PRESSING

The aim of this chapter is to address the optimization of the ECAP process for Ti-6Al-4V machining chips recycling, and to evaluate the recycled products.

5.1 Introduction

Solid state recycling by equal channel angular pressing (ECAP) has been proposed as a promising technique to recycle metallic machining chips. This method has been used to consolidate aluminium [171] [172] [173] [174], magnesium [175] [176] and pure titanium chips [106] [108] [107]. However, because of the relatively low ductility and poor deformability, Ti-6Al-4V recycling from machining chips using ECAP is more challenging. An earlier report [157] suggested that multiple-pass ECAP was capable of recycling Ti-6Al-4V chips at a relatively high temperature of 590 °C with a low back-pressure of 50 MPa, whereas high temperature (up to 1000 °C) and long (up to 20 hours) post heat treatments were necessary to remove the chip boundaries. However, the optimization of the ECAP processing parameters has not been reported, and very limited evaluation of the recycled products has been carried out in the literature [157].

This chapter gives a systematic study on the recycling of Ti-6Al-4V chips using ECAP, including the influences of the operating process parameters on: (1) the macroscopic consolidation of the recycled products (Section 5.2), (2) the relative density measurement (Section 5.3), (3) the microstructure and crystallographic texture evolution (Section 5.4 and 5.5), (4) the microhardness distribution across the flow plane (Section 5.6), and finally (5) the effect of the post heat treatment (Section 5.7). The overall results are summarised in Section 5.8.

5.2 Influence of the Process Parameters on the Macroscopic Consolidation of Recycled Ti-6Al-4V

The low workability alloy, such as Ti-6Al-4V is susceptible to shear failure during ECAP. In order to avoid crack forming, elevated temperature and the application of back-pressure are indispensable in the consolidation process. In the present work, the effect of the operating temperature, back-pressure and number of ECAP passes on the macroscopic consolidation of the sample was investigated.

5.2.1 Effect of temperature on crack formation

Fig. 5.1(a) to (d) shows the image of the recycled products using back-pressure of 50 MPa at different operating temperatures ranged from 300 °C to 500 °C. Although crack formed in all recycled samples, the crack length tended to reduce as the temperature increased.

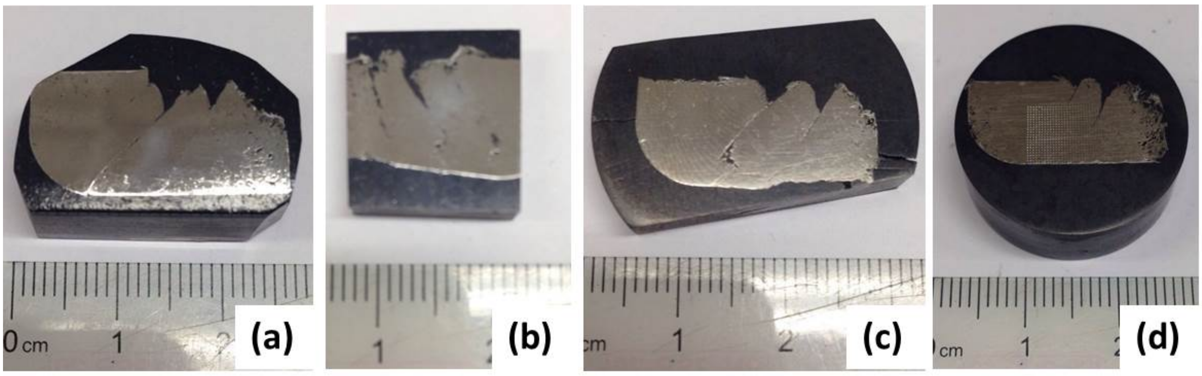

Fig. 5. 1 The appearance of crack in the recycled Ti-6Al-4V produced by ECAP with a back-pressure of 50 MPa at different temperatures: (a) 300 °C, (b) 350 °C, (c) 400 °C and (d) 500 °C.

As illustrated in Fig. 5.2, with a pre-set back-pressure of 100 MPa, in spite of the progressive reduction of the crack length, it is obvious that the number of cracks in the given length of sample decreased with the increasing temperature. At the temperature of 500 °C, as shown in Fig. 5.2(c), a sample free of major shear failure was obtained although there was still some surface cracking at the leading end and the top edge of the sample. Shear crack free sample is not possible for Ti-6Al-4V pressed through a die with 90° intersection angle below 500 °C. However, it was achieved by pressing a bulky Ti-6Al-4V sample at 600 °C without back-pressure [131]. Such ECAP was done under an isothermal condition, i.e. the die and the sample were heated to the same target temperature before pressing. Therefore, for the current study, due to the low workability of Ti-6Al-4V, a moderate processing temperature at least 500 °C is recommended.

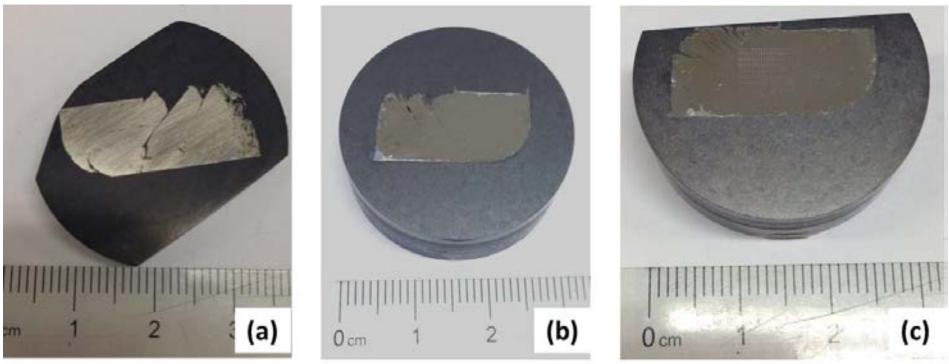

Fig. 5. 2 The appearances of crack formation in the recycled Ti-6Al-4V produced by ECAP with a back-pressure of 100 MPa at different temperatures: (a) 400 °C, 450 °C and (c) 500 °C.

5.2.2 Effect of back-pressure on crack formation

The effect of back-pressure on the crack forming at the temperature of 450 °C is shown in Fig. 5.3. Although the formation of cracks was significantly suppressed by the increasing back-pressure, clear segments can still be seen even with a back-pressure of 200 MPa, which implies that it is not possible to produce recycled samples free of cracks under the current settings at 450 °C or below, and further increase of back-pressure required larger forward pressing force which may lead to the damage of the die and plungers.

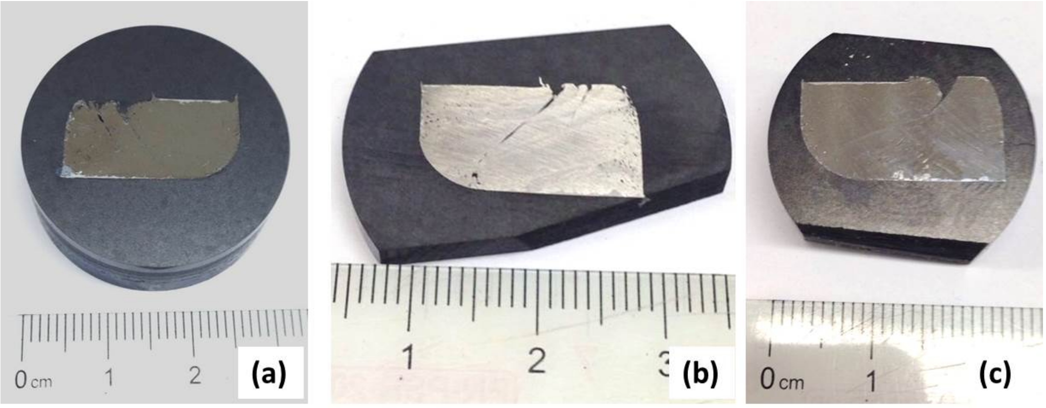

Fig. 5. 3 The appearances of crack formation in the recycled Ti-6Al-4V produced by ECAP at the temperature of 450 °C with different back-pressures: (a) 100 MPa, (b) 150 MPa and (c) 200 MPa.

Fig. 5.4(a) to (c) shows the optical images of the samples pressed at 500 °C with back-pressures increased systematically from 150 MPa to 250 MPa. Refer to Fig. 5.1(c) and Fig. 5.2(d) as well, at operating temperature of 500 °C, the major segment cracks can be eliminated by applying back-pressures greater than 100 MPa, and the surface crack on the top edge was also reduced with the increasing back-pressures. In addition, the crack at the leading end was also suppressed at higher back-pressure. According to the study on ECAPed bulk Ti-6Al-4V [131], when the sample was pressed at 500 °C without back-pressure, it exhibited severe shear fracture with pronounced shear bands. In the previous study on recycling Ti-6Al-4V chips [157], the back-pressure of 50 MPa and the processing temperature of 590 °C can give shear crack free samples. However, when performing ECAP at lower temperature, a higher back-pressure is required to suppress the formation of shear crack.

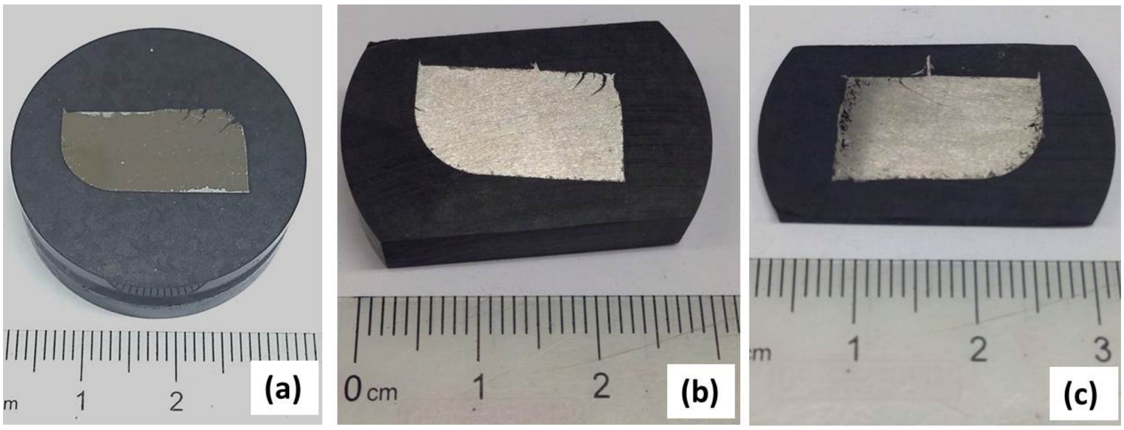

Fig. 5. 4 The appearances of cracking in the recycled Ti-6Al-4V produced by ECAP at the temperature of 500 °C with different back-pressures: (a) 150 MPa, (b) 200 MPa and (c) 250 MPa.

5.2.3 Effect of number of ECAP pass on crack formation

The appearances of the samples processed at 500 °C with a back-pressure of 100 MPa for a single pass, 4 passes and 8 passes via route B_C are shown in Fig. 5.5(a) to (c), respectively. There is no shear crack in all samples, but minor cracks on the top surface are still visible. In order to remove the small surface cracks, other process parameters such as slower strain rate should be taken into account because low strain rate can reduce the effect of stress localization [115] [177].

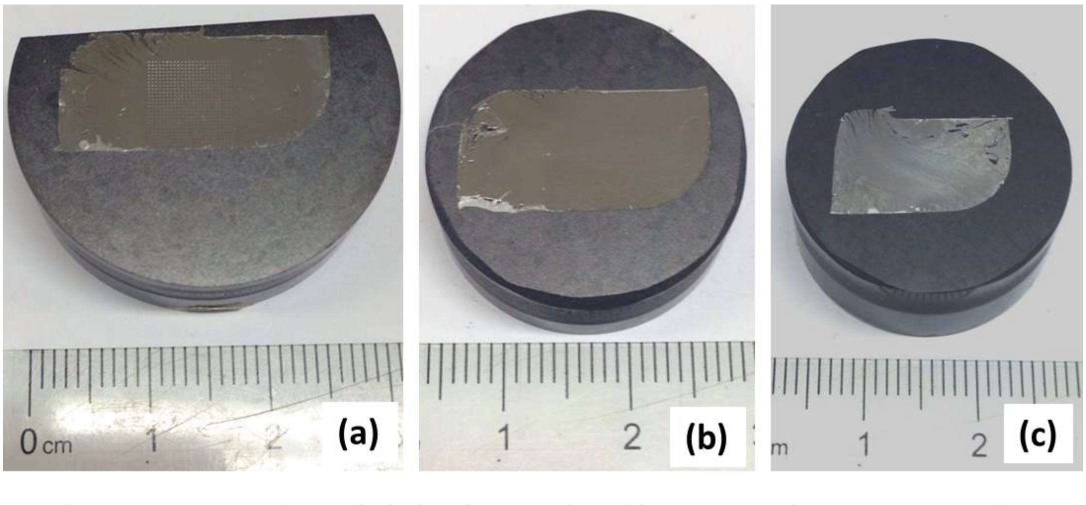

Fig. 5. 5 The appearances of recycled Ti-6Al-4V produced by ECAP at the temperature of 500 °C with a back-pressure of 100 MPa for (a) 1 pass, (b) 4 passes and (c) 8 passes.

5.3 Relative Density Measurement of Recycled Ti-6Al-4V

5.3.1 Single-pass samples

The relative density measurements were conducted on all the recycled samples underwent a single pass ECAP at the temperatures of 400 °C, 450 °C, 500 °C and 550 °C. The relative densities are summarised in Table 5.1. The relative density as a function of imposed back-pressures is plotted at each processing temperature, as shown in Fig. 5.6.

Table 5. 1 Summary of relative density measurement for single-pass Ti-6Al-4V at each condition

Imposed Back-pressure (MPa)	Operating Temperature (°C)			
	400	450	500	550
50	91.8%	95.8%	97.9%	N/A
100	95.8%	97.2%	98.7%	N/A
150	N/A	97.6%	98.7%	N/A
200	97.3%	98.3%	98.8%	N/A
250	N/A	N/A	99.0%	99.7%

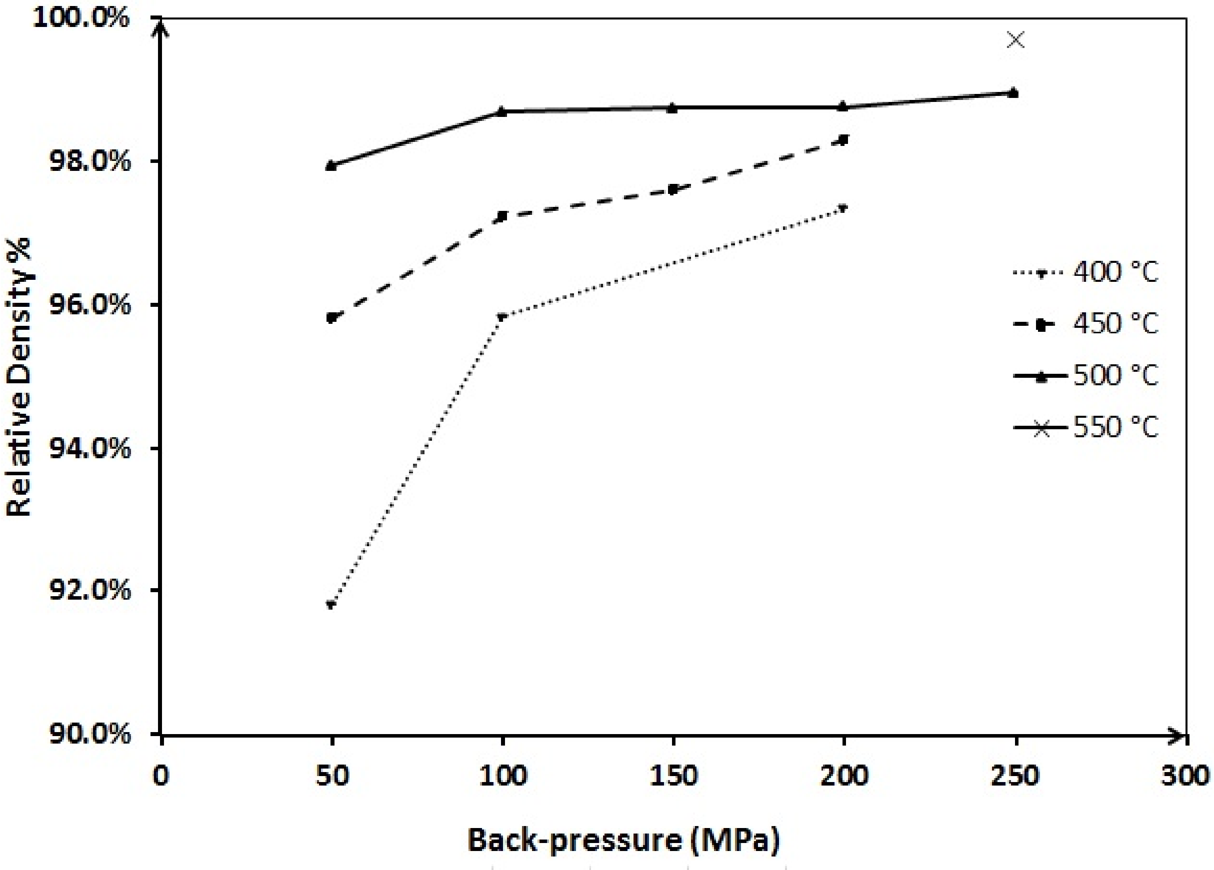

Fig. 5. 6 Relationship between the relative density and the back-pressure at different processing temperature for single-pass ECAP recycled Ti-6Al-4V.

5.3.1.1 Influence of the back-pressure on the relative density

The relative density increased with the applied back-pressure at each operating temperature. Similar trends have been reported in earlier studies for ECAP consolidation of Ti-6Al-4V powder **[178]** and magnesium swarf **[179]**. The influences of the back-pressure on the densification can be discussed in two stages during ECAP.

In stage I, the chips in the entry channel are compacted by the forward pressure while restricted by the rear plunger, which is similar to briquetting. In this stage, larger applied back-pressure leads to higher level of forward pressing force before the shear deformation commences, and hence the higher pre-compaction density. Fig. 5.7(a) and (b) shows the cross sections of the pre-compacted chips at 500 °C using the back-pressures of 100 MPa and 250 MPa, respectively. It is apparent that at the flow plane the chips were aligned perpendicular to the direction of the forward pressure. At a back-pressure of 100 MPa, a large number of pores were observed at the triple junction of chips as indicated by circles in Fig. 5.7(a). A higher back-pressure has a positive influence on pore closure and hence smaller pores are observed (Fig. 5.7(b)). It should be noted that compared with the original thickness of the machining chips (~180 µm), as shown in Fig. 4.11, the chips in the compacted region (~65.2 µm and ~61.5 µm using back-pressures of 100 MPa and 250 MPa, respectively) were significantly thinned due to the uniaxial compression.

It has been demonstrated in the study of Ti-6Al-4V powder consolidation using hot isostatic pressing [180], that the densification of metallic particles during early stages involves the deformation of neighbouring particles, subsequent fracture at the interfaces and relative motion between particles each other. This mechanism partially applies to the current study: the contiguous machining chips deformed and filled surrounding pores; nevertheless no surface fracture was observed within the compacted samples.

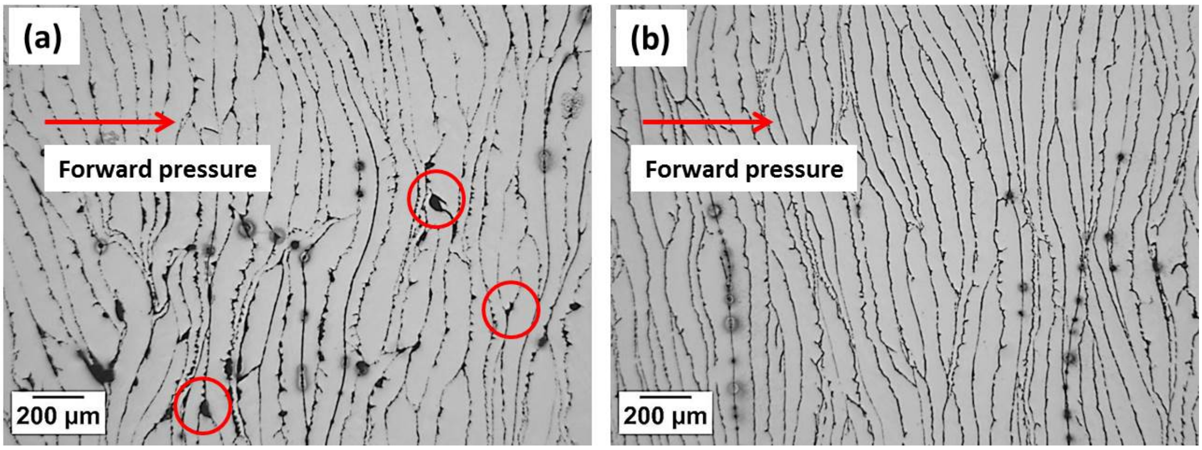

Fig. 5. 7 Optical micrographs of Ti-6Al-4V machining chips pre-compacted at 500 °C using the back-pressures of (a) 100 MPa and (b) 250 MPa.

In stage II, the specimen flows through the channels and simultaneously experiences the shear strain, until the whole work-piece passes through the die. Fig. 5.8(a) and (b) show the optical micrographs of the central region of the samples processed at 500 °C using back-pressures of 100 MPa and 250 MPa, respectively. The chips were re-arranged and aligned in parallel to the inclination direction during ECAP. It was measured that the inclination direction takes an incline angle of ~21° to the extrusion direction (ED), as shown in Fig. 5.9. Compared to the compacted region, most pores had been closed by shear deformation. It was suggested that the near equiaxed pores have been elongated even closed due to the sufficient simple shear deformation, and the boundaries of the pore may be welded by mechanical force [178].

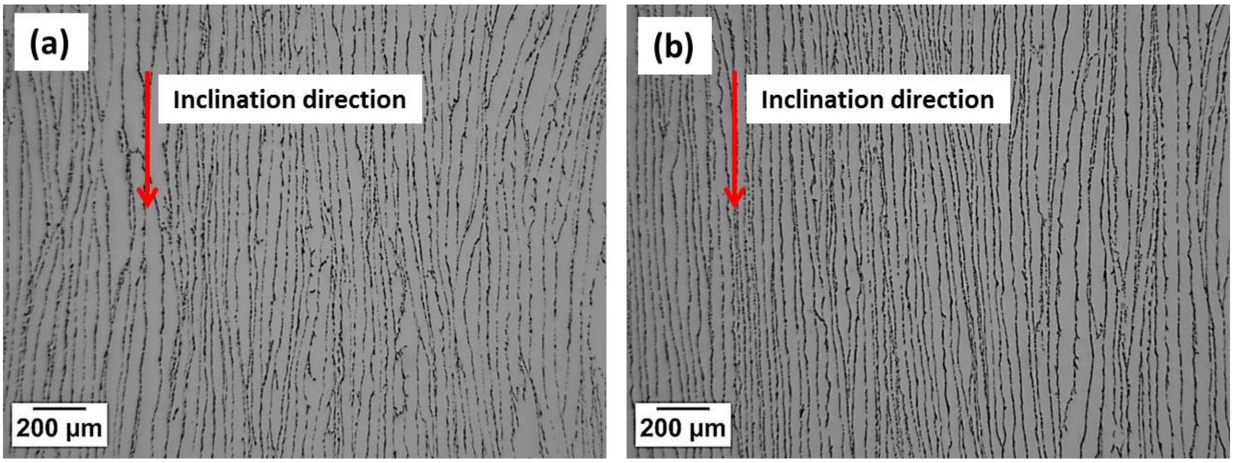

Fig. 5. 8 Optical micrographs showing Ti-6Al-4V machining chips subjected to ECAP shear deformation at 500 °C using the back-pressures of (a) 100 MPa and (b) 250 MPa.

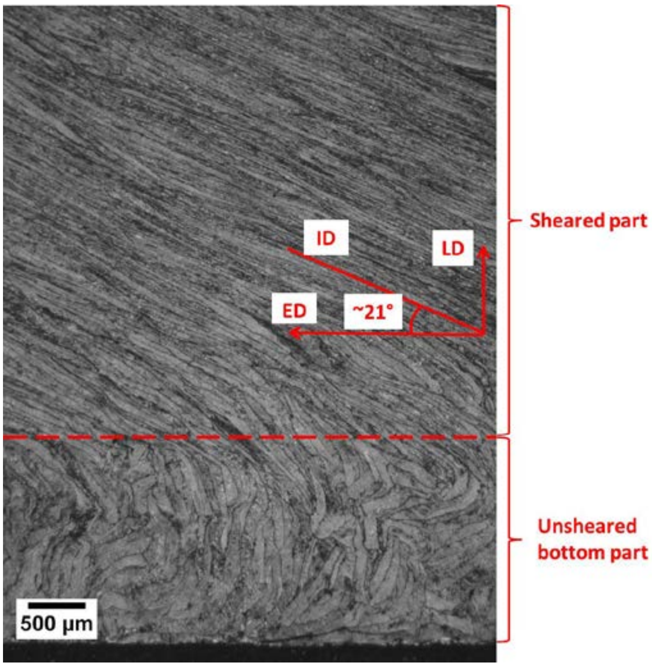

Fig. 5. 9 Optical micrograph showing the inclination direction of ECAP taking an angle of ~21° to the ED.

In comparison to the compacted sample before shearing, Fig. 5.8 indicates that the chips are further thinning down, and the higher back-pressure leads to slightly larger thickness reduction: ~34.3 µm at the back-pressure of 100 MPa and ~31.3 µm at the back-pressure of 250 MPa. It can be explained by the effect of the back-pressure on the shape of plastic deformation zone (PDZ). Lapovok [181] suggested that for Al 2124-T851 alloy subjected to one pass of ECAP, the PDZ changed from a fan shape to a narrow band when the back-pressure increased to 200 MPa. A narrow band at the intersection of the channels makes the shearing deformation during ECAP process close to the ideal simple shear model. The similar conclusion was drawn by finite element simulation. Kang *et al*. [139] showed that for the strain hardening material (1100Al alloy), the area of PDZ shrunk and the strain rate at the intersection of two channels increased with the back-pressure up to 100 MPa. However, it should be noted that in their report the smallest size of PDZ was achieved with a back-pressure of 100 MPa, exceeding which the PDZ had broadened rather than narrowed. Because of different material used, the present work demonstrates that the beneficial effect of back-pressure on the consolidation of Ti-6Al-4V chips extended to at least 250 MPa.

In Fig. 5.6, it is observed that the influence of the back-pressure on relative density is more significant for the samples pressed at a lower temperature: at 400 °C the relative density increased from ~91.8% (with the back-pressure of 50 MPa) up to ~97.3% (with the back-pressure of 200 MPa), while at the operating temperature of 500 °C, the relative density became saturated when the back-pressure exceeded 100 MPa. This phenomenon can be elucidated based on the poor workability of Ti-6Al-4V at low temperature. Major cracks are expected to generate and penetrate along the ECAP shear plane at a relatively lower temperature, as shown in Fig. 5.3, leading to less dense recycled samples. It is known that increasing the back-pressure can improve the workability, especially for the materials with low ductility, as experimental proved in [137]. For the samples pressed at a relatively low temperature, the potential cracks could be suppressed by applying higher back-pressures, which was responsible for the remarkable improvement of the density. In contrast, at a higher operating temperature, the material became more workable and the samples free of major cracks were possible to be produced even at a low back-pressure, as shown in Fig. 5.2(c).

5.3.1.2 Influence of the operating temperature on the relative density

For a given back-pressure, the relative density increased with the processing temperature, Fig. 5.6. This is attributed to the increasing mobility of dislocations and hence improves the ductility of Ti-6Al-4V chips at elevated temperature [178]. The optical micrographs, as illustrated in Fig. 5.10, shows an obvious reduction in the number of pores as the operating temperature increases: with the back-pressure of 200 MPa, more pores were found after single pass at 400 °C in comparison with that pressed at 500 °C.

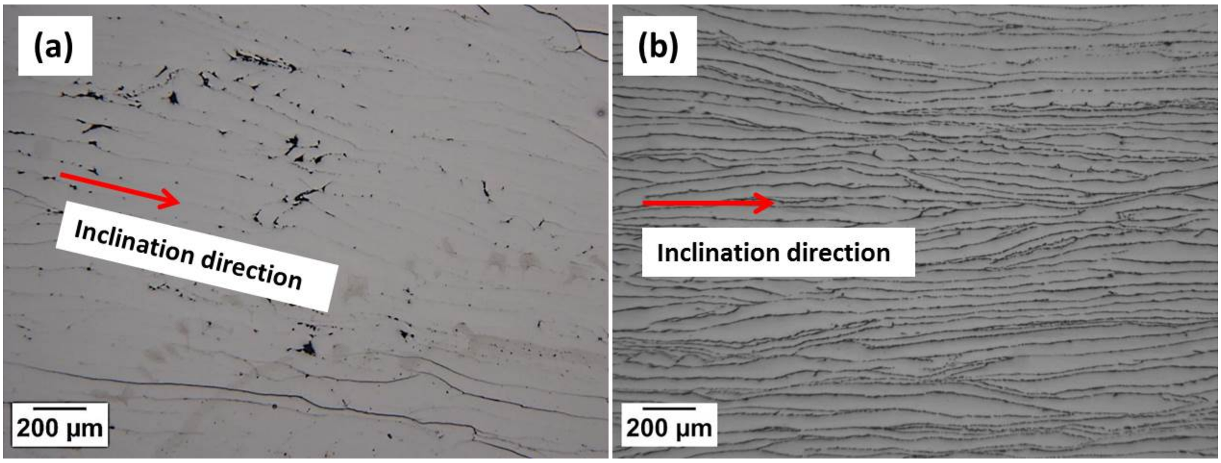

Fig. 5. 10 Optical micrographs showing the samples processed at (a) 400 °C and (b) 500 °C using a back-pressure of 200 MPa.

In addition to the pore closure, better solid state bonding at higher temperature increases the relative density of the recycled products. It has been demonstrated in the study on porthole die extrusion [182], the solid state bonding can be enhanced not only by larger interface pressure between chips, but also at higher temperature, because higher temperature facilitates the plastic deformation and atomic diffusion at the interface.

5.3.2 Multiple-pass samples

In order to avoid shear fractures, the operating temperature of multiple-pass ECAP was set at 500 °C. The relative density via multiple passes accompanying with various back-pressures are depicted in Fig. 5.11.

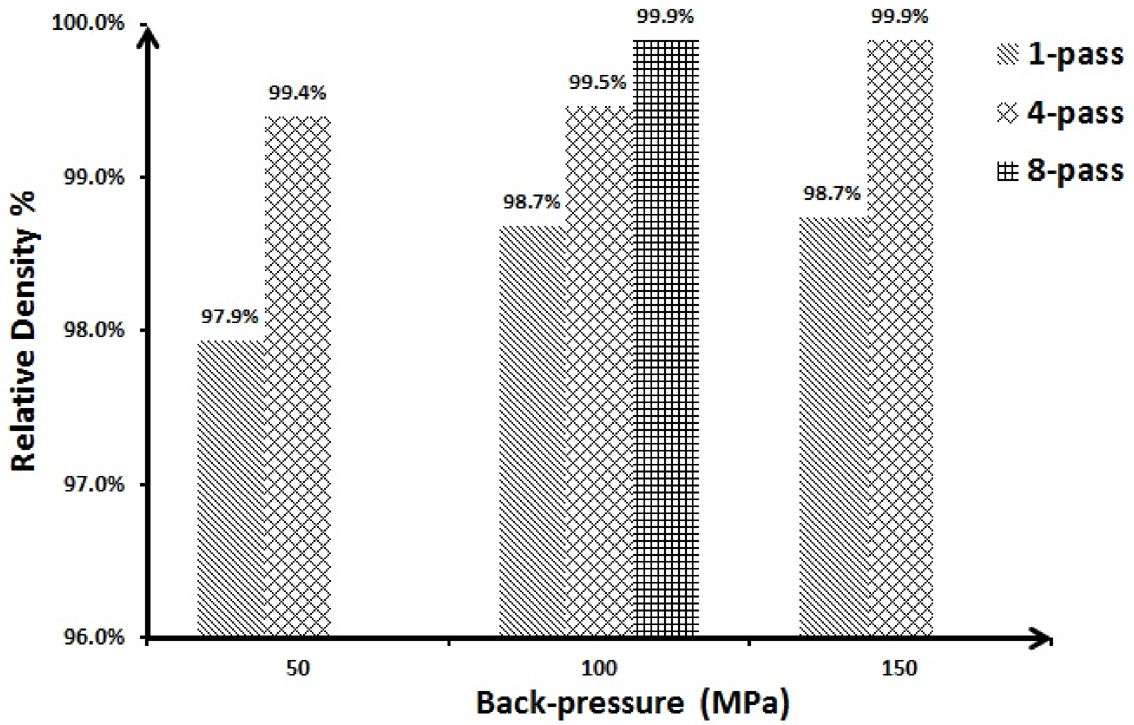

Fig. 5. 11 Relative density improved by multiple ECAP passes at 500 °C using various back-pressures.

It can be observed that the relative density was increased with the number of passes at different applied back-pressure. The densest specimens (~99.9%) were achieved using the back-pressure of 150 MPa via 4 passes or using the back-pressure of 100 MPa via 8 passes. Fig. 5.12(a) shows that chips boundaries were well defined after single pass. As the number of passes increased, some of the chip boundaries ‘disappeared’ (Fig. 5.12(b)), which implies that solid bonding occurred between the chips. When the sample was pressed for 8 times, most of the chip boundaries were eliminated, but a few discontinuous chip boundaries still remained, as shown in Fig. 5.12(c). A higher magnification SEM micrograph (Fig. 5.13) shows only few pores remained, and most of chip boundaries were eliminated. This enhancement in density is mainly attributed to the increase of the accumulated shear strain. Similar dependency of the consolidation level on the imposed strain was also identified for the consolidation of Al chips using hot extrusion [183]: the quality of the Al alloy bar consolidated from chips was improved as the extrusion ratio increased from 6.25:1 to 25:1. In their study, the increased extrusion ratio resulted in higher imposed strain, and hence improved solid state bonding [183]. Similarly, in the current experiments, increases in number of passes increases the accumulated strain, which facilitates the elimination of chip boundaries.

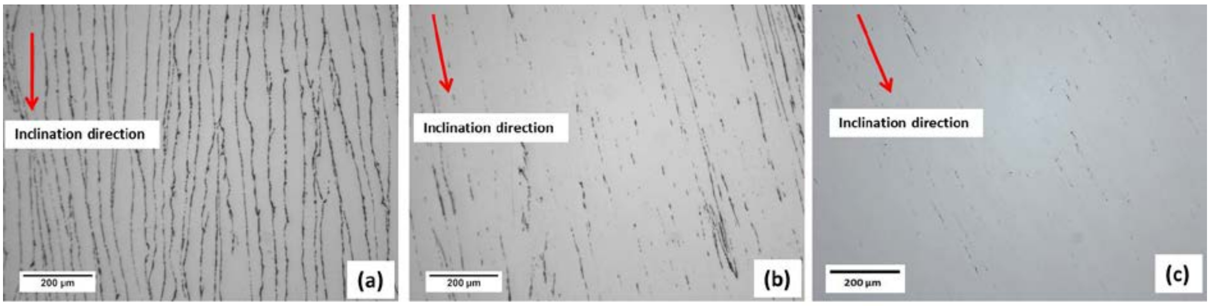

Fig. 5. 12 Chip boundaries in the samples processed at 500 °C with the back-pressure of 100 MPa after (a) 1 pass, (b) 4 passes and (c) 8 passes.

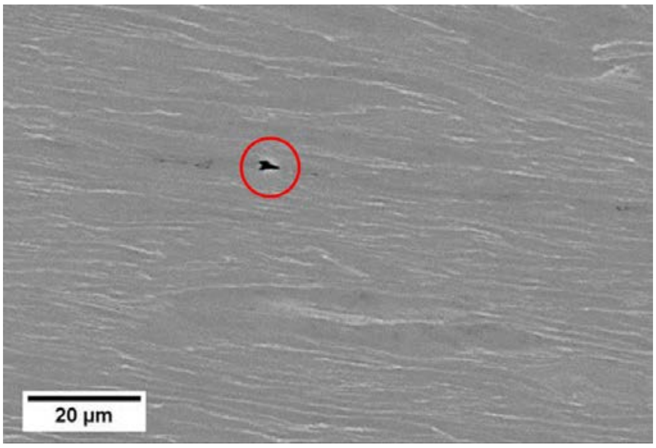

Fig. 5. 13 SEM-BSD micrograph showing a pore (marked by the circle) remained in sample after 4 passes at 500 °C with a back-pressure of 100 MPa

In addition, it has been reported in powder consolidation that the density of the consolidated sample during ECAP is governed by particle realignment, localised fragmentation and mechanical interlocking [178]. These mechanisms can also apply to the Ti-6Al-4V chip recycling process. The localised fragmentation and strong mechanical interlocking have been observed in the 4-pass samples and marked by ovals in Fig. 5.14.

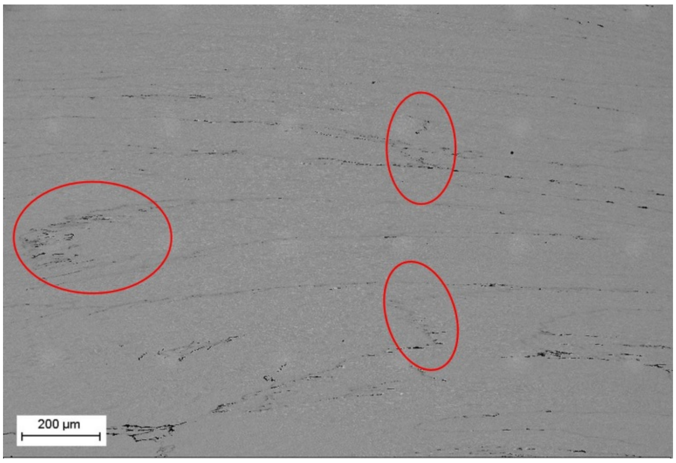

Fig. 5. 14 SEM micrograph showing surface fragmentation and mechanical interlocking of the sample pressed at 500 °C with a back-pressure of 100 MPa for 4 passes.

5.4 Microstructure Evolution of Recycled Ti-6Al-4V

5.4.1 Effects of number of passes on microstructure evolution

Fig. 5.15 is a representative optical micrograph of the sample after one pass pressed at 500 °C with a back-pressure of 250 MPa. The lamellar microstructure in the original chips was observed to be refined and re-arranged along with the inclination direction of ECAP process.

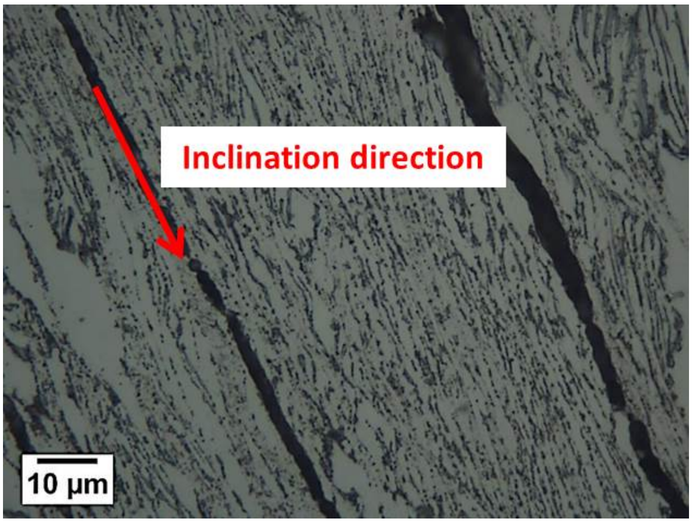

Fig. 5. 15 Optical micrograph showing the microstructure of the recycled Ti-6Al-4V ECAPed at 500 °C with a back-pressure of 250 MPa.

Fig. 5.16 shows the EBSD orientation map of the same sample in Fig. 5.15. It is apparent that the sample had a relatively low EBSD indexing rate (~44%), because the quality of EBSD patterns were impeded in the highly deformed regions that consisting ultrafine grains. Despite unindexed regions, it is observed that the elongated grains were parallel to the inclination direction. The misorientation within the elongated grains was measured along line AB, as indicated in Fig. 5.16. The profile (Fig. 5.17) demonstrated that the elongated grains were bounded with low angle grain boundaries (<15°).

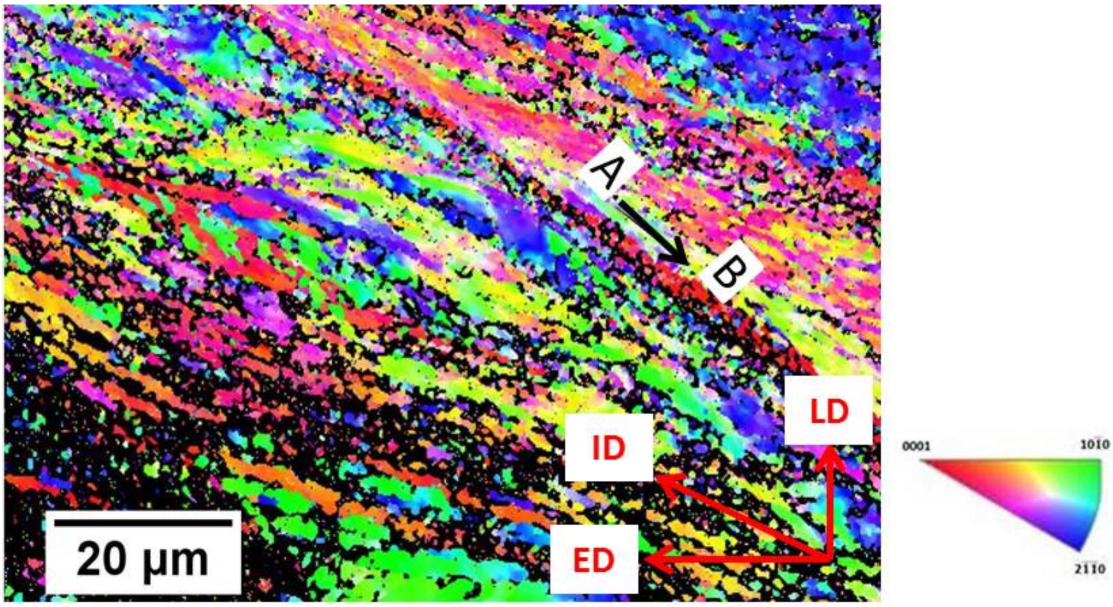

Fig. 5. 16 EBSD orientation map showing the microstructure of the recycled sample by single ECAP with a back-pressure of 250 MPa at 500 °C.

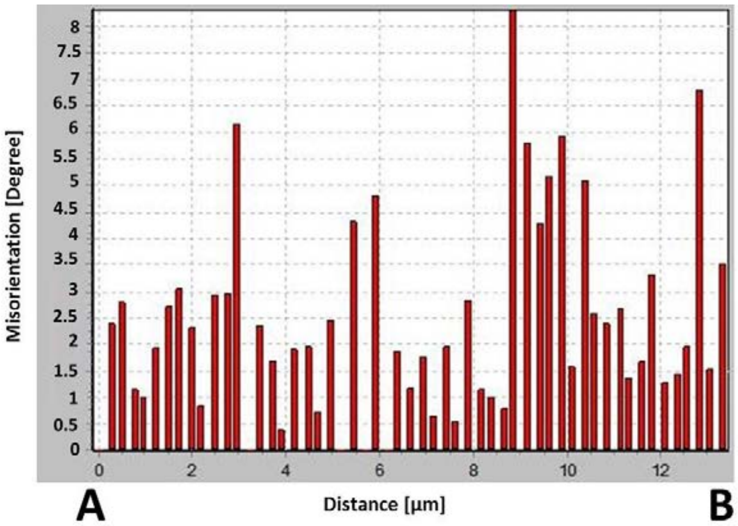

Fig. 5. 17 Misorientation profile measured along line AB in Fig. 5.16.

Finer microstructure has been revealed by the TEM examination. The TEM image (Fig. 5.18) confirms that α lamellae were initially refined from several micrometers down to ~300 nm – 500 nm in width after a single pass. As a result of shear deformation during ECAP, new subgrain boundaries transversely formed, as indicated by arrows.

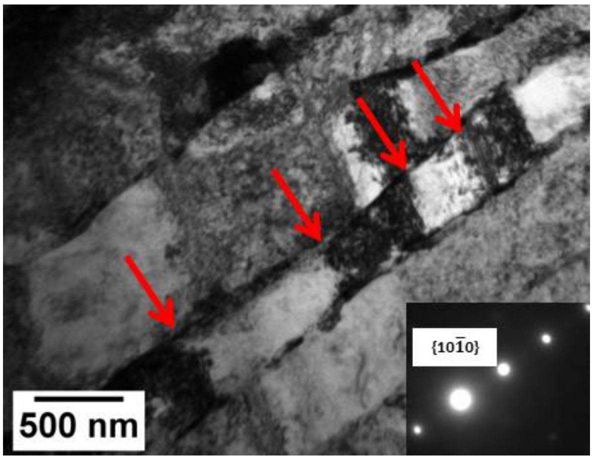

Fig. 5. 18 TEM images showing the microstructure of the sample after one pass pressed at 500 °C with a back-pressure of 250 MPa.

Apart from the α lamella, equiaxed grains can be found in the sample. For instance, as shown in Fig. 5.19, there is an equiaxed grain (marked as grain ‘a’) and the corresponding SAD pattern reveals a α phase with zone axis of $<\bar{1}2\bar{1}3>$. In addition, elongated grains (marked as grain ‘b’ and ‘c’) were also observed along the lamellar structures. The diameter of the equiaxed grain was identical with the width of the lamella, which was ~70 nm. For the elongated grains, the width and length were ~70 nm and ~110 nm, respectively. This phenomenon implies that the refinement and reconstruction of the lamellar structure was started, new grain boundaries started to form during the first ECAP pass, and the equiaxed grains were originated from the elongated structures. A coexistent microstructure of equiaxed and elongated grains in the single-pass ECAPed Al and Al-6061has been reported by Xu *et al*. [184]. They suggested that the majority of the boundaries in the substructure were low-angle boundaries. Similar result has been observed in recycled Ti-6Al-4V sample and the EBSD misorientation analysis is shown in Fig. 5.17. It is noteworthy that in the same research work [184], it has been reported that the proportion of elongated and equiaxed grains after the first pass was approximately 50 : 50, while in the present observation, the number of equiaxed grains is much less than elongated ones. In additional, a large amount of initially refined lamellar structures with width of ~300-

500 nm were found, as shown in Fig. 5.18. The plausible explanation is based on the fact that bulk Al and Al-6061 alloy have been examined in the previous study [184] are FCC structure and have 12 easy slip systems. However, in the case of HCP structure fewer dislocation slip systems can be activated, and hence less accumulated dislocations are generated. The accumulated of dislocations at cell walls are likely to be responsible to the equiaxed grain formation [185]. Moreover, in contrary to the bulk material used in the literature [184], the original material in the current study is machining chips, therefore a portion of shearing force was used to consolidate the chips rather than refining the grains.

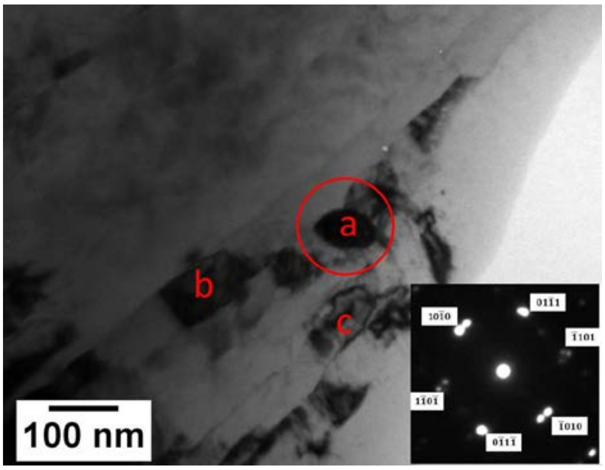

Fig. 5. 19 TEM micrograph showing an equiaxed grain ‘a’ and elongated grains ‘b’ and ‘c’ formed along the lamellar structure. The inset SAD pattern was taken from the equiaxed grain ‘a’.

Therefore, energy provided by a single ECAP pass is insufficient to produce uniform and ultrafine grains and strong bonding between chips. Apart from the dominated α phase, lamellar β phase was also identified in the single-pass sample, as shown in Fig. 5.20: The EDS analysis (Al: ~3.04 wt.%; V: ~26.11 wt.%) and corresponding SAD pattern confirmed that the lamellar structure was β phase. This observation is consistent with research on bulk Ti-6Al-4V ECAPed at 600 °C to 800 °C [186], where the β lamellae were thinned after the first pass. According to the earlier study [187], β phase is easily fragmented due to the weak capability of β phase to accommodate severe shearing strain. This observation implies that the shearing strain during the first pass has not fragmented initial β phase. In addition, a clear gap along the chip boundary, as shown in Fig. 5.21, suggests that the mechanical bonding between chips was fairly weak.

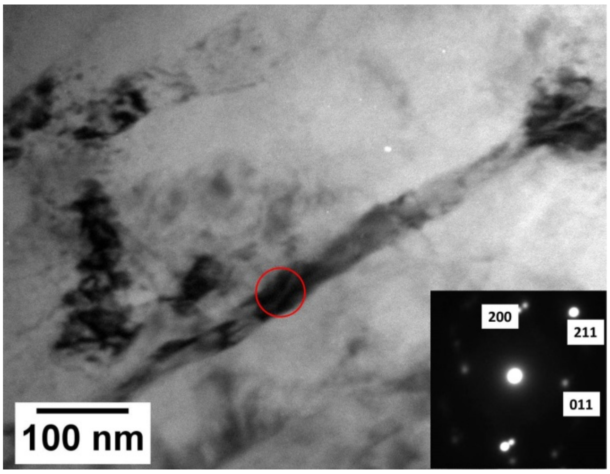

Fig. 5. 20 TEM micrograph and corresponding SAD pattern showing an integrated β phase lamella with a zone axis of <$\mathbf{01\bar{1}}$> in the specimen pressed at 500 °C for the single pass.

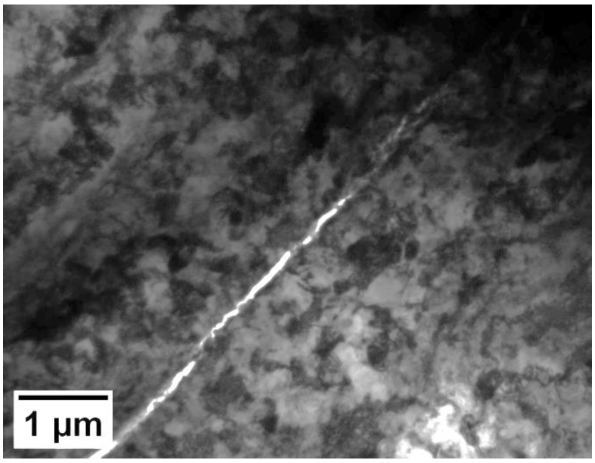

Fig. 5. 21 TEM micrograph showing the gap between the chip boundaries in the specimen pressed at 500 °C for the single ECAP pass.

Fig. 5.22 shows TEM bright field images of the microstructures of recycled Ti-6Al-4V produced by various numbers of passes. After 2 ECAP passes (Fig. 5.22(a)), lamellar microstructures become less profound, and more grains are equiaxed compared to the single-pass sample. The corresponding SAD pattern shows diffused spots, which implies an increase in the misorientations of grain boundaries and finer microstructure. After 4 and 8 ECAP passes, as shown in Fig. 5.22(b) and (c), respectively, the area fraction of the equiaxed grains increases, and no lamellar microstructure remains in the area of examination. In Fig. 5.22(b), the grain size in the central region was ~70 nm, as marked by ovals, while there were still a few elongated grains with size of ~70 nm × ~110 nm, as indicated by arrows. This implies that the microstructure after 4 passes has not reached the equilibrium state. In the 8-pass sample (Fig. 5.22(d)), the microstructure was dominated by equiaxed grains. As the number of passes increase, the SAD ring patterns become more continuous, which indicates the increase in volume fraction of high angle grain boundaries and fine microstructure in the samples processed with more ECAP passes. The results from the present study broadly agree with the grain refinement model proposed by Xu *et al*. [184]. The elongated substructure is formed in the first pass. Such substructure contains the elongated grains and equiaxed grains. The misorientation across the grain boundaries is relatively low. When the volume fraction of equiaxed grains increases with the number of ECAP passes, more high-angle grain boundaries are formed. A nearly equilibrium microstructure is established after certain passes, and the ultimate grain size of the equiaxed α grain was obtained, which is governed by the width of substructure formed in the first pass.

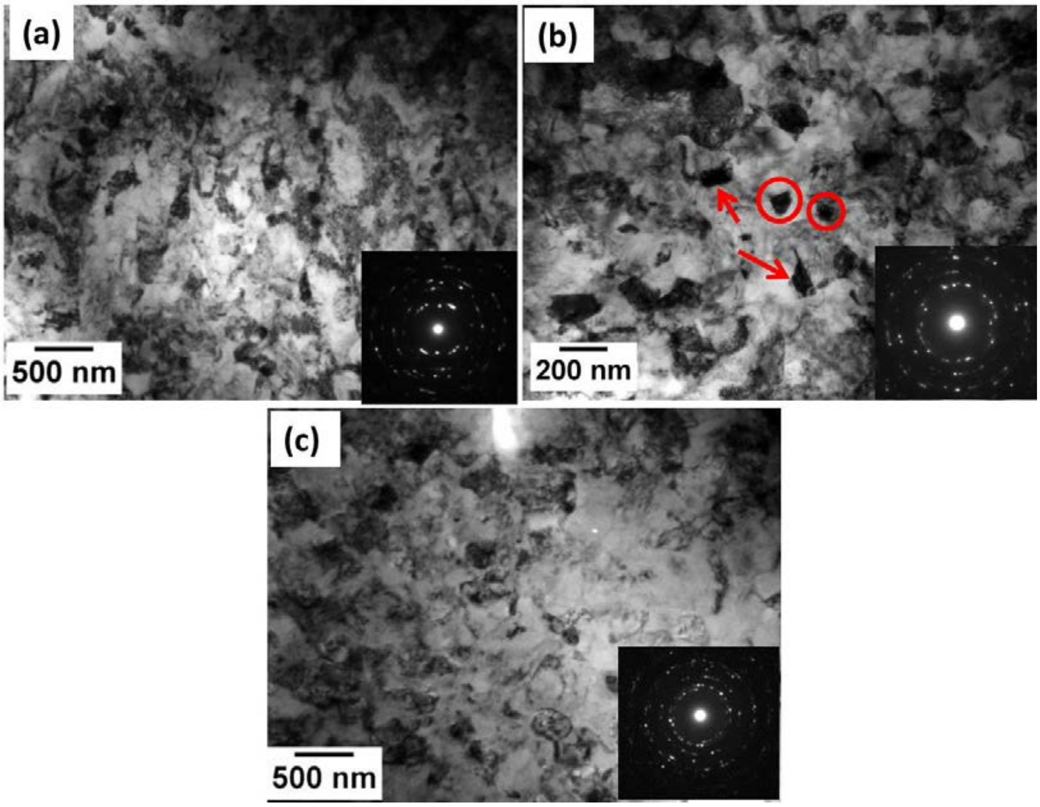

Fig. 5. 22 Microstructures and associated SAD patterns for recycled Ti-6Al-4V pressed at 500 °C after (a) 2 passes, (b) 4 passes and (c) 8 passes.

With the accumulated strain increasing, no nano-crystalline banded β phase has been inherited from the primary shear zone of the machining chips, as shown in Fig. 4.14. It is believed that those β lamellae and nano-crystalline β bands were fragmented due to the severe shearing deformation [131]. Evidence of individual β grain was found in the sample after 4 passes, as marked by the oval in Fig. 5.23.

The line profile of EDS across such grain gives noticeably higher vanadium concentration than the surrounding area, indicating the β phase.

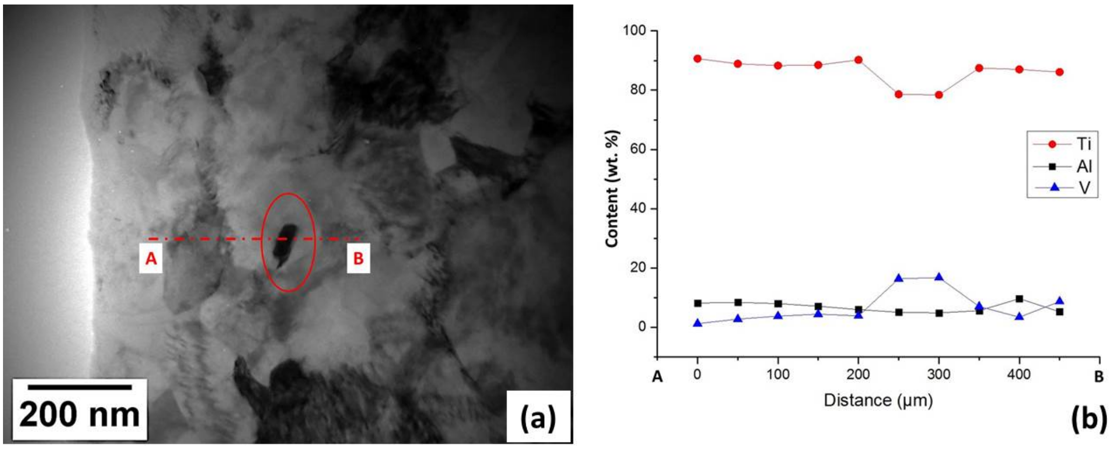

Fig. 5. 23 (a) An individual β grain and (b) the corresponding EDS spectrum observed in the sample pressed at 500 °C with a back-pressure of 100 MPa for 4 passes.

In addition to grain refinement, the increase in number of passes also facilitates the mechanical bonding between chips. Evidence of an interface between two chips was found in the sample pressed for 4 passes at 500 °C with a back-pressure of 150 MPa, as shown in Fig. 5.24. It is evident that the two chips were merged together, but some nano-sized gaps remained, as marked by arrows, indicating the weak merging regions. The grain boundaries in the bonding region are not well defined, the corresponding SAD pattern showing an integrated ring shape indicates that nano-crystalline microstructure is formed at the interface. The width of the bonding zone is ~300 nm – 400 nm, as shown in Fig. 5.24.

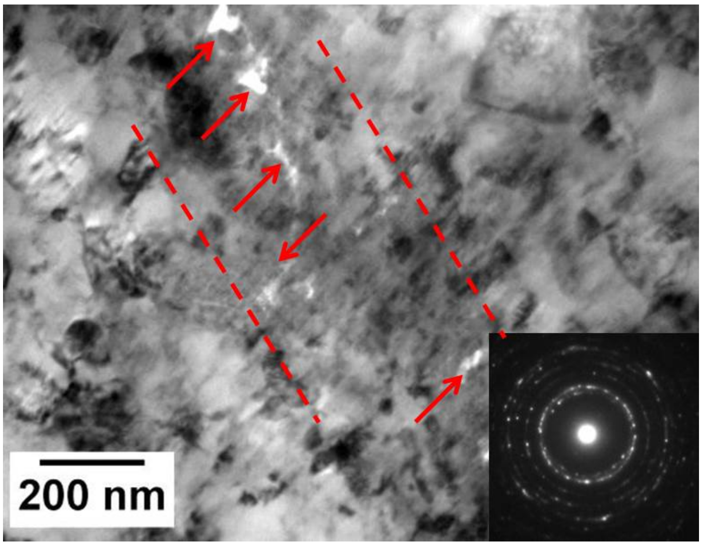

Fig. 5. 24 TEM micrograph showing a merged chip interface after pressed at 500 °C with a back-pressure of 150 MPa for 4 passes.

The sample processed by 8 passes shows a high number of dislocations, as shown in Fig. 5.25, which is the characteristic of metals underwent severe plastic deformation [142] [188].

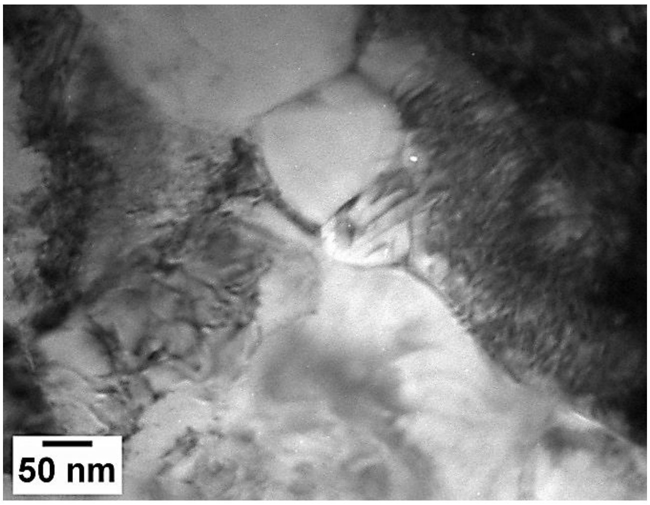

Fig. 5. 25 TEM image showing high dislocation density in the sample pressed after 8 passes at 500 °C with a back-pressure of 100 MPa.

5.4.2 Effect of processing temperature on microstructure evolution

To understand the microstructure changes when Ti-6Al-4V chips were recycled at higher temperature, EBSD was performed on an ECAP recycled sample processed at 550 °C with a back-pressure of 250 MPa for a single pass. The EBSD orientation map is shown in Fig. 5.26. Compared to the sample pressed at 500 °C (Fig. 5.16), it is obvious that the indexation rate is improved. The higher the processing temperature resulted in an increased dynamic recovery and the stress relief. As observed in Fig. 5.26, in addition to ultrafine grains (marked by ovals), elongated grains with width of a few micrometers were found (indicated by arrows). The average diameter of the ultrafine grains in regions 1 and 2 was ~250±60 nm. The misorientation profile (Fig. 5.27) measured along line CD suggests that the elongated grains were bounded with low angle grain boundaries.

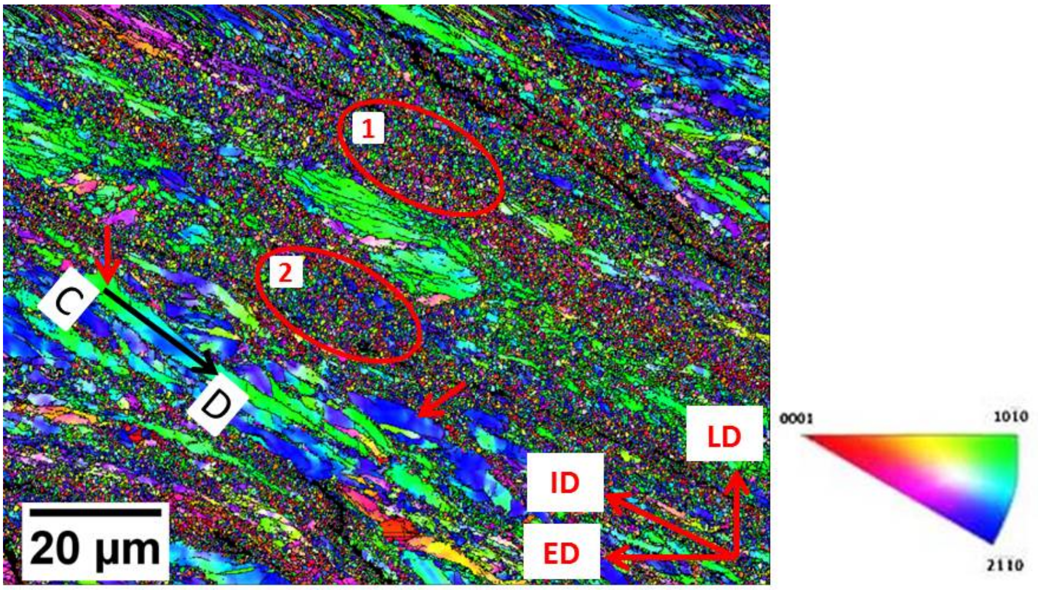

Fig. 5. 26 EBSD orientation map showing the microstructure of the recycled Ti-6Al-4V by single-pass ECAP at 550 °C with a back-pressure of 250 MPa.

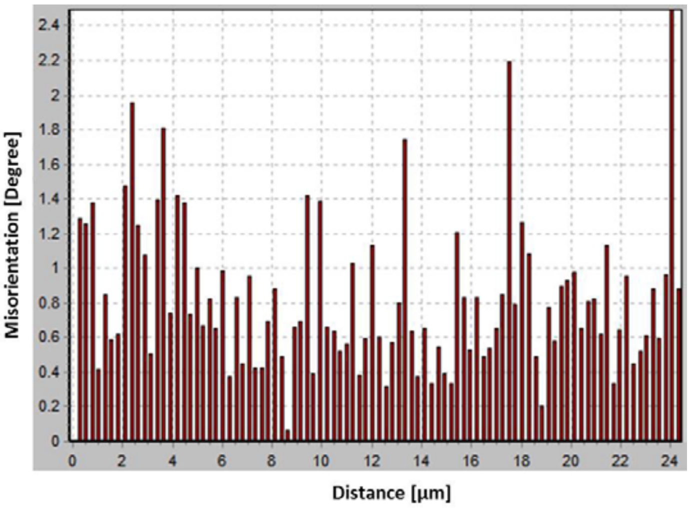

Fig. 5. 27 Misorientation profile measured along line CD in Fig. 5.26.

TEM examination of the sample processed at 550 °C revealed a relatively coarse and heterogeneous microstructure (Fig. 5.28). The grain size of the α phase fell into a wider range. Majority of the α grain diameter was ~300 nm (Fig. 5.28(a)), which is consistent with the EBSD results. In addition, some extra-large α grains with diameter of ~600 nm were observed (Fig. 5.28(b)). The grain growth also occurred in β phase: an individual β grain (V content of ~26.17 wt.%) with a diameter of ~100 nm is marked by the circle in Fig. 5.29.

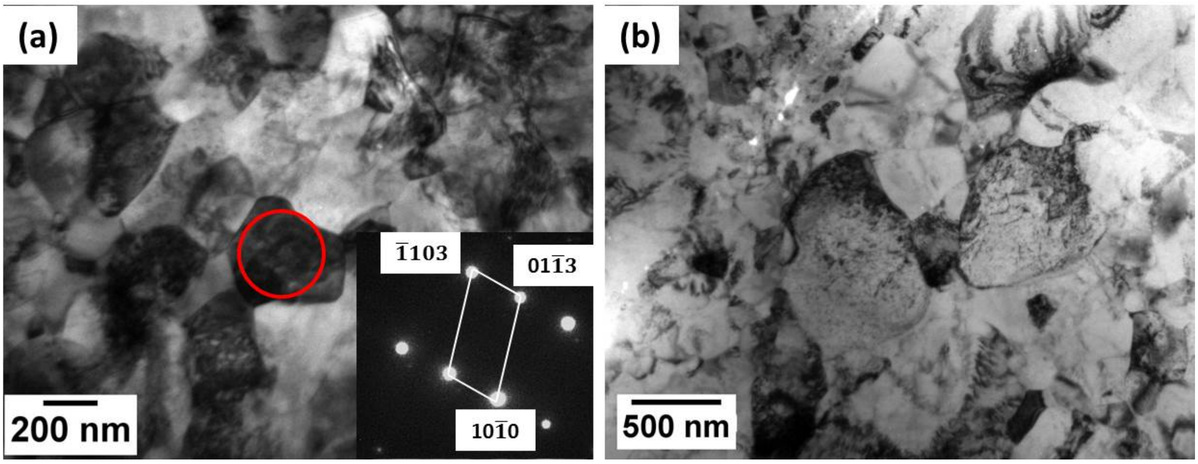

Fig. 5. 28 TEM micrographs showing (a) equiaxed grains of ~300 nm and (b) extra-large grains of ~600 nm within the sample pressed at 550 °C with a back-pressure of 250 MPa for a single pass.

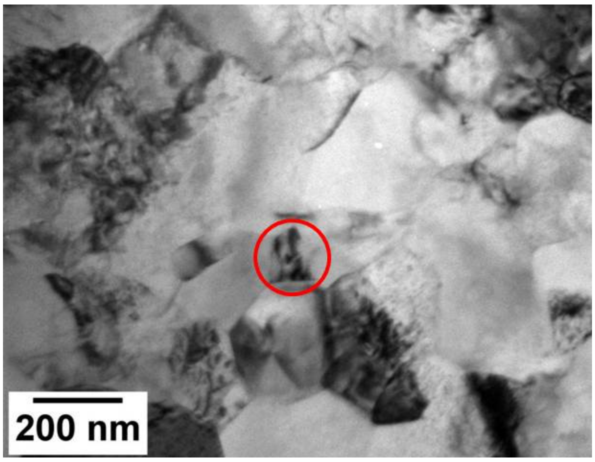

Fig. 5. 29 TEM microstructure in the sample pressed at 550 °C showing an equiaxed β grain of ~100 nm in diameter.

Fig. 5.30 represents the TEM bright field image and corresponding SAD pattern of the chip boundaries within the sample pressed at 550 °C. It was noted that a high oxygen content was present at the interface, the quantitative EDS results are summarised in Table 5.2. The continuous ring pattern suggests that the interface region comprised nano-crystalline grains. Compared to the SAD pattern in Fig. 5.24, two smallest rings are distinctive as shown in Fig. 5.30, which are contributed by titanium oxides. The most possible compound is TiO_2 as it is the most stable oxide [107]. After careful measurements, the two rings closest to the central spot are likely to be associated with the plane sets of (110) and (101) in tetragonal TiO_2. Further work is required to confirm the type of oxides.

The appearances of oxide layers along the chip/chip boundaries or particles dispersed within the matrix were reported in previous research concerning solid state recycling of metallic chips [189] [190] [157]. As suggested in [157], the existence of oxide layers on machining chip surfaces is believed to be introduced during the machining process because of the substantial heat generation at the chip/tool interface. However, in the current study, the oxide layer at the chip boundary was only detected in the sample processed at 550 °C. As reported in [191], the thickness of the native oxide layer on titanium alloys is less than 5 nm. Thus, it is plausible that the oxide layer in the samples pressed at 500 °C was too thin to be detected due to the resolution limitation of the machine. The present result implies that further oxidation might occur on the chip/chip interface when the sample was heated up with the mould. The oxide layer may be broken up into particles due to the severe deformation. The oxide dispersion strengthening (ODS) was reported to be partly responsible for the enhanced mechanical properties [108] [189] [190]. Further experimental study will be described in Section 5.6.

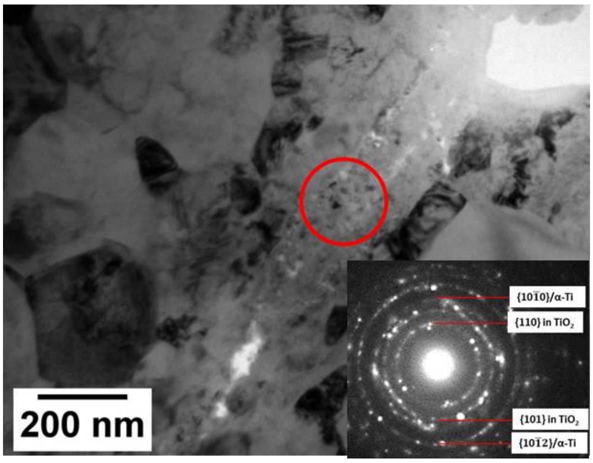

Fig. 5. 30 TEM micrograph and the corresponding SAD pattern showing chip-chip interface in the sample processed at 550 °C possessing both nano-crystalline microstructure and titanium oxides.

Table 5. 2 Weight percentage of the chemical elements detected by EDS analysis at the chip-chip interface of the specimen processed at 550 °C.

Element	Ti	Al	V	O
Concentration (wt.%)	58.5	5.7	2.6	33.2

In some area along the chip interface instead of nano-crystalline microstructure, well-defined and grown grains were observed (Fig. 5.31(a)). Fig. 5.31(b) and (c) show that the corresponding SAD patterns of the two contiguous α grains with zone axes of $\langle 2\bar{1}\bar{1}0 \rangle$ and $\langle 01\bar{1}1 \rangle$, respectively.

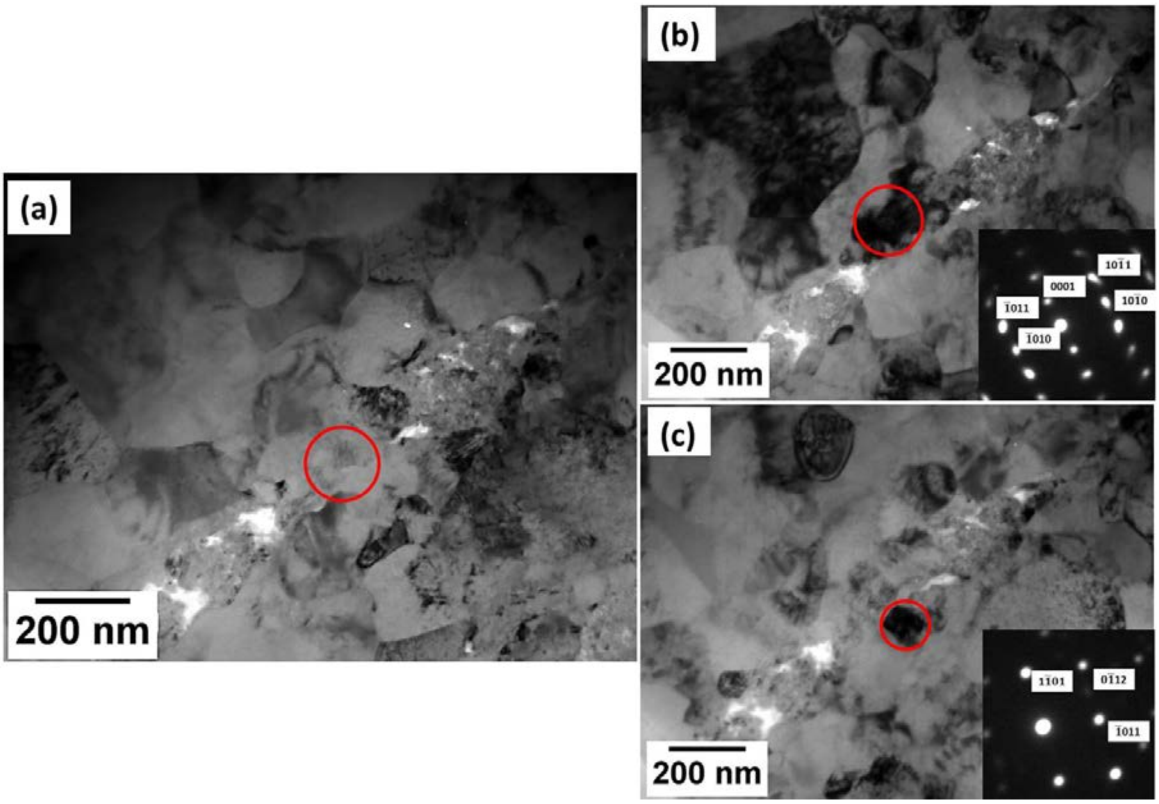

Fig. 5. 31 TEM micrograph showing (a) the interface consisting of well-defined grains with zone axes of (b) $\langle \mathbf{2\bar{1}\bar{1}0} \rangle$ *and (c)* $\langle \mathbf{01\bar{1}1} \rangle$*.*

Fig. 5.32 shows the bright field image of dislocations under two beam conditions using the reflection of $\vec{g} = [0002]$. Because the dislocations (marked by arrows) are visible in this reflection condition, based on the invisibility criterion of $\vec{g} \cdot \vec{B} = 0$, the dislocations must be non-basal $\langle \vec{a} + \vec{c} \rangle$ type with Burgers vector of $\frac{1}{3}[11\bar{2}3]$. Similar results have been reported in the research on Mg alloys [192] [193]. The plausible explanation is that the critical resolved shear stress (CRSS) for non-basal slip systems reduces with increasing temperature. Moreover, a relative high back-pressure was applied in the ECAP process. As the increasing back-pressure, the plastic deformation zone at the intersection of two channels tends towards narrowing [181] [194], making the ECAP process close to the simple shear model. This can aggravate the deformation heating during ECAP [195], resulting in the reduced CRSS for non-basal slip. This observation provides direct evidence for the assumption of texture evolution, which will be discussed in Section 5.5.

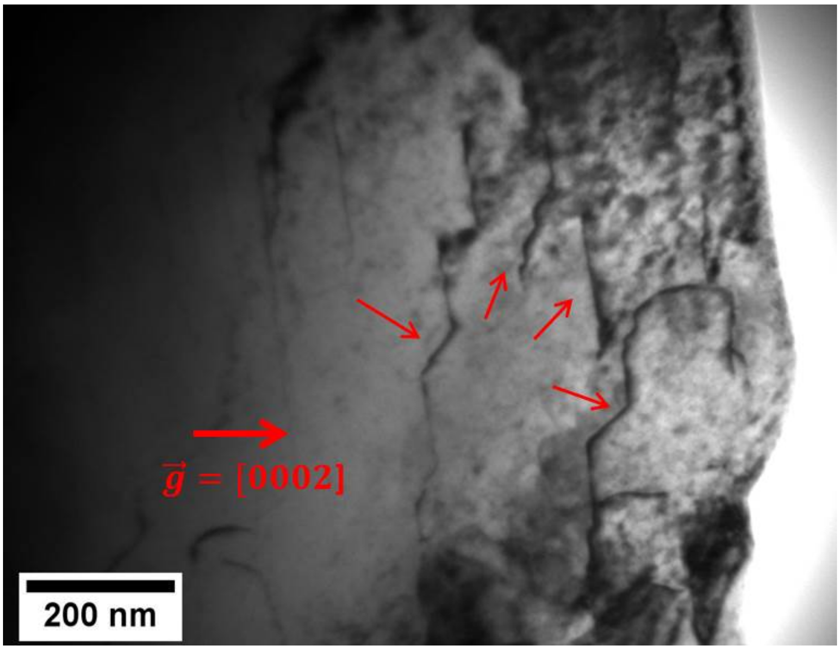

Fig. 5. 32 TEM iamges of dislocations in the sample processed at 550 °C with a back-pressure of 250 MPa after one pass, under two beam conditions using diffraction vector $\vec{g} = [\mathbf{0002}]$

5.5 Crystallographic Texture of Recycled Ti-6Al-4V

Due to the low symmetry of HCP crystal structure, the mechanical properties of α titanium or α phase in bi-phase titanium alloys are highly depended on crystallographic texture; i.e. the mechanical anisotropic. The ECAP process can induce a strong level of texture into HCP materials, including magnesium alloys [196] [197], zirconium [198] and pure titanium [142]. Because of the limited ductility of Ti-6Al-4V, only a few reports have focused on the texture evolution of Ti-6Al-4V during ECAP [152] [186]. In the present work, in order to determine the crystallographic texture of the recycled Ti-6Al-4V, unless otherwise stated, the flow plane, i.e. LD-ED plane, of specimens were examined by high-resolution electron backscatter diffraction (EBSD), with scan step size of 0.2 µm. The orientation of the as-pressed specimen and the coordinate system used for the pole figure construction are plotted in Fig. 5.33(a) and (b), respectively.

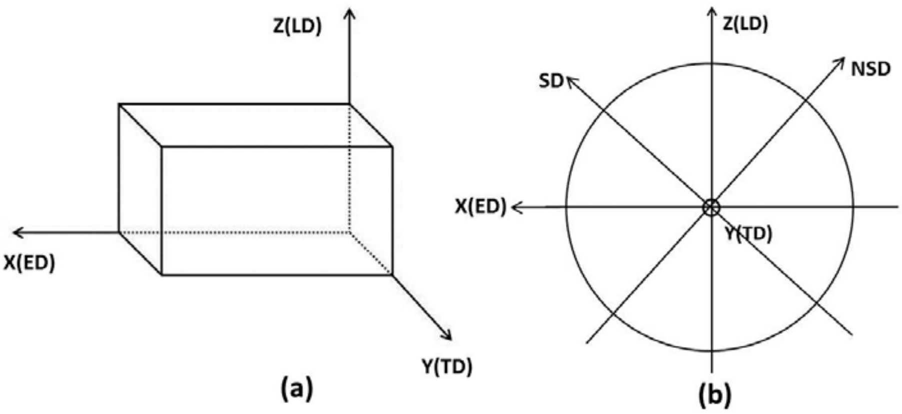

Fig. 5. 33 (a) The co-ordinate system of pressed specimen: the ED, LD and TD denote the extrusion direction, longitudinal direction and transverse direction, respectively; (b) the reference system used in the pole figures: the SD and NSD represent the shear direction and the normal to shear direction, respectively.

For the convenience of discussion, the ideal fibres for HCP materials subjected to ECAP are shown in Fig. 5.34 [148]. It is noteworthy that the ideal fibre map is obtained from pure magnesium with **c/a** ratio of 1.624.

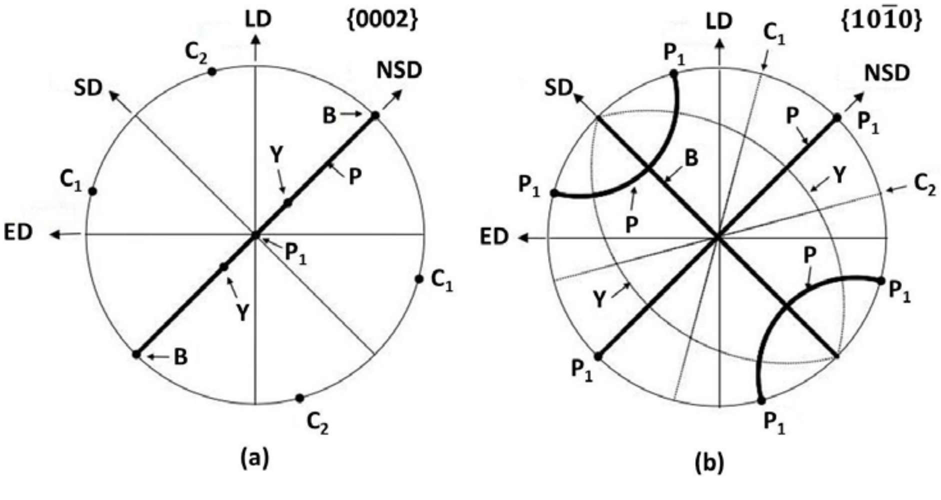

Fig. 5. 34 The ideal fibres of pure Mg after ECAP (modified from **[148]***).*

After the first pass, as shown in Fig. 5.35, it can be seen that the 0002 pole was tilted towards the normal to the inclination direction (NID), making an angle of ~21° with the longitudinal direction (LD). The maximum intensity is ~10.85 in the multiple of uniform density (MUD). Optical microscopy examination of the single-pass sample indicates that the chips aligned with an inclination angle with respect to the ED of ~21° (Fig. 5.36). This suggests that the basal plane was almost aligned with the inclination direction of ECAP and the orientation of HCP crystal with respect to the reference coordinate system is sketched in Fig. 5.37. Comparing with the ideal fibres, it is apparent that the texture here is dominated by the B fibre. This texture feature has been also observed in ECAPed bulk Ti-6Al-4V samples [152] [153] and many other HCP materials [148] [199] [200] [201], although there are slight deviations of the inclination angle.

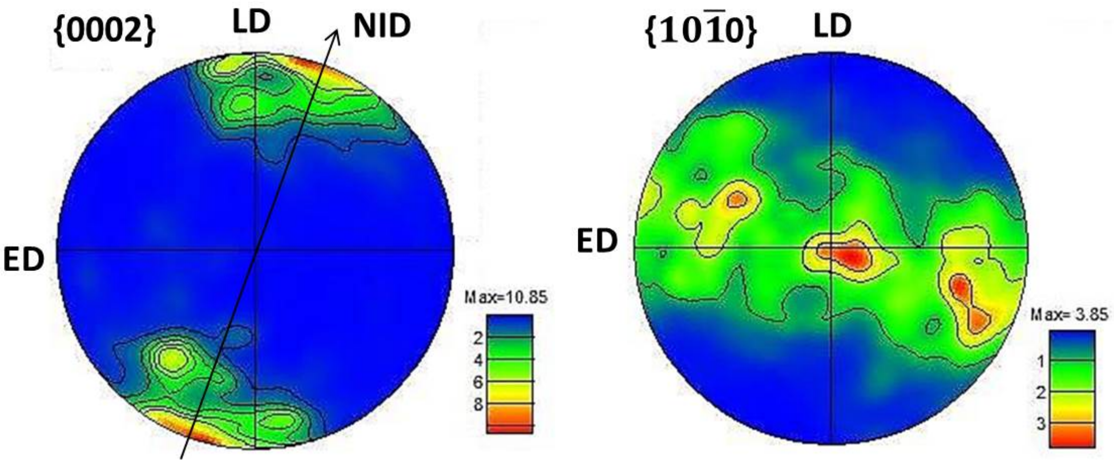

Fig. 5. 35 0002 and $\mathbf{10\bar{1}0}$ *contour pole figures of the specimen after one pass at 500 °C with a back-pressure of 100 MPa.*

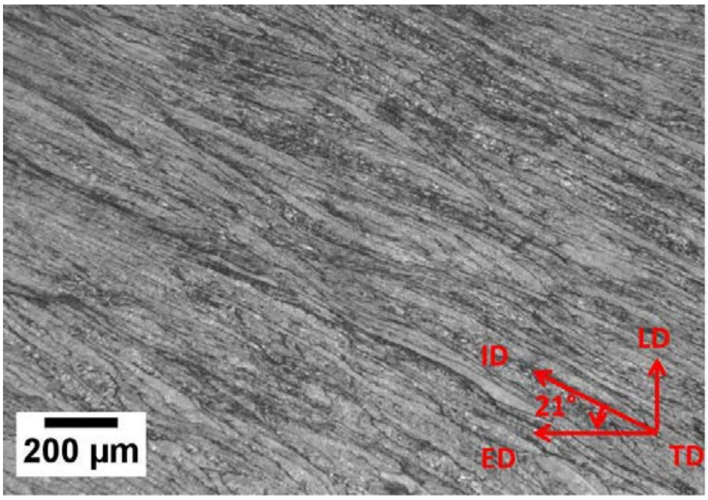

Fig. 5. 36 Optical micrograph showing the recycled Ti-6Al-4V chips after the first pass are orientated at the shear angle of ~21° to the ED.

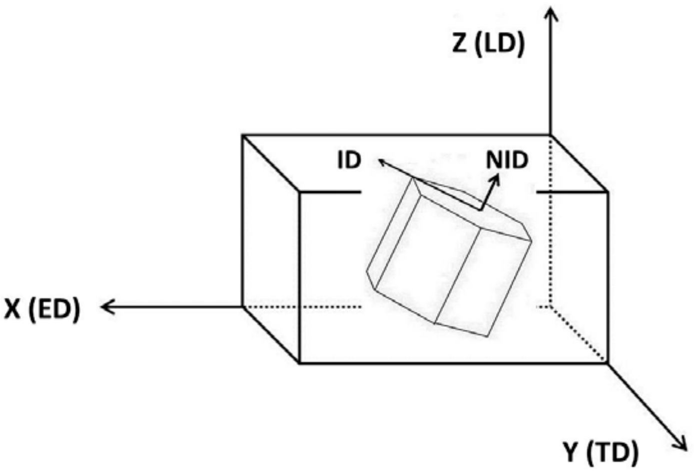

Fig. 5. 37 Schematic of the representative α-Ti crystal showing the crystal orientation with respect to the reference coordinate system after one pass at 500 °C with a back-pressure of 100 MPa.

Fig. 5.38 shows the textures before and after the second pass. Since in route B_c the sample was rotated around its ED by 90° in the same direction after each pass, the input pole figure (Fig. 5.38(a)) prior to the second pass can be deduced from the first-pass pole figure by denoting the 'TD' as the new 'LD'. It is clear that in 0002 pole figure, a single orientation peak is close the TD but with an angle of ~21° away from the TD. After the second pass, it can be seen that the resultant texture exhibits three strong peaks in the pole figure, as plotted in Fig. 5.38(b): peak 1 is ~17° away from the TD; peak 2 is comparatively weaker; peak 3 is formed ~6° away from the LD.

The texture component in peak 1 is likely to inherit from the first pass and was moved further toward the TD after the second pass. Peak 3 is attributed to the basal planes rotated along the inclination direction due to the imposed stress. Peak 2 is formed by the basal planes which did not rotate enough [149]. Comparing the texture of ECAPed pure Ti measured by XRD [143] [149], only peak 1 and 2 were observed in the previous researches. The appearance of peak 3 implies that for ECAP recycled Ti-6Al-4V it is easier to form basal texture normal to the ECAP inclination direction compared to bulk pure Ti. The shearing pattern in 2-pass ECAP via route B_c is depicted in Fig. 5.39.

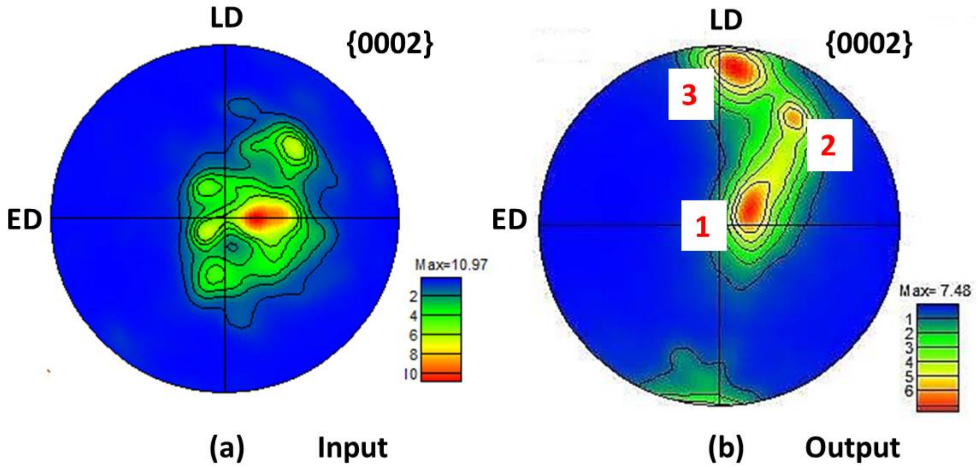

(a) Input

(b) Output

Fig. 5. 38 *Texture evolution in the second pass occurred in the sample processed at 500 °C: (a) input texture and (b) output texture.*

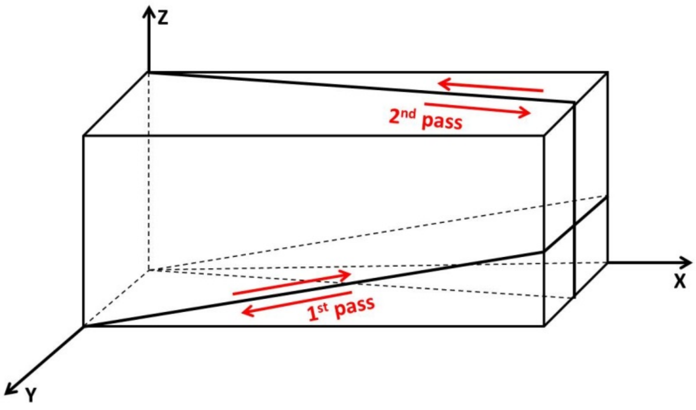

Fig. 5. 39 Shearing pattern occurring in the first and second ECAP passes via route B_c, following **[142]**.

Fig. 5.40 shows that the texture after 4 passes is in line with the P fibre. It can be seen that the most intensive peak of basal poles is inclined at ~40° to the TD (peak 4). Comparing 0002 and $10\bar{1}0$ pole figures to the ideal orientation map (Fig. 5.34), it is plausible that the spread of peak 4 in Fig. 5.40(a) is P_1 texture component, but has moved away from the ideal position. As shown in Fig. 5.41, it is observed that the texture after 8 passes is still dominated with the P fibre with a much narrower spread than those after 4 passes. The strongest texture, P_1 (peak 5) was found to be rotated back towards the TD and close to the ideal position. It can be concluded that the increase in number of passes can sharpen the fibre texture.

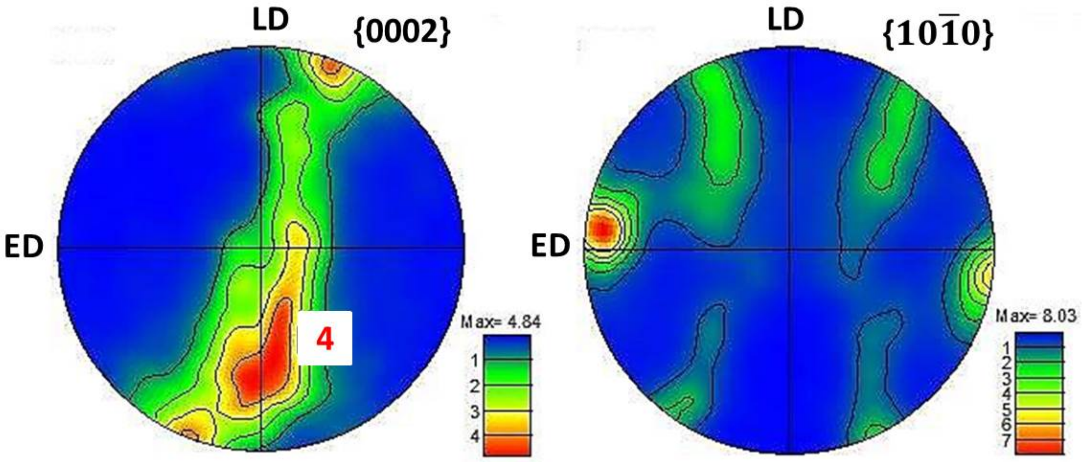

Fig. 5. 40 Pole figures of the sample pressed at 500 °C with a back-pressure of 100 MPa for 4 passes.

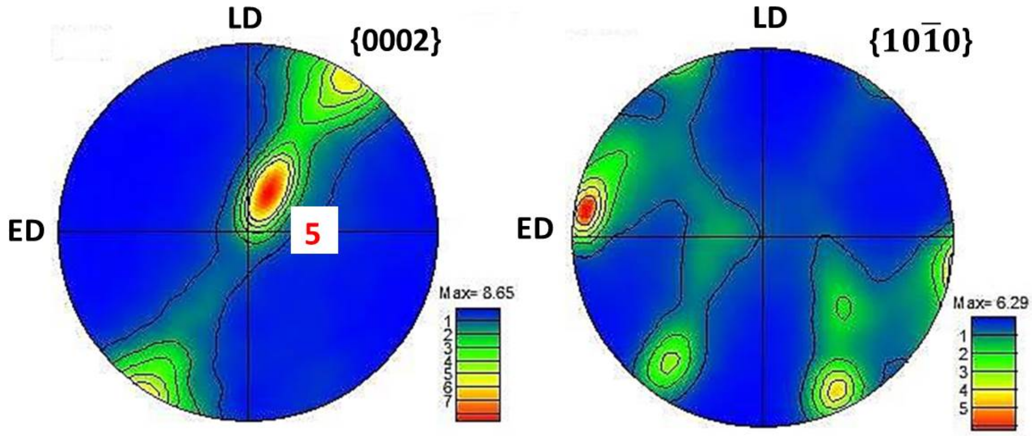

Fig. 5. 41 Pole figures of the sample pressed at 500 °C with a back-pressure of 100 MPa for 8 passes.

As the machining chips before ECAP were compacted as briquetting, the initial texture is regarded as random. The strong texture after the first pass as shown in Fig. 5.35 is mainly attributed to basal slip activity during ECAP, because basal slip {0001}<11$\bar{2}$0> is the dominant deformation system in Ti-6Al-4V subjected to moderate-temperature ECAP [153]. Although prismatic slip {10$\bar{1}$0}<11$\bar{2}$0> is usually considered as the easiest deformation mode to be activated in α-Ti, the alloying elements like Al suppress its activity [202]. Furthermore, the CRSS of basal slip reduced faster than prismatic slip with increasing temperature [152] [203]. As predicted in [143] [152], the relative activity of basal slip is much higher than other deformation systems.

The most significant feature of the texture evolution after multiple passes is the strongest basal poles orientated towards the TD with the simultaneous appearance of two centrosymmetric peaks located in line with the NID. This resembles the texture evolution of ECAPed pure Ti at 400 °C [143], although they only performed the ECAP experiments and simulations up to three passes and ignore the activity of twining in the simulation. It is known that the deformation in HCP materials is usually accommodated by combination of slip and twinning mechanisms. As reported in ECAPed pure Ti samples at 350 °C [204], twinning is the main deformation mechanism during the first pass. Nevertheless, as demonstrated by Agnew *et al.* [205], alloying has a significant influence on the activate slip and twinning. The alloying elements like Al usually suppress the occurrence of twinning in Ti alloy [24] [17]. Moreover, significant grain refinement occurs in the subsequent passes, and the increasement of CRSS for twinning arisen from grain refinement is much larger than that for dislocation slip [204]. Therefore, no twinning activity was observed in the present study and the simulation result ignoring twinning can be used in the case of ECAPed Ti-6Al-4V [143]. The only observation of twinning in ECAPed Ti-6Al-4V was reported by Yapici *et al*. [152], in which Ti-6Al-4V was pressed at 800 °C using route A. Thus, the plastic deformation during the ECAP is expected to be majorly accommodated by dislocation slips.

This texture evolution also implies that the recycled products have anisotropic mechanical properties. The intensive basal texture is usually line up with the direction possessing the highest strength [149]. Thus, it can be predicted that the recycled samples after 4 and 8 passes have the maximum strength along the TD, followed by the LD, and the strength in the ED might be the weakest.

In order to investigate the effect of back-pressure on the texture, the specimen processed at 500 °C with a higher back-pressure level of 250 MPa after a single pass was examined. The corresponding 0002 and $10\bar{1}0$ pole figures, which are deduced from the orientation map in Fig. 5.16, are shown in Fig. 5.42. Comparing to the ideal orientation in Fig. 5.34, prominent B and P fibres seem to appear. In contrast with the single-pass recycled Ti-6Al-4V using a lower back-pressure of 100 MPa (Fig. 5.35), the orientation peak has rotated towards the LD. This may be because of the activation of new non-basal slip systems initiated by the increased back-pressure. The plausible reason is that the shear heating aggravated by the higher applied back-pressure reduces the CRSS of non-basal slip (it has been mentioned in Section 5.4.2). In addition, it can be noticed that the texture has a larger spread and the maximum intensity is lower (~7.35 MUD) than that pressed sample with a back-pressure of 100 MPa (~10.85 MUD). This result contradicts with the previous literatures: it has reported that increasing back-press leads to narrowing the plastic deformation zone [181] [194], and hence stronger texture [206] [207]. The possible explanation to this phenomenon is that the aggravated shear heating due to the increased back-pressure facilitates dynamic recrystallization, and the recrystallized grains are likely to be randomly orientated. According to the previous research [127] [208] [209] [210], the abrupt increase in the temperature at the ECAP shearing plane can reach up to 40~85 K. The estimation of recrystallization fraction using Aztec EBSD microanalysis software confirms this assumption: the area fraction of recrystallization in the scanned area is ~7.95, which is higher than that for the specimen associated with a back-pressure of 100 MPa (~2.74%).

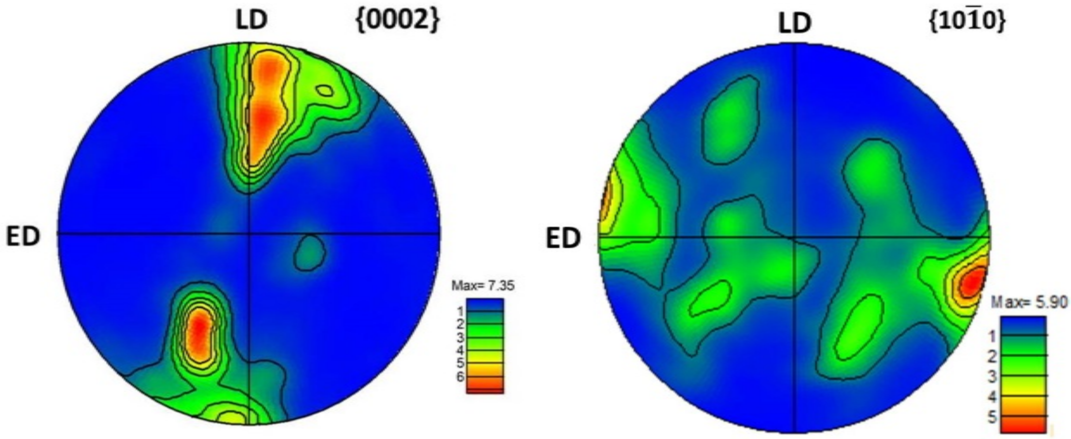

Fig. 5. 42 0002 contour pole figure of the specimen after one pass at 500 °C with a back-pressure of 250 MPa.

Fig. 5.43 shows 0002 pole figure of the sample pressed at higher temperature of 550 °C and keeping back-pressure of 250 MPa. It can be seen that the basal poles are aggregated on the LD. This is because except higher shear heating occurs at higher applied back-pressure, the CRSS for non-basal slip systems reduces with the increase in the operating temperature. As discussed in Section 5.4.2, Fig. 5.32 provides evidence showing the occurrence of non-basal slip dislocations. According to the software estimation, the fraction of recrystallization is ~21.6%, as a result of which larger spread and lower intensity of texture was observed.

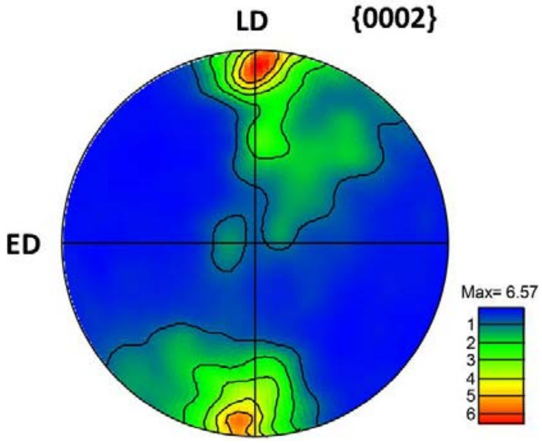

Fig. 5. 43 0002 contour pole figure of the specimen after one pass at 550 °C with a back-pressure of 250 MPa.

5.6 Microhardness and Homogeneity of Recycled Ti-6Al-4V

In order to reveal the homogeneity of the recycled product, hardness distribution throughout the flow plane was measured. Hardness contour maps of samples processed at 500 °C with a back-pressure of 100 MPa after 1, 4 and 8 passes are shown in Fig. 5.44(a) to (c), respectively, where the X and Z axes correspond to the normal of the transverse and longitudinal planes.

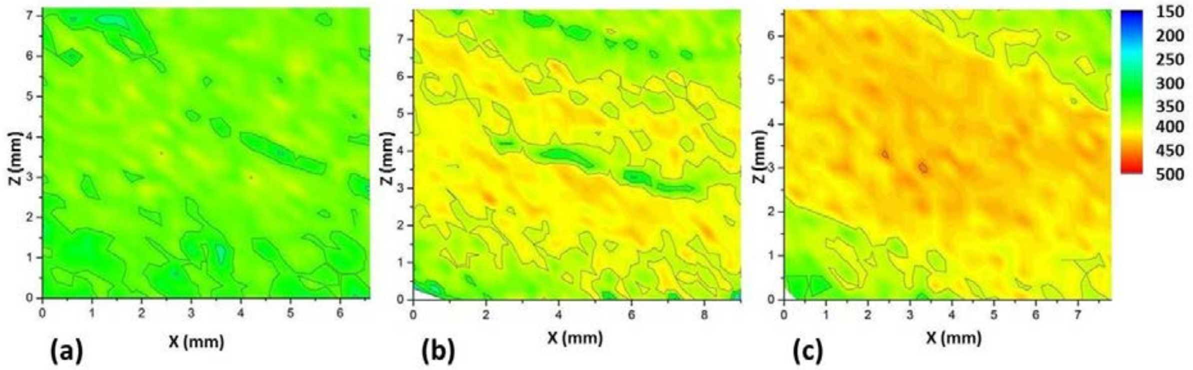

Fig. 5. 44 Microhardness distribution presented by colour-coded contour maps over the flow plane of chip-based recycled Ti-6Al-4V at 500 °C with a back-pressure of 100 MPa for (a) a single pass, (b) 4 passes and (c) 8 passes.

The sample processed after one pass (Fig. 5.44(a)) shows higher degree of heterogeneity: higher hardness at the centre region and lower values adjacent to the bottom surface. This result is consistent with finite element analyses [120] [211] [121] and other experimental investigations on aluminium [212] [123]. According to the finite element analysis [120], homogeneous shear deformation only occurs in the ECAP channel with a relief angle (ψ) of 0° and an intersection angle (φ) of 90°. As the relief angle increases, the effective shear strain at the bottom part of the specimen becomes lower than that at the upper part, and hence lower hardness values. In practice, the heterogeneity of hardness values occurs even when the relief angle is 0° due to the occurrence of a dead zone [184] and the friction between the sample and the channel walls [212]. In the current study, the relief angle of the channel is ~36°, which leads to lower hardness in the bottom part of the sample.

Both uniformity and hardness were enhanced after multiple passes, as shown in Fig. 5.44(b) and (c). Similar improvement in homogeneity with respect to ECAP passes has also been found in pure Al [212]. The optical micrograph in Fig. 5.45(a) shows that the single-pass ECAPed sample has more big pores at the bottom region, especially at triple junctions of the chips (marked by the arrows), and a higher magnification micrograph (Fig. 5.45(b)) reveals that there is no mechanical interlocking between chips at the bottom part of the sample. These observations imply that materials at the bottom part have experienced insufficient shear deformation after a single ECAP pass. After 4 passes, because the sample has been rotated by route B_C, all edges have been subjected to sufficient shear deformation. Strong interlocking between chips is shown in Fig. 5.45(c) and (d) and marked by the ovals. The homogeneity of the recycled product therefore has been improved by using multiple passes using Bc route.

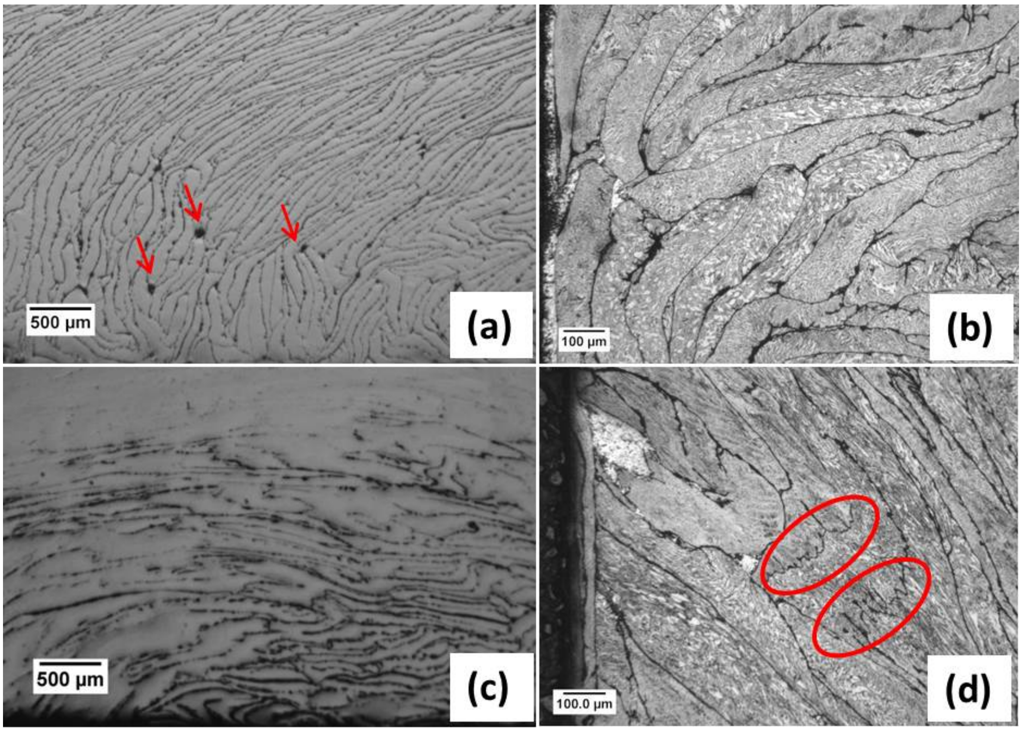

Fig. 5. 45 Optical micrographs of the chips adjacent to the bottom edge in the samples processed at 500 °C with a back-pressure of 100 MPa: (a) and (b) via a single pass; (c) and (d) via 4 passes.

The average hardness of the samples processed at 500 °C with a back-pressure of 100 MPa are plotted as a function of number of passes, as shown in Fig. 5.46. The figure shows that the hardness increases after the ECAP process. In comparison to the original Ti-6Al-4V (number of pass = 0) before machining, the hardness increased tremendously from 301HV to 359 HV (~19%) after the first pass and further increase to 415HV after 8 passes, the increment slowdown in the subsequent passes. Materials such as Al [213], Cu [214], Ti [215] and AM30 Mg alloy [216] have shown similar trends in terms of hardness increment: the hardness of the samples undergoing multiple-pass ECAP were significantly enhanced after the first pass, and tend to saturate after certain number of passes. None or less hardness increment after certain number of passes is due to the saturation of the dislocation density and the ultimate equilibrium grain size has been reached at high strains. Nevertheless, the continuous increase in hardness with imposed shear strain up to 8 passes or more was observed in some alloys, for example Al-6061 [184] and Al-3%Mg alloy [217]. It is because the dislocation mobility is hindered by alloying elements and hence the grain recovery, thus, more ECAP passes are required to establish a homogeneous microstructure. The trend in Fig. 5.46 implies the existing of non-equilibrium microstructure in Ti-6Al-4V after 4 passes, therefore, further increase in number of passes will increase the hardness of the recycled sample to the ultimate hardness.

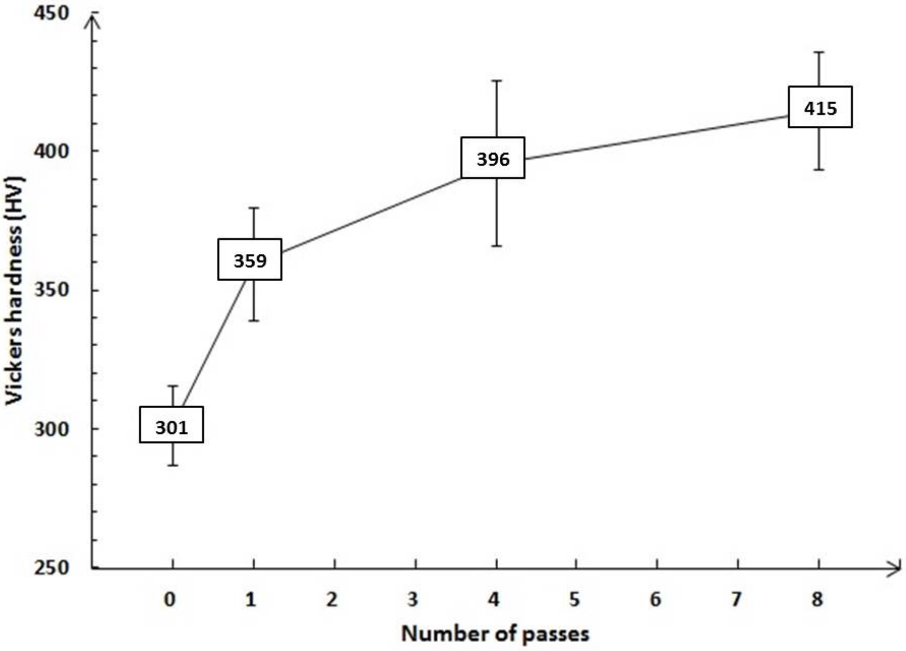

Fig. 5. 46 The average values of Vickers hardness as a function of number of passes.

In order to evaluate the effect of the imposed back-pressures, the colour-coded hardness maps of the samples undergoing a single pass at 500 °C with back-pressures of 100 MPa, 150 MPa and 200 MPa are shown in Fig. 5.47(a)-(c), respectively. The sample processed with a relatively high back-pressure still contained a region of lower hardness along the bottom edge. The extent of the hardness homogeneity across the flow plane is directly expressed by the histograms illustrated in Fig. 5.48. It is evident that the widths of the histograms for back-pressures of 150 MPa and 200 MPa are larger than that for the back-pressure of 100 MPa. This result can be elucidated by the finite element analysis modelling for strain hardening materials (1100Al alloy) [139]. As the back-pressure increased, the equivalent plastic strain in the vicinity of bottom surface increased and approached to that in the central part of the sample, until a certain value of the plastic strain has been reached, e.g.100 MPa for 1100Al. Thereafter further increases of the back-pressure led to the rapid increment of the equivalent plastic strain at the bottom, and hence worse homogeneity due to the widening of PDZ [139]. The effect of back-pressure on the equivalent plastic strain distribution from top to bottom for 1100Al alloy is shown in Fig. 5.49. This implies that although the presence of back-pressures can facilitate to decrease the dead zone and narrow the PDZ, it may aggravate the heterogeneity beyond the optimum back pressure. It is supposed that the applied back-pressures of 150 MPa and 200 MPa might have exceeded the optimum value for Ti-6Al-4V recycled at 500 °C, and hence worse homogeneity. As for the average hardness, despite the increase in back-pressure values, it remains essentially unchanged: 365$\pm$37 H_V1 and 365$\pm$32 H_V1 for the samples with back-pressures of 150 MPa and 200 MPa, respectively.

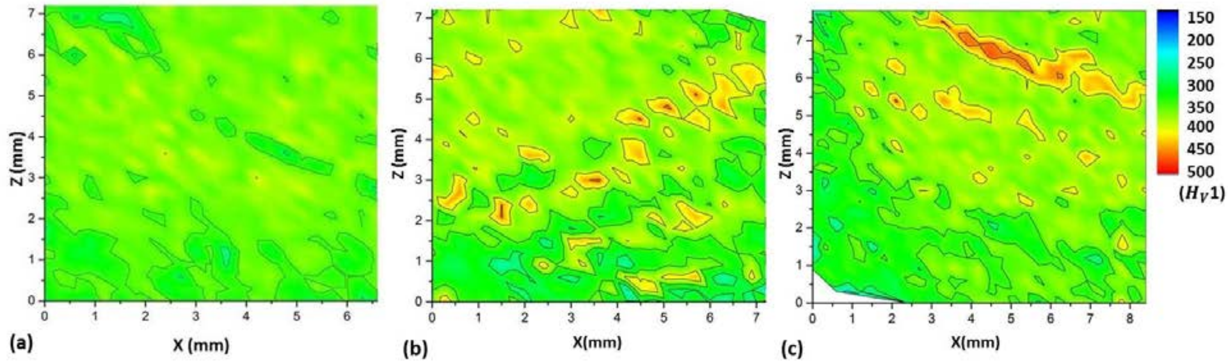

Fig. 5. 47 Colour-coded contour maps showing the hardness distribution for the samples after a single pass at 500 °C with back-pressures of (a) 100 MPa, (b)150 MPa and (c) 200 MPa.

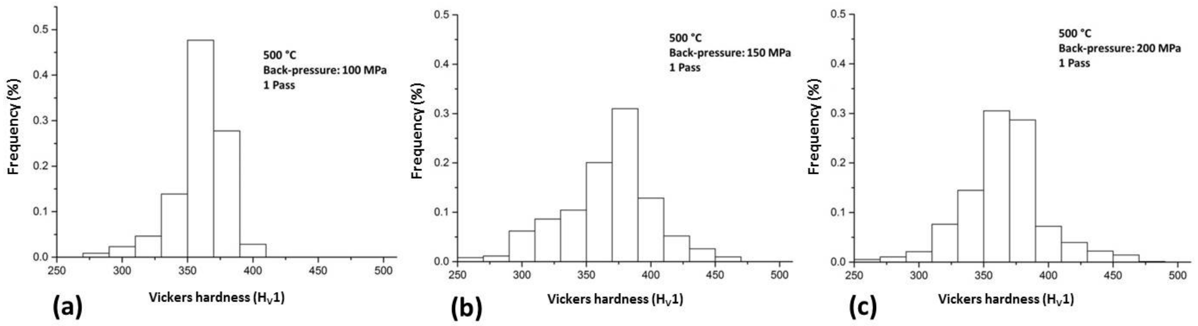

Fig. 5. 48 Histograms showing the number fractions of hardness measured for the samples processed at 500 °C for single pass with back-pressures of (a) 100 MPa, (b) 150 MPa and (c) 200 MPa.

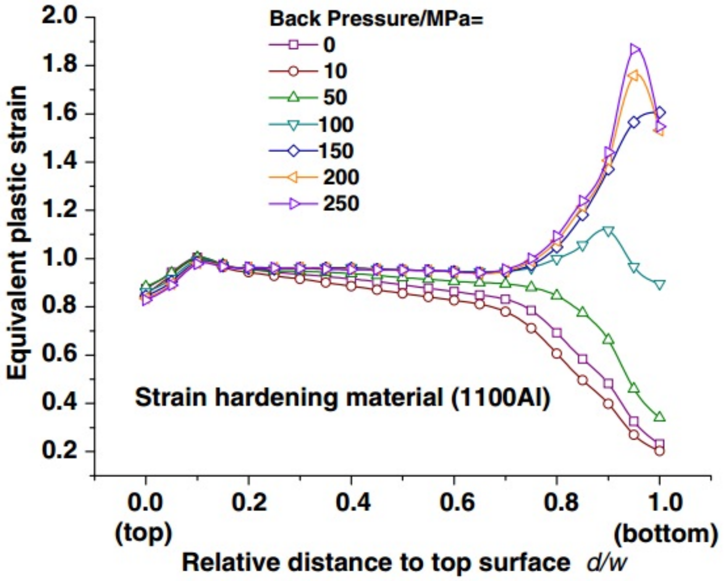

Fig. 5. 49 The effect of back-pressure on the equivalent plastic strain distribution from the top surface to bottom for a strain hardening material (1100Al alloy) **[139]**.

The microhardness histograms of the samples ECAPed at 500 °C and 550 °C using the same back-pressure of 250 MPa are plotted in Fig. 5.50(a) and (b), respectively. The red lines indicate the average hardness values. It is noticed that the degree of scattering for these two diagrams is almost identical; nonetheless, the sample pressed at 550 °C possessed a slightly higher average hardness (384±21 HV against 359±14 HV). The hardness measurement seems to be contrary to the Hall Petch relation. According to the Hall-Petch relationship, the polycrystalline materials usually can be strengthened via grain refinement. As described in Section 5.4.2, the sample processed at 550 °C has relatively coarse and heterogeneous grains with size of ~300-600 nm, while the microstructure in the sample pressed at 500 °C consists of equiaxed and elongated grains with size of ~70 – 100 nm. One plausible explanation is that the sample processed at higher temperature was enhanced because of the more effective ODS mechanism. Luo *et al*. [108] has modified the Hall-Petch relationship in consideration of the strengthening contribution from oxide dispersive strengthening (ODS). According to their calculation, the maximum enhanced strength by the dispersive TiO_2 particles with the average diameter of ~20 nm was ~29 MPa, which was only adopted as a fluctuating value. Another possible reason is that besides the nano-sized grains, the sample processed at 500 °C also contains micrometre scale lamellar structure with width of ~300 – 500 nm, as shown in Fig. 5.18, which weakens the grain refinement effect.

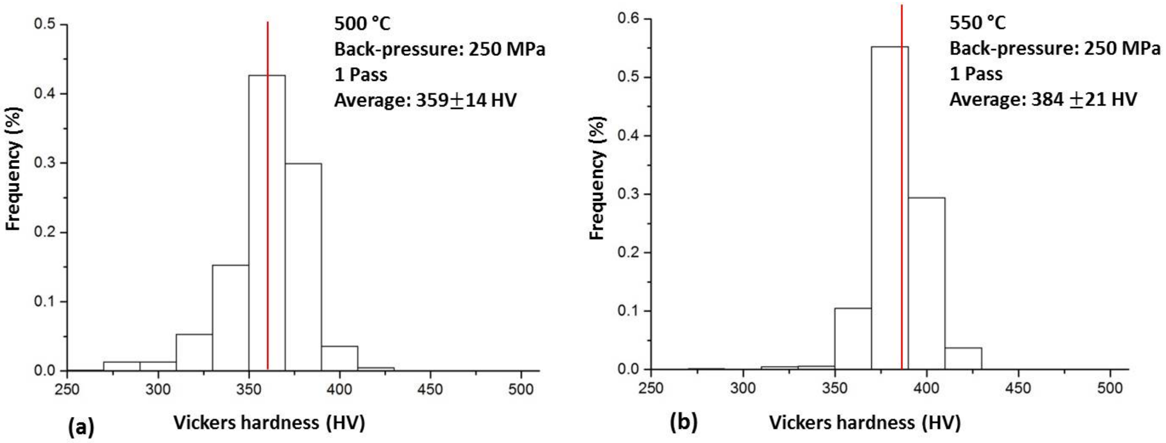

Fig. 5. 50 The histograms of the samples after the single pressing with a back-pressure of 250 MPa at (a) 500 °C and (b) 550 °C.

5.7 Effect of Post Heat Treatment on the Recycled Ti-6Al-4V

Since the considerable stress is imposed in the sample during ECAP process, a post heat treatment for stress relief has been carried out in an argon atmosphere furnace.

5.7.1 Annealing at 500 °C for 24 hours

The sample recycled at 500 °C using a back-pressure of 250 MPa for a single pass was annealed at 500 °C for 24 hours. The SEM micrograph in Fig. 5.51 reveals that the chip boundaries cannot be eliminated during such relatively low temperature annealing.

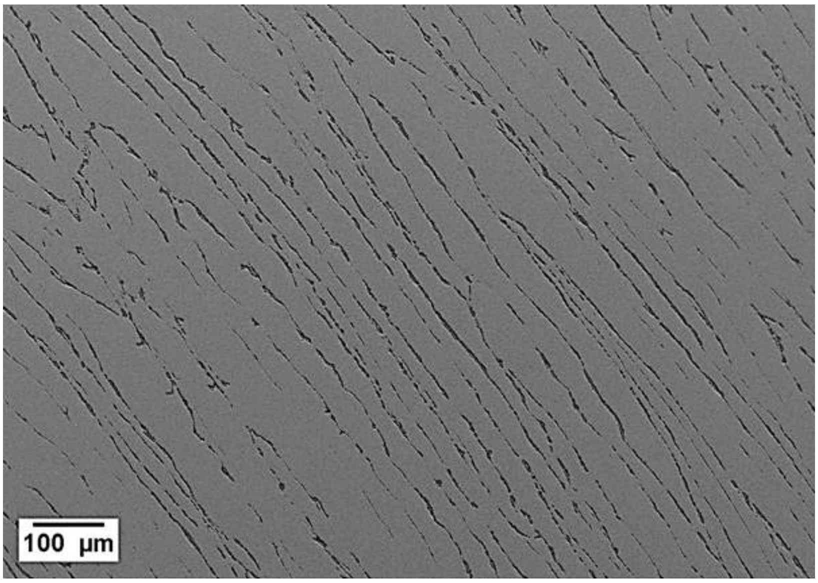

Fig. 5. 51 *SEM micrograph of the sample (Temperature: 500 °C, Back-pressure: 250 MPa, Number of passes: 1 pass) annealed at 500 °C for 24 hours.*

The EBSD orientation map, as shown in Fig. 5.52(a), indicates that the lamellar microstructures are aligned with the inclination direction. Fig. 5.52(b) suggests that the recrystallization fraction after 500 °C heat treatment for 24 hours only slightly increased to ~5.8% (~2.74% in the as-ECAPed sample). Fig. 5.53 represents the 0002 and $10\bar{1}0$ pole figures constructed from the scanned area. Compared to the pole figure before heat treatment (Fig. 5.35), it is apparent that the basal pole peak is split into two peaks: One is still almost aligned with the NID, same as the as-ECAPed sample; the other stronger peak is observed ~30° away. Additionally, the $10\bar{1}0$ pole figure exhibits three separate peaks although the intensity is relatively low. Similar observation was reported in [192] [193]. Splitting of the basal pole peak strongly implies the activation of a different deformation mechanism in the sample [205], although there is no direct evidence observed in the TEM examination.

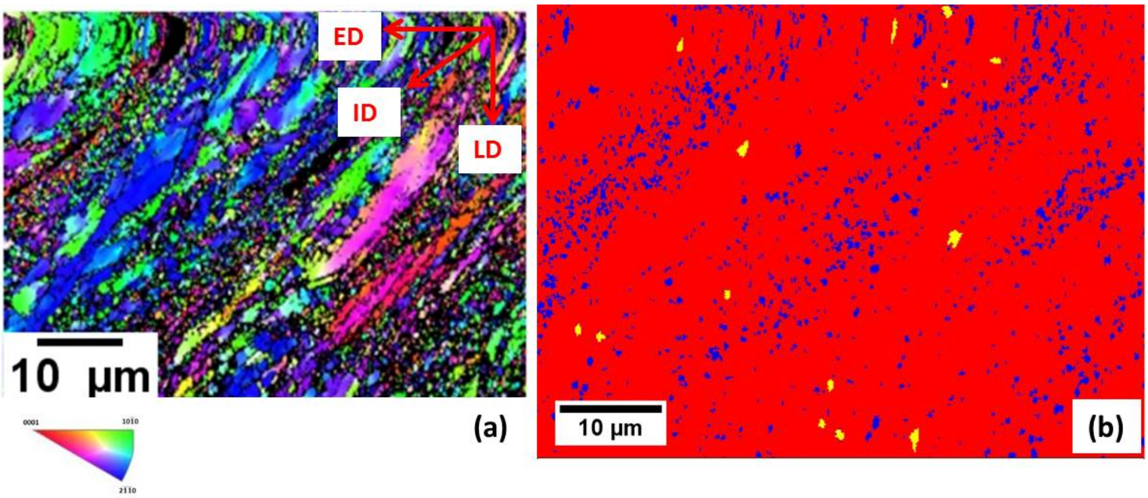

Fig. 5. 52 (a) SEM microstructure and (b) recrystallization map of the sample (Temperature: 500 °C, Back-pressure: 250 MPa, Number of passes: 1 pass) annealed at 500 °C for 24 hours.

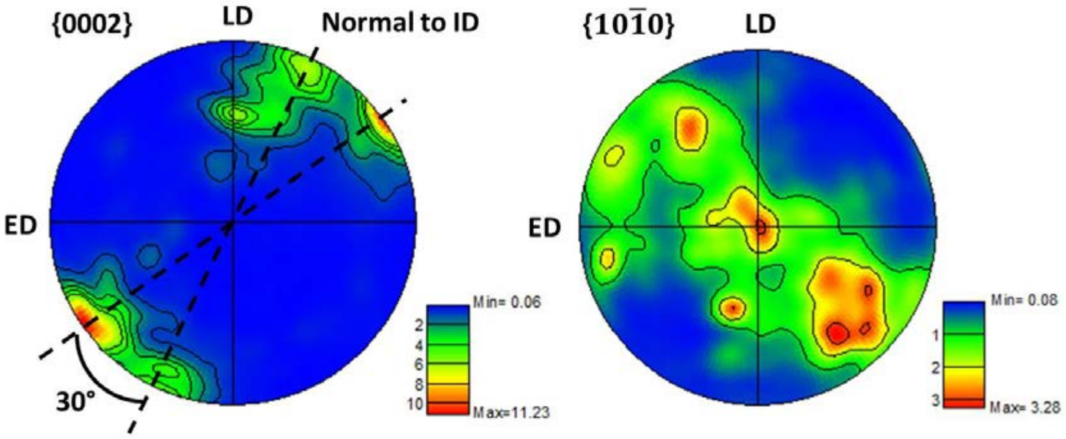

Fig. 5. 53 (0001) pole figure for the sample annealed at 500 °C for 24 hours.

5.7.2 Annealing at 700 °C for 2 hours

Fig. 5.54(a) shows the SEM microstructure of the sample (operating temperature: 500 °C, back-pressure: 100 MPa, number of passes: 1 pass) heat treated at 700 °C for 2 hours. In some areas, the lamellar structures remained; while in some other regions, recrystallization occurs and new equiaxed grains formed. At higher magnification, as shown in Fig. 5.54(b), coarsened β phase was observed to locate at the triple junction of the equiaxed α grains. Fig. 5.54(b) also reveals that most of the chip boundaries had been eliminated during the heat treatment, although only a few pores were still retained, as indicated by the red arrows. At elevated temperature, recrystallization and grain growth occur and accelerate the chip boundary dissolution. In comparison with the observation in the earlier research [157], the lower temperature (700 °C against 900 °C) and the relative shorter annealing time (2 hours against 20 hours) in the current study preserved the fine α phase but failed to completely eliminate the boundaries.

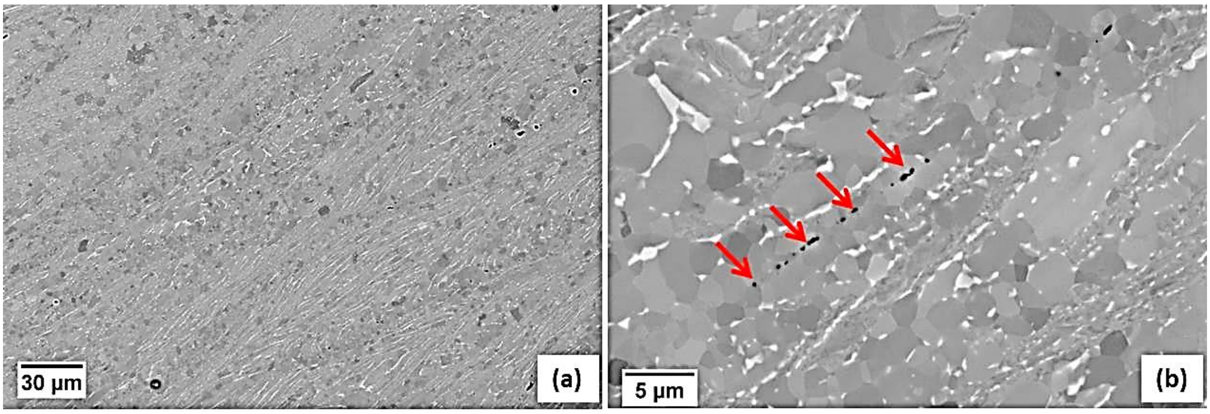

Fig. 5. 54 (a) Low magnification and (b) high magnification of backscatter electron micrographs of recycled Ti-6Al-4V (Temperature: 500 °C, Back-pressure: 100 MPa, Number of passes: 1 pass) heat-treated for 2 hours at 700 °C.

Fig. 5.55(a) shows the EBSD orientation map of the annealed sample. It is found the EBSD indexing rate after heat treatment increased up to almost 100%. The correlated misorientation distribution along line AB, as shown in Fig. 5.55(b), manifests that the grains are dominantly bounded by high angle grain boundaries.

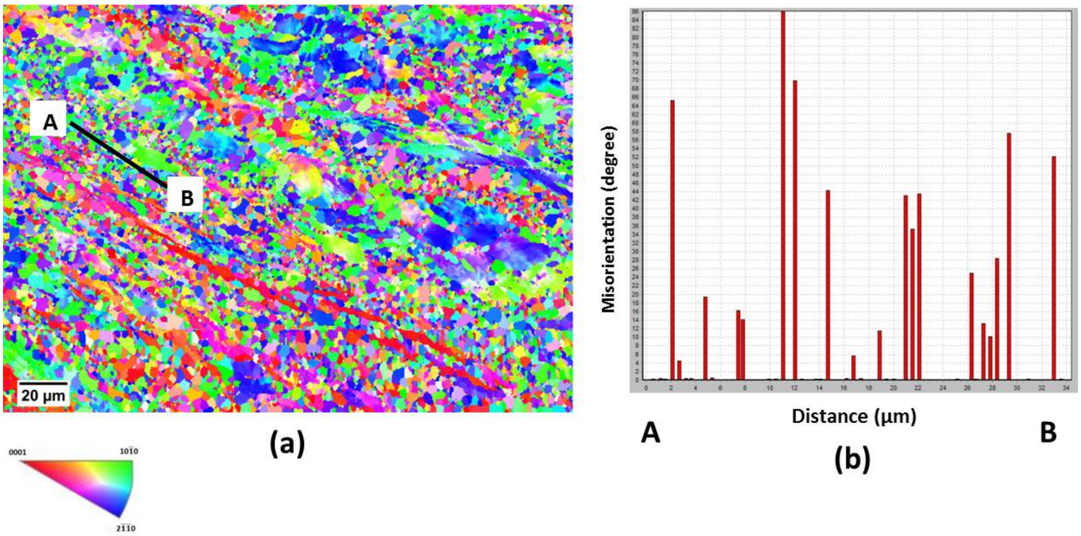

Fig. 5. 55 (a) EBSD orientation map and (b) misorientation profile along line AB in the sample annealed at 700 °C for 2 hours.

With assistance of Aztec EBSD microanalysis software, the area fraction of recrystallized grains (blue) in the same area in Fig. 5.55 was estimated, ~58.1%, but only ~37.7% deformed region (red) was retained after the heat treatment, as illustrated in Fig. 5.56. The sample is partially recrystallized when annealed at 700 °C for 2 hours.

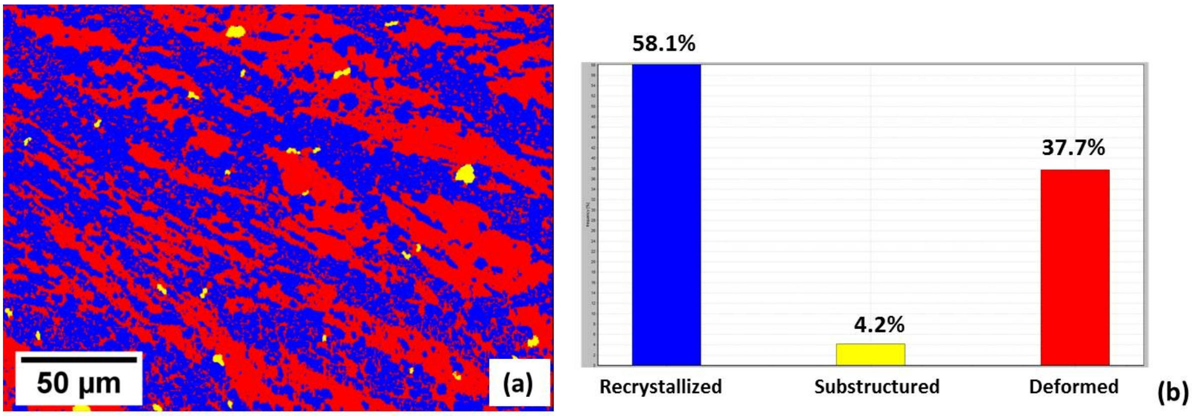

Fig. 5. 56 (a) Recrystallized grain distribution map (blue denotes recrystallized and red means deformed) and (b) the histogram of recrystallization fraction in the recycled sample annealed at 700 °C for 2 hours.

TEM micrographs in Fig. 5.57(a) to (d) reveal several features of the partially recrystallized microstructure. Fig. 5.57(a) shows the retained lamellar structure with an average width of ~250 nm, and Fig. 5.57(b) provides the direct evidence of recrystallized equiaxed grains with average size of ~1.5 μm (Region A) co-existing with deformed fine grains (Region B). The grain at the triple junction of the equiaxed grains (marked as the red oval) was found to have a relatively high V content (~19.54 wt.%), i.e. β phase. These observations are in good agreement with the SEM results (Fig. 5.54). Fig. 5.57(c) suggests that the equiaxed grains exhibited a relatively low dislocation density due to the dislocation annihilation during the heat treatment.

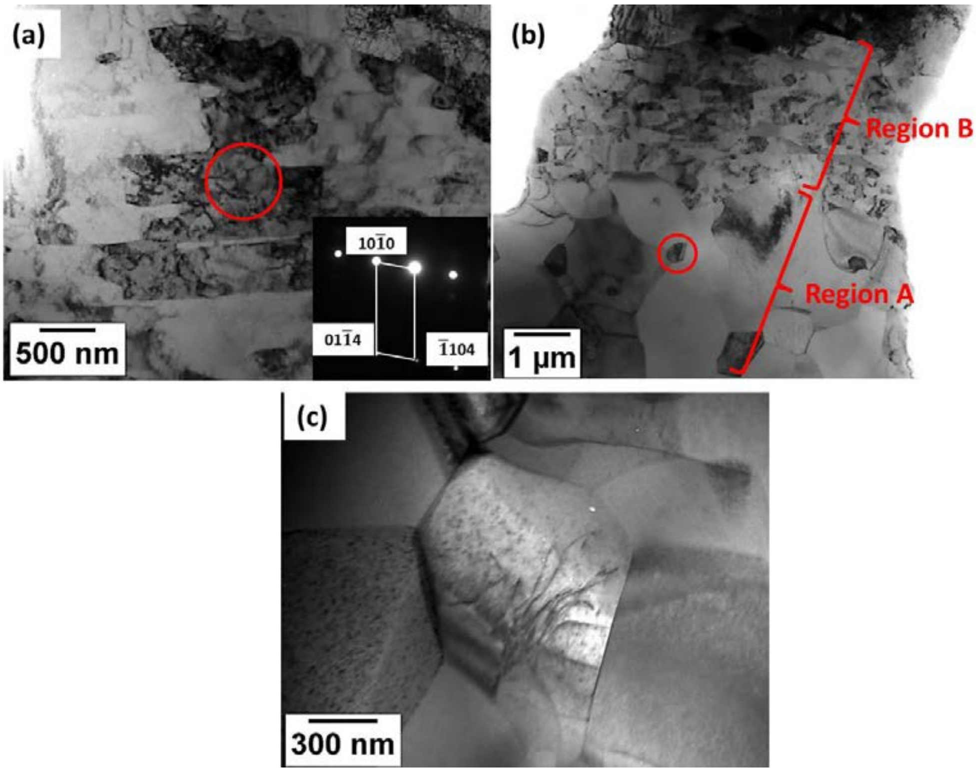

Fig. 5. 57 TEM micrographs of recycled Ti-6Al-4V annealed at 700 °C for 2 hours showing (a) lamellar structures, (b) recrystallized grains (Region A) accompanying with refined microstructure (Region B), (c) low dislocation density in the recrystallized grain and (d) extinction contours in the vicinity of the grain boundaries.

Fig. 5.58(a) shows the 0002 contouring pole figure deduced from the EBSD orientation map (Fig. 5.55). It can be seen that the main orientation of grains is essentially identical with that prior to heat treatment (Fig. 5.35). Nevertheless, larger spread is observed compared to the as-recycled sample. That can be attributed to the recrystallized grains. The scattering pole figure in Fig. 5.58(b) reveals each contribution of deformed grains and recrystallized grains (the blue spots represent recrystallized grains and the red spots denote the deformed grains).It is evident that the recrystallized grains have wider spread than deformed ones.

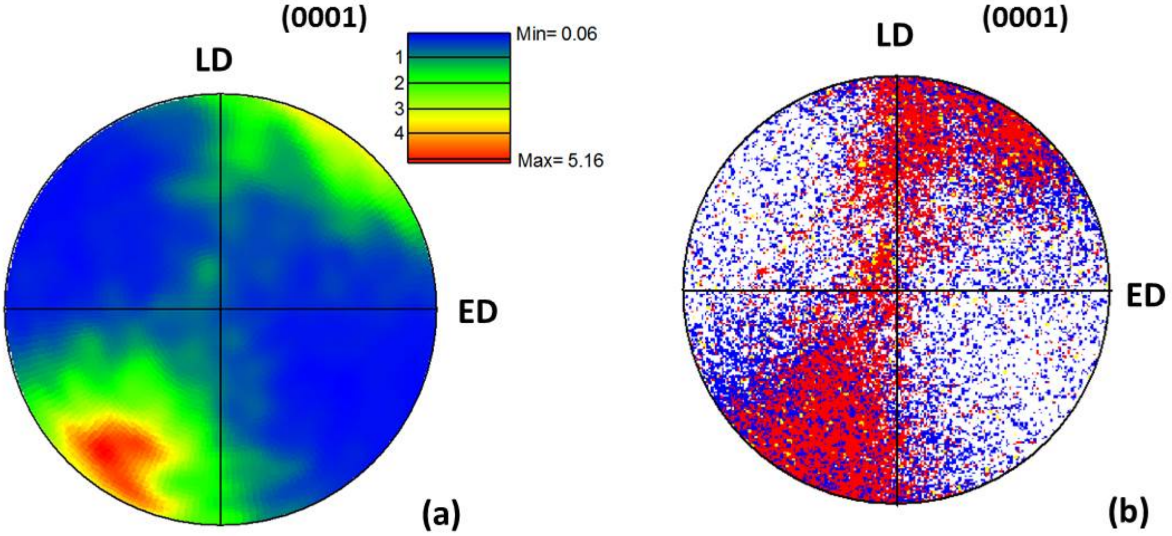

Fig. 5. 58 (a) Contouring and (b) scattering pole figures for the sample annealing at 700 °C for 2 hours.

The microhardness of the recycled Ti-6Al-4V before and after heat treatment was compared in Fig. 5.59. Similar hardness value is found after annealing. This is contradict to the literature [157], reporting that hardness reduced following heat treatment at 700°C for 1 and 20 hours. The explanation for this discrepancy is based on the fact that the result in the previous study [157] was measured at the sample processed for 4 passes, thus the consequent hardness reached ~420 HV. The hardness reduced from ~420 HV to ~370 HV because of the static restoration process during heat treatment, such as recovery and recrystallization. However, in the present experiment, the single-pass sample was used. After a single pass, not much stored energy was in the sample and hence less driving force during recrystallization. Further research is required in order to figure out the effect of post heat treatment on the Vickers hardness.

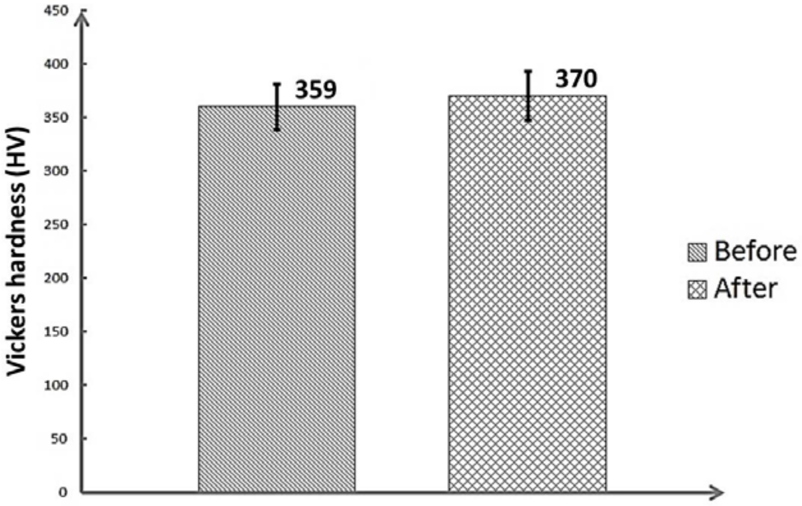

Fig. 5. 59 The comparison of microhardness before and after the heat treatment at 700 °C for 2 hours.

5.8 Summary

In this Chapter, Ti-6Al-4V recycled from machining chips using back-pressure assisted equal channel angular pressing (BP-ECAP) were examined. The results presented in this Chapter reveal the effects of processing parameters, including operating temperature, back-pressure and number of passes, on the properties of recycled products, such as macroscopic consolidation, relative density, microstructure and crystallographic texture evolution, and microhardness homogeneity. In addition, post heat treatment was carried out for stress relief.

It was found that in the current investigation, in order to obtain recycled Ti-6Al-4V products without major cracks, the lowest operating temperature is 500 °C and the minimum back-pressure required is 100 MPa, below which the generation and propagation of major cracks along the shear direction of ECAP cannot be avoided. In particular, applying higher back-pressure has a remarkable effect on suppressing the cracking formation. However, the minor cracks on the leading end and top edge seem inevitable even using highest back-pressure (250 MPa) or increasing number of ECAP passes up to 8 times.

The relative density of as-recycled products increased with the applied back-pressure and the number of passes. Near fully dense samples (~99.9%) were obtained through 4 passes with 150 MPa back-pressure and 8 passes with 100 MPa back-pressure. The mechanism behind the chip consolidation involves localised fragmentation and mechanical interlocking.

It was observed that the microstructure of the Ti-6Al-4V recycled at 500 °C after the first pressing was a combination of lamellar structures, equiaxed and elongated α grains. With the subsequent passes, the samples were progressively dominated by ultrafine equiaxed α grains with the ultimate size of ~70 nm. The schematic diagram of the grain refinement is illustrated in Fig. 5.60. The original β phase in the machining chips was fragmented into nano-crystalline grains due to the severe shearing deformation. In addition, the chip/chip boundary region after repetitive pressing consists of nano-crystalline microstructure. When Ti-6Al-4V chips were pressed at 550 °C, the resultant microstructure exhibited coarser and heterogeneous grains. According to the EDS analysis and the corresponding SAD pattern, it suggested that detectable oxide layers existed along the chip-chip interface. TEM analysis provided the direct evidence that $<\vec{a} + \vec{c}>$ slip activity occurred in the sample recycled at 550 °C.

The texture evolution of recycled Ti-6Al-4V was investigated after multiple passes and different temperatures. For ECAP processed at a temperature of 500 °C with a back-pressure of 100 MPa, the sample after the first pass exhibited a strong preferred orientation towards the NID. The further increase of passes to 2, 4 and 8 passes makes the basal poles orientated towards the TD and the NID (with a certain degree of rotation). The increase of the processing temperature by 50 °C resulted in the inclination of basal pole peak to the LD because of the activated non-basal slip system.

Detailed microhardness measurements were taken to determine the average value and the level of homogeneity for the Ti-6Al-4V recycled samples subjected to multiple-pass ECAP. The results show that the single-pass specimens were relatively heterogeneous, and the region adjacent to the bottom surface exhibited lower hardness values. It has been demonstrated that these results are consistent with the finite element modelling in the previous literature. The average hardness values were recorded to increase with the number of passes due to grain refinement. The homogeneity, in particular the lower hardness at the region near the bottom surface, was improved after multiple passes because the shear stress was imposed to all edges during ECAP. As the imposed back-pressure increased, the average hardness and homogeneity remained essentially unchanged. In addition, the sample processed at 550 °C possessed a similar hardness with that processed at 500 °C.

In order to remove the stress introduced during the ECAP process and obtain better texture information, the post heat treatments were carried out. In the sample (operating temperature: 500 °C, back-pressure: 250 MPa, number of passes: 1 pass) annealed at 500 °C for 24 hours, the microstructure was not significantly affected, but the obvious split of 0002 pole peaks was observed. In the sample (operating temperature: 500 °C, back-pressure: 100 MPa, number of passes: 1 pass) heat treated at 700 °C for 2 hours, the recycled sample was partially recrystallized. The equiaxed grains after recrystallization were characterized by low dislocation density and extinction contours along the boundaries. It was demonstrated that the sample after heat treatment had texture similar to that as-ECAPed but with much wider spread.

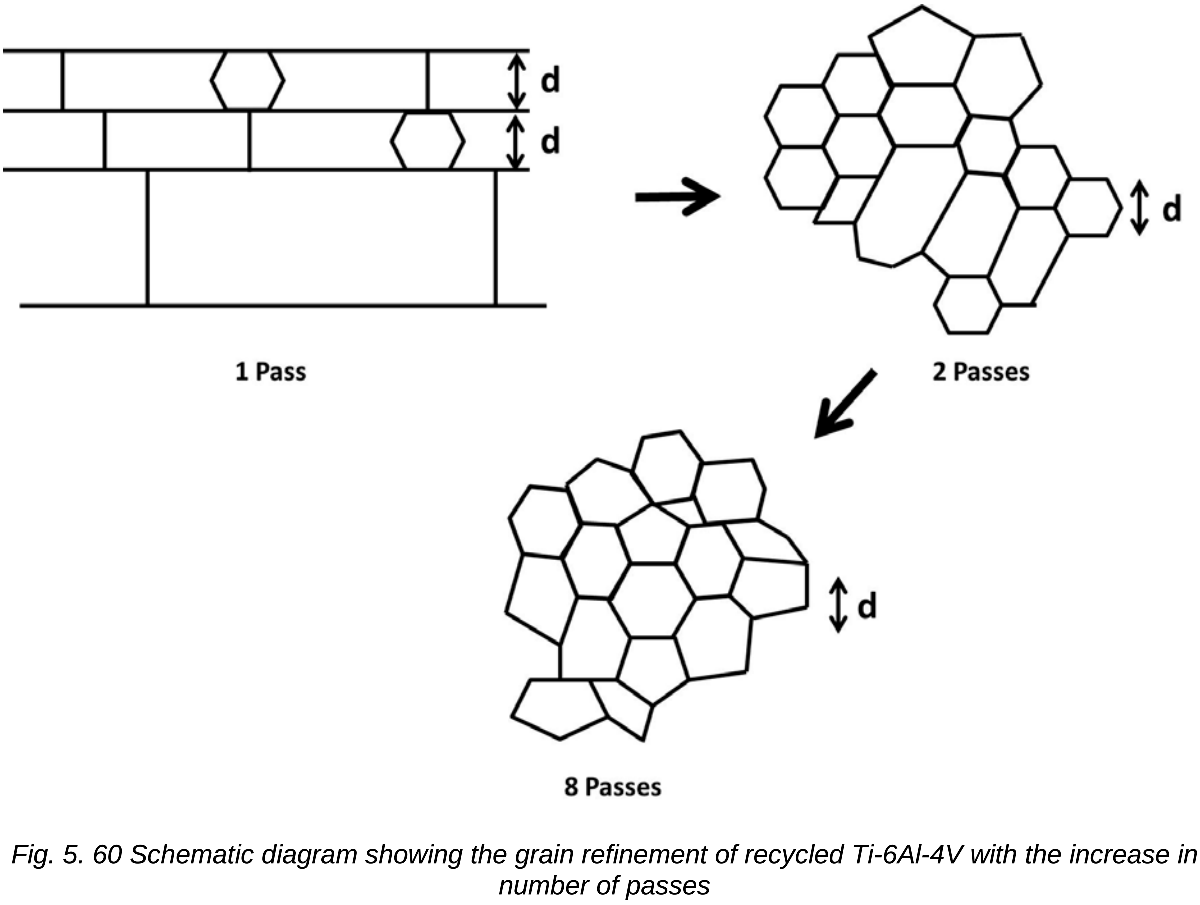

Fig. 5. 60 Schematic diagram showing the grain refinement of recycled Ti-6Al-4V with the increase in number of passes

6. RECYCLING OF β-Ti alloy Ti-15V-3Cr-3Al-3Sn MACHINING CHIPS USING EQUAL CHANNEL ANGULAR PRESSING

Apart from Ti-6Al-4V, recycling experiments were also carried out on Ti-15V-3Cr-3Al-3Sn machining chips. The aim of this chapter is to investigate the feasibility of recycling Ti-15V-3Cr-3Al-3Sn machining chip using ECAP and examine the microstructure and microhardness homogeneity of the recycled samples.

6.1 Introduction

In the present study, the recyclability of Ti-15V-3Cr-3Al-3Sn chips using ECAP is explored, in particular the processing parameters (Section 6.2), relative density measurement (Section 6.3), microstructure evolution (Section 6.4), microhardness homogeneity (Section 6.5) and the effect of post heat treatment (Section 6.6) have been investigated. A summary (Section 6.7) is made at the end of this chapter.

6.2 Influence of the Process Parameters on the Macroscopical Consolidation of Recycled Ti-15V-3Cr-3Al-3Sn

The feasibility of ECAP recycling of Ti-15V-3Cr-3Al-3Sn machining chips at room temperature was conducted without back-pressure. The recycled product exhibited fairly loose as extruded from the exit channel, as shown in Fig. 6.1. In order to optimize the processing parameters for Ti-15V-3Cr-3Al-3Sn recycling, the operating temperature was increased from 300 °C up to 500 °C with 50 °C increment and the imposed back-pressure was set at 50 MPa, 100 MPa and 150 MPa. Furthermore, the effect of multiple passes was examined. Detailed experimental scenarios have been summarised in Table 3.2.

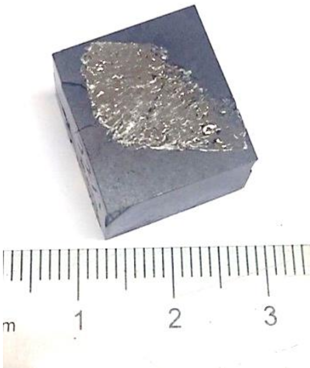

Fig. 6. 1 Ti-15V-3Cr-3Al-3Sn chips pressed at room temperature without back-pressure.

6.2.1 Effect of processing temperature

Fig. 6.2(a) to (d) show the optical macrographs of the single-passed products with a low back-pressure of 50 MPa at 300 °C, 350 °C, 450 °C and 500 °C, respectively. It can be observed that major cracks periodically appeared in the samples processed at the temperature lower than 500 °C, and the cracks emanating from the surface of the sample and aligned with the shear plane of ECAP. An increase in the processing temperature to 500 °C removed the shear cracks in the recycled products (Fig. 6.2(d)). In comparison with Ti-6Al-4V, in which the major shear cracks still remained at 500 °C (Fig. 5.1(d)), the elimination of macrocracks of Ti-15V-3Cr-3Al-3Sn at 500 °C is due to the better deformability.

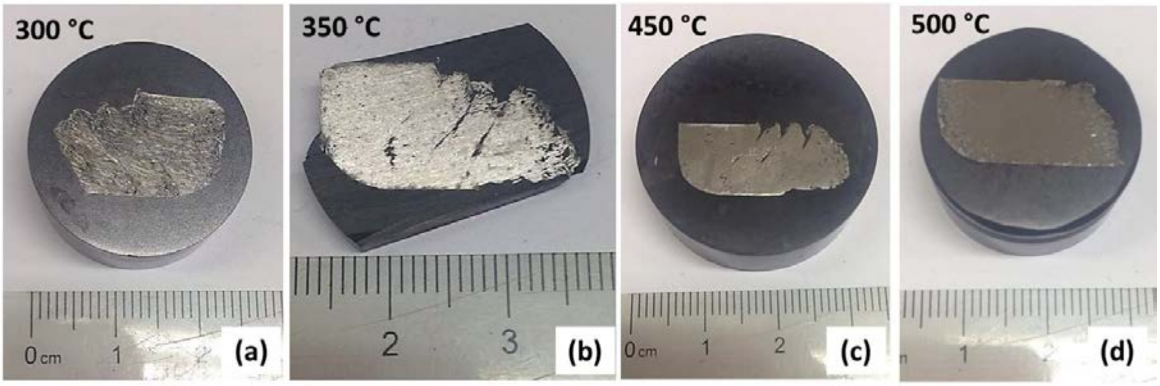

Fig. 6. 2 Optical macrographs of the recycled Ti-15V-3Cr-3Al-3Sn pressed at (a) 300 °C, (b) 350 °C, (c) 400 °C and (d) 500 °C with a back-pressure of 50 MPa after a single ECAP pass.

Optical macrographs of recycled samples processed with a higher back-pressure of 150 MPa at temperatures of 450 °C and 500 °C are shown in Fig. 6.3(a) and (b), respectively. Applying a larger back-pressure facilitates the suppression of the crack formation: compared with Fig. 6.2(c), the number of cracks within the sample pressed at 450 °C (Fig. 6.3(a)) reduces with the increasing back-pressure. On the other hand, it is observed that the major cracks cannot be completely removed below 500 °C even with the aid of a high back-pressure.

In conclusion, in order to eliminate shear cracks, the approved lowest processing temperature is 500 °C in the current experimental conditions.

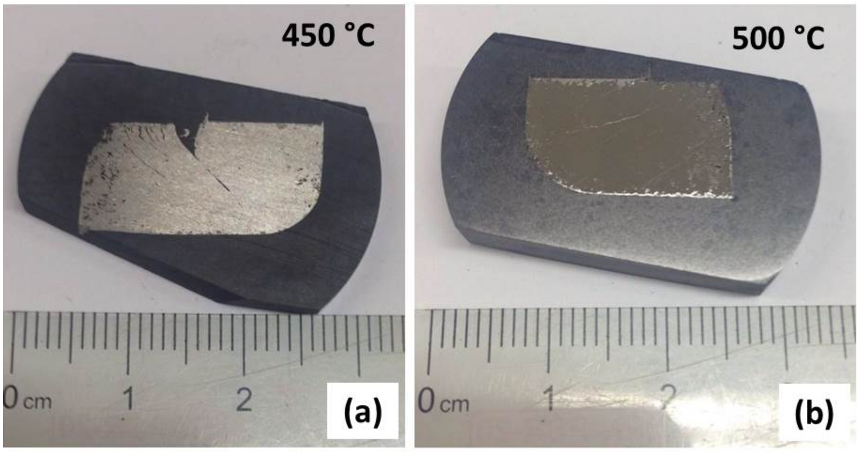

Fig. 6. 3 The appearances of recycled Ti-15V-3Al-3Cr-3V-3Sn samples pressed at (a) 450 °C and (b) 500 °C with a back-pressure of 150 MPa for one ECAP pass.

6.2.2 Effect of imposed back-pressure

In order to understand the role of back-pressure on the recycled product appearances, the ECAPs were conducted at 500 °C with back-pressures of 50, 100 and 150 MPa. Fig. 6.4(a) reveals that large amount of pores (as marked by the oval) remained at the head of the sample pressed using a low back-pressure of 50 MPa. As the back-pressure increased, the residual pores and minor cracks at the head significantly reduced, as shown in Fig. 6.4(b) and (c).

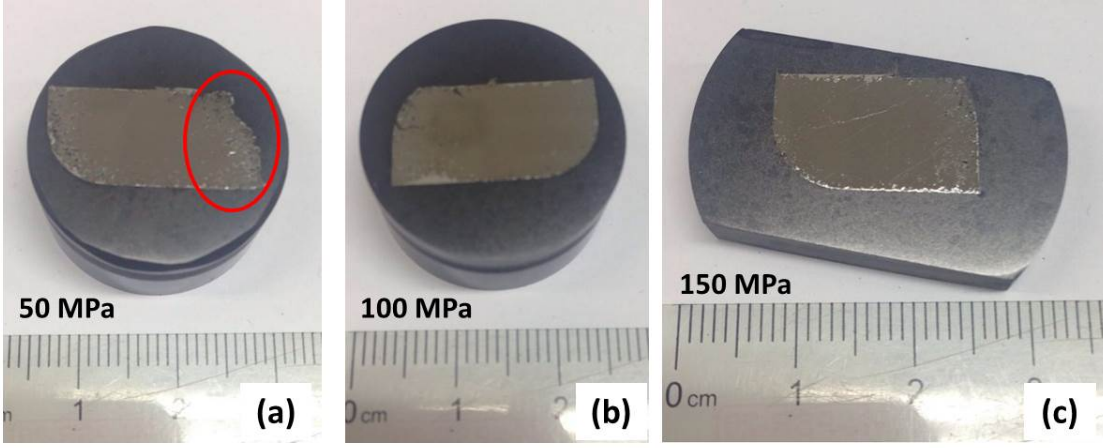

Fig. 6. 4 Macrographs of recycled Ti-15V-3Cr-3Al-3Sn pressed at 500 °C after a single ECAP pass with back-pressures of (a) 50 MPa, (b) 100 MPa and (c) 150 MPa.

6.2.3 Effect of number of passes

Fig. 6.5(a) to (c) show the samples recycled at 500 °C with a back-pressure of 100 MPa for 1, 4 and 8 passes, respectively. It is found that the minor cracks at the leading edge reduced with the increase in number of passes. However, minor cracks in the vicinity of top surface had not been eliminated even after 8 passes. In order to completely remove the surface cracks, recycling at higher temperature and slower ram speed are required [115] [177].

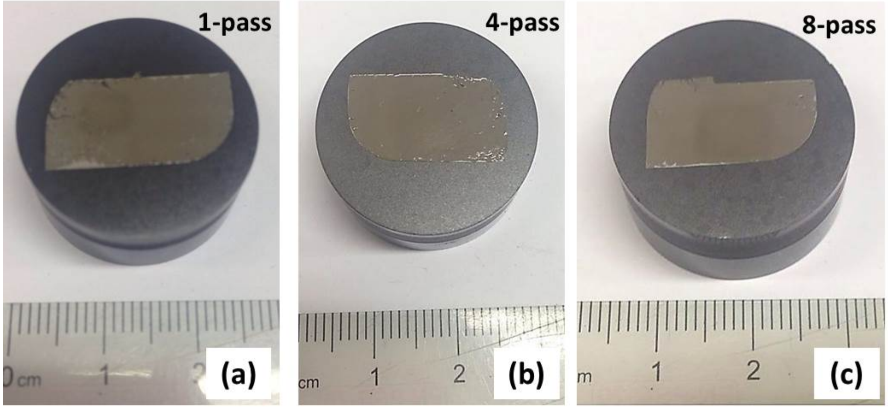

Fig. 6. 5 The appearances of recycled Ti-15V-3Cr-3Al-3Sn produced by ECAP at 500 °C with a back-pressure of 100 MPa after (a) 1 pass, (b) 4 passes and (c) 8 passes.

6.3 Relative Density Measurement of Recycled Ti-15V-3Cr-3Al-3Sn

6.3.1 Single-pass samples

Table 6.1 summarises the measured relative densities of the single-pass samples processed at 400 °C, 450 °C and 500 °C with different applied back-pressures. Fig. 6.6 shows the relationship of the relative density as a function of applied back-pressures at different temperatures.

Table 6.1 Summary of the relative density measurements for recycled Ti-15V-3Cr-3Al-3Sn in the current experiments.

Imposed Back-pressure (MPa)	Operating Temperature (°C)		
	400	450	500
50	92.8%	93.7%	98.0%
100	94.4%	97.4%	98.9%
150	N/A	97.5%	99.1%

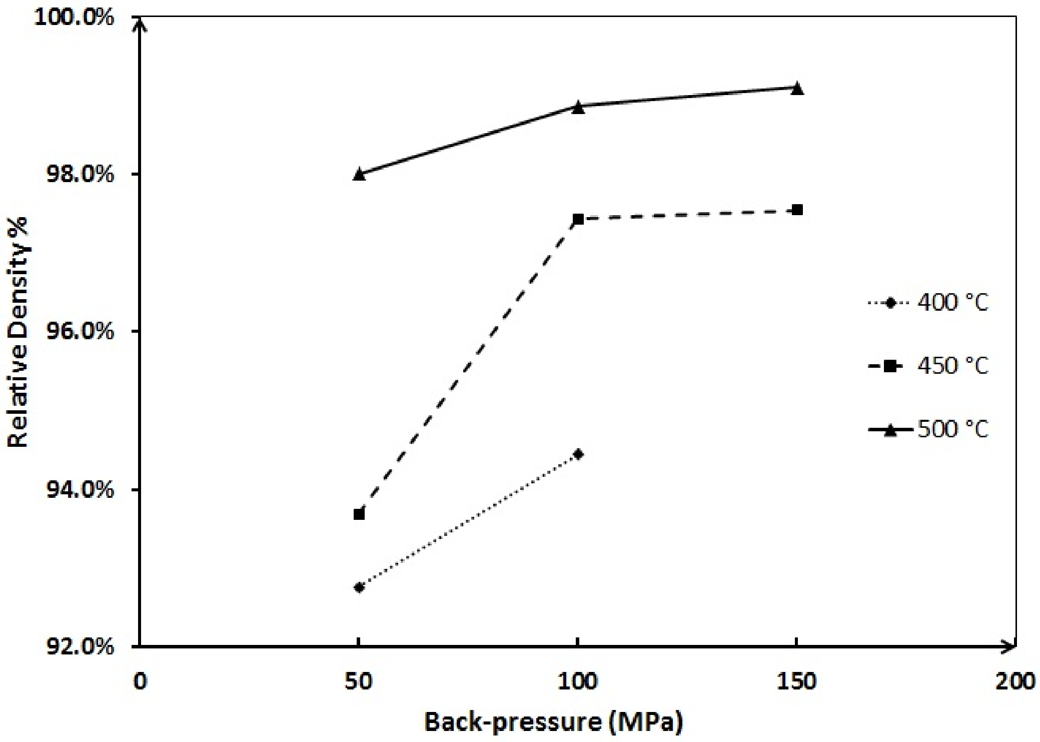

Fig. 6. 6 Relative densities as a function of imposed back-pressure at different temperatures for single-pass recycled Ti-15V-3Cr-3Al-3Sn.

The trend of the curve in Fig. 6.6 is similar to the recycled Ti-6Al-4V, which can be concluded that at each operating temperature, the relative density increases with the applied back-pressure, when fixing the applied back-pressure, a higher processing temperature results in a denser recycled product. Despite the major in different phases and structures, the effects of back-pressure and temperature on the as-pressed sample relative density have been discussed in Section 5.3.1 and can be also applied to β-Ti. In order to further understand the roles of the applied back-pressure and the processing temperature on Ti-15V-3Cr-3Al-3Sn chip consolidation, some representative optical micrographs are selected and compared below.

A comparison was made of specimens recycled after a single ECAP pass at 500 °C with back-pressures of 50 and 100 MPa (Fig. 6.7). It can be seen that a large number of pores are present in the sample processed with the lower back-pressure, as indicated by arrows (Fig. 6.7(a)), while no exposed pores are found in the sample using a back-pressure of 100 MPa. The implication is that the increase of back-pressure leads to a significant reduction of macro pores.

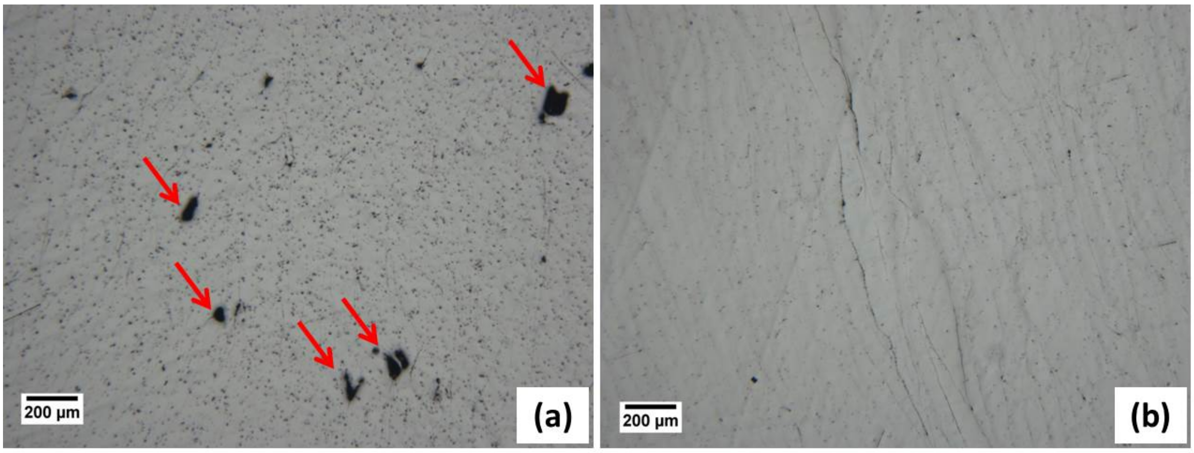

Fig. 6. 7 Optical micrographs of single-pass Ti-15V-3Cr-3Al-3Sn processed at 500 °C with back-pressures of (a) 50 MPa and (b) 100 MPa.

The effect of processing temperature is shown in Fig. 6.8. In the sample pressed for single pass at 450 °C with a back-pressure of 150 MPa (Fig. 6.8(a)), there were a large number of pores retained at the triple junction (as marked by ovals) and gaps between chips (as marked by arrows). By increasing the operating temperature of 50 °C, the recycled sample appeared fairly dense and free of macro-pores, as shown in Fig. 6.8(b).

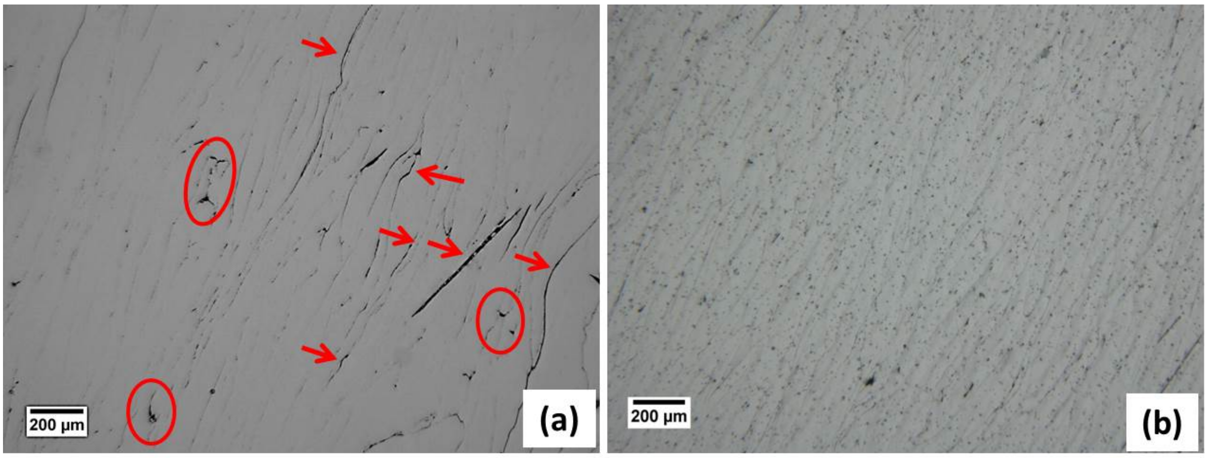

Fig. 6. 8 Optical micrographs of samples recycled at (a) 450 °C and (b) 500 °C with a back-pressure of 150 MPa after single pass.

6.3.2 Multiple-pass samples

All multiple-pass samples were ECAPed at the temperature of 500 °C. The increases in relative density observed with increasing number of passes are illustrated in Fig. 6.9. In the current study, the highest relative density of ~99.9% was achieved by the sample pressed for 8 passes with the aid of a back-pressure of 100 MPa, the optical micrograph of which is shown in Fig. 6.10. In comparison to the samples after single pass (Fig. 6.7(b)), number of exposed pores and width of chip boundaries were reduced. This observation is consistent with density measurement.

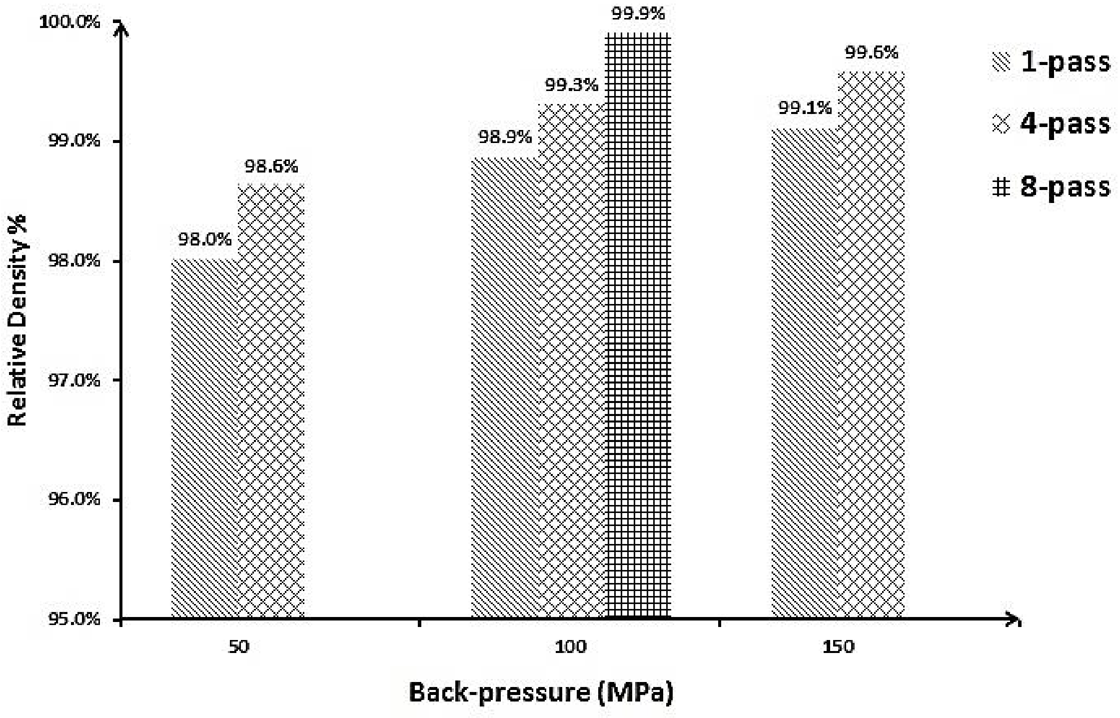

Fig. 6. 9 Relative densities of the recycled Ti-15V-3Cr-3Al-3Sn after multiple-pass ECAP at 500 °C using different back-pressures

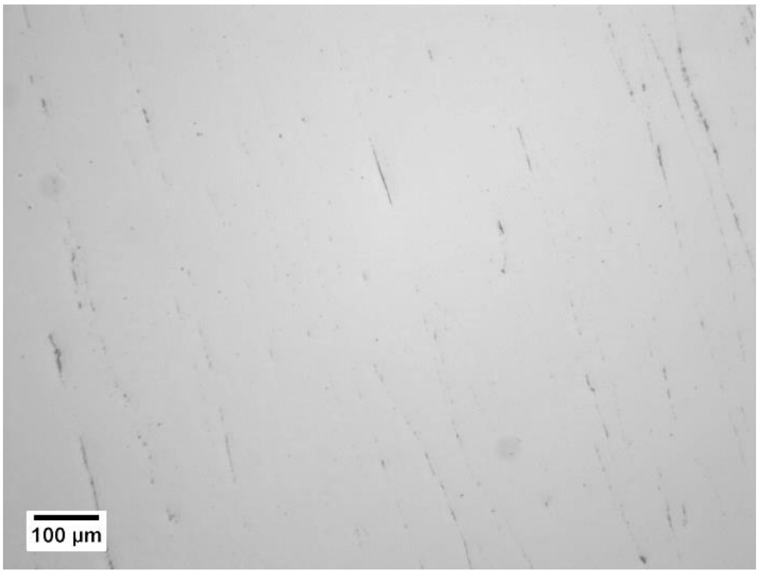

Fig. 6. 10 Optical micrograph of recycled Ti-15V-3Cr-3Al-3Sn after 8 passes at 500 °C with a back-pressure of 100 MPa.

6.4 Microstructure Evolution of Recycled Ti-15V-3Cr-3Al-3Sn

The EBSD IPF orientation map (Fig. 6.11(a)) shows the coarse grain microstructure of raw Ti-15V-3Cr-3Al-3Sn alloy prior to machining. The corresponding phase map

(Fig. 6.11(b)) confirms the β titanium alloy in solution treated condition without any observable α phase. After machining, except the primary shear zones where EBSD patterns was heavily distorted and unresolvable, no α phase was observed in the chips (Fig. 6.11(d)). According to the description in Section 4.2, the primary shear zones consist of nano-crystalline β grains. Therefore, it can be concluded that the starting material before ECAP is β titanium.

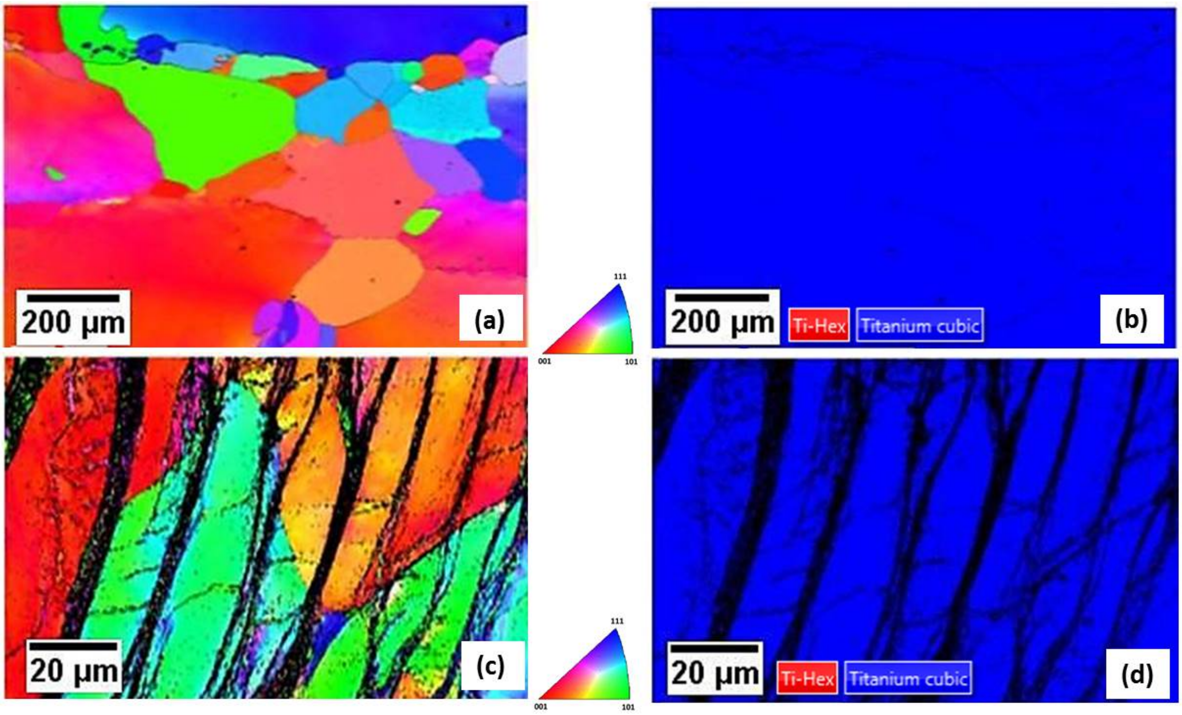

Fig. 6. 11 EBSD analyses of bulk Ti-15V-3Cr-3Al-3Sn: (a) IPF map, (b) phase distribution and original machining chip: (c) IPF map and (d) phase distribution.

Fig. 6.12 shows an SEM micrograph of the recycled sample by single-pass ECAP at 250 °C with a back-pressure of 50 MPa. It is noted that there was no apparent change in the microstructure of the primary and secondary shear zones compared to that of the original machining chips (Fig. 4.2). A chip boundary gap was clearly observed. The implication is that the shear deformation introduced by single-pass ECAP at 250 °C is insufficient to bond the chips mechanically.

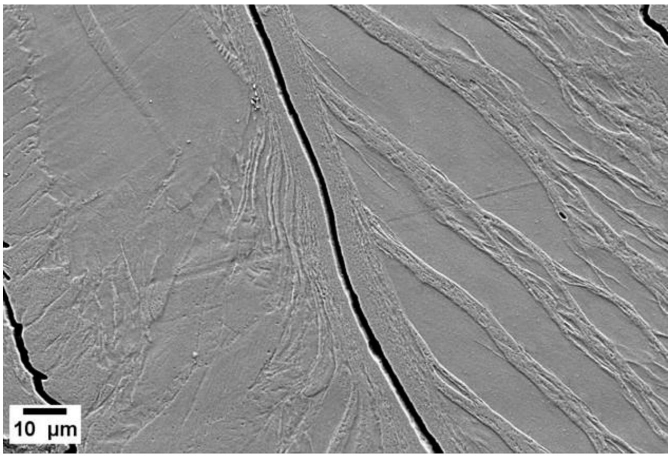

Fig. 6. 12 SEM micrograph of the recycled Ti-15V-3Cr-3Al-3Sn by one-pass ECAP at 250 °C with a back-pressure of 50 MPa.

The microstructure of recycled Ti-15V-3Cr-3Al-3Sn processed by 4-pass ECAP at 500 °C with a back-pressure of 100 MPa is shown in Fig. 6.13. A dual microstructure was clearly observed by backscattered image in the recycled specimen: equiaxed α grains (dark contrast) were present in β matrix (bright contrast). The size of α grains ranges from 150 to 200 nm.

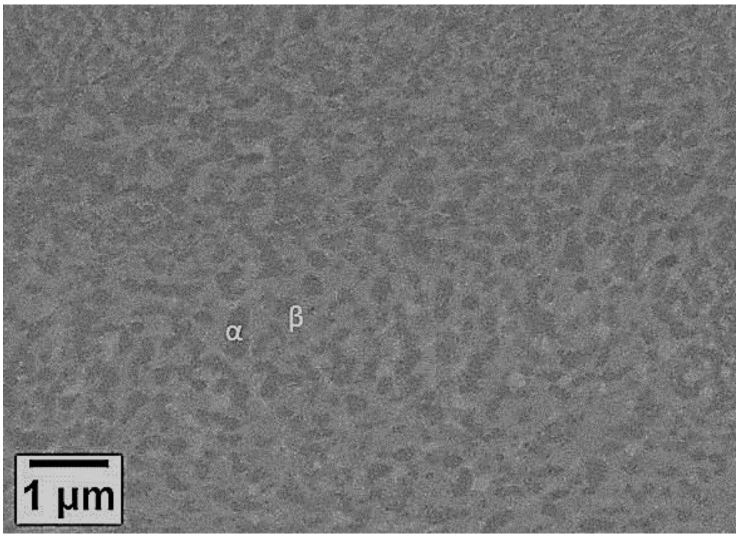

Fig. 6. 13 SEM backscattered image showing the microstructure of Ti-15V-3Al-3Cr-3V pressed at 500 °C with a back-pressure of 100 MPa for 4 passes.

A TEM bright field image (Fig. 6.14(a)) from the 4-pass sample processed at 500 °C with a back-pressure of 100 MPa confirms the fully equiaxed ultrafine microstructure with average grain diameter of ~180 nm. As demonstrated in the corresponding SAD pattern (Fig. 6.14(b)) taken from the red circle, α-Ti phase performs the ring shape pattern which implies the ultrafine grains with high angle misorientations. A careful inspection of the diffraction pattern reveals the β reflections of 110_{β} and 200_{β} close to

$10\bar{1}0_\alpha$ and $10\bar{1}2_\alpha$ reflections, respectively, as indicated by the arrows in Fig. 6.14(b). As shown in Fig. 6.14(b), the reflections contributed by β matrix are fairly weak.

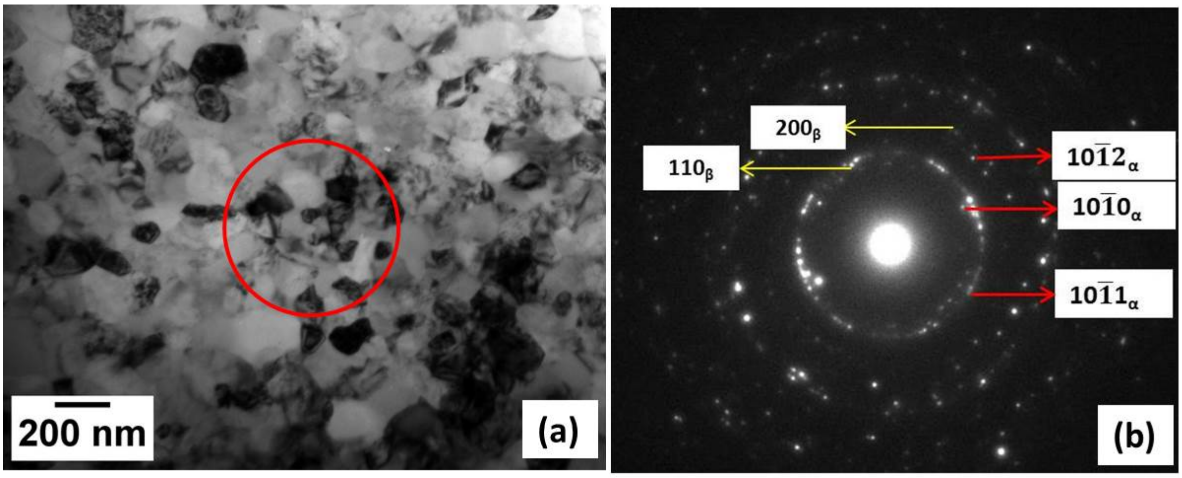

Fig. 6. 14 (a) TEM microstructure and (b) the corresponding SAD pattern of Ti-15V-3Cr-3Al-3Sn recycled at 500 °C with a back-pressure of 100 MPa after 4 passes.

In order to further confirm the formation of the equiaxed α precipitates in β matrix, STEM analysis accompanying with EDS was carried out in the same sample. A TEM bright field image (Fig. 6.15(a)) confirms equiaxed ultrafine grains with clear grain boundaries. The elemental mappings, as shown in Fig. 6.15(c) to (e), revealed that Al-rich and V/Cr-depleted α grains are distributed in the β matrix. It is noteworthy that the distribution profile of Sn is identical with that of Al (Fig. 6.15(d)), although Sn is usually considered as a neutral element. The distribution of α and β grains in a local region is indicated in the STEM image (Fig. 6.15(b)) and the Al mapping (Fig. 6.15(d)).

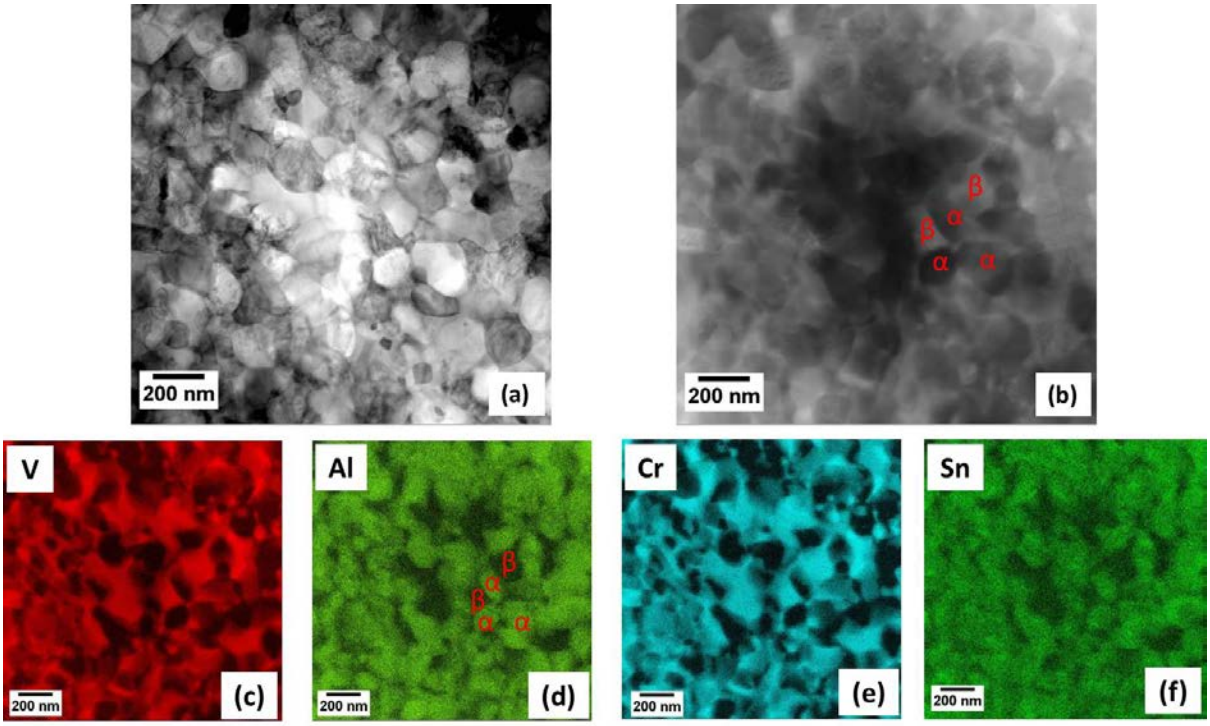

Fig. 6. 15 TEM and STEM analyses of the recycled Ti-15V-3Cr-3Al-3Sn pressed at 500 °C with a back-pressure of 100 MPa after 4 passes: (a) conventional TEM bright field image, (b) a STEM image indicating the distribution of α and β grains, (c) vanadium, (d) aluminium, (e) chromium and (f) tin elemental mappings.

In addition to the ultrafine α grains, some nano-sized α grains were also observed. Fig. 6.16(a) shows a bright field TEM micrograph of an individual α grain with size of ~22 nm in diameter, as marked by the red circle. The corresponding SAD pattern and the indexing (Fig. 6.16(b)) indicate that the zone axis is $[\bar{1}2\bar{1}3]$. The dark field image (Fig. 6.16(c)) is excited with the $(10\bar{1}0)_\alpha$ reflection.

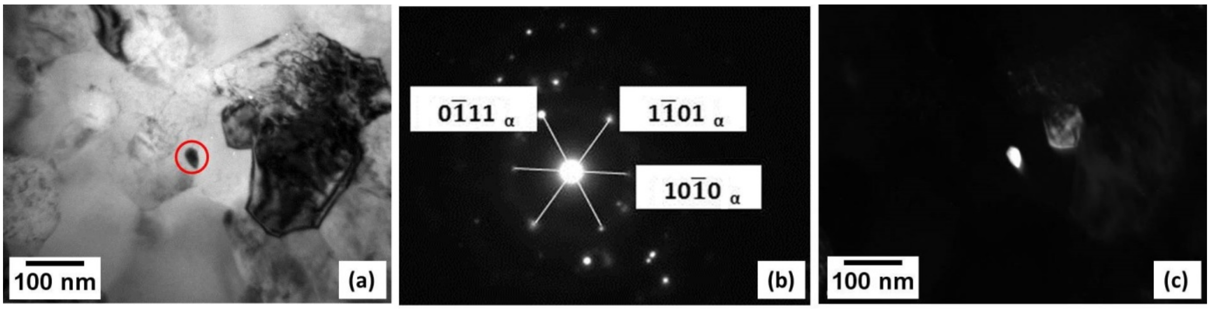

Fig. 6. 16 (a) Bright field micrograph, (b) the corresponidng SAD pattern and (c) $(10\bar{1}0)_\alpha$ dark field micrograph of a nano-sized α grain in Ti-15V-3Cr-3Al-3Sn recycled at 500 °C for 4 passes.

The morphology of α precipitation in the ECAP-recycled Ti-15V-3Cr-3Al-3Sn is different from that in the coarse-grained alloy after aging. For coarse-grain and slightly deformed β-Ti, the α precipitates are usually in the form of needle shapes [218]. The acicular α phase usually forms heterogeneously, they preferentially nucleates at dislocations, grain boundaries, sub-grain boundaries [218], and interface between β and secondary phases (e.g. ω phase) [219]. In order to minimize the activation energy for the nucleation, the α precipitates nucleate at lattice defects in the way coherent with the β matrix [220]. Thus the formation of α phase is restricted by the variant selections, and hence acicular shape. As demonstrated by Guo *et al*. [221], the habit plane of α precipitates was $\{111\}_\beta$ and the orientation relationship between α precipitates and β matrix was $<11\bar{2}0>_\alpha \parallel <111>_\beta$ and $\{0001\}_\alpha \parallel \{110\}_\beta$. These relationships were also confirmed by the experimental results obtained from hot-drawn Ti-15Nb-2Mo-2Zr-1Sn alloy [222]. Furthermore, the needle-shaped α precipitates coarsen with the increasing aging temperature [223]. Similar phenomena were also observed when the β titanium alloy was subjected to duplex aging treatments [45] [224], i.e. pre-aging at low temperature for a long time, e.g. at 250 °C for 24 hours, and then aging at relatively high temperatures, for example at 350-500 °C [45]. The consequent ultrafine α phase appears as long and narrow laths.

In contrast, the α precipitates in the present study appear to be equiaxed (Fig.6.13 to Fig. 6.16). Moreover, in comparison to the microstructure obeying the Burgers orientation relationship in references [221] [222], the observed α phase in the current experiment appear to be randomly orientated. There is no previous research was carried out on studying the microstructure of Ti-15V-3Cr-3Al-3Sn subjected to ECAP, however, similar equiaxed ultrafine-duplex (α+β) microstructures with random orientations were observed in other β-type titanium alloys after SPD, for example ECAPed [225] and high-pressure torsion (HPT) of Ti-20Mo [226]. It should be noted that in the previous investigations the equiaxed α precipitates formed inside the shear bands generated during ECAP and HPT, and they usually co-occurred with acicular α phase outside the shear bands. In the present study, no acicular α precipitates were observed in the sample after 4 passes ECAP, and the resultant microstructure is fully equiaxed.

The different morphologies of α precipitates can be explained based on the fact that high density of dislocations [218] and abundant grain and sub-grain boundaries [227] are introduced during ECAP, and they act as the nucleation sites and accelerate the kinetics of α precipitation. As suggested by Valiev *et al*. [228], the high-angle grain boundaries introduced by the SPD mostly lead to grain refinement, and these grain boundaries possess non-equilibrium structures [229]. The non-equilibrium grain boundary is characterized by an increased free energy density, increased width and high dislocation density. Thereby, profuse newly-formed grain boundaries become preferred nucleation sites. In addition, the atom diffusivity after the SPD is increased by several orders of magnitude [226] [230], and the diffusion length can reach up to tens of micrometres [231], which is larger than the size of ultrafine α and β grains. It is supposed that vacancies and non-equilibrium grain boundaries introduced by the SPD play a role as a fast diffusion path for atomic transport, which facilitates the rapid growth of α nucleus into the equiaxed precipitates [229] [231] [232]. Furthermore, the high concentrations of vacancies caused by ECAP weaken the preferred variant selection of α precipitates [225], and hence more randomly orientated α precipitates were achieved.

In addition to the nucleation and growth of α precipitates promoted by ECAP, dynamic recovery or even dynamic recrystallization occurring during the shear deformation of ECAP promote the formation of equiaxed microstructure. As demonstrated by Inaba *et al*. [227], the morphology of (α+β) bi-phase in the deformed Ti-15V-3Cr-3Al-3Sn is strongly dependent on the recovery process of the β matrix: slow recovery processes resulting from slight deformation will lead to the α nucleation at the dislocation arrays and thus traditional acicular shape precipitates form; in contrast, heavy deformation results in a large amount of stored energy, which facilitates the formation of recovered dislocation structure, i.e. β sub-grain. It precedes α precipitation, thereby the α nucleation preferably occurs at β sub-grain boundary nodes, and hence the formation of equiaxed α grains [227]. The schematic of the formation of equiaxed α precipitates in β matrix is illustrated in Fig. 6.17. In the present study, the ECAP processing temperature was maintained at ~500 °C (~773 K), and it has been reported that there is an increase in temperature within the shear plane of ~40 – 85 K per ECAP pass [127] [208] [209] [210], therefore the absolute temperature in the shear band during ECAP is supposed to be ~813 – 858 K. This temperature is high enough for dynamic recovery, and it reaches or even exceeds the recrystallization temperature of Ti-15V-3Cr-3Al-3Sn (~776 – 971 K). Further work is required in order to confirm the occurrence of recrystallization.

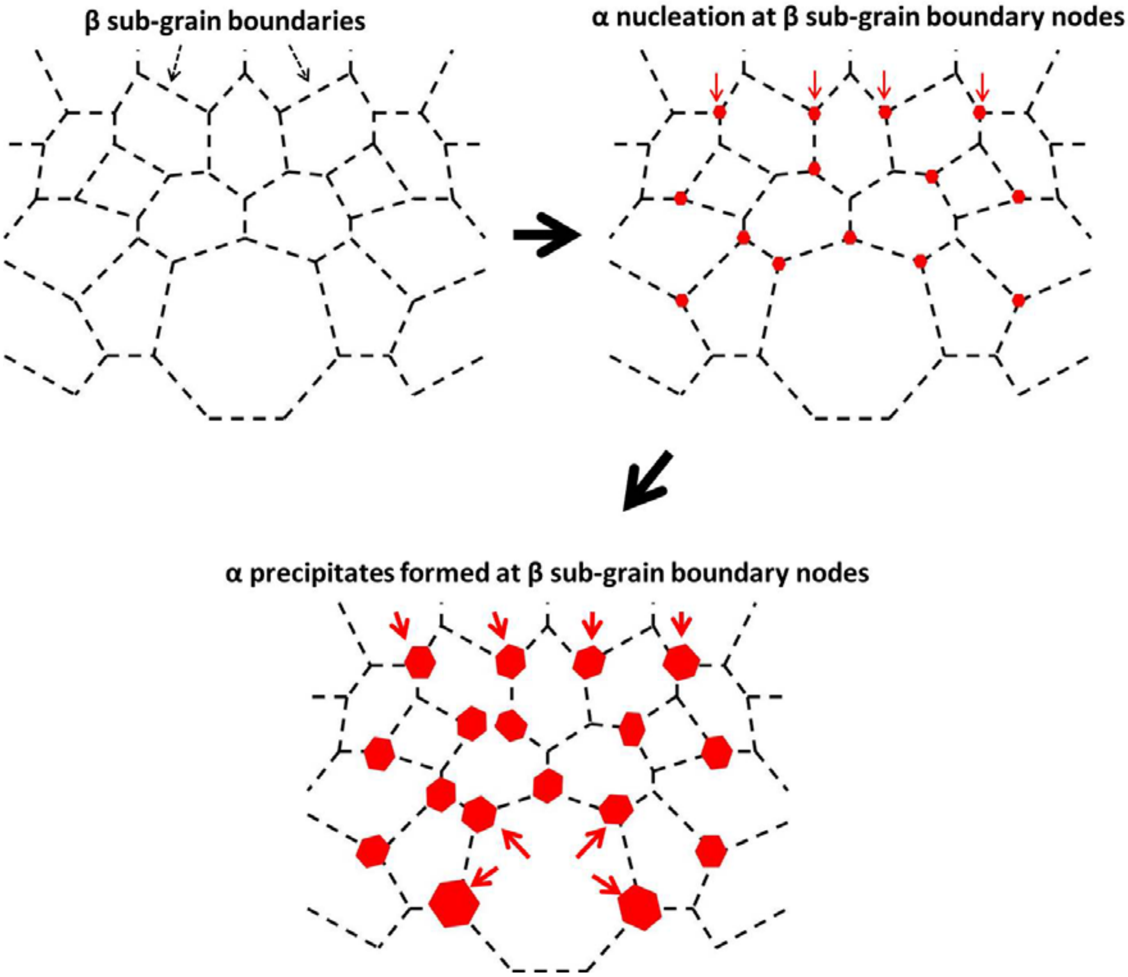

Fig. 6. 17 Schematic diagram showing the formation of equiaxed grains in β matrix (reproduced from **[227]***)*.

Although the orientation relationship between α precipitates and β matrix is random, it is noteworthy that the α precipitation coinciding with the variant selections was still found in some areas. Fig. 6.18(a) is a bright field image showing equiaxed microstructure of the ECAP-recycled Ti-15V-3Cr-3Al-3Sn at 500 °C after 4 passes. As seen in Fig. 6.18(b), the SAD pattern taken from the individual β grain shows zone axis of $[\bar{1}10]_{\beta}$. An identical SAD pattern has been also reported in [221], and the calibrated pattern is shown in Fig. 6.18(c). It can be found that the diffraction spots of variants $(100)_{2\alpha}$ and $(100)_{12\alpha}$ spread along the $[111]_{\beta}$ and $[11\bar{1}]_{\beta}$ directions, respectively. When the diffraction pattern is in the zone axis of $[\bar{1}10]_{\beta}$, the incident beam is parallel to $(111)_{\beta}$ and $(11\bar{1})_{\beta}$ planes. Based on the summary of the investigation conducted by Guo *et al*. [221], the α variant 2 and α variant 12 lie on the planes of $(111)_{\beta}$ and $(11\bar{1})_{\beta}$, respectively.

Another feature in Fig. 6.18(a) is that the coarsened α precipitate with a diameter of ~220 nm. This implies the fast α grain growth which is promoted by the SPD enhanced diffusivity. The corresponding SAD pattern and indexing (Fig. 6.18(d)) show a zone axis of $[2\bar{1}\bar{1}0]$. It is known that due to the structure factor of 0, the (0001) plane should be forbidden by electron diffraction. The appearance of 0001 reflection is due to double diffraction [233].

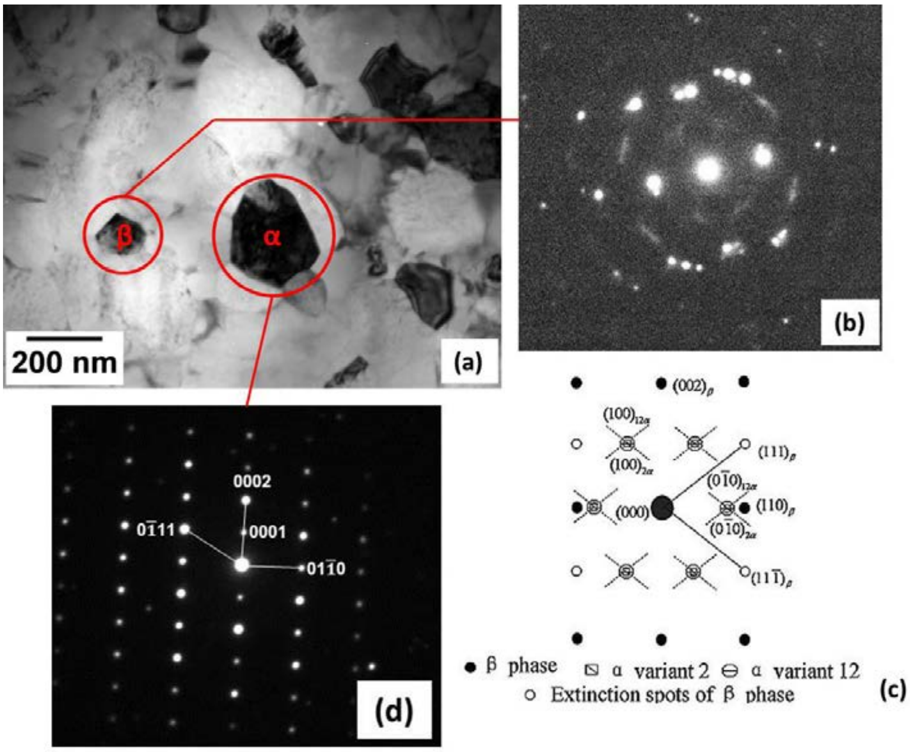

Fig. 6. 18 (a) TEM micrograph of Ti-15V-3Cr-3Al-3Sn recycled by ECAP at 500 °C for 4 passes, (b) SAD pattern taken from the β grain in (a), (c) calibrated SAD pattern of (b) **[221]***, and (d) SAD pattern taken from the α grain in (a).*

Fig. 6.19(a) shows a β grain with size (length and width) of ~75 nm and ~40 nm, as marked by the red circle. The corresponding SAD pattern in Fig. 6.19(b) exhibits $(10\bar{1}0)_\alpha$ and $(110)_\beta$ reflections. The dark field image obtained using the $(10\bar{1}0)_\alpha$ reflection (Fig. 6.19(c)) reveals the α precipitates located at the β grain boundary. The appearance of α phase at the interface was also observed in Ti-15Nb-2Mo-2Zr-1Sn subjected to hot-drawn at 640 °C [222]. In their study, the α phase was restricted to the selection variant of $(0001)_\alpha \parallel (110)_\beta$.

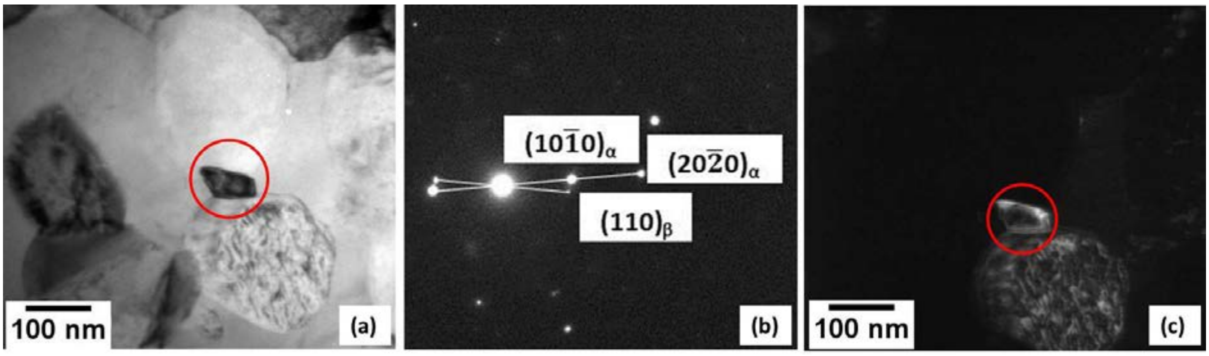

Fig. 6. 19 TEM micrograph of Ti-15V-3Cr-3Al-3Sn recycled at 500 °C for 4 passes. (a) Bright field image, (b) the corresponding SAD pattern from the red circle in (a), and (c) dark field image taken from $(10\bar{1}0)_\alpha$ *reflection as indicated in (b).*

Fig. 6.20(a) is a TEM micrograph showing an interface between two chips in the sample processed after 4 passes at 500 °C with a back-pressure of 100 MPa. It is obvious that although the chip boundaries were eliminated by diffusion bonding, there is still some nano-sized pores remained along the chip boundary, as indicated by arrows. The corresponding ring-shaped SAD pattern taken from the bonding area, as shown in Fig. 6.20(b), reveals the presence of nano-sized α phase, and very weak $\{110\}_\beta$ reflection was also observed. A relatively higher magnification TEM image (Fig. 6.20(c)) reveals that the width of the diffusion bonding zone was ~250 nm. In addition, the grains in the vicinity of the bonding region were observed only ~30 nm or even smaller in diameter, which were much finer than those away from the bonding zone. Next to the bonding area is the mechanical bonding affected zone caused by severe shearing deformation. The width of the affected zone is ~500 nm on each side of the interface.

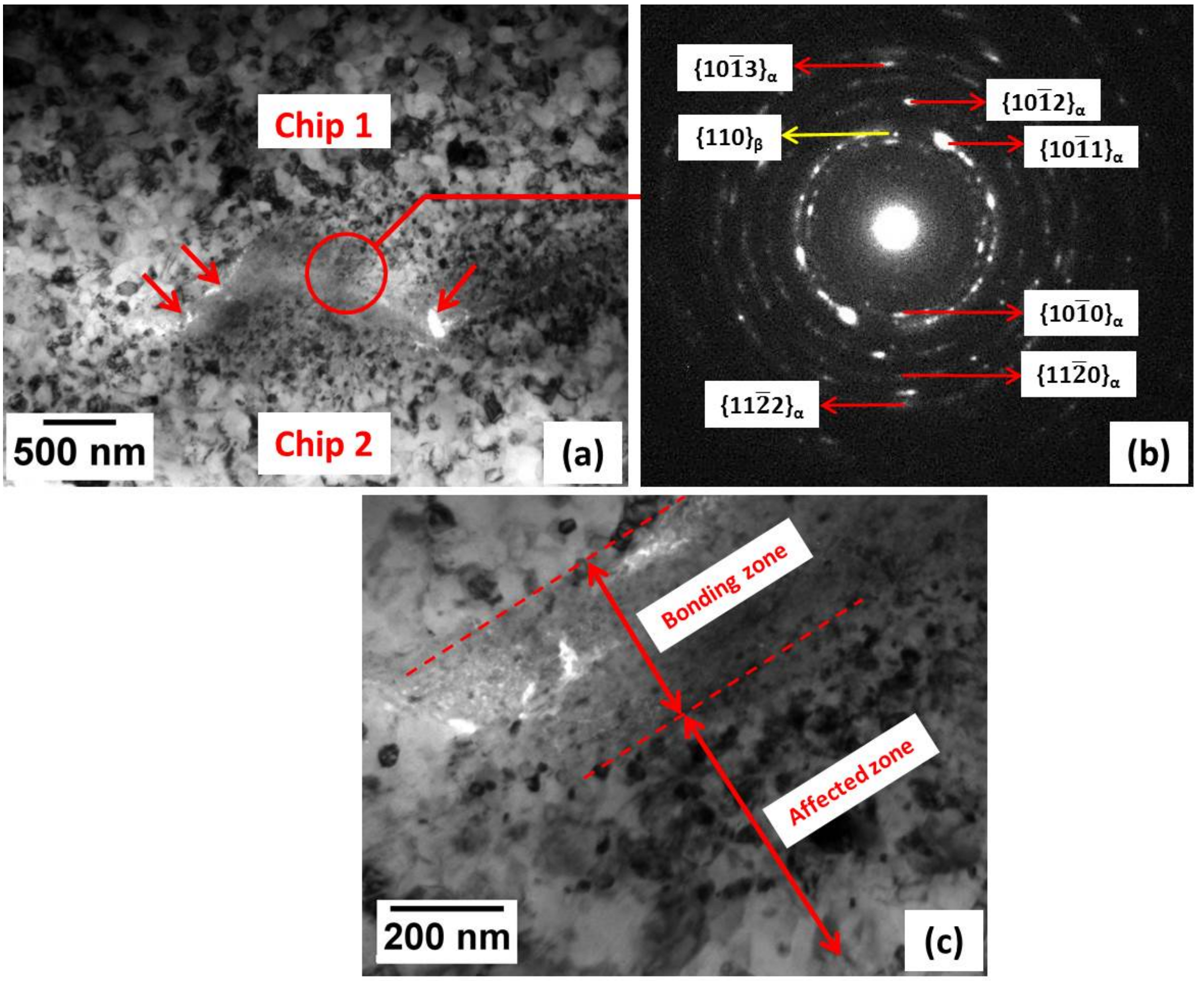

Fig. 6. 20 (a) Low magnification TEM image showing the chip boundary, (b) the corresponding SAD pattern and (c) higher magnification TEM image showing the bonding zone and the affected zone.

Fig. 6.21 is a TEM micrograph from the recycled specimen after 4-pass ECAP at 500 °C with a back-pressure of 50 MPa. It shows entangled dislocations in an equiaxed grain. The relatively high dislocation density is caused by the multiple pass shear deformation.

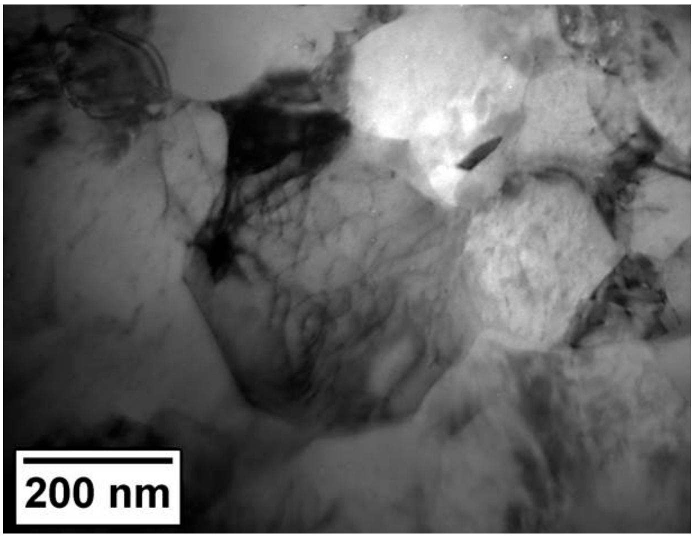

Fig. 6. 21 Entangled dislocations within an equiaxed grain for the specimen recycled at 500 °C with a back-pressure of 50 MPa for 4 passes.

6.5 Microhardness of Recycled Ti-15V-3Cr-3Al-3Sn

The mechanical property of the recycled Ti-15V-3Cr-3Al-3Sn was studied by Vickers microhardness measurement over the flow plane.

Fig. 6.22(a) to (c) show the colour-coded contour hardness maps of Ti-15V-3Cr-3Al-3Sn recycled by single-pass ECAP with a back-pressure of 50 MPa at 400 °C, 450 °C and 500 °C, respectively. It can be seen that after a single ECAP pass there is a profound heterogeneity showing in microhardness map. The heterogeneity is mainly caused by the remaining pores and chips boundaries. The extent of the inhomogeneity is directly and quantitatively depicted by the distribution curves in Fig. 6.22(d), showing the frequency of certain hardness of samples with an inceasement of 100 HV. It is apparent that the width of the distribution narrowed with the increasing temperature. It can be explained by the fact that the sample recycled at a relatively high temperature possessed a better deformability and physical bonding, thus eliminating pores and chip boundaries, and enhancing homogeneity.

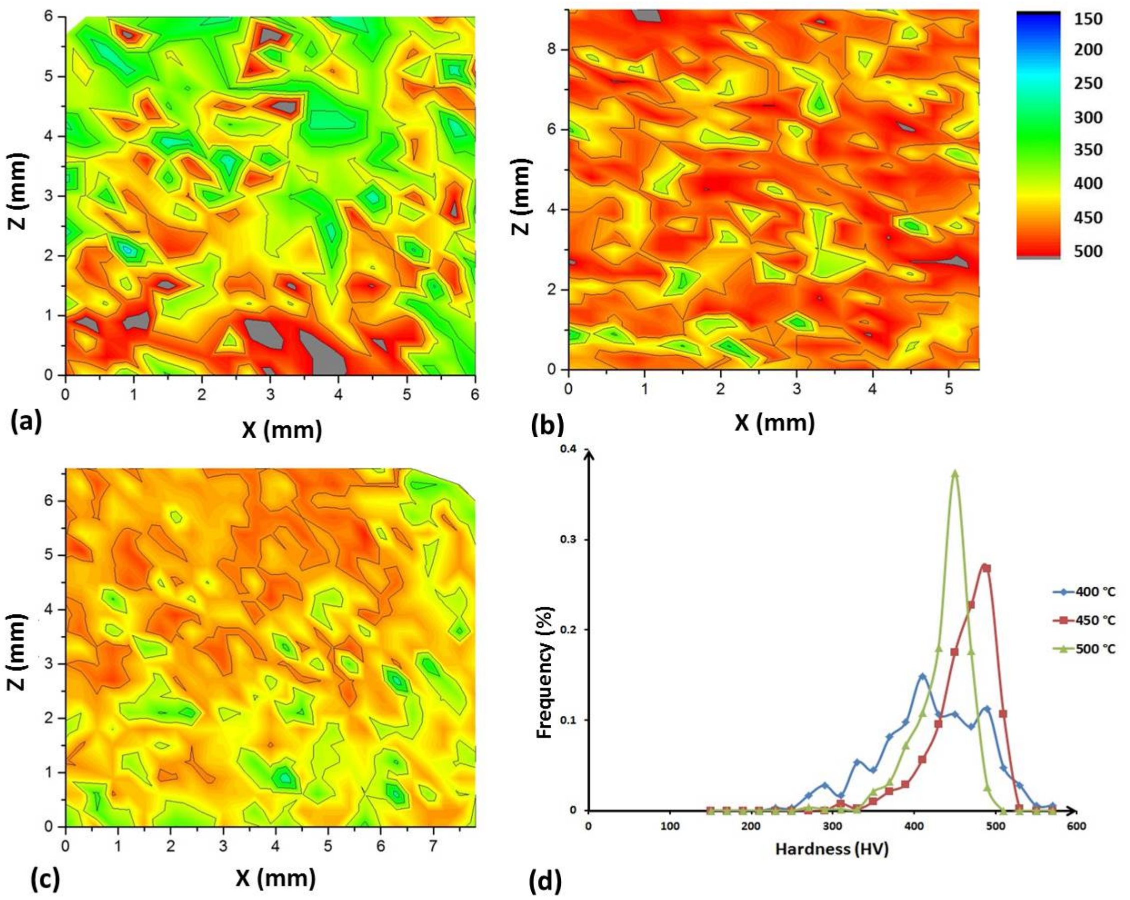

Fig. 6. 22 Colour-coded contour maps showing the microhardness distribution on the specimen recycled by single pass ECAP with a back-pressure of 50 MPa at (a) 400 °C, (b) 450 °C and (c) 500 °C; (d) the corresponding distribution curves.

The average hardness and corresponding standard derivations of as-received bulk material and the single-pass recycled samples are illustrated in Fig. 6.23. The results demonstrate a significant increase in microhardness after the first pass compared to the as-received bulk material. It is because of the formation of ultrafine grains and increase in dislocation density induced by the imposed strain during ECAP, sufficient evidences of which have been provided in Section 6.4. Apart from grain refinement and work hardening, age hardening simultaneously occurred during the ECAP process. Large amount of previous research [218] [223] [45] [234] [235] have been reported the aging effect on the mechanical properties of Ti-15V-3Cr-3Al-3Sn. In the present study the specimen processed at 450 °C possessed the highest hardness (~452.3 HV). Low aging temperature had little influence on Ti-15V-3Cr-3Al-3Sn hardening, and the hardness increased with the aging temperature until the peak hardness was achieved at the optimum temperature, which was ~435 °C [223].

Further increase in aging temperature would lead to over-aging and result in hardness drop because of the α precipitation coarsening.

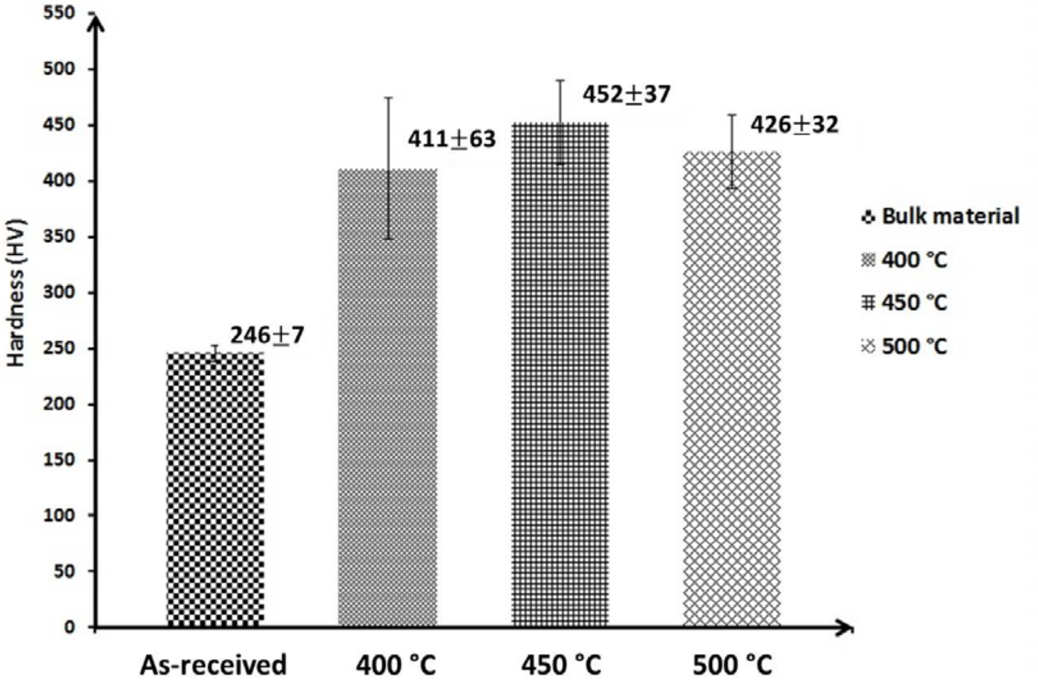

Fig. 6. 23 The average hardness for as-received bulk Ti-15V-3Cr-3Al-3Sn and recycled samples.

Fig. 6.24 shows colour-coded contour maps of the Ti-15V-3Cr-3Al-3Sn samples recycled at 500 °C with a back-pressure of 100 MPa for (a) 1, (b) 4 and (c) 8 passes, respectively. It can be seen that regions of lower hardness are clearly adjacent to the bottom surface after 1 and 4 passes, while it is almost eliminated after 8 passes. A similar phenomenon has been described and discussed in details in Section 5.6 for Ti-6Al-4V; same explanation can be applied to Ti-15V-3Cr-3Al-3Sn. As indicated in Fig. 6.24(d), there is a narrowing in the width of distribution in microhardness after multiple-pass ECAP, and the distribution curves directly demonstrate that higher homogeneity is achieved with the number of passes increasing from 1 to 8. The average hardness remained essentially unchanged with the increasing number of passes: 402.6±148.5 HV, 400.7±53.1 HV and 407.2±13.2 HV for 1, 4 and 8 passes samples, respectively. The colour-coded maps demonstrate that the hardness at the central region even slightly decreased with the number of passes. This implies that the maximum hardness was achieved after the first pass of ECAP. The possible reason is the saturation of the dislocation density and many of the subgrain boundaries evolve into high-angle grain boundaries [236].

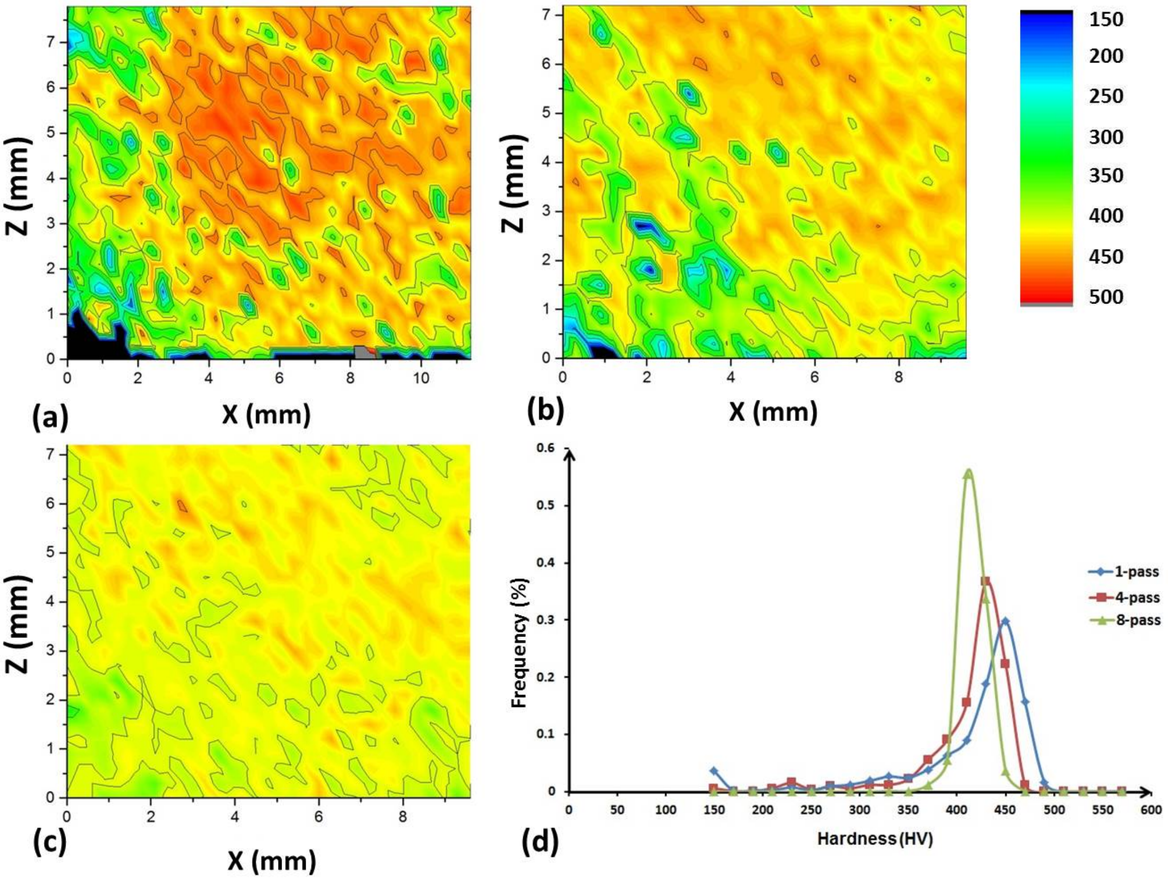

Fig. 6. 24 Colour-coded contour maps showing the microhardness distribution across the flow planes on Ti-15V-3Cr-3Al-3Sn recycled at 500 °C with a back-pressure of 100 MPa after (a) 1 pass, (b) 4 passes and (c) 8 passes, and (d) the corresponding distribution curves.

The colour-coded hardness maps for the samples recycled at 500 °C for 4 passes with back-pressures of 50 and 150 MPa are illustrated in Fig. 6.25 (a) and (b), respectively. It is obvious that higher applied back-pressure slightly reduce the area of lower hardness immediately adjacent to the bottom surface. This observation is discrepant with the previous study on pure Al [212], and also inconsistent with the result for recycled Ti-6Al-4V in Section 5.6. As illustrated in Fig. 5.49, for the strain hardening materials, such as 1100Al alloy [139] and Ti-6Al-4V recycled at 500 °C, as the back-pressure increase, the equivalent strain near the bottom surface increases from a fairly low to a much higher level, and the best homogeneity is achieved using a moderate back-pressure. However, for quasi-perfect plastic materials, such as 6061Al-T6 alloy [139], as illustrated in Fig. 6.26, the equivalent strain adjacent to the bottom surface slightly increases with the imposed back-pressure. Therefore, in the current study, the change of microhardness homogeneity with the applied back-pressure for recycled Ti-15V-3Cr-3Al-3Sn is consistent with the simulation for the quasi-perfect plastic materials.

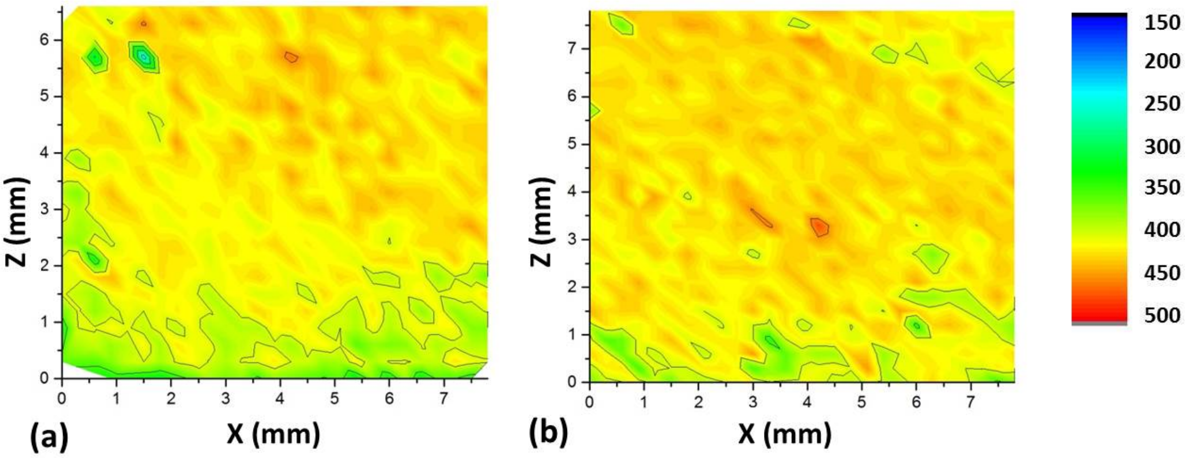

Fig. 6. 25 Colour-coded hardness maps for the Ti-15V-3Cr-3Al-3Sn recycled at 500 °C after 4 passes with back-pressures of (a) 50 MPa and (b) 150 MPa.

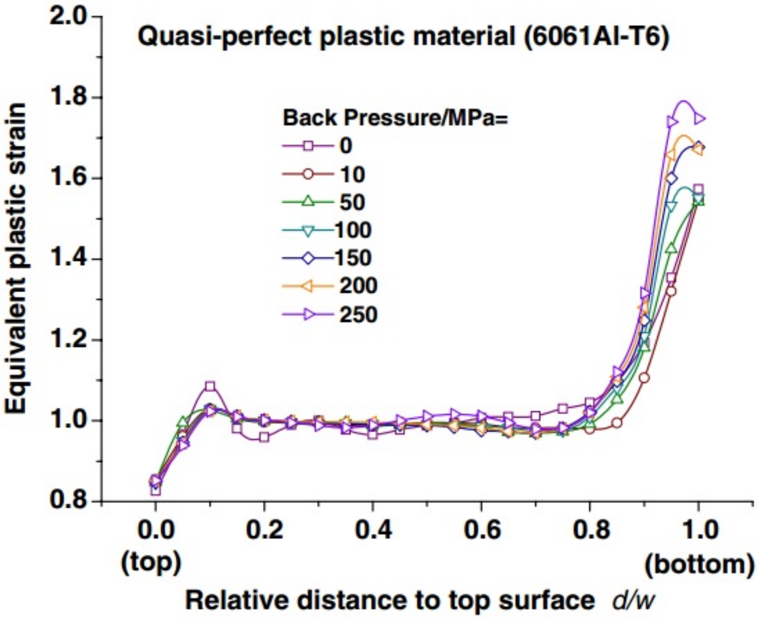

Fig. 6. 26 The effect of back-pressure on the equivalent plastic strain distribution from the top surface to bottom for a quasi-perfect plastic material (6061Al-T6) **[139]**.

6.6 Post Heat Treatment of Recycled Ti-15V-3Cr-3Al-3Sn

In order to remove the residual stress, the Ti-15V-3Cr-3Al-3Sn recycled by 4 passes of ECAP at 500 °C with a back-pressure of 150 MPa was annealed at 600 °C for 2 hours in an argon atmosphere furnace.

As shown in Fig. 6.27(a), after heat treatment α grains are equiaxed, and the diameter is ~280 nm, which is coarser than that in the as-recycled specimen (~150 – 250 nm). A higher magnification micrograph reveals that the microstructure in the annealed specimen is not homogenous: in some regions, a band of finer α grains with diameter ~120 nm in β matrix were observed, marked as area A in Fig. 6.27(b), which implies that some grains has not grown at the same rate during the annealing heat treatment. Similar result of inhomogeneous grain growth was reported in the study of Mg alloy AZ31 processed by extrusion and ECAP followed by subsequent annealing at 190 to 400 °C [237]. The grain growth mechanism during annealing process can be determined by the general equation:

$${d_t}^n - {d_0}^n = kt$$

where d_t is the grain diameter (assuming equiaxed shape) at given annealing time, d_0 is the initial diameter, n is the grain growth exponent, t is the annealing time and k is a temperature-dependent constant, which can be calculated by:

$$k = k_0 exp\left(-\frac{Q}{RT}\right)$$

where k_0 is a constant, Q is the activation energy for grain growth, R is the gas constant and T is the temperature. At the given temperature (T) and annealing time (t), the grain growth process is highly dependent on the exponent n. As the resistance to grain boundary motion, the grain growth exponent n is affected by the free surface effect, second-phase particles, dislocation substructure, texture and impurity-drag [238]. Previous study [239] reported that for conventional pure metals or alloys, the value n ranges from 2 to 5, however, ultrafine grained microstructure produced by severe plastic deformation methods possess a higher value of n ($n \geq 5$) [240] [241]. This implies that compared to conventional coarse grains, the growth for ultrafine grains requires more activation energy.

The band of fine grains (area A) observed in Fig. 6.27(b) is likely the primary shear zone in the original machining chips. Due to the severe shear strain imposed during the machining process, the grains were refined to nano-sized (Fig. 4.5) and dislocation substructure was developed in the primary shear zone. It is plausible that during the annealing process, the grain growth resistance in the primary shear zone is larger than that for other regions, and hence remained fine grains. In order to obtain homogeneous microstructure, higher temperature or longer annealing time is necessary.

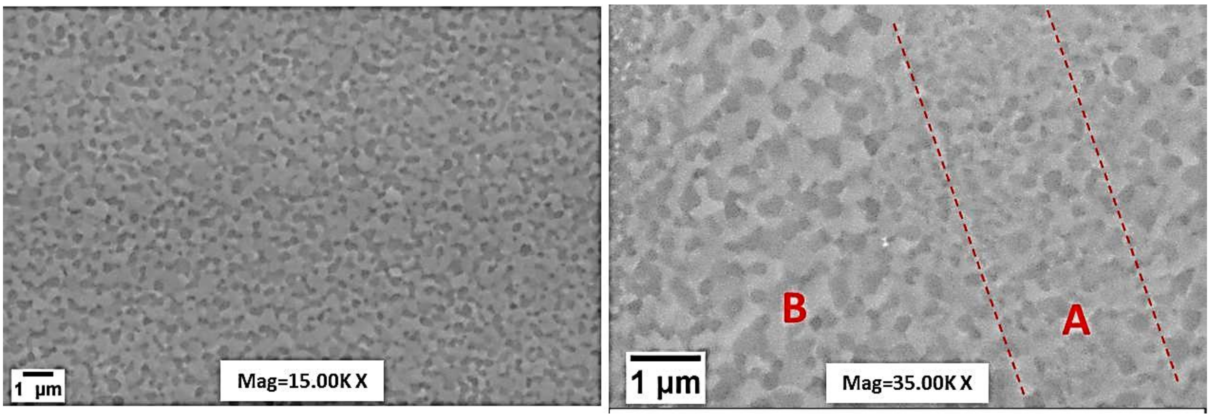

Fig. 6. 27 SEM microstructure of Ti-15V-3Cr-3Al-3Sn (recycled by ECAP at the temperature of 500 °C for 4 passes with a back-pressure of 150 MPa) heat treated at 600 °C for 2 hours.

TEM images as shown in Fig. 6.28(a) and (b) represent equiaxed microstructure and a region containing un-grown grains in the heat treated sample, respectively. Using the intercept method, the average grain sizes in Fig. 6.28(a) and the central region in Fig. 28(b) were ~288 nm and ~124 nm in diameter, respectively. The measurements are consistent with the estimation in the SEM study. In addition, the presence of discrete spots in the SAD pattern taken from the circle in Fig. 6.28(b) reveals bigger grain size and low-angle grain boundaries. In comparison to the microstructure prior to heat treatment (Fig. 6.14), it implies that the misorientation between ultrafine grains reduced during the annealing process.

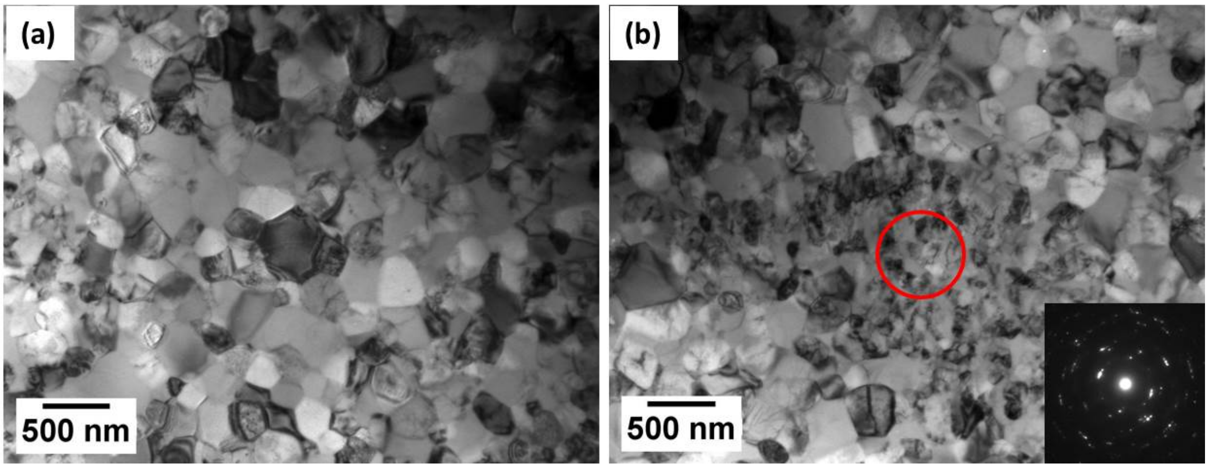

Fig. 6. 28 TEM micrographs showing (a) equiaxed microstructure and (b) un-grown grains in the specimen (recycled by ECAP at 500 °C for 4 passes with a back-pressure of 100MPa) annealed at 600 °C for 2 hours.

The chip/chip interface microstructure is revealed by a backscattered SEM micrograph (Fig. 6.29(a)). It is obvious that after annealing process, the grains along the interface were finer than the surrounding ones, as confined between the two dash lines. The plausible explanation is that the fine grains along the interface are originally at the secondary shear zone of the initial machining chips. The development of nano-sized grains during the machining process had a relatively high grain growth exponent *n*, and hence the inhibition in the annealing process. In addition, the fine grains are also possible created by the relative motion between two chips during ECAP.

The TEM images (Fig. 6.29(b) and (c)) reveal the internal microstructure of the chip interface. The width of the diffusion bonding zone was ~200 nm. The ring SAD pattern in Fig. 6.29(b) demonstrates the bonding zone consisting of nano-crystalline grains. Besides, the width of the affected zones in the vicinity of the bonding zone was ~500 nm. Compared with the interface microstructure in the as-recycled specimen in Fig. 6.20, the grain size in the affected zones of the annealed sample was ~90 nm, which is coarser than the as-recycled (~30 nm).

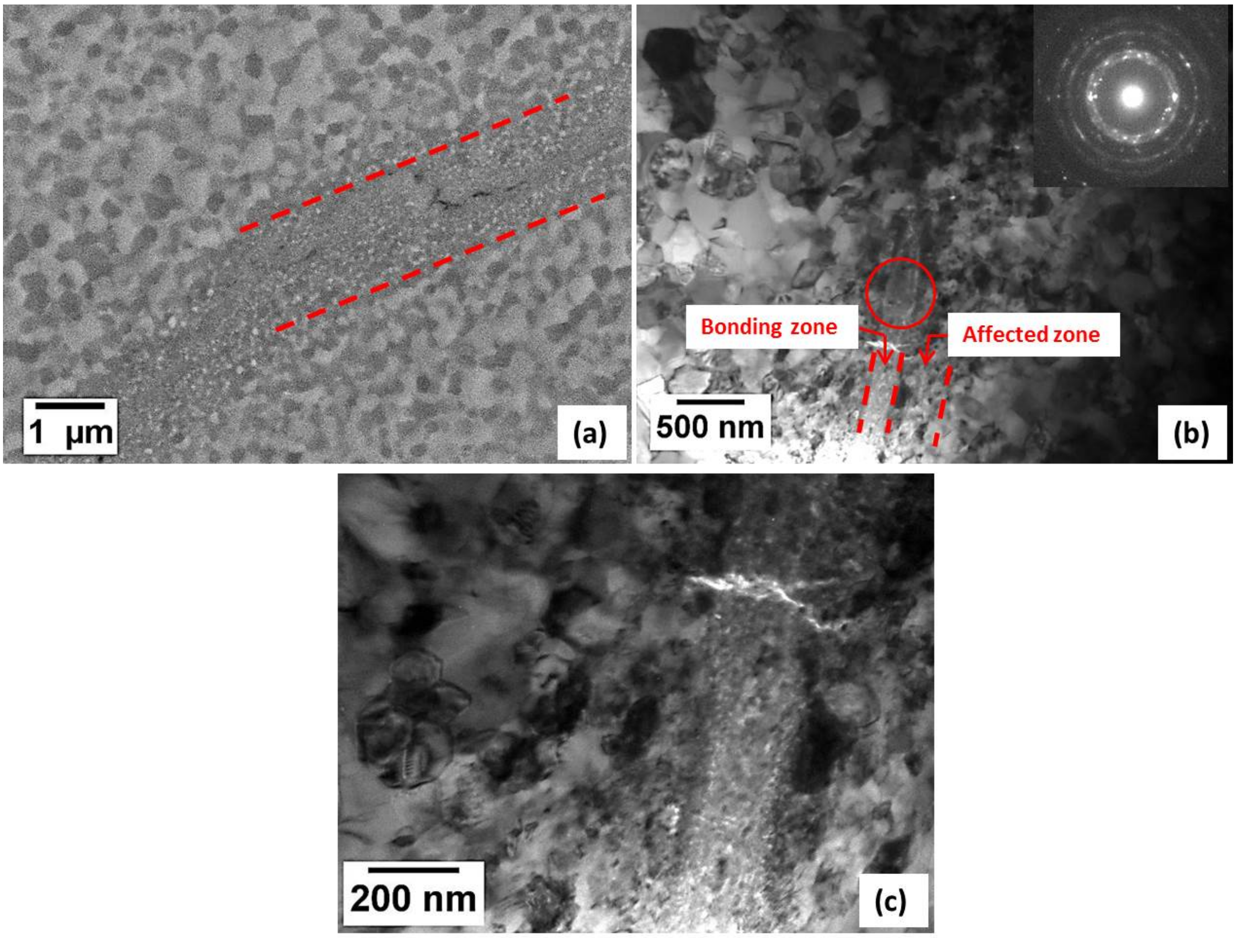

Fig. 6. 29 (a) SEM micrograph, (b) low magnification and (c) high magnification TEM micrographs showing the microstructure of the chip interface in the recycled Ti-15V-3Cr-3Al-3Sn after annealing at 600 °C for 2 hours.

A grain with relatively low dislocation density is shown in Fig. 6.30, in which the dislocations exhibited $\vec{g}$ vector of <10$\bar{1}$1>. The lower dislocation density can be reasoned by the annihilation during the annealing process.

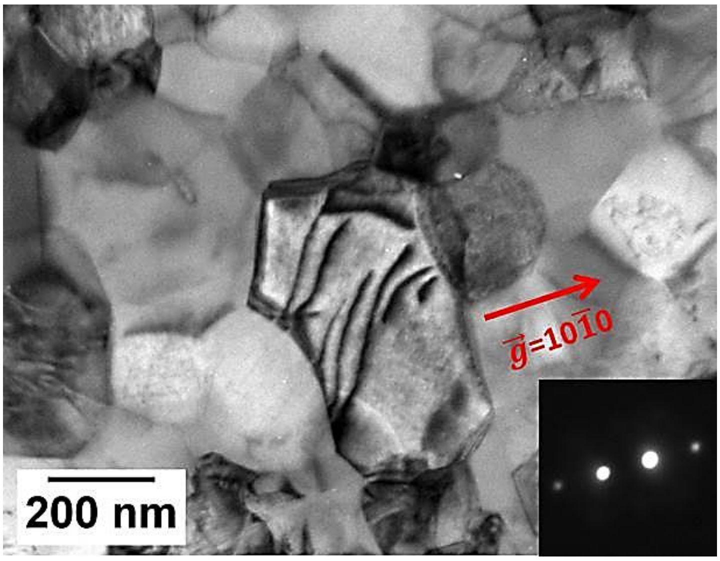

Fig. 6. 30 TEM micrograph showing low-density dislocations in the recycled Ti-15V-3Cr-3Al-3Sn annealed at 600 °C for 2 hours.

Fig. 6.31 shows the variation of hardness before and after the heat treatment. It can be seen that annealing process at 600 °C for 2 hours resulted in decrease in hardness from ~417.2 HV to 379.0 HV. The hardness reduction can be ascribed to grain growth and dislocation annihilation.

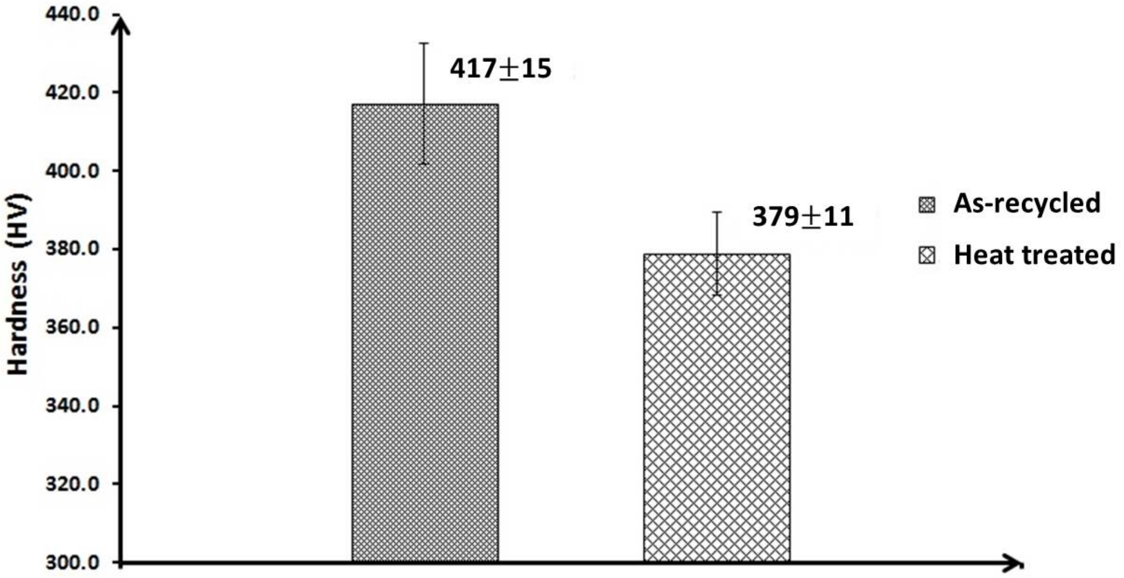

Fig. 6. 31 The comparison of the average microhardness of as-recycled Ti-15V-3Cr-3Al-3Sn and sample after heat treatment at 600 °C for 2 hours.

6.7 Summary

In this Chapter, Ti-15V-3Cr-3Al-3Sn machining chips were recycled by equal channel angular pressing with various back-pressures for up to 8 passes at moderate temperatures. The relative density, microstructure evolution, microhardness homogeneity and subsequent annealing treatment at 600 °C for 2 hours were investigated.

The lowest processing temperature to avoid macrocracks in the recycled samples is 500 °C regardless the imposed back-pressure. The increase in back-pressures and number of passes suppress the formation of minor cracks at the front part of the specimens.

The relative density measurements show that the increases of applied back-pressures, temperatures and number of passes improve the density of the recycled products. The near fully dense specimen with relative density of ~99.9% was obtained after 8 passes at 500 °C with a back-pressure of 100 MPa.

SEM and (S)TEM studies demonstrate the presence of equiaxed α precipitates among the β matrix in the recycled specimens. Severe shear deformation occurred during the ECAP process and introduced high dislocation density and abundant grain/sub-grain boundaries, which offer substantial nucleation sites for α precipitates. Furthermore, large amount of vacancies and grain boundaries facilitate atom diffusion, which accelerates the growth of equiaxed α precipitates. The high concentration of vacancies weaken variant selection, and hence a more random orientation relationship between α precipitates and the β matrix. The chip/chip interface consists of bonding zone of ~250 nm and affected zone of ~500 nm in width. Nano-sized pores were observed at the interface.

The microhardness test results have shown maximum hardness was achieved in the single-pass sample processed at 450 °C. By increasing the processing temperature, an improving homogeneity in the microhardness values has been observed. For the multiple-pass specimens, the increasing number of passes results in a significant improvement in microhardness homogeneity but an essentially unchanged average value. A higher back-pressure leads to a more homogenous microhardness distribution, especially at the bottom part of the ECAPed samples.

The annealing treatment at 600 °C for 2 hours results in some grains coarsening with characteristic of low dislocation density, leading to the decrease of average hardness value. Bands of smaller grains after annealing can be found which are originated from the primary shear zone of the chips and the chip/chip interfaces.

7. CONCLUSIONS

In this project, machining chips of Ti-6Al-4V (α+β Ti alloy) and Ti-15V-3Cr-3Al-3Sn (β Ti alloy) have been successfully recycled using back-pressure assisted equal channel angular pressing (BP-ECAP). A horizontal hydraulic system has been built and a new ECAP die has been designed for this research work.

In order to comprehend the microstructural evolutions from the machining chips to the recycled products, the starting microstructures of conventional turning (CT) and ultrasonically assisted turning (UAT) chips were initially examined. It was found that the materials in the primary and secondary shear zones were subjected to severe shear strain. For Ti-6Al-4V machining chips, the β phase in the shear zones was refined into nano-crystalline equiaxed grains and constituted banded structures. For CT - Ti-15V-3Cr-3Al-3Sn chips, the shear zones consisted of ultrafine grained microstructure with clear boundaries to the surrounding matrix. It was noted that apart from the larger shear angle, the microstructure of UAT chips was identical to the CT ones. Thus, there is no need to distinguish CT and UAT machining chips in the subsequent recycling process.

7.1 Ti-6Al-4V Machining Chip Recycling

One of the objectives of the research work is to identify the optimum processing conditions to produce quality recycled Ti-6Al-4V. Based on current results, in order to avoid the major cracks, the lowest permissible operating temperature is 500 °C with the aid of a back-pressure of 100 MPa. The higher back-pressure can suppress the formation of major cracks. However, it is impossible to eliminate the minor cracks on the surface regardless of back-pressures and temperatures.

The relative density was measured to assess the quality of recycled samples. For the single-pass samples, the relative density increases with the applied back-pressures and processing temperatures. It was found that multiple-pass ECAP is able to produce near fully dense recycled samples. Localized fragmentation and mechanical interlocking between chips were observed in the recycled products.

The microstructure of the recycled Ti-6Al-4V using various ECAP conditions was investigated by EBSD and TEM. The results agree with the grain refinement model: the fraction of equiaxed grains increases with the number of passes and the equilibrium equiaxed grain size is determined by the width of the subgrain bands introduced into the material in the first pass. The original β bands in the machining chips were fragmented into nano-crystalline grains due to the severe shear strain. Nano-crystalline microstructures were found in the chip/chip interface, and nano-sized pores were retained at the interface. Increasing the operating temperature to 550 °C, the microstructure was observed to be coarse and heterogeneous. In the chip/chip interface of the sample processed at 550 °C, oxide layers were detected by using the EDS analysis and SAD pattern.

In order to examine the crystallographic texture of recycled Ti-6Al-4V, extensive EBSD analysis was carried out. The main characteristic of the texture after the first pass is the basal poles orientated towards the NID, i.e. basal plane ∥ ID. After multiple passes, it appears that except for the NID, the basal poles exhibit a rotation towards the TD. The increase of the operating temperature to 550 °C shows most of the basal poles line up with the LD because of the activated non-basal slip system.

The effects of the number of passes and applied back-pressure on the microhardness and homogeneity were then evaluated. In terms of microhardness, it was found that the average hardness increased with the number of passes due to the grain refinement, while the imposed back-pressure had little effect on the hardness. As for the homogeneity, the results show that the single-pass sample is heterogeneous, in particular, the region adjacent to the bottom surface had relatively low hardness. The further increase of number of passes improved the homogeneity because all edges were subjected to the shear stress. In turn, the applied back-pressure had little effect on the region of lower hardness near the bottom surface.

The heat treatments for stress relief were conducted in an Argon atmosphere. For the sample annealed at 500 °C for 24 hours, the basal peak is split into two peaks, implying the activity of non-basal slip system. The annealing treatment at 700 °C for 2 hours caused partial recrystallization with random texture. EBSD analysis demonstrates that the non-recrystallized grains inherited the as-pressed texture.

7.2 Ti-15V-3Cr-3Al-3Sn Machining Chip Recycling

Ti-15V-3Cr-3Al-3Sn machining chips can be successfully recycled at 500 °C with a relatively low back-pressure of 50 MPa. Beyond that, the effects of back-pressures, temperatures and the number of passes on the appearances and relative density of recycled Ti-15V-3Cr-3Al-3Sn are similar to Ti-6Al-4V.

In the microstructure of recycled Ti-15V-3Cr-3Al-3Sn, equiaxed α precipitates in the β matrix were observed. The high density dislocations and large amount of sub-grain boundaries were introduced during ECAP which promoted the nucleation and growth of α grains. Nano-sized pores remained at the chip/chip interfaces. In addition, diffusion bonding zones with nano-crystalline grains and affected zones with ultrafine grains were also observed in the interface.

The microhardness measurement shows a significant increase in hardness for the recycled samples compared to the virgin material. The reason for this improvement is twofold. Firstly, the high shear strain introduced by ECAP leads to grain refinement and increase in dislocation density. Secondly, age hardening simultaneously occurred during the ECAP produces α precipitates. It was found that the average hardness value is dependent on the processing temperature. The specimen pressed at 450 °C after single pass had the peak value. The increasing back-pressure and number of passes have no effects on the hardness enhancement but improve the homogeneity.

An annealing treatment at 600 °C for 2 hours resulted in a heterogeneous grain growth, in particular the fine grains at the primary shear zone and secondary shear zone of the original machining chips. The hardness of the stress relieved sample had a decreased hardness due to the grain growth and dislocation density reduction.

8. FURTHER WORK

The present research work has demonstrated the feasibility of ECAP for recycling Ti-6Al-4V and Ti-15V-3Cr-3Al-3Sn from machining chips at moderate temperature with assistance of back-pressure.

Macroscopic examination has suggested that minor cracks on the surface of the as-recycled samples (Ti-6Al-4V and Ti-15V-3Cr-3Al-3Sn) are inevitable: even using the highest back-pressure (250 MPa) or after maximum number of passes (8 passes). In order to remove the minor surface cracks, the application of slower strain rate (i.e. slower pressing velocity) would be beneficial. Further work is required to investigating the effect of strain rate on consolidation of the recycled product. High back-pressure in conjunction with multiple passes (e.g. 200 MPa and 8 passes) has not been studied. These working conditions will help to remove surface crack which is worth investigating further.

It has been shown that titanium oxide layers appeared at the chip/chip interface when the sample was pressed at 550 °C. According to the SAD pattern, it is speculated that the oxide is TiO_2. However, further work is required to quantify the chemical composition. The techniques that may be employed are high resolution TEM-EDS.

In this research work, the mechanical property of recycled products was only measured by microhardness. In order to comprehensively evaluate the recycled samples, mechanical testing on a macro scale, such as tensile and fatigue test, could be performed.

Very limited samples were selected for post heat treatment in this research. In order to fully understand the effect of annealing on the microstructure and microhardness of recycled samples, more heat treatment experiments are required, in particular multiple-pass samples.

Finite element analysis has been widely used to explain the consolidation process and microhardness distribution in this research work. However, most of the finite element analyses are initially for bulk materials. Further work will be required to develop simulation that describes the plastic deformation of the titanium alloy machining chips during ECAP recycling.

9. REFERENCES

[1] C. X. Cui, B. M. Hu, L. C. Zhao and S. J. Liu, “Titanium alloy production technology, market prospects and industry development,” *Mater. Design,* vol. 32, no. 3, pp. 1684-1691, (2011).

[2] D. Banerjee and J. C. Williams, “Perspectives on titanium science and technology,” *Acta Mater.,* vol. 61, no. 3, pp. 844-879, (2013).

[3] F. H. Froes, M. N. Gungor and M. A. Iman, “Cost - affordable titanium: the component fabrication perspective,” *J. Mater.,* pp. 28-31, (2007).

[4] F. H. Froes and M. A. Iman, “Cost affordable development in titanium technology and applications,” *Key Eng. Mat.,* vol. 436, pp. 1-11, (2010).

[5] A. Modrzynski, K. Grezeskowiak and R. Namyslak, “Recycling of titanium alloys in plasma furnace,” *Czech. J. Phys.,* vol. 54, no. S3, pp. C1016-C1021, (2004).

[6] R. Burkhard, W. Hoffelner and R. C. Eschenbach, “Recycling of metals from waste with thermal plasma,” *Resour. Conserv. Recy.,* vol. 10, no. 1-2, pp. 11-16, (1994).

[7] R. Chiba and M. Yoshimura, “Solid-state recycling of aluminium alloy swarf into c-channel by hot extrusion,” *J. Manuf. Process,* vol. 17, pp. 1-8, (2015).

[8] J. R. Duflou, A. E. Tekkaya, M. Haase, T. Welo, K. Vanmeensel, K. Kellens, W. Dewulf and D. Paraskevas, “Environmental assessment of solid state recycling routes for aluminium alloys: Can solid state processes significantly reduce the environmental impact of aluminium recycling?,” *CIRP Ann-Manuf. Techn.,* p. In Press, (2015).

[9] J. Miao, B. Ye, Q. D. Wang and T. Peng, “Mechanical properties and corrosion resistance of Mg–10Gd–2Y–0.5Zr alloy by hot extrusion solid-state recycling,” *J. Alloy. Compd. ,* vol. 561, pp. 184-192, (2013).

[10] N. R. Muktinutalapati, “Materials for Gas Turbines - An Overview,” in *Advances in Gas Turbine Technology*, InTech, (2011), pp. 293-314.

[11] M. Geetha, A. K. Singh, R. Asokamani and A. K. Gogia, “Ti based biomaterials,

the ultimate choice for orthopaedic implants - A review," *Prog. Mater. Sci. ,* vol. 54, pp. 397-425, (2009).

[12] R. R. Boyer, "An overview on the use of titanium in the aerospace industry," *Mater. Sci. Eng. A,* vol. 213, pp. 103-114, (1996).

[13] M. Semlitsch, "Titanium alloys for hip joint replacements," *Clin. Mater.,* vol. 2, no. 1, pp. 1-13, (1987).

[14] L. E. Murr, S. A. Quinones, S. M. Gaytan, M. I. Lopez, A. Rodela, E. Y. Martinez, D. H. Hernandez, E. Martinez, F. Medina and R. B. Wicker, "Microstructure and mechanical behavior of Ti-6Al-4V produced by rapid-layer manufacturing, for biomedical applications," *J. Mech. Behav. Biomed. Mater.,* vol. 2, no. 1, pp. 20-32, (2009).

[15] I. Inagaki, T. Takechi, Y. Shirai and N. Ariyasu, "Application and Features of Titanium for the Aerospace Industry," Nippon Steel & Sumitomo Metal Technical Report, Osaka, (2014).

[16] G. Lütjering and J. C. Williams, Titanium, New York: Springer, (2007).

[17] H. Conrad, "Effect of interstitial solutes on the strength and ductility on titanium," *Prog. Mater. Sci. ,* vol. 26, pp. 123-403, (1981).

[18] H. Okamoto, "O-Ti (Oxygen - Titanium)," *J. Phase Equilib. Diff.,* vol. 32, no. 5, pp. 473-474, (2011).

[19] C. P. Biswas, "Strain hardening of titanium by severe plastic deformation," Thesis for the Degree of Doctor of Science, Massachusetts Institute of Technology, (1973).

[20] N. E. Paton and W. A. Backofen, "Plastic deformation of titanium at elevated temperatures," *Metall. Trans. ,* vol. 1, pp. 2839-2847, (1970).

[21] I. P. Jones and W. B. Hutchinson, "Stress-state dependence of slip in Titanium-6Al-4V and other H.C.P. metals," *Acta Metall.,* vol. 29, no. 6, pp. 951-968, (1981).

[22] D. Banerjee and J. C. Williams, "Microstructure and slip character in titanium alloys," *Defence Sci. J. ,* vol. 36, no. 2, pp. 191-206, (1986).

[23] A. Akhtar, "Basal slip and twinning in α-titanium single crystals," *Metall. Trans. A,* vol. 6A, pp. 1105-1113, (1975).

[24] J. C. Williams, R. G. Baggerly and N. E. Paton, “Deformation Behavior of HCP Ti-Al Alloy Single Crystals,” *Metall. Mater. Trans. A,* vol. 33A, pp. 837-850, (2002).

[25] H. Li, D. E. Mason, Y. Yang, T. R. Bieler, M. A. Crimp and C. J. Boehlert, “Comparison of the deformation behaviour of commercially pure titanium and Ti-5Al-2.5Sn (wt.%) at 296 and 728 K,” *Philos. Mag. ,* vol. 93, no. 21, pp. 2875-2895, (2013).

[26] N. E. Paton and J. C. Williams, “Deformation of body-centered-cubic titanium--vanadium single crystals,” in *Second International Conference on the Strength of Metals and Alloys*, Pacific Grove, California, (1970).

[27] H. G. Paris, B. G. LeFevre and J. E. A. Starke, “Deformation behavior in quenched and aged beta Ti-V alloys,” *Metall. Trans. A,* vol. 7A, pp. 273-278, (1976).

[28] S. Hanada and O. Izumi, “Transmission electron microscopic observations of mechanical twinning in metastable beta titanium alloys,” *Metall. Trans A,* vol. 17A, pp. 1409-1420, (1986).

[29] H. J. Rack, D. Kalish and K. D. Fike, “Stability of as-quenched beta-III titanium alloy,” *Mater. Sci. Eng. ,* vol. 6, no. 3, pp. 181-198, (1970).

[30] X. H. Min, S. Emura, T. Nishimura, K. Tsuchiya and K. Tsuzaki, “Microstructure, tensile deformation mode and crevice corrosion resistance in Ti–10Mo–xFe alloys,” *Mater. Sci. Eng. A,* vol. 527, no. 21-22, pp. 5499-5506, (2010).

[31] G. C. Obasi, S. Birosca, J. Quinta da Fonseca and M. Preuss, “Effect of β grain growth on variant selection and texture memory effect during α → β → α phase transformation in Ti–6Al–4V,” *Acta Mater.,* vol. 60, no. 3, pp. 1048-1058, (2012).

[32] M. J. Mills, D. H. Hou, S. Suri and G. B. Viswanathan, Boundaries and Interfaces in Materials, Warrendale, Pennsylvania:: TMS, (1998).

[33] S. Suri, G. B. Viswanathan, T. Neeraj, D. -H. Hou and M. J. Mills, “Room temperature deformation and mechanisms of slip transmission in oriented single-colony crystals of an α/β titanium alloy,” *Acta Mater.,* vol. 47, no. 3, pp. 1019-1034, (1999).

[34] M. F. Savage, J. Tatalovich and M. J. Mills, “Anisotropy in the room-temperature deformation of α–β colonies in titanium alloys: role of the α–β interface,” *Philos. Mag.* , vol. 84, no. 11, pp. 1127-1154, (2004).

[35] A. A. Salem and S. L. Semiatin, “Hot deformation of Ti-6Al-4V single-colony samples,” Air Force Research Laboratory, Materials and Manufacturing Directorate, Wright-Patterson Air Force Base, OH, (2008).

[36] O. Engler and V. Randle, Introduction to Texture analysis: Macrotexture, Microtexture, and Orienation Mapping, 2nd Edition, Boca Raton: Taylor and Francis Group, (2010).

[37] M. Hatherley and W. B. Hutchinson, An Introduction to Textures in Metals, London: Institution of Metallurgists, (1979).

[38] R. Boyer, G. Welsch and E. W. Collings, Materials properties handbook: titanium alloys, Ohio: ASM International, (1994).

[39] “Titanium - Aluminum (Ti-Al) Phase Diagram,” Calculation of Phase Diagram using the CALPHAD Method, (2011). [Online]. Available: http://www.calphad.com/titanium-aluminum.html. [Accessed 04 11 2015].

[40] M. Motyka, K. Kubiak, J. Sieniawski and W. Ziaja, “Hot Plasticity of Alpha Beta Alloys,” in *Titanium Alloys - Towards Achieving Enhanced Properties for Diversified Applications, edited by A. K. M. Nurul Amin*, Rijeka, Croatia, InTech, (2012), pp. 87-116.

[41] A. W. Bowen, “Texture Stability in Heat Treated Ti-6A1-4V,” *Mater. Sci. Eng.* , vol. 29, pp. 19-28, (1977).

[42] W. J. Evans, J. P. Jone and M. T. Whittaker, “Texture effects under tension and torsion loading conditions in titanium alloys,” *Int. J. Fatigue,* vol. 27, no. 10-12, pp. 1244-1250, (2005).

[43] O. Schauerte, “Titanium in automotive production,” *Adv. Eng. Mater.* , vol. 5, no. 6, pp. 411-418, (2003).

[44] E. Breslauer and A. Rosen, “Relationship betvveen microstructure and mechanical properties in metastable β titanium 15-3 alloy,” *Mater. Sci. Tech.* , vol. 7, pp. 441-446, (1991).

[45] R. Santhosh, M. Geetha, V. K. Saxena and M. Nageswararao, “Studies on

single and duplex aging of metastable beta titanium alloy Ti–15V–3Cr–3Al–3Sn," *J. Alloy. Compd. ,* vol. 605, pp. 222-229, (2014).

[46] S. M. Kazanjian and E. A. Starke Jr. , "Effects of microstructural modification on fatigue crack growth resistance of Ti-15V-3Al-3Sn-3Cr," *Int. J. Fatigue,* vol. 21, pp. S127-S135, (1999).

[47] R. R. Boyer and R. D. Briggs, "The use of β titanium alloys in the aerospace," *J. Mater. Eng. Perform. ,* vol. 14, no. 6, pp. 681-685, (2005).

[48] H. A. El-Hofy, Fundamentals of Machining Processes: Coventional and Nonconventional Processes, 2nd Edition, Boca Raton: Taylor & Francis Group, (2014).

[49] M. P. Groover, Principles of Modern Manufacturing, 4th Edition, John Wiley & Sons Inc, (2011).

[50] E. M. Trent and P. K. Wright, Metal Cutting, 4th Edition, Boston: Butterworth Heinemann, (2000).

[51] G. Boothroyd and W. A. Knight, Fundamentals of Machining and Machine Tools, 3rd Edition, Boca Raton: Taylor & Francis Group, (2006).

[52] A. Vyas and M. C. Shaw, "Mechanics of saw-tooth chip formation in metal cutting," *J. Manuf. Sci. E-T ASME,* vol. 121, pp. 163-172, (1999).

[53] M. C. Shaw, S. O. Dirke, P. A. Smith, N. H. Cook, E. G. Leowen and C. T. Yang, "Machining titanium," MIT Report to U. S. Air Force, (1954).

[54] R. Komanduri and B. F. v. Turkovich, "New observations on the mechanism of chip formation when machining titanium alloys," *Wear,* vol. 69, pp. 179-188, (1981).

[55] M. A. Davies, Y. Chou and C. J. Evans, "On chip morphology, tool wear and cutting mechanics in finish hard turning," *Annals of the CIRP,* vol. 45, no. 1, pp. 77-82, (1996).

[56] J. Barry, G. Byrne and D. Lennon, "Observations on chip formation and acoustic emission in machining Ti–6Al–4V alloy," *Int. J. Mach. Tool Manu. ,* vol. 41, no. 7, pp. 1055-1070, (2001).

[57] K. Nakayama, "The formation of saw tooth chips," in *Proc. Int. Conf. on Prod. Engr.*, Tokyo, (1974).

[58] T. Obikawa and E. Usui, “Computational machining of titanium alloy—finite element modeling and a few results,” *J. Manuf. Sci. E-T ASME,* vol. 118, pp. 208-215, (1996).

[59] M. C. Shaw, “Sawtooth chip formation,” in *Metal Cutting Principles, 2nd Edition*, New York, Oxford University Press, Inc, (2005), pp. 544-572.

[60] J. Sun and Y. B. Guo, "A comprehensive experimental study on surface integrity by end milling Ti-6Al-4V," *J. Mater. Process. Tech.,* vol. 209, pp. 4036-4042, (2009).

[61] C. Brecher, C. J. Rosen and M. Emonts, "Laser-assisted milling of advanced materials," *Physics Procedia,* vol. 5/Part B, pp. 259-272, (2010).

[62] T. Childs, K. Maekawa, T. Obikawa and Y. Yamane, Metal machining: theory and applications, New York: John Wiley & Sons Inc., (2000).

[63] C. Veiga, J. P. Davim and A. J. R. Loureiro, “Review on machinability of titanium alloys: the process perspective,” *Rev. Adv. Mater. Sci.,* vol. 34, pp. 148-164, (2013).

[64] P. J. Bridges and B. Magnus, “Manufacture of titanium alloy components for aerospace and military applications,” in *Cost Effective Application of Titanium Alloys in Military Platforms*, Loen, Norway, (2001).

[65] E. O. Ezugwu and Z. M. Wang, “Titanium alloys and their machinability - a review,” *J. Mater. Process. Tech. ,* vol. 68, pp. 262-274, (1997).

[66] C. R. Dandekar, Y. C. Shin and J. Bames, “Machinability improvement of titanium alloy (Ti–6Al–4V) via LAM and hybrid machining,” *Int. J. Mach. Tool Manu. ,* vol. 50, no. 2, pp. 174-182, (2010).

[67] T. Nagata, W. Takahashi, M. Nishimoto, S. Kitayama and Y. W. Sugimoto, “Method for improving machinability of titanium and titanium alloys and free-cutting titanium alloys”. Patent EP0479212 A1, 8 April (1992).

[68] C. Siemers, F. Brunke, M. Stache, J. Laukart, B. Zahra, J. Rösler, P. Rokicki and K. Saksl, “Advanced titanium alloys containing micrometer-size particles,” in *12th World Conference on Titanium*, Beijing, China, (2011).

[69] M. S. Hussain, C. Siemers and J. Rösler, “Development of a free-machining titanium alloy based on Ti 6Al 2Sn 4Zr 6Mo,” *Mater. Manuf. Process. ,* vol. 28,

pp. 545-549, (2013).

[70] R. A. R. Rashid, S. Sun, G. Wang and M. S. Dargusch, “An investigation of cutting forces and cutting temperatures during laser-assisted machining of the Ti–6Cr–5Mo–5V–4Al beta titanium alloy,” *Int. J. Mach. Tool. Manu. ,* vol. 63, pp. 58-69, (2012).

[71] Y. Ayed, G. Germain, W. Ben Salem and H. Hamdi, “Experimental and numerical study of laser-assisted machining of Ti6Al4V titanium alloy,” *Finite Elem. Anal. Des. ,* vol. 92, pp. 72-79, (2014).

[72] V. I. Babitsky, A. V. Mitrofanov and V. V. Silberschmidt, “Ultrasonically assisted turning of aviation materials: simulations and experimental study,” *Ultrasonics,* vol. 42, no. 1-9, pp. 81-86, (2004).

[73] H. El-Hofy, Advanced Machining Processes: Nontraditional and Hybrid Machining Processes, New York: The McGraw-Hill Companies, Inc, (2005).

[74] V. I. Babitsky, A. N. Kalashnikov, A. Meadows and A. A. H. P. Wijesundara, “Ultrasonically assisted turning of aviation materials,” *J. Mater. Process. Tech. ,* vol. 132, no. 1-3, pp. 157-167, (2003).

[75] A. Maurotto, R. Muhammad, A. Roy and V. V. Silberschmidt, “Enhanced ultrasonically assisted turning of a β-titanium alloy,” *Ultrasonics,* vol. 53, pp. 1242-1250, (2013).

[76] V. V. Silberschmidt, S. M. A. Mahdy, M. A. Gouda, A. Naseer, A. Maurotto and A. Roy, “Surface-roughness improvement in ultrasonically assisted turning,” *Procedia CIRP,* vol. 13, pp. 49-54, (2014).

[77] R. Z. Valiev and T. G. Langdon, “Principles of equal-channel angular pressing as a processing tool for grain refinement,” *Prog. Mater. Sci.,* vol. 51, pp. 881-981, (2006).

[78] M. W. Fu, Y. W. Tham, H. H. Hng and K. B. Lim, “The grain refinement of Al-6061 via ECAE processing: Deformation behavior microstructure and property,” *Mater. Sci. Eng. A,* vol. 526, pp. 84-92, (2009).

[79] R. Z. Valiev, N. A. Krasilnikov and N. K. Tsenev, “Plastic deformation of alloys with submicron-grain structure,” *Mater. Sci. Eng. A,* vol. A137, pp. 35-40, (1991).

[80] V. M. Segal, “Materials processing by simple shear,” *Mater. Sci. Eng. A,* vol. 197, no. 2, pp. 157-164, (1995).

[81] Y. Saito, N. Tsuji, H. Utsunomiya, T. Sakai and R. G. Hong, “Ultra-fine grained bulk aluminum produced by accumulative roll-bonding (ARB) process,” *Scripta Mater.,* vol. 39, no. 9, pp. 1221-1227, (1998).

[82] Y. Saito, H. Utsunomiya, N. Tsuji and T. Sakai, “Novel ultra-high straining process for bulk materials—development of the accumulative roll-bonding (ARB) process,” *Acta Mater.,* vol. 47, no. 2, pp. 579-583, (1999).

[83] A. P. Zhilyaev and T. G. Langdon, “Using high-pressure torsion for metal processing: Fundamentals and applications,” *Prog. Mater. Sci.,* vol. 53, no. 6, pp. 893-979, (2008).

[84] A. P. Zhilyaev, G. V. Nurislamova, B. -K. Kim, M. D. Baró, J. A. Szpunar and T. G. Langdon, “Experimental parameters influencing grain refinement and microstructure evolution during high-pressure torsion,” *Acta Mater.,* vol. 51, no. 3, pp. 753-765, (2003).

[85] M. Richert, Q. Liu and N. Hansen, “Microstructure evolution over a large strain range in aluminium deformed by cyclic-extrusion-compression,” *Mater. Sci. Eng. A,* vol. 260, pp. 275-283, (1999).

[86] D. Orlov, Y. Beygelzimer, S. Synkov, V. Varyukhin, N. Tsuji and Z. Horita, “Plastic flow, structure and mechanical properties in pure Al deformed by twist extrusion,” *Mater. Sci. Eng. A,* vol. 519, no. 1-2, pp. 105-111, (2009).

[87] Y. Y. Beygelzimer, D. V. Orlov and V. N. Varyukhin, “A new severe plastic deformation method: twist extrusion,” in *Ultrafine Grained Materials II. Proceedings of a Symposium, TMS Annual Meeting*, Seattle, Washington, (2002).

[88] A. P. Zhilyaev, A. A. Gimazov, G. I. Raab and T. G. Langdon, “Using high-pressure torsion for the cold-consolidation of copper chips produced by machining,” *Mater. Sci. Eng. A,* vol. 486, no. 1-2, pp. 123-126, (2008).

[89] J. M. Cubero-Sesin and Z. Horita, “Powder consolidation of Al–10 wt% Fe alloy by High-Pressure Torsion,” *Mater. Sci. Eng. A,* vol. 558, pp. 462-471, (2012).

[90] H. Asgharzadeh, S.-H. Joo, J.-K. Lee and H. S. Kim, “Consolidation of Cu-based amorphous alloy powders by high-pressure torsion,” *J. Mater. Sci.,* vol.

50, pp. 3164-3174, (2015).

[91] T. Tsakalakos, I. A. Ovid’ko and A. K. Vasudevan, Nanostructures: Synthesis, Functional Properties and Applications, Crete, Greece: Kluwer Academic Publishers, (2003).

[92] Y. Estrin, A. Molotnikov, C. H. J. Davies and R. Lapovok, “Strain gradient plasticity modelling of high-pressure torsion,” *J. Mech. Phys. Solids,* vol. 56, pp. 1186-1202, (2008).

[93] M. Haase, N. Ben Khalifa, A. E. Tekkaya and W. Z. Misiolek, “Improving mechanical properties of chip-based aluminum extrudates by integrated extrusion and equal channel angular pressing (iECAP),” *Mater. Sci. Eng. A,* vol. 539, no. 30, pp. 194-201, (2012).

[94] A. Sivaraman and U. Chakkingal, “Flow properties of commercial purity aluminum processed by equal channel angular pressing,” *Mater. Sci. Eng. A,* vol. 487, no. 1-2, pp. 264-270, (2008).

[95] W. Wei, G. Chen, J. Wang and G. Chen, “Microstructure and tensile properties of ultrafine grained copper processed by equal-channel angular pressing,” *Rare Metals,* vol. 25, no. 6, pp. 697-703, (2006).

[96] S. V. Dobatkin, J. A. Szpunar, A. P. Zhilyaev, J. -Y. Cho and A. A. Kuznetsov, “Effect of the route and strain of equal-channel angular pressing on structure and properties of oxygen-free copper,” *Mater. Sci. Eng. A,* vol. 462, no. 1-2, pp. 132-138, (2007).

[97] Y. Li, H. P. Ng, H. Jung, H. Kim and Y. Estrin, “Enhancement of mechanical properties of grade 4 titanium by equal channel angular pressing with billet encapsulation,” *Mater. Lett. ,* vol. 114, no. 1, pp. 144-147, (2014).

[98] R. B. Figueiredo, E. R. d. C. Barbosa, X. Zhao, X. Yang, X. Liu, P. R. Cetlin and T. G. Langdon, “Improving the fatigue behavior of dental implants through processing commercial purity titanium by equal-channel angular pressing,” *Mater. Sci. Eng. A,* vol. 619, no. 1, pp. 312-318, (2014).

[99] Y. Zhao, H. Guo, M. W. Fu, Y. Ning and Z. Yao, “Fabrication of bulk ultrafine grained titanium alloy via equal channel angular pressing based thermomechanical treatment,” *Mater. Design,* vol. 46, pp. 889-894, (2013).

[100] Y. Zhao, H. Guo, Z. Shi, Z. Yao and Y. Zhang, “Microstructure evolution of

TA15 titanium alloy subjected to equal channel angular pressing and subsequent annealing at various temperatures," *J. Mater. Process. Tech.,* vol. 211, no. 8, pp. 1364-1371, (2011).

[101] M. H. Paydar, M. Reihanian, E. Bagherpour, M. Sharifzadeh, M. Zarinejad and T. A. Dean, "Consolidation of Al particles through forward extrusion-equal channel angular pressing (FE-ECAP)," *Mater. Lett. ,* vol. 62, no. 17, pp. 3266-3268, (2008).

[102] B. Martin, S. Frantisek, B. Otto and G. Requena, "ECAP vs direct extrusion techniques for consolidation of ultra fine Al particles," *Mater. Sci. Eng. A,* vol. 504, pp. 1-7, (2009).

[103] W. Hu, X. Wu, D. Sadedin and K. Xia, "Equal channel angular consolidation and deformation of titanium based alloys," *Mater. Forum,* vol. 32, pp. 29-34, (2008).

[104] X. Wu, W. Xu and K. Xia, "Pure aluminum with different grain size distributions by consolidation of particles using equal-channel angular pressing with back pressure," *Mater. Sci. Eng. A,* vol. 493, no. 1-2, pp. 241-245, (2008).

[105] B. Mani, M. Jahedi and M. H. Paydar, "Consolidation of commercial pure aluminum powder by torsional-equal channel angular pressing (T-ECAP) at room temperature," *Powder Technol. ,* vol. 219, pp. 1-8, (2012).

[106] P. Luo, D. T. McDonald, S. M. Zhu, S. Palanisamy, M. S. Dargusch and K. Xia, "Analysis of microstructure and strengthening in pure titanium recycled from machining chips by equal channel angular pressing using electron backscatter diffraction," *Mater. Sci. Eng. A,* vol. 538, pp. 252-258, (2012).

[107] P. Luo, D. T. McDonald, S. Palanisamy, M. S. Dargusch and K. Xia, "Ultrafine-grained pure Ti recycled by equal channel angular pressing with high strength and good ductility," *J. Mater. Process. Tech. ,* vol. 213, no. 3, pp. 469-476, (2013).

[108] P. Luo, D. T. McDonald, W. Xu, S. Palanisamy, M. S. Dargusch and K. Xia, "A modified Hall–Petch relationship in ultrafine-grained titanium recycled from chips by equal channel angular pressing," *Scripta Mater. ,* vol. 66, no. 10, pp. 785-788, (2012).

[109] A. V. Nagasekhar, U. Chakkingal and P. Venugopal, "Candidature of equal

angular pressing for processing of tubular commercial purity-titanium," *J. Mater. Process. Tech.* , vol. 173, pp. 53-60, (2006).

[110] D. H. Kang and T. W. Kim, "Mechanical behavior and microstructural evolution of commercially pure titanium in enhanced multi-pass equal channel angular pressing and cold extrusion," *Mater. Design,* vol. 30, pp. 554-560, (2010).

[111] V. M. Segal, "Engineering and commercialization of equal channel angular extrusion (ECAE)," *Mater. Sci. Eng. A,* vol. 386, no. 1-2, pp. 269-276, (2004).

[112] S. Ferrasse, V. M. Segal, F. Alford, J. Kardokus and S. Strothers, "Scale up and application of equal-channel angular extrusion for the electronics and aerospace industries," *Mater. Sci. Eng. A,* vol. 493, no. 1-2, pp. 130-140, (2008).

[113] Y. Iwahashi, J. T. Wang, Z. Horita, M. Nemoto and T. G. Langdon, "Principle of equal-channel angular pressing for the processing of ultra-fine grained materials," *Scripta Mater.* , vol. 35, no. 2, pp. 143-146, (1996).

[114] K. Furuno, H. Akamatsu, K. Oh-ishi, M. Furukawa, Z. Horita and T. G. Langdon, "Microstructural development in equal-channel angular pressing using a 60° die," *Acta Mater.* , vol. 52, no. 9, pp. 2494-2507, (2004).

[115] S. L. Semiatin, V. M. Segal, R. E. Goforth, N. D. Frey and D. P. DeLo, "Workability of commercial-purity titanium and 4340 steel during equal channel angular extrusion at cold-working temperatures," *Metall. Mater. Trans. A,* vol. 30A, pp. 1425-1435, (1999).

[116] X. C. Zhao, W. J. Fu, X. R. Yang and T. G. Langdon, "Microstructure and properties of pure titanium processed by equal-channel angular pressing at room temperature," *Scripta Mater.,* vol. 59, no. 5, pp. 542-545, (2008).

[117] K. Nakashima, Z. Horita, M. Nemoto and T. G. Langdon, "Influence of channel angle on the development of ultrafine grains in equal-channel angular pressing," *Acta Mater.* , vol. 46, no. 5, pp. 1589-1599, (1998).

[118] H. S. Kim, M. H. Seo and S. I. Hong, "On the die corner gap formation in equal channel angular pressing," *Mater. Sci. Eng. A,* vol. 291, no. 1-2, pp. 86-90, (2000).

[119] P. B. Prangnell, C. Harris and S. M. Roberts, "Finite element modelling of equal channel angular extrusion," *Scripta Mater.* , vol. 37, pp. 983-989, (1997).

[120] J. Y. Suh, H. S. Kim, J. W. Park and J. Y. Chang, “Finite element analysis of material flow in equal channel angular pressing,” *Scripta Mater.,* vol. 44, no. 4, pp. 677-681, (2001).

[121] S. L. Semiatin, D. P. DeLo and E. B. Shell, “The effect of material properties and tooling design on deformation and fracture during equal channel angular extrusion,” *Acta Mater. ,* vol. 48, no. 8, pp. 1841-1851, (2000).

[122] A. Shan, I. G. Moon, H. S. Ko and J. W. Park, “Direct observation of shear deformation during equal channel angular pressing of pure aluminum,” *Scripta Mater.,* vol. 41, no. 4, pp. 353-357, (1999).

[123] C. Xu and T. G. Langdon, “Influence of a round corner die on flow homogeneity in ECA pressing,” *Scripta Mater.,* vol. 48, no. 1, pp. 1-4, (2003).

[124] I. Balasundar, M. S. Rao and T. Raghu, “Equal channel angular pressing die to extrude a variety of materials,” *Mater. Design,* vol. 30, no. 4, pp. 1050-1059, (2009).

[125] P. B. Berbon, M. Furukawa, Z. Horita, M. Nemoto and T. G. Langdon, “Influence of pressing speed on microstructural development in equal-channel angular pressing,” *Metall. Mater. Trans. A,* vol. 30A, pp. 1989-1997, (1999).

[126] I. Y. Kim, J. Y. Kim, D. H. Shin and K. T. Park, “Effects of grain size and pressing speed on the deformation mode of commercially pure Ti during equal channel angular pressing,” *Metall. Mater. Trans. A,* vol. 34A, pp. 1555-1558, (2003).

[127] D. Yamaguchi, Z. Horita, M. Nemoto and T. G. Langdon, “Significance of adiabatic heating in equal-channel angular pressing,” *Scripta Mater.,* vol. 41, no. 8, pp. 791-796, (1999).

[128] D. H. Shin, J. J. Pak, Y. K. Kim, K. T. Park and Y. S. Kim, “Effect of pressing temperature on microstructure and tensile behavior of low carbon steels processed by equal channel angular pressing,” *Mater. Sci. Eng. A,* vol. 323, no. 1-2, pp. 409-415, (2002).

[129] A. Yamashita, D. Yamaguchi, Z. Horita and T. G. Langdon, “Influence of pressing temperature on microstructural development in equal-channel angular pressing,” *Mater. Sci. Eng. A,* vol. 287, no. 1, pp. 100-106, (2000).

[130] D. P. DeLo and S. L. Semiatin, “Hot working of Ti-6Al-4V via equal channel

angular extrusion," *Metall. Mater. Trans. A,* vol. 30A, pp. 2473-2481, (1999).

[131] Y. G. Ko, W. S. Jung, D. H. Shin and C. S. Lee, "Effects of temperature and initial microstructure on the equal channel angular pressing of Ti–6Al–4V alloy," *Scripta Mater. ,* vol. 48, no. 2, pp. 197-202, (2003).

[132] I. Kim, J. Kim, D. H. Shin, C. S. Lee and S. K. Hwang, "Effects of equal channel angular pressing temperature on deformation structures of pure Ti," *Mater. Sci. Eng. A,* vol. 342, no. 1-2, pp. 302-310, (2003).

[133] Y. C. Chen, Y. Y. Huang, C. P. Chang and P. W. Kao, "The effect of extrusion temperature on the development of deformation microstructures in 5052 aluminium alloy processed by equal channel angular extrusion," *Acta Mater. ,* vol. 51, no. 7, pp. 2005-2015, (2003).

[134] W. H. Huang, C. Y. Yu, P. W. Kao and C. P. Chang, "The effect of strain path and temperature on the microstructure developed in copper processed by ECAE," *Mater. Sci. Eng. A,* vol. 366, no. 2, pp. 221-228, (2004).

[135] R. K. Oruganti, P. R. Subramanian, J. S. Marte, M. F. Gigliotti and S. Amancherla, "Effect of friction, backpressure and strain rate sensitivity on material flow during equal channel angular extrusion," *Mater. Sci. Eng. A,* vol. 406, no. 1-2, pp. 102-109, (2005).

[136] R. Y. Lapovok, "The role of back-pressure in equal channel angular extrusion," *J. Mater. Sci.,* vol. 40, pp. 341-346, (2005).

[137] V. V. Stolyarov, R. Lapovok, I. G. Brodova and P. F. Thomson, "Ultrafine-grained Al–5 wt.% Fe alloy processed by ECAP with backpressure," *Mater. Sci. Eng. A,* vol. 357, no. 1-2, pp. 159-167, (2003).

[138] I. H. Son, J. H. Lee and Y. T. Im, "Finite element investigation of equal channel angular extrusion with back pressure," *J. Mater. Process. Tech.,* vol. 171, no. 3, pp. 480-487, (2006).

[139] F. Kang, J. T. Wang, Y. L. Su and K. N. Xia, "Finite element analysis of the effect of back pressure during equal channel angular pressing," *J. Mater. Sci. ,* vol. 42, pp. 1491-1500, (2007).

[140] Y. Iwahashi, Z. Horita, M. Nemoto and T. G. Langdon, "The process of grain refinement in equal-channel angular pressing," *Acta Mater. ,* vol. 46, no. 9, pp. 3317-3331, (1998).

[141] Y. G. Kim, Y. G. Ko, D. H. Shin and S. Lee, “Effect of equal-channel angular pressing routes on high-strain-rate deformation behavior of ultra-fine-grained aluminum alloy,” *Acta Mater.,* vol. 58, no. 7, pp. 2545-2554, (2010).

[142] D. H. Shin, I. Kim, J. Kim, Y. S. Kim and S. L. Semiatin, “Microstructure development during equal-channel angular pressing of titanium,” *Acta Mater.,* vol. 51, no. 4, pp. 983-996, (2003).

[143] S. Suwas, B. Beausir, L. S. Tóth, J. -J. Fundenberger and G. Gottstein, “Texture evolution in commercially pure titanium after warm equal channel angular extrusion,” *Acta Mater.,* vol. 59, no. 3, pp. 1121-1133, (2011).

[144] S. Xu, G. Zhao, Y. Luan and Y. Guan, “Numerical studies on processing routes and deformation mechanism of multi-pass equal channel angular pressing processes,” *J. Mater. Process. Tech.,* vol. 176, no. 1-3, pp. 251-259, (2006).

[145] K. Oh-Ishi, Z. Horita, M. Furukawa, M. Nemoto and T. G. Langdon, “Optimizing the rotation conditions for grain reginement in equal-channel angular pressing,” *Metall. Mater. Trans. A ,* vol. 29A, pp. 2011-2013, (1998).

[146] M. Furukawa, Y. Iwahashi, Z. Horita, M. Nemoto and T. G. Langdon, “The shearing characteristics associated with equal-channel angular pressing,” *Mater. Sci. Eng. A,* vol. 257, no. 2, pp. 328-332, (1998).

[147] B. Beausir, L. S. Tóth and K. W. Neale, “Ideal orientations and persistence characteristics of hexagonal close packed crystals in simple shear,” *Acta Mater.,* vol. 55, no. 8, pp. 2695-2705, (2007).

[148] B. Beausir, S. Suwas, L. S. Tóth, K. W. Neale and J. -J. Fundenberger, “Analysis of texture evolution in magnesium during equal channel angular extrusion,” *Acta Mater.,* vol. 56, pp. 200-214, (2008).

[149] C. S. Meredith and A. S. Khan, “Texture evolution and anisotropy in the thermo-mechanical response of UFG Ti processed via equal channel angular pressing,” *Int. J. Plast.,* Vols. 30-31, pp. 202-217, (2012).

[150] A. Jäger, V. Gärtnerova and K. Tesař, “Microstructure and anisotropy of the mechanical properties in commercially pure titanium after equal channel angular pressing with back pressure at room temperature,” *Mater. Sci. Eng. A,* vol. 644, pp. 114-120, (2015).

[151] L. Wang, Y. C. Wang, A. P. Zhilyaev, A. V. Korznikov, S. K. Li, E. Korznikova

and T. G. Langdon, “Microstructure and texture evolution in ultrafine-grained pure Ti processed by equal-channel angular pressing with subsequent dynamic compression,” *Scripta Mater.,* vol. 77, pp. 33-36, (2014).

[152] G. G. Yapici, I. Karaman and Z. P. Luo, “Mechanical twinning and texture evolution in severely deformed Ti–6Al–4V at high temperatures,” *Acta Mater.,* vol. 54, no. 14, pp. 3755-3771, (2006).

[153] G. G. Yapici and I. Karaman, “Common trends in texture evolution of ultra-fine-grained hcp materials during equal channel angular extrusion,” *Mater. Sci. Eng. A,* vol. 503, no. 1-2, pp. 78-81, (2009).

[154] S. Xiang, K. Matsuki, N. Takatsuji, M. Tokizawa, T. Yokote, J. Kusui and K. Yokoe, “Microstructure and mechanical properties of PM 2024Al-3Fe-5Ni alloy consolidated by a new process, equal channel angular pressing,” *J. Mater. Sci. Lett.,* vol. 16, pp. 1725-1727, (1997).

[155] K. Matsuki, T. Aida, T. Takeuchi, J. Kusui and K. Yokoe, “Microstructural characteristics and superplastic-like behavior in aluminum powder alloy consolidated by equal-channel angular pressing,” *Acta Mater. ,* vol. 48, no. 10, pp. 2625-2632, (2000).

[156] K. Xia and X. Wu, “Back pressure equal channel angular consolidation of pure Al particles,” *Scripta Mater.,* vol. 53, no. 11, pp. 1225-1229, (2005).

[157] D. T. McDonald, P. Luo, S. Palanisamy, M. S. Dargusch and K. Xia, “Ti-6Al-4V recycled from machining chips by equal channel angular pressing,” *Key Eng. Mat. ,* vol. 520, pp. 295-300, (2012).

[158] R. Muhammad, A. Maurotto, M. Demiral, A. Roy and V. V. Silberschmidt, “Thermally enhanced ultrasonically assisted machining of Ti alloy,” *CIRP J. Manuf. Sci. Tech. ,* vol. 7, no. 2, pp. 159-167, (2014).

[159] R. Muhammad, M. S. Hussain, A. Maurotto, C. Siemers, A. Roy and V. V. Silberschmidt, “Analysis of a free machining α+β titanium alloy using conventionaland ultrasonically assisted turning,” *J. Mater. Process. Tech. ,* vol. 214, pp. 906-915, (2014).

[160] S. J. Oh and S. B. Kang, “Analysis of the billet deformation during equal channel angular pressing,” *Mater. Sci. Eng. A,* vol. 343, no. 1-2, pp. 107-115, (2003).

[161] P. Rokicki, Z. Spotz, L. Fusova, K. Saksl, C. Sieners and B. Zahra, "Chip formation process of Ti-15V-3Al-3Sn-3Cr alloy," *19th International Conference on Metallurgy and Materials,* vol. METAL, pp. 844-849, (2010).

[162] P. Rokicki, K. Nowag, Z. Spotz, L. Fusova, K. Saksl, R. Ghisleni and C. Sieners, "Microstructural characteristic of Ti-15V-3Al-3Sn-3Cr chips," *International Journal of Earth Sciences,* vol. 55, pp. 452-456, (2010).

[163] M. P. Groover, Fundamentals of Modern Manufacturing Materials, Processes, and Systems, 3rd Edition ed., John Wiley & Sons INC, 2007.

[164] S. Swaminathan, M. R. Shankar, S. Lee, J. Hwang, A. H. King, R. F. Kezar, B. C. Rao, T. L. Brown, S. Chandrasekar, W. D. Compton and K. P. Trumble, "Large strain deformation and ultrafine grained materials by machining," *Mater. Sci. Eng. A,* Vols. 410-411, pp. 358-363, (2005).

[165] U. F. Kocks and H. Mecking, “Physics and phenomenology of strain hardening: the FCC case,” *Prog. Mater. Sci.,* vol. 48, no. 3, pp. 171-273, (2003).

[166] Y. Estrin, L. S. Tóth, A. Molinari and Y. Bréchet , “A dislocation-based model for all hardening stages in large strain deformation,” *Acta Mater.,* vol. 46, no. 15, pp. 5509-5522, (1998).

[167] W. J. Deng, W. Xia, C. Li and Y. Tang, "Ultrafine grained material produced by machining," *Mater. Manuf. Process.,* vol. 25, pp. 355-359, (2010).

[168] R. Muhammad, A. Maurotto, A. Roy and V. V. Silberschmidt, “Hot ultrasonically assisted turning of β-Ti alloy,” *Procedia CIRP,* vol. 1, pp. 336-341, (2012).

[169] C. Z. Duan, M. J. Wang and Y. J. Cai, "Mechanism of material softening primary shear zone during serrated chip formation in high speed machining of high strength steel," *Key Eng. Mat. ,* Vols. 407-408, pp. 504-508, (2009).

[170] J. D. P. Velásquez, B. Bolle, P. Chevrier, G. Geandier and A. Tidu, "Metallurgical study on chips obtained by high speed machining of a Ti-6 wt.%Al-4 wt.%V alloy," *Mater. Sci. Eng. A,* Vols. 452-453, pp. 469-474, (2007).

[171] M. Haase, N. B. Khalifa, A. E. Tekkaya and W. Z. Misiolek, “Improving mechanical properties of chip-based aluminum extrudates by integrated extrusion and equal channel angular pressing (iECAP),” *Mater. Sci. Eng., A,* vol. 539, pp. 194-204, (2012).

[172] W. Z. Misiolek, M. Haase, N. B. Khalifa, A. E. Tekkaya and M. Kleiner, “High quality extrudates from alunimum chips by new billet compaction and deformation routes,” *CIRP Ann. - Manuf. Techn.,* vol. 61, no. 1, pp. 239-242, (2012).

[173] K. Kuzman, I. Kacmarcik, T. Pepelnjak, M. Plancak and D. Vilotic, “Experimental consolidation of aluminium chips by cold compression,” *J. Prod. Eng.,* vol. 15, no. 2, pp. 79-82, 2012.

[174] A. Hyodo, C. Bolfarini and T. T. Ishikawa, “Chemistry and tensile properties of a recycled AA7050 via spray forming and ECAP/E,” *Mat. Res.,* vol. 15, no. 5, pp. 739-748, (2012).

[175] T. Ying, M. Y. Zheng, X. S. Hu and K. Wu, “Recycling of AZ91 Mg alloy through consolidation of machined chips by extrusion and ECAP,” *Trans. Nonferrous Met. Soc. China,* vol. 20, no. Supplement 2, pp. s604-s607, (2010).

[176] T. Aida, N. Takatsuji, K. Matsuki, S. Kamado and Y. Kojima, “Homogeneous consolidation process by ECAP for AZ31 cutting chips,” *J. Jpn. Inst. Light Met.,* vol. 54, no. 11, pp. 532-537, 2004.

[177] Y. G. Ko, D. Y. Hwang, D. H. Shin, S. Lee and C. S. Lee, “Factors influencing the equal-channel angular pressing of Ti–6Al–4V alloy having lamellar microstructure,” *Mater. Sci. Eng., A,* vol. 493, no. 1-2, pp. 164-169, (2008).

[178] R. Lapovok, D. Tomus and B. C. Muddle, “Low-temperature compaction of Ti–6Al–4V powder using equal channel angular extrusion with back pressure,” *Mater. Sci. Eng., A,* vol. 490, no. 1-2, pp. 171-180, (2008).

[179] R. Y. Lapovok and P. F. Thomson, “Densification of magnesium particles by ECAP with a back-pressure,” in *Nanomaterials by Severe Plastic Deformation*, Vienna, Austria, 2002.

[180] D. P. Delo and H. R. Piehler, “Early stage consolidation mechanisms during hot isostatic pressing of Ti-6Al-4V powder compacts,” *Acta Mater.,* vol. 47, no. 9, pp. 2841-2852, (1999).

[181] R. Y. Lapovok, “The positive role of back-pressure in equal channel angular extrusion,” *Mater. Sci. Forum,* vol. 37, pp. 503-504, (2006).

[182] E. Ceretti, L. Fratini, F. Gagliardi and C. Giardini, “A new approach to study material bonding in extrusion porthole dies,” *CIRP Ann. - Manuf. Techn.,* vol.

58, pp. 259-262, (2009).

[183] J. B. Fogagnolo, E. M. Ruiz-Navas, M. A. Simón and M. A. Martinez, “Recycling of aluminium alloy and aluminium matrix composite chips by pressing and hot extrusion,” *J. Mater. Process. Technol. ,* Vols. 143-144, pp. 792-795, (2003).

[184] C. Xu, M. Furukawa, Z. Horita and T. G. Langdon, “The evolution of homogeneity and grain refinement during equal-channel angular pressing: A model for grain refinement in ECAP,” *Mater. Sci. Eng., A,* vol. 398, no. 1-2, pp. 66-76, (2005).

[185] R. Z. Valiew, Y. V. Ivanisenko, E. F. Rauch and B. Baudelet, “Structure and deformation behaviour of Armco iron subjected to severe plastic deformation,” *Acta Mater. ,* vol. 44, no. 12, pp. 4705-4712, (1996).

[186] G. G. Yapici, I. Karaman, Z. P. Luo and H. Rack, “Microstructure and mechanical properties of severely deformed powder processed Ti–6Al–4V using equal channel angular extrusion,” *Scripta Mater.,* vol. 49, no. 10, pp. 1021-1027, (2003).

[187] P. G. Partridge, “The crystallography and deformation modes of hexagonal close-packed metals,” *Int. Mater. Rev.,* vol. 12, no. 1, pp. 169-194, (1967).

[188] D. H. Shin, B. C. Kim, K. T. Park and W. Y. Choo, “Microstructural changes in equal channel angular pressed low carbon steel by static annealing,” *Acta Mater.,* vol. 48, no. 12, pp. 3245-3252, (2000).

[189] Y. Chino, T. Hoshika and J. S. Lee, “Mechanical properties of AZ31 Mg alloy recycled by severe deformation,” *J. Mater. Res.,* vol. 21, no. 3, pp. 754-760, (2006).

[190] P. Luo, H. Xie, M. Paladugu, S. Palanisamy, M. S. Dargusch and K. Xia, “Recycling of titanium machining chips by severe plastic deformation consolidation,” *J. Mater. Sci.,* vol. 45, pp. 4606-4612, (2010).

[191] C. Hertl, E. Werner, R. Thull and U. Gbureck, “Oxygen diffusion hardening of cp-titanium for biomedical applications,” *Biomed. Mater. ,* vol. 5, pp. 1-8, (2010).

[192] F. Kang, J. Q. Liu, J. T. Wang and X. Zhao, “The effect of hydrostatic pressure on the activation of non-basal slip in a magnesium alloy,” *Scripta Mater.,* vol.

61, no. 8, pp. 844-847, (2009).

[193] F. Kang, J. Q. Liu, J. T. Wang and X. Zhao, “Equal channel angular pressing of a Mg–3Al–1Zn alloy with back pressure,” *Adv. Eng. Mater.,* vol. 12, pp. 730-734, (2010).

[194] A. Panigrahi, N. Scheerbaum, P. Chekhonin, J. Scharnweber, B. Beausir, M. Hockauf, S. Sankaran and W. Skrotzki, “Effect of back pressure on material flow and texture in ECAP of aluminum,” in *6th International Conference on Nanomaterials by Severe Plastic Deformation the IOP Conference Series - Materials Science and Engineering*, Metz, (2014).

[195] S. L. Semiatin, P. B. Berbon and T. G. Langdon, “Deformation heating and its effect on grain size evolution during equal channel angular extrusion,” *Scripta Mater.,* vol. 44, pp. 135-140, (2001).

[196] S. Suwas, G. Gottstein and R. Kumar, “Evolution of crystallographic texture during equal channel angular extrusion (ECAE) and its effects on secondary processing of magnesium,” *Mater. Sci. Eng., A,* vol. 471, pp. 1-14, (2007).

[197] S. R. Agnew, P. Mehrotra, T. M. Lillo, G. M. Stoica and P. K. Liaw, “Crystallographic texture evolution of three wrought magnesium alloys during equal channel angular extrusion,” *Mater. Sci. Eng., A ,* vol. 408, pp. 72-78, (2005).

[198] S. H. Yu, Y. B. Chun, S. K. Hwang and D. H. Shin, “Texture development and Monte-Carlo simulation of microstructure evolution in pure Zr grain-refined by equal channel angular pressing,” *Philos. Mag.,* vol. 85, pp. 345-371, (2005).

[199] R. B. Figueiredo, I. J. Beyerlein, A. P. Zhiyaev and T. G. Langdon, “Evolution of texture in a magnesium alloy processed by ECAP through dies with different angles,” *Mater. Sci. Eng. A,* vol. 527, no. 7-8, pp. 1709-1718, (2010).

[200] I. J. Beyerlein, R. D. Field, K. T. Hartwig and C. T. Necker, “Texture development in two-pass ECAE-processed beryllium,” *J. Mater. Sci.,* vol. 43, pp. 7465-7473, (2008).

[201] M. Al-Maharbi, I. Karaman, I. J. Beyerlein, D. Foley, K. T. Hartwig, L. J. Kecskes and S. N. Mathaudhu, “Microstructure, crystallographic texture, and plastic anisotropy evolution in an Mg alloy during equal channel angular extrusion processing,” *Mater. Sci. Eng. A,* vol. 528, no. 25-26, pp. 7616-7627,

(2011).

[202] T. Sakai and M. E. Fine, “Plastic deformation of Ti-Al single crystals in prismatic slip,” *Acta Metall.,* vol. 22, no. 11, pp. 1359-1372, (1974).

[203] S. M. Kim, J. Kim, D. H. Shin, Y. G. Ko, C. S. Lee and S. L. Semiatin, “Microstructure development and segment formation during ECA pressing of Ti–6Al–4V alloy,” *Scripta Mater.,* vol. 50, no. 7, pp. 927-930, (2004).

[204] D. H. Shin, I. Kim, J. Kim and S. L. Semiatin, “Microstructure development during equal-channel angular pressing of titanium,” *Acta Mater.,* vol. 51, no. 4, pp. 983-996, (2003).

[205] S. R. Agnew, P. Mehrotra, T. M. Lillo, G. M. Stoica and P. K. Liaw, “Texture evolution of five wrought magnesium alloys during route A equal channel angular extrusion: Experiments and simulations,” *Acta Mater.,* vol. 53, p. 3135–3146, (2005).

[206] I. J. Beyerlein, S. Li and D. J. Alexander, “Modeling the plastic anisotropy in pure copper after one pass of ECAE,” *Mater. Sci. Eng., A,* Vols. 410-411, pp. 201-206, (2005).

[207] R. A. Massion, L. S. Tóth and J. -P. Mathieu, “Modeling of deformation and texture development of copper in a 120° ECAE die,” *Scripta Mater.,* vol. 54, pp. 1667-1672, (2006).

[208] Y. Nishida, T. Ando, M. Nagase, S. Lim, I. Shigematsu and A. Watazu, “Billet temperature rise during equal-channel angular pressing,” *Scripta Mater.,* vol. 46, pp. 211-216, (2002).

[209] Q. X. Pei, B. H. Hu, C. Lu and Y. Y. Wang, “A finite element study of the temperature rise during equal channel angular pressing,” *Scripta Mater.,* vol. 49, pp. 303-308, (2003).

[210] Y. B. Xu, J. H. Zhang, Y. L. Bai and M. A. Meyers, “Shear localization in dynamic deformation: microstructural evolution,” *Metall. Mater. Trans. A,* vol. 39A, pp. 811-843, (2008).

[211] B. S. Moon, H. S. Kim and S. I. Hong, “Plastic flow and deformation homogeneity of 6061 Al during equal channel angular pressing,” *Scripta Mater.,* vol. 46, pp. 131-136, (2002).

[212] C. Xu, K. Xia and T. G. Langdon, “The role of back pressure in the processing of pure aluminum by equal-channel angular pressing,” *Acta Mater.,* vol. 55, pp. 2351-2360, (2007).

[213] Y. Iwahashi, Z. Horita, M. Nemoto and T. G. Langdon, “An investigation of microstructural evolution during equal-channel angular pressing,” *Acta Mater.,* vol. 45, no. 11, pp. 4733-4741, (1997).

[214] F. D. Torre, R. Lapovok, J. Sandlin, P. F. Thomson, C. H. J. Davies and E. V. Pereloma, “Microstructures and properties of copper processed by equal channel angular extrusion for 1–16 passes,” *Acta Mater.,* vol. 52, no. 16, pp. 4819-4832, (2004).

[215] D. V. Gunderov, A. V. Polyakov, I. P. Semenova, G. I. Raab, A. A. Churakova, E. I. Gimaltdinova, I. Sabirov, J. Segurado, V. D. Sitdikov, I. V. Alexandrov, N. A. Enikeev and R. Z. Valiev, “Evolution of microstructure, macrotexture and mechanical properties of commercially pure Ti during ECAP-conform processing and drawing,” *Mater. Sci. Eng., A,* vol. 562, no. 1, pp. 128-136, (2013).

[216] R. Jahadi, M. Sedighi and H. Jahed, “ECAP effect on the micro-structure and mechanical properties of AM30 magnesium alloy,” *Mater. Sci. Eng., A,* vol. 593, no. 21, pp. 178-184, (2014).

[217] Y. Iwahashi, Z. Horita, M. Nemoto and T. G. Langdon, “Factors influencing the equilibrium grain size in equal-channel angular pressing: role of Mg additions to aluminum,” *Metall. Mater. Trans. A,* vol. 29A, pp. 2503-2510, (1998).

[218] T. Makino, R. Chikaizumi, T. Nagaoka and T. Furuhara, “Microstructure development in a thermomechanically processed Ti-15V-3Cr-3Sn-3Al alloy,” *Mater. Sci. Eng. A,* vol. 213, pp. 51-60, (1996).

[219] S. Nag, R. Banerjee, R. Srinivasan, J. Y. Hwang, M. Harper and H. L. Fraser, “ω-Assisted nucleation and growth of α precipitates in the Ti–5Al–5Mo–5V–3Cr–0.5Fe β titanium alloy,” *Acta Mater.,* vol. 57, pp. 2136-2147, (2009).

[220] T. Furuhara and T. Maki, “Variant selection in heterogeneous nucleation on defects in diffusional phase transformation and precipitation,” *Mater. Sci. Eng. A,* vol. 312, no. 1-2, pp. 145-154, (2001).

[221] Q. Guo, Q. Wang, X. L. Han, D. L. Sun, X. Wang and G. H. Wu, “Crystalline

characteristics of alpha precipitates in Ti-15V-3Sn-3Al-3Cr alloy," *Micron,* vol. 41, pp. 565-570, (2010).

[222] T. Li, D. Kent, G. Sha, M. S. Dargusch and J. M. Cairney, "Precipitation of the α-phase in an ultrafine grained beta-titanium alloy processed by severe plastic deformation," *Mater. Sci. Eng. A,* vol. 605, pp. 144-150, (2014).

[223] H. H. Hsu, Y. C. Wu and L. W. Tsay, "Notch brittleness of Ti–15V–3Cr–3Sn–3Al alloys," *Mater. Sci. Eng. A,* vol. 545, pp. 20-25, (2012).

[224] R. Santhosh, M. Geetha, V. K. Saxena and M. Nageswara Rao, "Effect of duplex aging on microstructure and mechanical behavior of beta titanium alloy Ti–15V–3Cr–3Al–3Sn under unidirectional and cyclic loading conditions," *Int. J. Fatigue,* vol. 73, pp. 88-97, (2015).

[225] W. Xu, X. Wu, M. Stoica, M. Calin, U. Kuhn, J. Eckert and K. Xia, "On the formation of an ultrafine-duplex structure facilitated by severe shear deformation in a Ti–20Mo β-type titanium alloy," *Acta Mater.,* vol. 60, pp. 5067-5078, (2012).

[226] W. Xu, D. P. Edwards, X. Wu, M. Stoica, M. Calin, U. Kühn, J. Eckert and K. Xia, "Promoting nano/ultrafine-duplex structure via accelerated α precipitation in a β-type titanium alloy severely deformed by high-pressure torsion," *Scripta Mater.,* vol. 68, no. 1, pp. 67-70, (2013).

[227] T. Inaba, K. Ameyama and M. Tokizane, "Formation of (α+β) microduplex structure in a Ti-15V-3Cr-3Sn-3Al alloy," *ISIJ International,* vol. 31, no. 8, pp. 792-798, (1991).

[228] R. Z. Valiev, R. K. Islamgaliev and I. V. Alexandrov, "Bulk nanostructured materials from severe plastic deformation," *Prog. Mater. Sci. ,* vol. 45, pp. 103-189, (2000).

[229] X. Sauvage, G. Wilde, S. V. Divinski, Z. Horita and R. Z. Valiev, "Grain boundaries in ultrafine grained materials processed by severe plastic deformation and related phenomena," *Mater. Sci. Eng. A,* vol. 540, pp. 1-12, (2012).

[230] X. Sauvage, F. Wetscher and P. Pareige, "Mechanical alloying of Cu and Fe induced by severe plastic deformation of a Cu–Fe composite," *Acta Mater.,* vol. 53, pp. 2127-2135, (2005).

[231] S. V. Divinski, G. Reglitz, H. Rösner, Y. Estrin and G. Wilde, “Ultra-fast diffusion channels in pure Ni severely deformed by equal-channel angular pressing,” *Acta Mater.,* vol. 59, pp. 1974-1985, (2011).

[232] S. V. Divinski, J. Ribbe, D. Baither, G. Schmitz, G. Reglitz, H. Rösner , K. Sato, Y. Estrin and G. Wilde, “Nano- and micro-scale free volume in ultrafine grained Cu–1 wt.%Pb alloy deformed by equal channel angular pressing,” *Acta Mater.,* vol. 57, pp. 5706-5717, (2009).

[233] M. Yan, S. D. Luo, G. B. Schaffer and M. Qian, “TEM and XRD characterisation of commercially pure α-Ti made by powder metallurgy and casting,” *Mater. Lett. ,* vol. 72, pp. 64-67, (2012).

[234] J. Ma and Q. Wang, “Aging characterization and application of Ti–15–3 alloy,” *Mater. Sci. Eng. A,* vol. 243, no. 1-2, pp. 150-154, (1998).

[235] H. C. Lin and L. M. Wang, “Improved mechanical properties of Ti–15V–3Cr–3Sn–3Al alloy by electron beam welding process plus heat treatments and its microstructure evolution,” *Mater. Chem. Phys.,* vol. 126, no. 3, pp. 891-897, (2011).

[236] V. Sklenicka, J. Dvorak, M. Svoboda, P. Kral and M. Kvapilova, “Equal-channel angular pressing and creep in ultrafine-grained aluminium and its alloys,” in *Aluminium Alloys - New Trends in Fabrication and Applications*, InTech, (2012), p. Chapter 1.

[237] J. Stráská, M. Janeček, J. Čížek, J. Stráský and B. Hadzima, “Microstructure stability of ultra-fine grained magnesium alloy AZ31 processed by extrusion and equal-channel angular pressing (EX–ECAP),” *Mater. Charact.,* vol. 94, pp. 69-79, (2014).

[238] G. T. Higgins, “Grain-boundary migration and grain growth,” *Metal Sci.,* vol. 8, pp. 143-150, (1974).

[239] L. Z. Zhou and J. T. Guo, “Grain growth and kinetics for nanocrystalline NiAl,” *Scripta Metall.,* vol. 40, no. 2, pp. 139-144, (1999).

[240] P. Cao, L. Lu and M. O. Lai, “Grain growth and kinetics for nanocrystalline magnesium alloy produced by mechanical alloying,” *Mater. Res. Bull.,* vol. 36, pp. 981-988, (2001).

[241] M. A. Thein, L. Lu and M. O. Lai, “Kinetics of grain growth in nanocrystalline

magnesium-based metal–metal composite synthesized by mechanical alloying," *Compos. Sci. Technol.,* vol. 66, pp. 531-537, (2006).

10. APPENDIX

A. Configuration of Hydraulic System

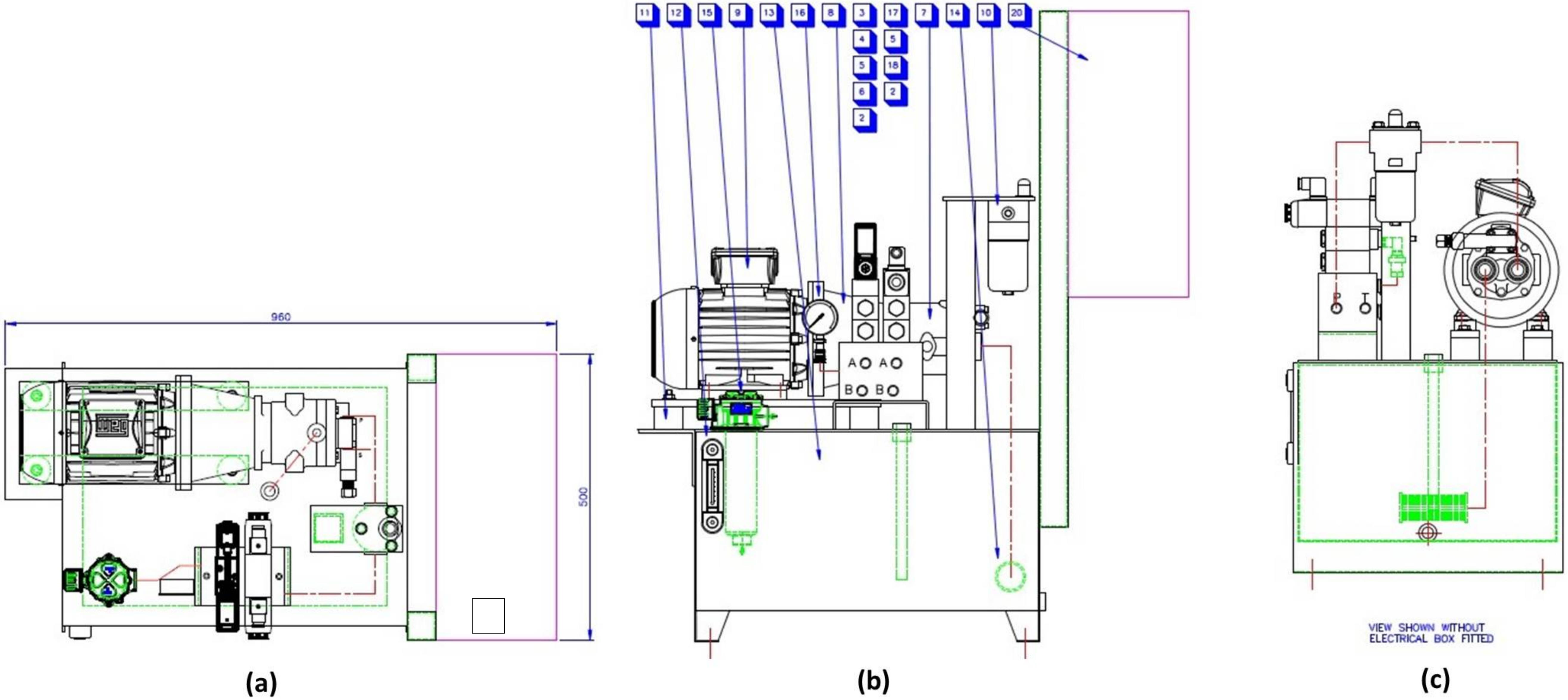

Fig. A. 1 Configuration of hydraulic machine (a) Top view, (b) front view and (c) left

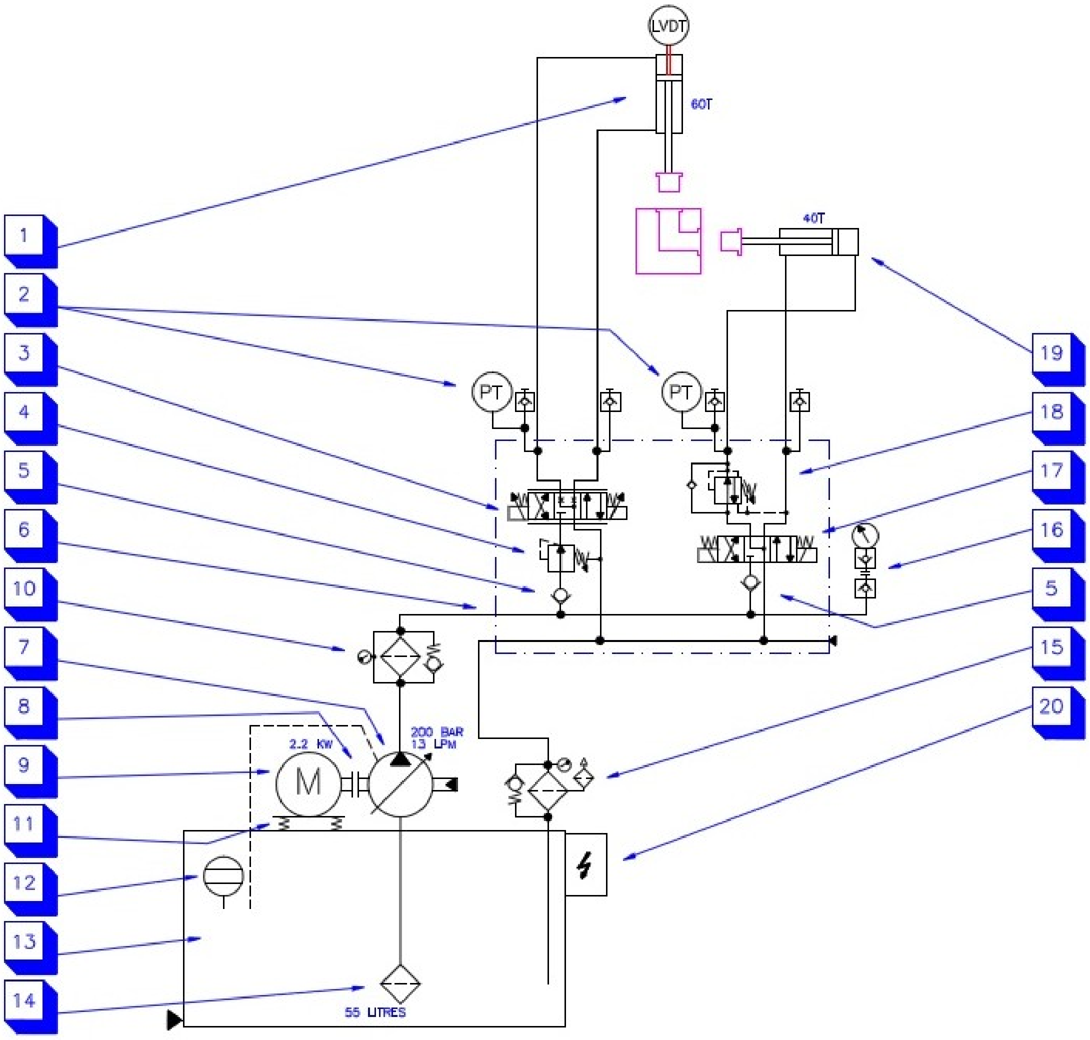

ITEM	DESCRIPTION	PART NUMBER	SUPPLIER	QTY.
1	FOOT MOUNT CYLINDER FITTED WITH LVDT	200MM BORE, 90MM ROD, 200MM STROKE + BTL7 TRANSDUCER	SWP	1
2	PRESSURE TRANSDUCER, 4–20 MA	NAT 250 OA	TRAFAG	2
3	MINI 4 PROPORTIONAL VALVE + INTEGRAL ELECTRONICS MATING PLUG CETOP 3 TO MINI 4 REDUCER	BRW4D41–04–24A2 219.2330 RC–12S1N1280U1 173.1352	WANDFLUH	1
4	CETOP 3 PRESSURE REDUCING VALVE	DGMX2 3 PP FWB 41	VICKERS	1
5	CETOP 3 P LINE CHECK VALVE	DGMPC 3 YPK 41	VICKERS	2
6	CETOP 3 DOUBLE MANIFOLD BLOCK WITH TEST POINTS METRIC TEST POINTS	125161/2 20 10 66	BEP ISIS	1 5
7	PRESSURE COMPENSATED PUMP	A10VSO 10 DFR1/52R VUC14N00	REXROTH	1
8	BELLHOUSING DRIVE COUPLING,	TH1 825A ND65B/R62/ND65HD37–SA16/32 I Z09 0	PEARSONS	1 1
9	2.2KW, 4 POLE, D90, F&F ELECTRIC MOTOR	400/3/50	WEG	1
10	1/2" BSP PRESSURE FILTER	FMM 050 1 BA C A06 N V7	MP FILTRI	1
11	ANTI VIBRATION MOUNTS	5040M25	AV	4
12	FLUID LEVEL GAUGE	LVA20TAM12	MP FILTRI	1
13	55 LITRE TANK	CF55GC	PEARSONS	1
14	1" BSP SUCTION FILTER ELEMENT	STR 070 4S G1 M90	MP FILTRI	1
15	1/2" BSP RETURN LINE FILTER + FILLER BREATHER	MPT 020 3 CA G2 A25 HB V1	MP FILTRI	1
16	0–280 BAR PRESSURE GAUGE TEST POINT & GAUGE CONNECTOR	9332817 20 10 66 + 20 21 33	ISIS	1 1
17	CETOP 3 SOLENOID VALVE	DG4V3 6C MUH7 60	VICKERS	1
18	CETOP 3 A LINE PRESSURE REDUCING/ RELIEVING VALVE	PPDB LAN EB2	SUN	1
19	FOOT MOUNT CYLINDER	200MM BORE, 90MM ROD, 200MM STROKE	SWP	1
20	ELECTRICAL BOX	ELEC–3473	VIKING	1

Fig. A. 1 Layout of the hydraulic system and the component list

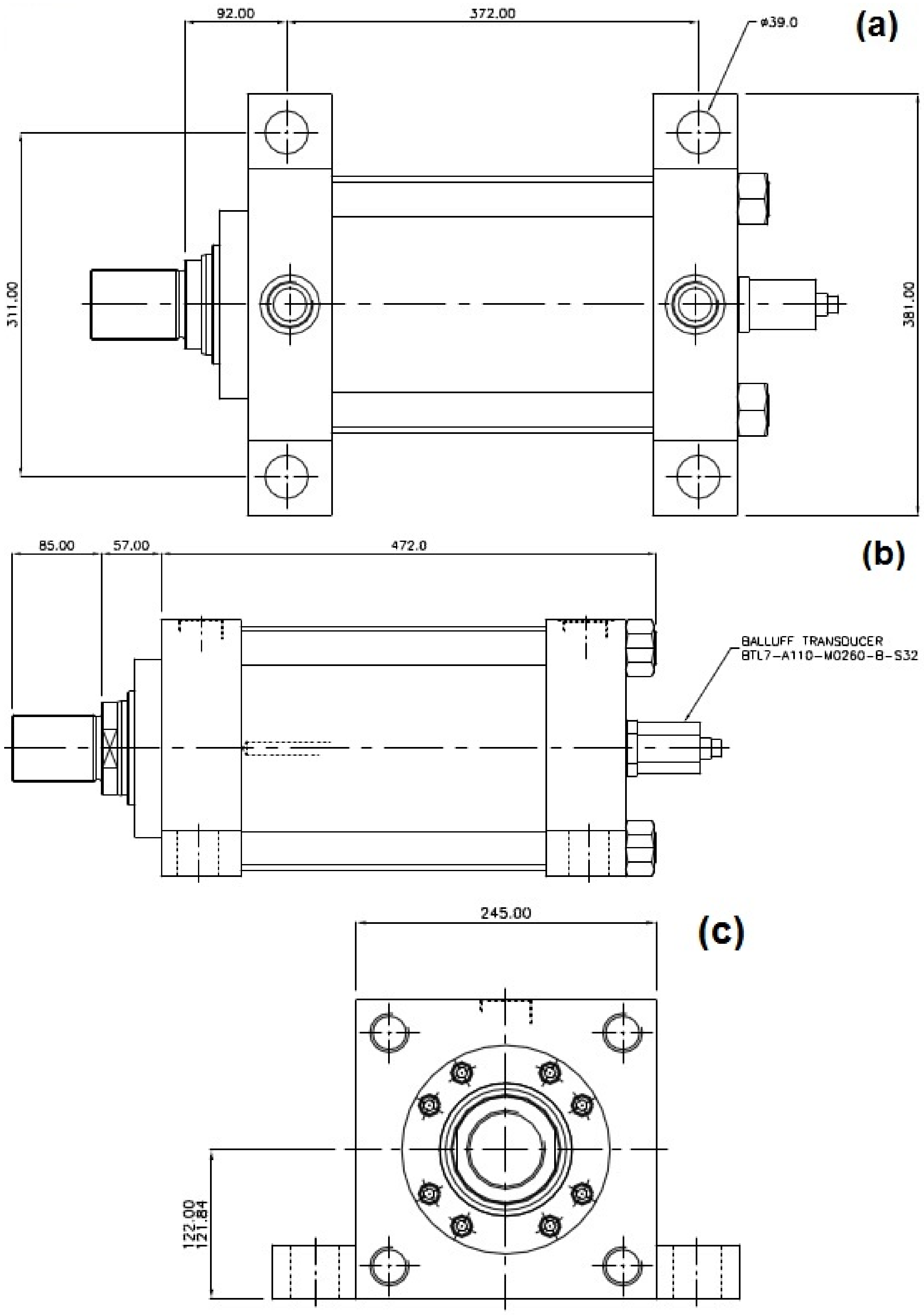

Fig. A. 2 Overall dimensions of the forward cylinder (a) Top view, (b) front view and (c) left view

B. Operation Instruction of A1 Hydraulic Pressing Machining

Ⅰ. Before operation

1. Remove the plunger from the mould; make sure it is clean in the way of the cylinder moving in.

   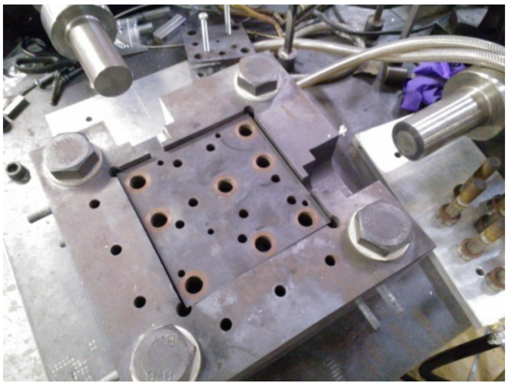

2. Check that the four, 3-way switches are in the mid positions, (items 6,9, 10 &13), which means nothing will happen.
3. Ensure that the emergency stop button (item 3) is pulled out, allowing the motor to be started (item 3)

Ⅱ. Experimental procedure

1. Fit the adaptors, plungers and test sample.
2. Close the mould and tighten the eight screws using torque wrench at the rate of 150ft pounds.
3. Fit the cartridge heaters into the mould.
4. After wearing thermal protective gloves, cover the mould with insulation jacket and put the meshed cage above the mould.
5. After the temperature reaches the target temperature, switch on the machine (item 1), start the motor by pressing ‘Motor Start’ (item 8)
6. Turn the ‘system’ switch (item 6) to ‘Set’ mode, and turn the ‘rear cylinder’ (item 9) switch to ‘out’, extend the rear cylinder towards the sample, until it nearly touches the sample. Centralise the ‘rear cylinder’ (item 9) switch to the off position.
7. Leave the ‘system’ (item 6) switch’ at ‘Set’ mode; turn the ‘front cylinder’ (item 10) switch to ‘out’. Press ‘front cylinder fast’ can extract the front cylinder at the maximum speed of 10 mm/min. Bring the Front Cylinder ‘In’ until it

touches the sample, centralize the ‘front cylinder’ (item 10) switch to the off position.

8. Turn the ‘System’ switch (item 6) to ‘Test’. ‘Test’ running lamp (item 7) should be lit.
9. The Front cylinder will now extend, at the speed set on Item 13. Normally, the speed is 4 mm/min, the maximum speed that can be set is 10mm/min. During the pressing, if the ‘overload’ bottom (item 12) is lit, press ‘emergence stop’ bottom (item 3) to stop the machine.
10. When the limit line on the plunger is pressed into the mould, i.e. the sample is fully pressed through the channels; the test is ended by turning the ‘system’ (item 6) switch to ‘off’.
11. Turn the ‘system’ switch (item 6) to ‘set’ mode, switch the ‘rear cylinder’ (item 9) to ‘in’ to retract the rear cylinder, and retract the front cylinder by turning the ‘front cylinder’ (item 10) to ‘in’.
12. After wearing the thermal protective gloves, remove the cage and the insulation jacket. Fit two cooling plates onto the mould, wait 2 hours for the mould cooling down.
13. After the mould cooling down to room temperature, open the mould using torque wrench and take the sample out.
14. Tidy up the table after finish the experiment. Move the torque wrench to the drawer.

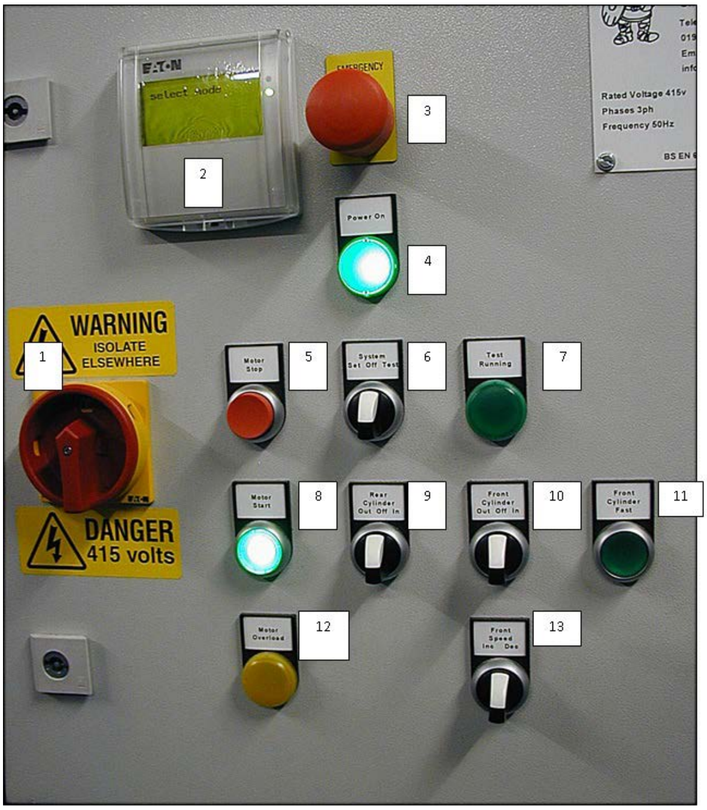

III. Daily inspection for the hydraulic power unit

1. The hydraulic power unit is a self-contained device. It should be filled with oil, to the upper level on the fluid level gauge before being run.
2. The return line filter element condition gauge should be checked daily, the element changed if the gauge shows in the red portion.
3. The pressure filter element condition gauge should be checked daily, the element changed if the gauge shows in the red portion.
4. The overall pressure capability of the power unit is controlled by the compensator mounted to the tank. This should not be set any higher than 200 Bar, as the system has not been designed for this.

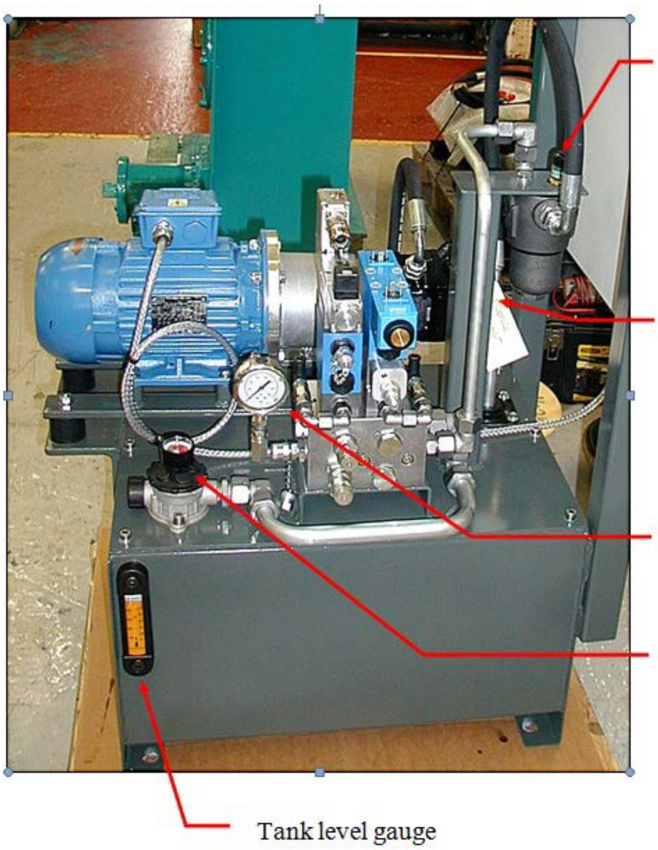

Pressure filter element condition gauge

Pump pressure compensator (pressure control), is just behind the filter support. It is the adjuster nearest the tank. Unscrew to reduce pressure (anti-clockwise)

System Pressure gauge

Return line filter element condition gauge.
Remove top of filter to fill tank

Tank level gauge

C. Design of Die and Accessories

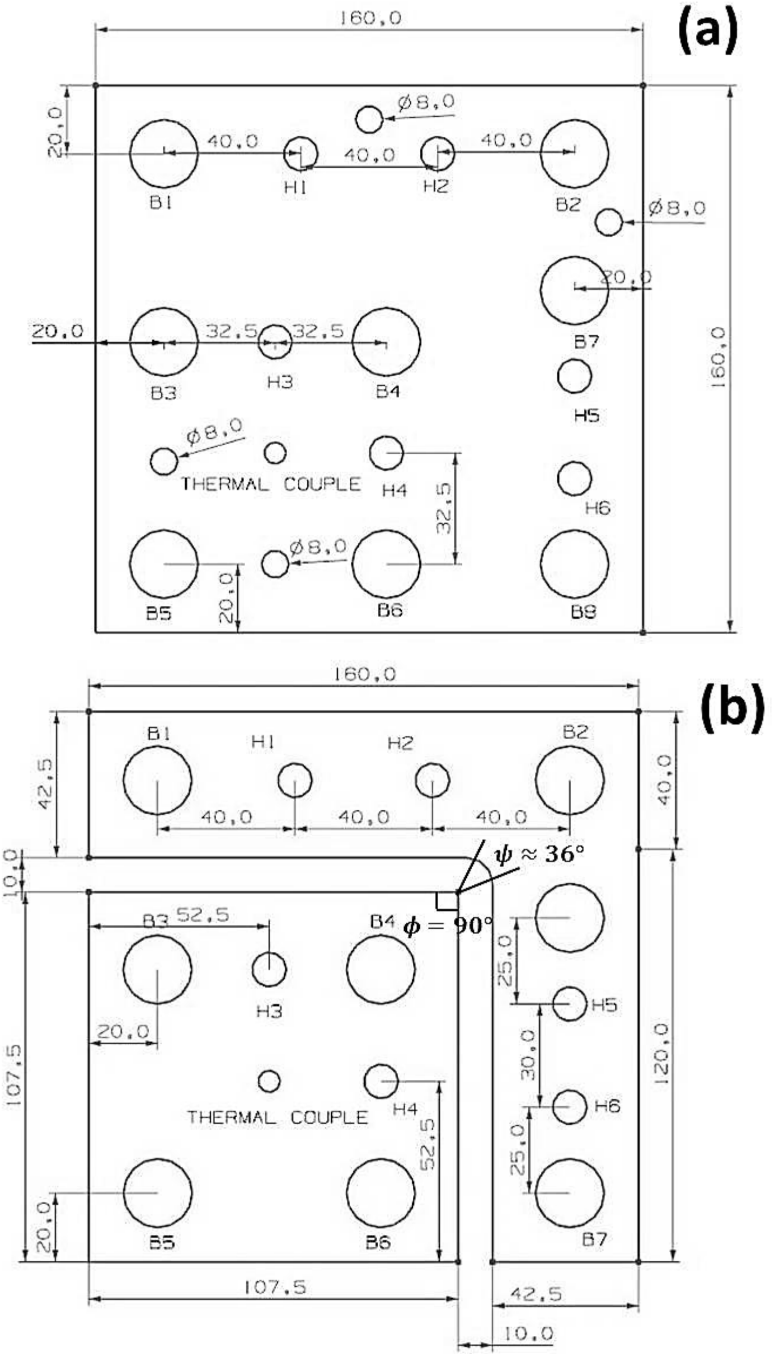

Fig. C. 1 Design of the inner mould: (a) the upper part and (b) the bottom part.

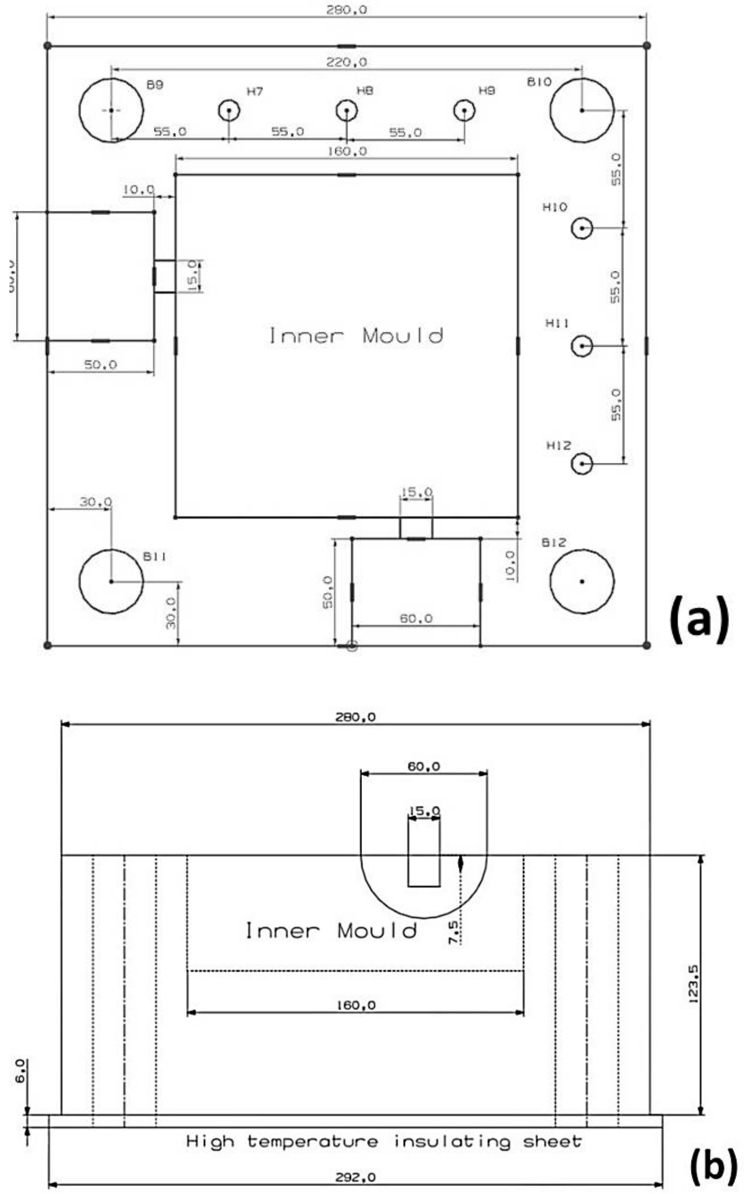

Fig. C. 2 (a) The top view and (b) the front view of the die housing.

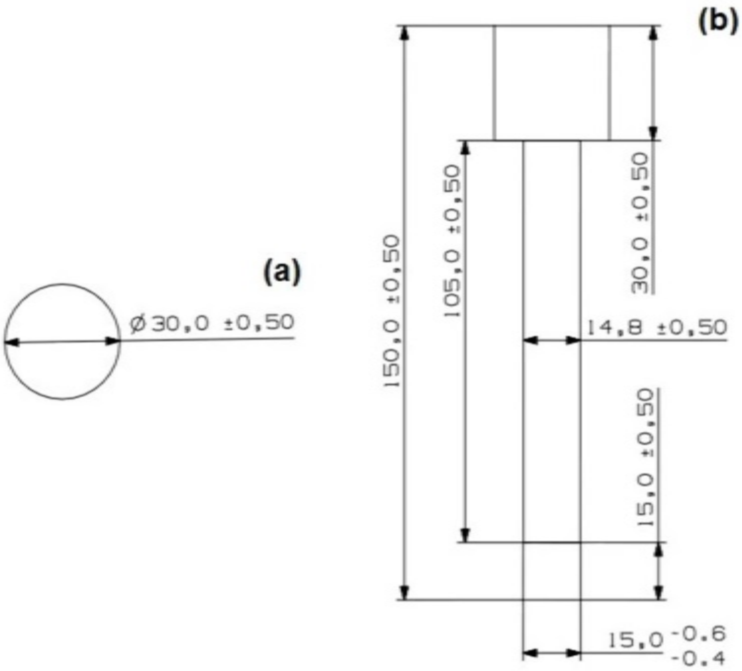

Fig. C. 3 (a) The top view and (b) the front view of the plungers

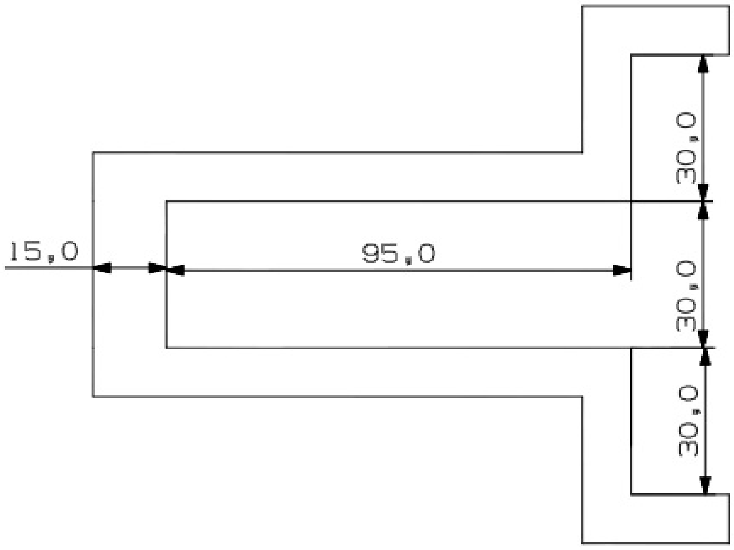

Fig. C. 4 The cross-section of the adaptor